New dimensions in cardiovascular CT

Robbert W. van Hamersvelt

New dimensions in cardiovascular CT

Thesis, Utrecht University, The Netherlands

Copyright © R.W. van Hamersvelt, 2019

New dimensions in cardiovascular CT

Nieuwe dimensies in cardiovasculaire CT
(met een samenvatting in het Nederlands)

Proefschrift

ter verkrijging van de graad van doctor aan de Universiteit Utrecht
op gezag van de rector magnificus, prof. dr. H.R.B.M. Kummeling,
ingevolge het besluit van het college voor promoties in het openbaar te verdedigen
op donderdag 14 maart 2019 des ochtends te 10.30 uur

door

Robbert Willem van Hamersvelt

geboren op 6 augustus 1989 te Nijmegen

Promotoren: Prof. dr. T. Leiner
                    Prof. dr. P.A. de Jong

Copromotoren: Dr. M.J. Willemink
                    Dr. I. Išgum

Contents

Part IV – Rationale for comprehensive dual-energy CT imaging of coronary artery disease

Part V – Summary and Discussion

Chapter 1

General introduction

1

Cardiovascular diseases are the leading cause of death globally, accounting for an estimated 17.9 million deaths in 2016 (31% of all deaths) [1]. In the Netherlands, cardiovascular diseases are no longer the leading cause of death, accounting for 26% of all deaths in 2016 (around 38,500 deaths) [2]. Coronary artery disease (CAD) is a major component of cardiovascular diseases, with each year around 80,000 newly diagnosed patients and an overall prevalence of 730,000 in the Netherlands [3]. Due to aging of the population, this number is expected to increase even further to 931,000 in 2040 [4]. The pathological mechanism underlying CAD is atherosclerosis, which is a chronic inflammatory disease of the vessel wall leading to plaque deposition [5]. This can lead to luminal narrowing of the coronary artery, also known as coronary stenosis. A coronary stenosis may lead to a reduction of blood flow to the myocardium, which subsequently could lead to myocardial ischemia based on an imbalance between oxygen supply and demand. Atherosclerosis can also lead to rupture of a vulnerable plaque, which may induce an acute obstruction of coronary flow due to thrombosis and thereby lead to myocardial infarction [5]. In case of myocardial infarction, acute percutaneous coronary intervention (PCI) is the preferred treatment for myocardial revascularization [6]. In patients with stable CAD, treatment consist of optimal medical therapy, PCI or coronary artery bypass graft (CABG) and is guided based on the presence of a significant obstructive coronary stenosis and the presence of ischemia [7]. A large trial has shown that in patients with functionally significant stenosis as indicated by invasive fractional flow reserve (FFR), PCI with a drug eluting stent or CABG improved outcome compared to optimal medical therapy alone, while for patients without functionally significant stenosis, optimal medical therapy alone was favourable [7, 8]. This indicates that when evaluating CAD, both anatomical and functional analyses are essential.

Imaging of CAD using computed tomography

Cardiac computed tomography (CT) is an established diagnostic tool to detect and rule out CAD with consistently high sensitivity and negative predictive value [9]. Therefore, it has been suggested as a gatekeeper to the catheterization laboratory in patients with suspected CAD [10]. Typically, an investigation comprises a non-contrast cardiac CT scan followed by a contrast enhanced coronary CT scan (CCTA). The non-contrast CT scan is used for stratification of risk for future cardiovascular events by quantification of atherosclerotic calcifications in the coronary arteries, thoracic aorta and on the cardiac valves [11, 12]. The CCTA is used to evaluate CAD in the coronary lumen. By evaluation of the coronary anatomy, together with the morphology of plaques, narrowing of the lumen can be defined as degree of

1

coronary stenosis. In daily clinical practice, a stenosis with ≥50% luminal narrowing is considered significant and is referred for further testing. However, a significant degree of coronary stenosis does not necessarily imply myocardial ischemia. When compared to invasive FFR, degree of stenosis evaluation on CT lacks specificity in indicating the functional significance of a coronary stenosis [13]. Additional testing with single photon emission computed tomography, positron emission tomography or magnetic resonance imaging allows for evaluation of ischemia in the myocardium. However, these modalities have difficulties visualizing the coronary arteries and are therefore mainly focused on analysis of the myocardium.

Functional analysis of CAD using CT

Recent developments in CT- and software techniques offer the opportunity for functional analysis of CAD on CT. One of these methods is CCTA-derived fractional flow reserve (CT-FFR). Lumen segmentations derived from CCTA are used as input for CT-FFR algorithms. Algorithms, based on computational fluid dynamics or lumped models, simulate blood flow and pressure drop, thereby allowing for virtual FFR evaluation [14, 15].

Another approach to functional CAD analysis is evaluation of ischemia in the myocardium. With CT perfusion (CTP), the distribution of contrast media is evaluated during drug-induced stress. As the distribution of contrast media is determined by the blood flow to the myocardium, perfusion defects causing ischemia can be detected [16]. There are two ways to acquire CTP; dynamic or static. With dynamic CTP, a continuous scan is made over multiple cardiac phases to acquire the first pass of the contrast media, allowing for quantitative analysis of perfusion. However, the downside of continuous scanning is that dynamic CTP comes at the cost of relatively high radiation dose. The radiation dose is much lower for static CTP, where the contrast media distribution is evaluated at a single moment in time by acquiring only one scan at a predefined optimal time point. New developments in machine learning may even allow for ischemia evaluation on resting CCTA without performing an extra stress scan, as initial results of an automatic deep learning study showed the potential to identify patients with functionally significant stenosis by analysis of the myocardium on CCTA scans acquired at rest [17].

1

Evaluation of CAD using dual-energy CT

Dual-energy CT (DECT) is a technique that discriminates low and high energy X-ray photons, thereby allowing for reconstruction of virtual monochromatic images at discrete energy levels between 40-200 keV. Images at high keV are less prone to artefacts of calcified plaques, while images at low keV will enhance the iodine contrast in the lumen (**Figure 1**). Therefore, plaque specific virtual monochromatic images can be used to improve detection and quantification of coronary plaques and degree of coronary stenosis [18, 19]. This might also improve CT-FFR evaluation, as lumen segmentations can be affected by these artefacts.
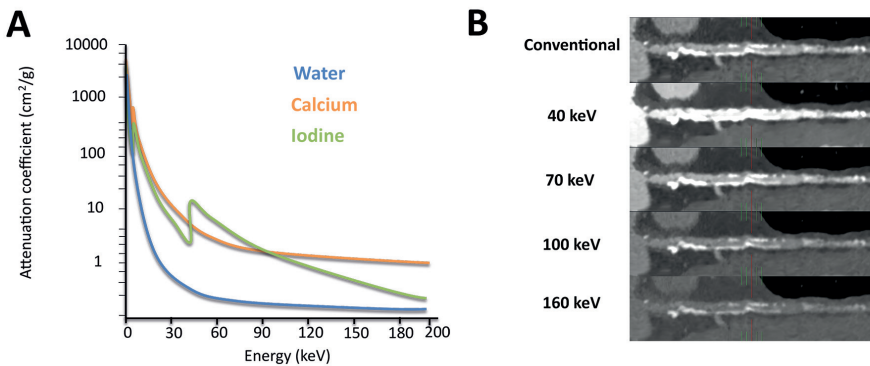
Figure 1 Virtual monochromatic imaging. Image **A** shows a graphical depiction of the attenuation coefficient as a function of energy for water, calcium and iodine. At each discrete energy level between 40-200 keV virtual monochromatic images can be created. Image **B** shows stretched multiplanar reconstructions of the left anterior descending coronary artery at different energy levels. At lower energy (keV), the attenuation of iodine increases. Whereas at higher energy (keV) the attenuation of iodine is decreased and artefacts of the calcified plaques are reduced.

Another feature that is enabled by DECT is material decomposition. Materials with high atomic numbers (e.g. iodine and gadolinium) can be characterized by their high attenuation profiles at low keV caused by the substantial increase in photoelectric effect when nearing the K-edge of these materials. DECT uses these material specific attenuation profiles and allows for assessment of myocardial iodine distribution and quantification. This can be applied in both rest CCTA and static CTP images as a surrogate for tissue perfusion, quantifying the amount of contrast in the myocardium at a single point in time [20]. Together with virtual monochromatic imaging, DECT may allow for improved anatomical and functional evaluation of CAD.

1

Drawbacks of CT

Although CT has the potential to perform both anatomical and functional evaluation of CAD in one investigation, it also has some potential drawbacks, which need to be addressed. This includes the use of ionizing radiation dose, which potentially induces a small individual risk on cancer [21]. With the application of iterative reconstruction, cardiac CT can be performed at low dose while preserving image quality [22]. Furthermore, the use of iodinated contrast media can cause allergic reactions or contrast-induced nephropathy and its use can be limited in patients with impaired renal function [23]. By using lower iodine concentrations or by switching to other contrast agents such as gadolinium, the risk of contrast-induced nephropathy is reduced [23].

Outline of this thesis

In light of the above, this thesis will focus on reduction of the drawbacks of CT and evaluate the possibilities of the described non-invasive CT techniques for both anatomical and functional analysis of CAD. This thesis aspires to expand the diagnostic performance of CT for the evaluation of functionally significant CAD.

This thesis consists of five parts. **Part I** of this thesis is focused on evaluation of calcium scoring at reduced radiation dose. In **chapters 2 & 3**, prospective studies on low-dose non-contrast CT will focus on the clinical implementation of dose reduction in cardiothoracic CT. In **chapter 2**, the inter-observer and inter-examination reliability and agreement for quantification of cardiac valve calcifications on low-dose unenhanced ungated lung cancer screening CT scans is evaluated. Lung cancer screening with low-dose CT is of growing interest. As heavy smoking is associated with cardiovascular mortality, and the heart is also depicted on these scans, individualized risk of adverse cardiovascular events can be assessed by evaluating the presence and extent of calcifications in the coronary arteries, cardiac valves and thoracic aorta. This may also be worthwhile in patients who receive a cardiac CT or chest CT in daily clinical practice, where quantification of these calcifications may add to individual risk assessment for cardiovascular events. In **chapter 3**, we explore the maximally achievable radiation dose reduction with iterative reconstruction at which quantification of aortic valve and thoracic aorta calcification is still feasible in patients who received a cardiac or chest CT.

Part II consists of preclinical research performed on phantoms and is focused on safety and quality control in DECT. In **chapter 4**, the feasibility and extent to which iodine concentration can be reduced without loss of objective image quality using

1

low tube voltage and virtual monochromatic images is investigated. In **chapter 5**, the accuracy of iodine quantification in latest generation DECT scanners is evaluated and in **chapter 6** the use of gadolinium as an alternative contrast agent for DECT is explored.

In **part III**, new technical developments for functional evaluation of CAD on CCTA at rest are investigated. In **chapter 7**, the diagnostic performance of an on-site CT-FFR algorithm for the evaluation of functionally significant stenosis is investigated. In **chapter 8**, both anatomical and functional analyses are combined for the identification of functionally significant stenoses. In this chapter, the potential added value of deep learning analysis of the myocardium over determination of degree of stenosis is evaluated.

Part IV is focused on the clinical perspective, and sheds light on the rationale for comprehensive DECT imaging for the evaluation of CAD. In **chapter 9**, the rational and design of the CLARITY study (application of speCtraL computed tomogrAphy to impRove specIficity of cardiac compuTed tomographY) is described. By combining different (DE)CT- and software techniques, the CLARITY study strives to improve the specificity of CCTA for the identification of functionally significant stenosis and will shed light on the possibility of a one-stop shop in the evaluation of CAD.

Part V consists of **chapter 10**, which contains a summary of the results presented in this thesis and a general discussion elaborating on these findings and future perspectives on this topic.

1

References

1. World Health Organisation (2017) Key facts Cardiovascular diseases (CVDs). http://www.who.int/en/news-room/fact-sheets/detail/cardiovascular-diseases-(cvds). Accessed 17 Sep 2018

2. Centraal Bureau voor de Statistiek (2018) Deaths; underlying cause of death (shortlist), sex, age. https://opendata.cbs.nl/statline/#/CBS/en/dataset/7052eng/table?ts=1541668612724. Accessed 8 Nov 2018

3. Leening MJG, Siregar S, Vaartjes I, et al (2014) Heart disease in the Netherlands: a quantitative update. Netherlands Hear J 22:3–10. doi: 10.1007/s12471-013-0504-x

4. van Dis I, Buddeke J, Vaartjes I, et al (2015) Hart- en vaatziekten in Nederland 2015, cijfers over heden, verleden en toekomst. Den Haag: Hartstichting, 2015.

5. Weber C, Noels H (2011) Atherosclerosis: current pathogenesis and therapeutic options. Nat Med 17:1410–22. doi: 10.1038/nm.2538

6. Neumann F-J, Sousa-Uva M, Ahlsson A, et al (2018) 2018 ESC/EACTS Guidelines on myocardial revascularization. Eur Heart J. doi: 10.1093/eurheartj/ehy394

7. Task Force Members, Montalescot G, Sechtem U, et al (2013) 2013 ESC guidelines on the management of stable coronary artery disease. Eur Heart J 34:2949–3003. doi: 10.1093/eurheartj/eht296

8. Xaplanteris P, Fournier S, Pijls NHJ, et al (2018) Five-Year Outcomes with PCI Guided by Fractional Flow Reserve. N Engl J Med 379:250–259. doi: 10.1056/NEJMoa1803538

9. Budoff MJ, Dowe D, Jollis JG, et al (2008) Diagnostic performance of 64-multidetector row coronary computed tomographic angiography for evaluation of coronary artery stenosis in individuals without known coronary artery disease: results from the prospective multicenter ACCURACY (Assessment by Coronary Computed Tomographic Angiography of Individuals Undergoing Invasive Coronary Angiography) trial. J Am Coll Cardiol 52:1724–32. doi: 10.1016/j.jacc.2008.07.031

10. Rudziński PN, Kruk M, Kępka C, et al (2018) The value of Coronary Artery computed Tomography as the first-line anatomical test for stable patients with indications for invasive angiography due to suspected Coronary Artery Disease: CAT-CAD randomized trial. J Cardiovasc Comput Tomogr. doi: 10.1016/j.jcct.2018.08.004

11. Jacobs PC, Prokop M, van der Graaf Y, et al (2010) Comparing coronary artery calcium and thoracic aorta calcium for prediction of all-cause mortality and cardiovascular events on low-dose non-gated computed tomography in a high-risk population of heavy smokers. Atherosclerosis 209:455–462. doi: 10.1016/j.atherosclerosis.2009.09.031

12. Owens DS, Budoff MJ, Katz R, et al (2012) Aortic valve calcium independently predicts coronary and cardiovascular events in a primary prevention population. JACC Cardiovasc Imaging 5:619–25. doi: 10.1016/j.jcmg.2011.12.023

13. Ko BS, Wong DTL, Cameron JD, et al (2014) 320-row CT coronary angiography predicts freedom from revascularisation and acts as a gatekeeper to defer invasive angiography in stable coronary artery disease: a fractional flow reserve-correlated study. Eur Radiol 24:738–47. doi: 10.1007/s00330-013-3059-8

14. Min JK, Leipsic J, Pencina MJ, et al (2012) Diagnostic Accuracy of Fractional Flow Reserve From Anatomic CT Angiography. JAMA 308:1237. doi: 10.1001/2012.jama.11274

15. Donnelly PM, Kolossváry M, Karády J, et al (2018) Experience With an On-Site Coronary Computed Tomography-Derived Fractional Flow Reserve Algorithm for the Assessment of Intermediate Coronary Stenoses. Am J Cardiol 121:9–13. doi: 10.1016/j.amjcard.2017.09.018

1

16. Rossi A, Merkus D, Klotz E, et al (2014) Stress myocardial perfusion: imaging with multidetector CT. Radiology 270:25–46. doi: 10.1148/radiol.13112739

17. Zreik M, Lessmann N, van Hamersvelt RW, et al (2018) Deep learning analysis of the myocardium in coronary CT angiography for identification of patients with functionally significant coronary artery stenosis. Med Image Anal 44:72–85. doi: 10.1016/j.media.2017.11.008

18. Symons R, Choi Y, Cork TE, et al (2018) Optimized energy of spectral coronary CT angiography for coronary plaque detection and quantification. J Cardiovasc Comput Tomogr 12:108–114. doi: 10.1016/j.jcct.2018.01.006

19. Stehli J, Clerc OF, Fuchs TA, et al (2016) Impact of monochromatic coronary computed tomography angiography from single-source dual-energy CT on coronary stenosis quantification. J Cardiovasc Comput Tomogr 10:135–40. doi: 10.1016/j.jcct.2015.12.008

20. Delgado Sánchez-Gracián C, Oca Pernas R, Trinidad López C, et al (2016) Quantitative myocardial perfusion with stress dual-energy CT: iodine concentration differences between normal and ischemic or necrotic myocardium. Initial experience. Eur Radiol 26:3199–207. doi: 10.1007/s00330-015-4128-y

21. Lin EC (2010) Radiation Risk From Medical Imaging. Mayo Clin Proc 85:1142–1146. doi: 10.4065/mcp.2010.0260

22. Willemink MJ, Leiner T, de Jong PA, et al (2013) Iterative reconstruction techniques for computed tomography part 2: initial results in dose reduction and image quality. Eur Radiol 23:1632–42. doi: 10.1007/s00330-012-2764-z

23. Tepel M, Aspelin P, Lameire N (2006) Contrast-induced nephropathy: a clinical and evidence-based approach. Circulation 113:1799–806. doi: 10.1161/CIRCULATIONAHA.105.595090

Part I

Low dose
calcium scoring
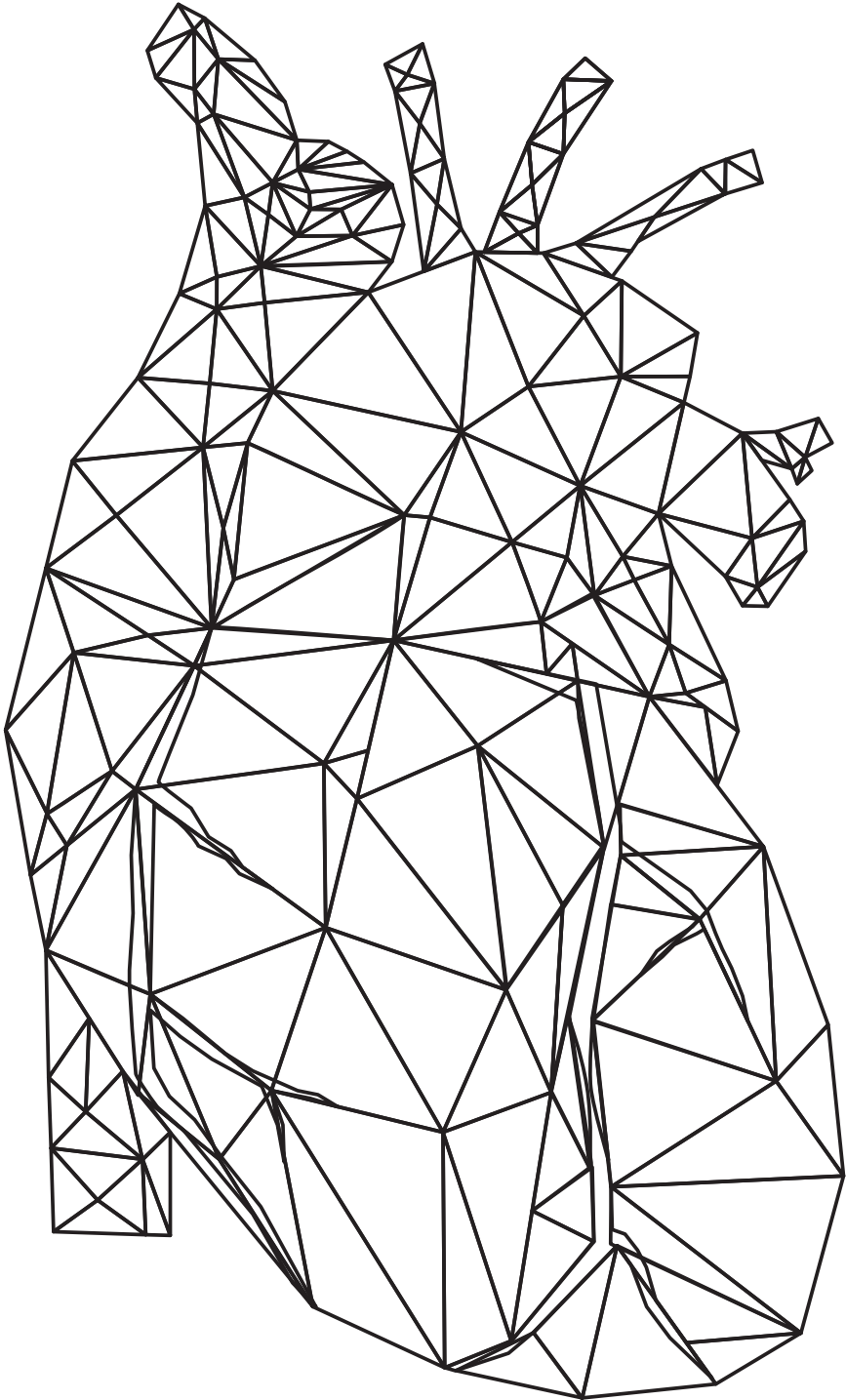
Chapter 2

Cardiac valve calcifications on low-dose unenhanced ungated chest computed tomography: inter-observer and inter-examination reliability, agreement and variability

Robbert W. van Hamersvelt
Martin J. Willemink
Richard A. P. Takx
Anouk L. M. Eikendal
Ricardo P. J. Budde
Tim Leiner
Christian P. Mol
Ivana Išgum
Pim A. de Jong

2

Abstract

Objectives

To determine inter-observer and inter-examination variability for aortic valve calcification (AVC) and mitral valve and annulus calcification (MC) in low-dose unenhanced ungated lung cancer screening chest computed tomography (CT).

Methods

We included 578 lung cancer screening trial participants who were examined by CT twice within 3 months to follow indeterminate pulmonary nodules. On these CTs, AVC and MC were measured in cubic millimetres. One hundred CTs were examined by five observers to determine the inter-observer variability. Reliability was assessed by kappa statistics (κ) and intraclass correlation coefficients (ICCs). Variability was expressed as the mean difference ± standard deviation (SD).

Results

Inter-examination reliability was excellent for AVC (κ = 0.94, ICC = 0.96) and MC (κ = 0.95, ICC = 0.90). Inter-examination variability was 12.7 ± 118.2 mm^3 for AVC and 31.5 ± 219.2 mm^3 for MC. Inter-observer reliability ranged from κ = 0.68 to κ = 0.92 for AVC and from κ = 0.20 to κ = 0.66 for MC. Inter-observer ICC was 0.94 for AVC and ranged from 0.56 to 0.97 for MC. Inter-observer variability ranged from -30.5 ± 252.0 mm^3 to 84.0 ± 240.5 mm^3 for AVC and from -95.2 ± 210.0 mm^3 to 303.7 ± 501.6 mm^3 for MC.

Conclusions

AVC can be quantified with excellent reliability on ungated unenhanced low-dose chest CT, but manual detection of MC can be subject to substantial inter-observer variability. Lung cancer screening CT may be used for detection and quantification of cardiac valve calcifications.

2

Introduction

Cardiovascular disease is a major cause of morbidity and mortality worldwide, especially in heavy smokers [1, 2]. Lung cancer screening with low-dose computed tomography (CT) is a growing interest [3]. Since the heart is also depicted on these ungated low-dose screening CT examinations and the use of tobacco is also a risk factor for cardiovascular disease, the scope of screening could be extended with markers for cardiovascular disease [4, 5]. It is known that calcifications of the thoracic aorta and coronary arteries, obtained from ungated CT examinations, can predict cardiovascular events [6, 7]. Additionally, aortic valve calcifications (AVC) and mitral valve and annulus calcifications (MCs) may also reflect relevant subclinical disease. AVC and mitral annulus calcifications (MACs) are both associated with cardiovascular disease [8, 9], and AVC has been shown to be an independent predictor of cardiovascular and coronary events, beyond traditional risk factors [10]. However, application of this finding in prognostic and aetiological studies would only be of value if calcifications could be measured with acceptable inter-examination and inter-observer variability on lung cancer screening CT. AVC and MAC have been proven to be sensitive measures and reproducible to allow serial investigations on electrocardiogram gated electron beam tomography and multidetector CT [11–14]; however, the reproducibility of AVC and MC detection and quantification on ungated low-dose chest CT examinations is unknown.

The aim of the current study was to determine the inter-observer and inter-examination reliability, agreement and variability in ungated low-dose unenhanced lung cancer screening CT examinations.

Materials and Methods

Study population

The Dutch Belgium lung cancer screening trial (NELSON study) is a randomised controlled population-based trial comprising 15,822 men and women aged 50 to 75 years [15]. The subjects are current or former (who quit less than 10 years before baseline) smokers with a smoking history of at least 16 cigarettes per day for 25 years or at least 11 cigarettes per day for 30 years (resulting in more than 16.5 pack-years). Exclusion criteria for participating in the trial were self-reported moderate or bad health with inability to climb two flights of stairs, a recent chest CT, current or past cancer and a body weight ≥140 kg. From 2004 to 2006, baseline CTs were performed in 7,557 participants randomly allocated to the screening group. The Medical Ethics Committees of all four participating hospitals approved the NELSON study protocol, and written informed consent was obtained from all participants.

2

CTs were performed at baseline, 1-, 3.5- and 5.5-year follow-up. Subjects with an intermediate risk lung nodule received a short-term repeat CT after 3 months. A more detailed description of patient selection and data collection has been published elsewhere [16]. For the present study we retrospectively included 578 consecutive subjects who underwent a short-term repeat CT after 3 months because of an indeterminate pulmonary nodule at the University Medical Center Utrecht. These subjects were selected because the short interval enabled the assessment of inter-examination variability for slowly progressive disease processes such as cardiac valve calcifications.

Imaging acquisition

All subjects underwent an ungated low-dose chest CT without injection of intravenous contrast at both time points. All images were obtained with a 16-slice multidetector CT system with a collimation of 16 × 0.75 mm (Mx8000 IDT or Brilliance-16P; Philips Healthcare, Best, The Netherlands). Low-dose exposure settings were applied based on body weight: 120 kVp for subjects <80 kg or 140 kVp for subjects >80 kg both at 30 mAs, yielding an effective dose of <0.9 and <1.6 mSv, respectively. Axial images with a slice thickness of 1 mm at 0.7 mm increment were reconstructed using a standard thorax reconstruction kernel (filter B).

Measurement of heart valve calcifications

Calcium quantification was manually performed using in house-developed software in which the observer identifies calcification by a mouse click and assigns it to either the mitral annulus/valve or aortic valve. The computer uses a three-dimensional connected component labelling and a threshold of 130 Hounsfield units to calculate the amount of calcium as volume in cubic millimetres [17]. The absence of calcification was assigned a volume of 0. Because of the difficulty to anatomically discern the mitral valve and annulus on an ungated low-dose CT without contrast, both values were summed as total mitral calcification (MC).

Inter-examination variability

For the inter-examination variability one chest radiologist (10 years of experience in chest radiology) examined the baseline (examination 1) and the follow-up CT after 3 months (examination 2) in all 578 subjects for the presence of AVC and MC. Calcifications were quantified as described previously. To minimise the intra-observer variability, the two examinations of each subject were scored in succession. The potential difference in outcome is therefore mostly due to the inter-examination variability and not to intra-observer variability.

Inter-observer variability

From a total of 578 subjects (1,156 examinations), 100 examinations were selected by one observer from the database to be scored by 5 observers. Selection was made to enrich the database with a sufficient number of cases with mitral valve or annulus calcifications, since these calcifications are relatively rare. Observers 1 and 2 are board-certified radiologists who have 10 and 7 years' experience in chest radiology respectively. Observers 3, 4 and 5 are MDs doing a PhD study on cardiovascular CT imaging. All examinations were analysed for the presence of AVC and MC and quantified as described earlier. The observers were blinded to subjects' characteristics and the findings of the other observers.

Statistical analysis

To evaluate the inter-examination and inter-observer variability, we first defined the reliability of the examinations/observers by using kappa statistics (κ) for present versus absent calcifications. κ-values were interpreted as follows: absence of agreement 0, poor agreement <0.20, fair agreement 0.21–0.40, moderate agreement 0.41–0.60, good agreement 0.61–0.80 and excellent agreement >0.80 [18]. For subjects in whom at least one examination (inter-examination) or one observer (inter-observer) reported a volumetric score higher than 0, the inter-examination or inter-observer variability was calculated as the absolute mean difference ± standard deviation (SD). Intra-class correlation coefficients (ICCs) were used to assess the reliability of the volumetric measurements. ICCs can be interpreted as the percentage of variability between ratings due to differences between patients, not due to errors caused by different observers [19]. The two-way random single measure ICC (2, 1) was computed for inter-examination and inter-observer ICCs, since a sample of patients and a sample of examinations or observers was evaluated. ICCs exceeding 0.7 are considered good and ICCs above 0.8 are considered excellent [20]. The limits of inter-examination agreement were defined as the mean difference ± 1.96 × SD. The limits of agreement, mean differences and variabilities were plotted using the Bland-Altman method [21]. Inter-observer variabilities were plotted using a method described by Jones et al. [22], which is a modification of the Bland-Altman plot [21] that can be used for more than two observers and retains the ability to evaluate consistency of agreement over different magnitudes of continuous measurements using a single plot. The difference of each observer pertaining to the mean of all observers is plotted against the mean of all observers. The limits of agreement with the mean were estimated as the mean ± 1.96 × SD, where SD is an estimate of the standard deviation for all observers and can be evaluated as described in the article of Jones et al. Bland- Altman plots and ICCs were calculated using MedCalc version 12.7.5.0,

Mariakerke Belgium. κ-values, means and standard deviations were calculated using IBM SPSS version 20.0.

Results

Subject characteristics

Our study population consisted of 578 subjects with a median age (interquartile range, IQR) of 59 (8) years at the time of baseline CT, of which 490 (85 %) were male. The baseline characteristics are presented in **Table 1**. The prevalence of AVC and MC and the mean valve calcification volume of the subjects with calcifications are listed in **Table 2**. An example of a subject with a calcified aortic valve is demonstrated in **Figure 1**.

Table 1 Baseline characteristics (N = 578)

	Values
Gender (N, %)	
Male	490 (85%)
Female	88 (15%)
Age (median, IQR)	59 (8)
Smoking status (N, %)	
Current smoker	335 (58%)
Former smoker	243 (42%)
Pack years (median, IQR)	38.7 (135.7)

IQR = interquartile range

Table 2 Prevalence and volume of aortic valve and mitral valve or annulus calcifications per examination.

	Aortic Valve Calcifications		Mitral valve or Annulus Calcifications	
	Prevalence N (% total)	Volume (mm^3) Mean (SD)*	Prevalence N (% total)	Volume (mm^3) Mean (SD)*
First exam	163 (28.2)	216.9 (382.7)	32 (5.5)	304.5 (353.1)
Follow up exam	158 (27.3)	210.3 (363.3)	33 (5.7)	262.8 (464.0)
Observer 1	55 (55)	414.1 (569.6)	30 (30)	358.6 (490.3)
Observer 2	53 (53)	455.9 (589.2)	21 (21)	438.2 (557.7)
Observer 3	47 (47)	456.5 (598.2)	11 (11)	513.5 (745.0)
Observer 4	42 (42)	548.6 (677.2)	7 (7)	538.0 (518.3)
Observer 5	46 (46)	426.7 (594.4)	7 (7)	235.4 (204.4)

*Mean (SD) includes only those subjects in whom calcification is present. Total number of both first and follow-up examinations is 578, total number of examinations evaluated by the five observers is 100. SD = standard deviation
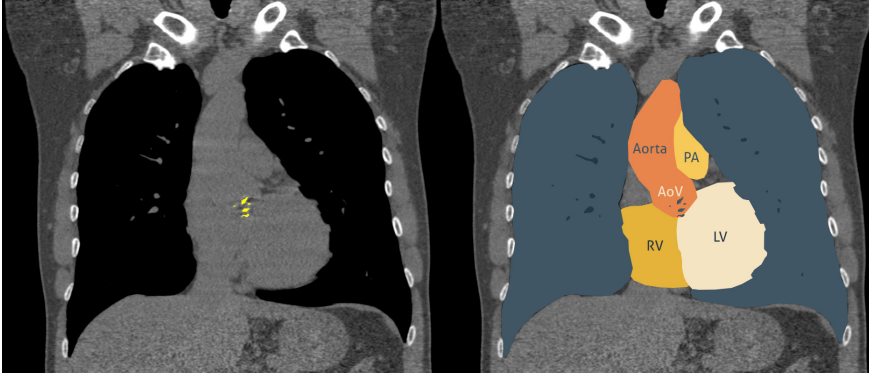
Figure 1 Example image of a subject with a calcified aortic valve.
PA = pulmonary artery; AoV = calcified aortic valve; LV = left ventricle; RV = right ventricle

Aortic Valve Calcifications

Inter-examination variability

Four hundred ten of 578 subjects had no AVC on both CTs. The inter-examination reliability for the presence of calcifications was excellent with a κ-value of 0.94. In the subjects with AVC on any CT, absolute mean (SD) inter-examination variability was 12.7 (118.2) mm^3. The reliability of the volumetric measurements was excellent with an ICC of 0.96. The inter-examination agreement for all subjects is displayed in **Figure 2**.

Inter-observer variability

Of all 100 CT examinations the observers detected AVC in 42 to 55 subjects. Inter-observer reliability for detecting AVC presence was excellent when comparing observers 1, 2, 3 and 5 with a κ-value of 0.82 to 0.92 and good when comparing observer 4 with the rest with a κ-value of 0.68 to 0.74 (**Table 3**). Taking only the CTs with AVC, seen by at least one of the compared observers, the absolute difference in interobserver variability ranged from -30.5 (252.0) mm^3 to 84.0 (240.5) mm^3 (**Table 3**). The ICC for all observers was excellent with a value of 0.94. The inter-observer agreement for AVC in all 100 examinations is displayed in **Figure 3**.

Mitral Valve and Annulus Calcifications

Inter-examination variability

In 544 of 578 subjects no MC was present on any examination. Inter-examination reliability of observing MC presence was excellent with a κ-value of 0.95. In the

2
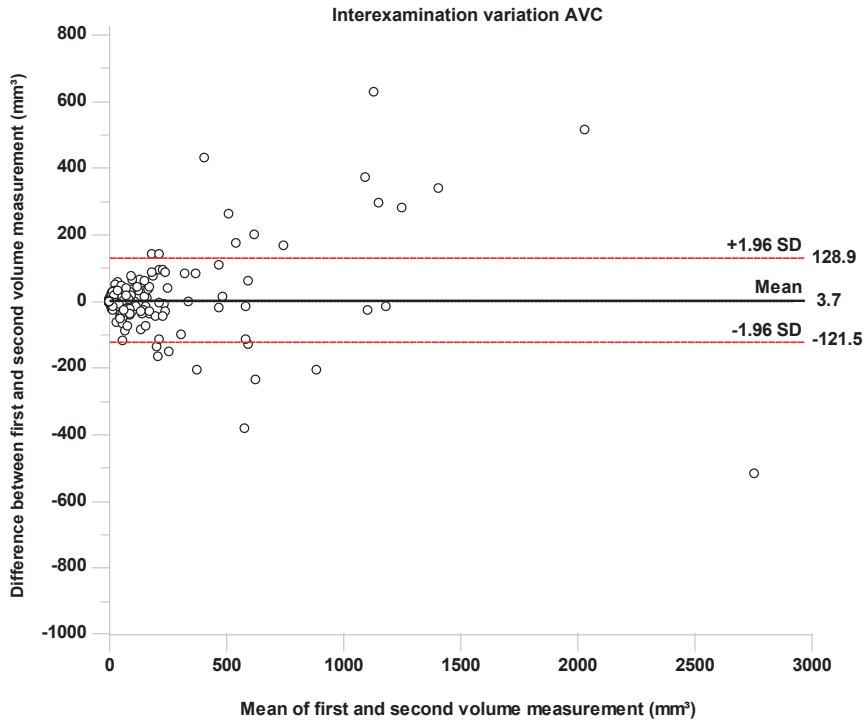
Figure 2 Bland-Altman plot of aortic valve inter-examination agreement for all subjects (n = 578)

Table 3 Aortic valve calcium scoring, inter-observer reliability for all subjects and absolute difference between observers only for subjects with calcifications

	Observer 1	Observer 2	Observer 3	Observer 4	Observer 5
Observer 1		κ = 0.92	κ = 0.84	κ = 0.74	κ = 0.82
Observer 2	-24.8 (145.2)		κ = 0.88	κ = 0.70	κ = 0.82
Observer 3	24.0 (91.3)	51.1 (156.7)		κ = 0.74	κ = 0.82
Observer 4	-4.8 (236.8)	20.4 (284.5)	-30.5 (252.0)		κ = 0.68
Observer 5	57.2 (191.0)	84.0 (240.5)	35.8 (190.0)	65.6 (304.6)	

κ = kappa value, other data represent mean volume variability (SD) in mm^3

subjects with MC on any CT, absolute mean (SD) inter-examination variability was 31.5 (219.2) mm^3. The reliability of the measurements was excellent with an ICC of 0.90. Inter-examination agreement for all subjects is displayed in **Figure 4**.

Interobserver variation AVC
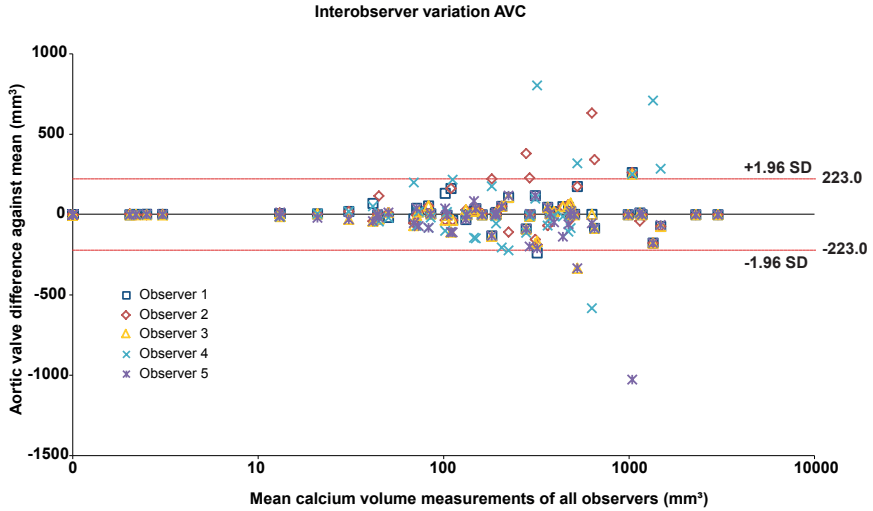
Figure 3 Inter-observer agreement for aortic valve calcifications plotted according to Jones et al. The difference of each observer pertaining to the mean of all observers is plotted against the mean of all observers

Interexamination variation MC
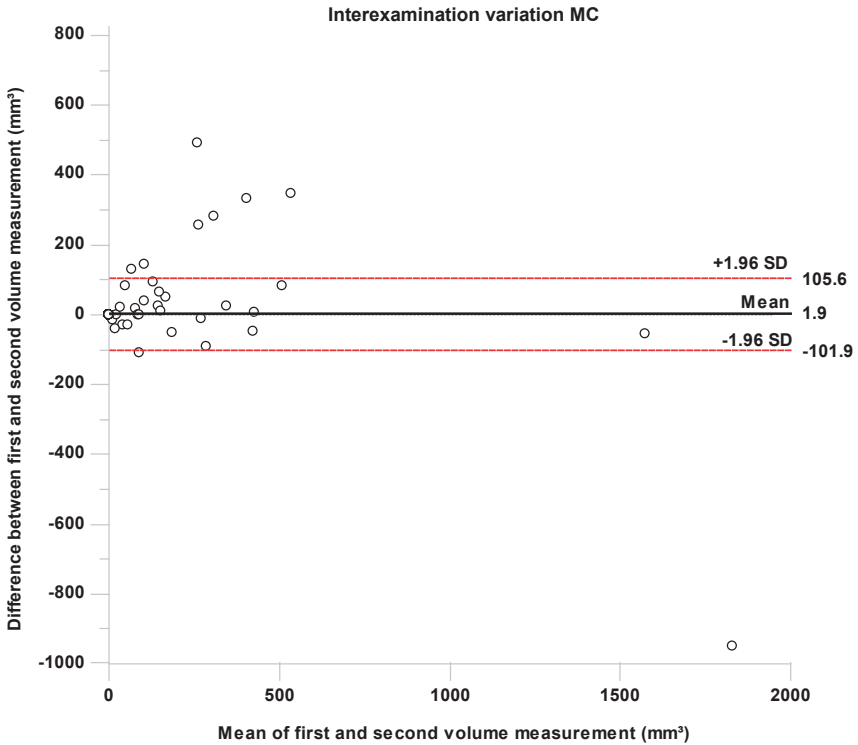
Figure 4 Bland-Altman plot of mitral valve inter-examination agreement for all subjects (n = 578)

2

Inter-observer variability

Of the 100 CT examinations, the observers scored MC in 7 to 30 subjects. Comparing observer 1 and 2, the inter-examination reliability was good with a κ-value of 0.66 and ranges from poor to moderate when comparing the other observers, with a κ-value of 0.20 to 0.45 (**Table 4**). The absolute inter-observer variability for the subjects with MC on one of the two CTs ranged from -95.2 (210.0) mm^3 to 303.7 (501.6) mm^3 (**Table 4**). The ICC for all observers was 0.56, whereas the ICC for observer 1 and 2 was 0.97. Inter-observer agreement for MC in all 100 examinations is displayed in **Figure 5**.

Table 4 Mitral valve calcium scoring, inter-observer agreement for all subjects and absolute difference between observers only for subjects with calcifications

	Observer 1	Observer 2	Observer 3	Observer 4	Observer 5
Observer 1		κ = 0.66	κ = 0.45	κ = 0.30	κ = 0.30
Observer 2	59.9 (124.3)		κ = 0.42	κ = 0.20	κ = 0.36
Observer 3	170.3 (226.6)	1.7 (80.8)		κ = 0.39	κ = 0.27
Observer 4	233.1 (437.6)	-95.2 (210.0)	134.5 (668.9)		κ = 0.39
Observer 5	303.7 (501.6)	106.5 (301.6)	266.7 (728.1)	-27.0 (63.5)	

κ = kappa value, other data represent mean volume variability (SD) in mm^3
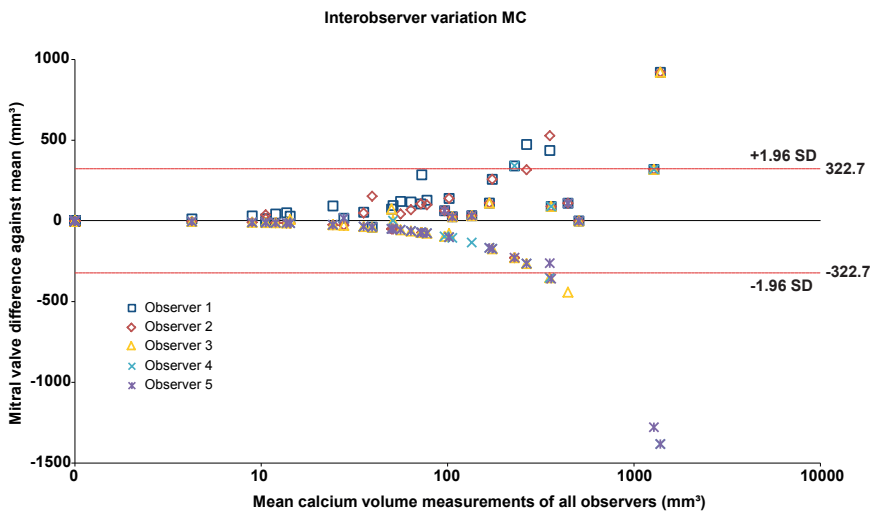
Figure 5 Inter-observer agreement for MC plotted according to Jones et al. The difference of each observer pertaining to the mean of all observers is plotted against the mean of all observers

Discussion

We found good to excellent inter-examination and inter-observer agreement for AVC and good inter-examination, but only poor to good inter-observer agreement for MC on ungated unenhanced low-dose chest CT. Therefore lung cancer screening chest CTs can be used to detect the presence of AVC and MC and to quantify the amount of AVC, but care should be taken with MC volume measurements. Lung cancer screening CT examinations may therefore prove useful for the detection of subclinical cardiac valve disease, to differentiate individuals with non-calcified cardiac valves from individuals with calcified cardiac valves, to predict cardiovascular events and to study the aetiology and progression of AVC.

This is the first study to describe the inter-examination and inter-observer agreement and variability for AVC and MC on an ungated low-dose chest CT. When comparing our data to a study that included 100 subjects of the MESA study and used a dedicated cardiac CT protocol and 2 experienced observers to determine the inter-examination and inter-observer variability for AVC and MC, we found a consistent inter-examination and inter-observer reliability for AVC, in both cases excellent [14]. Mean (SD) inter-examination variability for AVC in this study was -5.63 (50.65) mm^3 and mean inter-observer variability was 25.28 (82.80) mm^3, whereas our data have an inter-examination variability of 12.7 (118.2) mm^3 and an inter-observer variability ranging from -30.5 (252.0) mm^3 to 84.0 (240.5) mm^3 whereas SDs ranged from 91.3 mm^3 to 304.6 mm^3. We summed mitral annulus and mitral valve calcifications, which limits the possibility to compare our findings on mitral pathology with previous studies.

The extent of differences that we found comparing our study with the previously described study and the low inter-observer reliability and high inter-observer variability for MC can be found in the fact that this study was performed on ungated low-dose CT examinations without contrast injection. Motion of the heart during the acquisition, which limits clear depiction of anatomical details and causes motion artefact [23], might be the explanation. Especially in the mitral valve region anatomical details are important to discern the location of the calcium whereas the left circumflex artery runs next to the mitral valve. This also explains that the level of experience of the observer seems to become more important for MC compared to AVC as the AVC is easier to locate, especially on coronal views. However, discrimination between calcifications of the aortic and the mitral annulus was also more difficult for the less experienced observers. Prospective ECG triggering would decrease motion artefacts and provide a clearer depiction of anatomical details,

2

which could make the level of experience, to identify MC properly, less important. However, current lung cancer screening trials and screening programmes do not use prospective whole-chest ECG-triggered CT.

In our study, calcium quantification was manually performed using in-house developed software. Conventional coronary calcium score software from all vendors is validated for certain image acquisition settings. This software could be used if these settings are able to derive calcification volumes for aortic and mitral valve calcification on non-gated unenhanced CTs.

As image acquisition is performed repeatedly in lung cancer screening, these longitudinal data can provide an opportunity to study biomarkers associated with disease progression, for example, whether smoking cessation or medicine use slows the progression of arterial calcification. Furthermore, by linking longitudinal imaging biomarkers to medication use, it may be possible to discover unknown beneficial or harmful pleiotropic drug effects. Studies in which calcium decreased after medicine use in animals, such as calcium channel blockers, have been reported [24]. Besides research purposes, lung cancer screening CT examinations also offer the opportunity to detect other abnormalities besides lung cancer, such as chronic obstructive pulmonary disease [4]. Another potential application is the prediction of future cardiovascular events based on coronary artery calcifications [5]. The current study indicates that lung cancer screening CT examinations may also be used for the detection of subclinical diseases of the cardiac valves and to differentiate individuals with non-calcified cardiac valves from individuals with calcified cardiac valves. Additional attention to the detection of calcification is feasible and may become important, also on ungated low-dose CT, as most non-cardiac radiologists currently do not report aortic and mitral valve calcification when reporting chest CTs for other indications, whereas heart valve calcification detected incidentally on routine chest CT is an independent predictor of future cardiovascular events [25].

The strengths of our study are a substantial sample size, the number of observers and that all imaging was performed on a 16-detector-row CT system from a single vendor with the same protocol. A limitation of our study is the 3-month follow-up period between the two CT examinations in which the amount of calcification present may have altered. However, we judged this to be a minor problem as progression of heart valve calcifications is slow. The mean AVC progression is 80 mm^3 in 15 months [26]. Nevertheless, a repeated CT examination directly after the initial CT would be more ideal to eliminate changes over time. Another limitation

is the possible intra-observer variability. For the inter-examination, the two CTs of each subject were scored right after each other to eliminate intra-observer variability as much as possible, but we cannot completely rule out that it plays a role in different outcomes.

In conclusion, this study shows that AVC and MC can be detected on ungated unenhanced low-dose chest CT examinations. Moreover, AVC can be quantified with sufficient reproducibility to allow longitudinal studies. MC is found to be more difficult to detect and quantify than AVC and observers experience becomes increasingly important. Further research is needed to determine the prognostic significance of these calcifications and may provide insight into the aetiology.

2

2

References

1. Gu D, Kelly TN, Wu X, et al (2009) Mortality Attributable to Smoking in China. N Engl J Med 360:150–159. doi: 10.1056/NEJMsa0802902

2. Ezzati M, Lopez AD (2003) Estimates of global mortality attributable to smoking in 2000. Lancet 362:847–852. doi: 10.1016/S0140-6736(03)14338-3

3. Humphrey LL, Deffebach M, Pappas M, et al (2013) Screening for Lung Cancer With Low-Dose Computed Tomography: A Systematic Review to Update the U.S. Preventive Services Task Force Recommendation. Ann Intern Med 159:411. doi: 10.7326/0003-4819-159-6-201309170-00690

4. Mets OM, de Jong PA, Prokop M (2012) Computed tomographic screening for lung cancer: an opportunity to evaluate other diseases. JAMA 308:1433. doi: 10.1001/jama.2012.12656

5. Mets OM, Vliegenthart R, Gondrie MJ, et al (2013) Lung Cancer Screening CT-Based Prediction of Cardiovascular Events. JACC Cardiovasc Imaging 6:899–907. doi: 10.1016/j.jcmg.2013.02.008

6. Jacobs PC, Prokop M, van der Graaf Y, et al (2010) Comparing coronary artery calcium and thoracic aorta calcium for prediction of all-cause mortality and cardiovascular events on low-dose non-gated computed tomography in a high-risk population of heavy smokers. Atherosclerosis 209:455–462. doi: 10.1016/j.atherosclerosis.2009.09.031

7. Xie X, Zhao Y, de Bock GH, et al (2013) Validation and Prognosis of Coronary Artery Calcium Scoring in Nontriggered Thoracic Computed Tomography. Circ Cardiovasc Imaging 6:514–521. doi: 10.1161/CIRCIMAGING.113.000092

8. Benjamin EJ, Plehn JF, D'Agostino RB, et al (1992) Mitral Annular Calcification and the Risk of Stroke in an Elderly Cohort. N Engl J Med 327:374–379. doi: 10.1056/NEJM199208063270602

9. Otto CM, Lind BK, Kitzman DW, et al (1999) Association of Aortic-Valve Sclerosis with Cardiovascular Mortality and Morbidity in the Elderly. N Engl J Med 341:142–147. doi: 10.1056/NEJM199907153410302

10. Owens DS, Budoff MJ, Katz R, et al (2012) Aortic Valve Calcium Independently Predicts Coronary and Cardiovascular Events in a Primary Prevention Population. JACC Cardiovasc Imaging 5:619–625. doi: 10.1016/j.jcmg.2011.12.023

11. Kizer JR, Gefter WB, deLemos AS, et al (2001) Electron beam computed tomography for the quantification of aortic valvular calcification. J Heart Valve Dis 10:361–6

12. Budoff MJ, Mao S, Takasu J, et al (2002) Reproducibility of electron-beam CT measures of aortic valve calcification. Acad Radiol 9:1122–7

13. Budoff MJ, Katz R, Wong ND, et al (2007) Effect of Scanner Type on The Reproducibility of Extracoronary Measures of Calcification: The Multi-Ethnic Study of Atherosclerosis. Acad Radiol 14:1043–1049. doi: 10.1016/j.acra.2007.05.021

14. Budoff MJ, Takasu J, Katz R, et al (2006) Reproducibility of CT Measurements of Aortic Valve Calcification, Mitral Annulus Calcification, and Aortic Wall Calcification in the Multi-Ethnic Study of Atherosclerosis. Acad Radiol 13:166–172. doi: 10.1016/j.acra.2005.09.090

15. Horeweg N, van der Aalst CM, Thunnissen E, et al (2013) Characteristics of Lung Cancers Detected by Computer Tomography Screening in the Randomized NELSON Trial. Am J Respir Crit Care Med 187:848–854. doi: 10.1164/rccm.201209-1651OC

16. van Iersel CA, de Koning HJ, Draisma G, et al (2007) Risk-based selection from the general population in a screening trial: Selection criteria, recruitment and power for the Dutch-Belgian randomised lung cancer multi-slice CT screening trial (NELSON). Int J Cancer 120:868–874. doi: 10.1002/ijc.22134

17. Isgum I, Prokop M, Niemeijer M, et al (2012) Automatic Coronary Calcium Scoring in Low-Dose Chest Computed Tomography. IEEE Trans Med Imaging 31:2322–2334. doi: 10.1109/TMI.2012.2216889

18. Landis JR, Koch GG (1977) The measurement of observer agreement for categorical data. Biometrics 33:159–74

19. Kottner J, Audigé L, Brorson S, et al (2011) Guidelines for Reporting Reliability and Agreement Studies (GRRAS) were proposed. J Clin Epidemiol 64:96–106. doi: 10.1016/j.jclinepi.2010.03.002

20. Nunnally JC, Bernstein IH (1994) Psychometric Theory (McGraw-Hill Series in Psychology). McGraw-Hill New York

21. Bland JM, Altman DG (1986) Statistical methods for assessing agreement between two methods of clinical measurement. Lancet (London, England) 1:307–10

22. Jones M, Dobson A, O'Brian S (2011) A graphical method for assessing agreement with the mean between multiple observers using continuous measures. Int J Epidemiol 40:1308–1313. doi: 10.1093/ije/dyr109

23. Brown SJ, Hayball MP, Coulden RA (2000) Impact of motion artefact on the measurement of coronary calcium score. Br J Radiol 73:956–962. doi: 10.1259/bjr.73.873.11064648

24. Wallin R, Wajih N, Greenwood GT, Sane DC (2001) Arterial calcification: a review of mechanisms, animal models, and the prospects for therapy. Med Res Rev 21:274–301

25. Gondrie MJA, van der Graaf Y, Jacobs PC, et al (2011) The association of incidentally detected heart valve calcification with future cardiovascular events. Eur Radiol 21:963–973. doi: 10.1007/s00330-010-1995-0

26. Pohle K, Mäffert R, Ropers D, et al (2001) Progression of aortic valve calcification: association with coronary atherosclerosis and cardiovascular risk factors. Circulation 104:1927–32

2
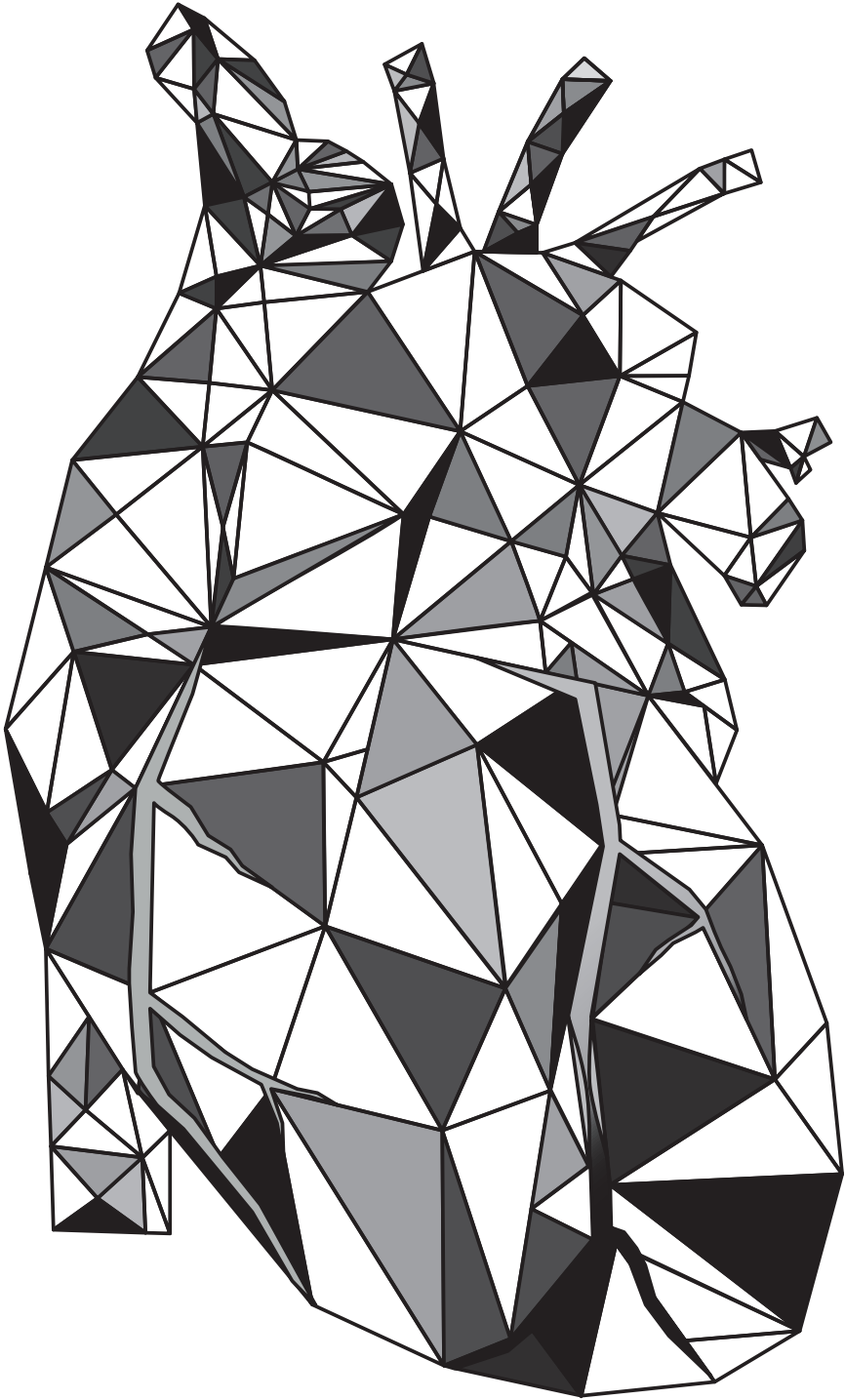
Chapter 3

Aortic valve and thoracic aortic calcification measurements: how low can we go in radiation dose?

Robbert W. van Hamersvelt
Annemarie M. den Harder
Martin J. Willemink
Arnold M.R. Schilham
Jan-Willem J. Lammers
Hendrik M. Nathoe
Ricardo P. J. Budde
Tim Leiner
Pim A. de Jong

3

Abstract

Objectives

This study aimed to determine the lowest radiation dose and iterative reconstruction level(s) at which computed tomography (CT)-based quantification of aortic valve calcification (AVC) and thoracic aortic calcification (TAC) is still feasible.

Methods

Twenty-eight patients underwent a cardiac CT and 20 patients a chest CT at four different dose levels (routine dose and approximately 40%, 60% and 80% reduced dose). Data were reconstructed with filtered back projection (FBP), three iDose[4] levels and three iterative model-based reconstruction (IMR) levels. Two observers scored subjective image quality. AVC and TAC were quantified using mass and compared to the reference scan (routine dose reconstructed with FBP).

Results

In cardiac CT at 0.35 mSv (60% reduced) all scans reconstructed with iDose[4] (all levels) were diagnostic, calcification detection errors occurred in only 1 patient and there were no significant differences in mass scores compared to the reference scan. Similar results were found for chest CT at 0.48 mSv (75% reduced) with iDose[4] levels 4 and 6 and IMR levels 1 and 2.

Conclusions

Iterative reconstruction enables AVC and TAC quantification on CT at submillisievert dose.

3

Introduction

Thoracic aortic calcification (TAC) and aortic valve calcification (AVC) are associated with coronary heart disease, stroke and mortality [1–5]. Aortic valve calcification is an independent predictor of adverse cardiovascular outcomes [6, 7]. Furthermore, quantification of AVC provides prognostic information in patients with aortic valve stenosis [8]. In addition, TAC is recently found to be an independent predictor for future development of coronary artery calcifications (CACs) [9, 10], which is a strong predictor of adverse cardiovascular outcomes [11, 12].

Cardiac and chest computed tomography (CT) are commonly performed for a wide range of indications, including chest pain, trauma and lung cancer screening. Aortic valve calcification and TAC can be reliably quantified on electrocardiogram (ECG)-triggered unenhanced cardiac CT as well as on unenhanced untriggered chest CT [13, 14]. However, radiation exposure is thought to be associated with an increased risk of developing cancer. It is estimated that about 0.4% of all cancers in the United States of America are caused by CT examinations [15]. Dose optimization is therefore important.

When using standard filtered back projection (FBP), dose reduction is associated with more image noise and thereby reduced image quality. Image quality and noise are important for the assessment of calcifications. Image noise can be mistaken for calcifications and can, if severe, even render an examination non-diagnostic [16]. To allow image acquisition at reduced dose levels, iterative reconstruction (IR) techniques have been developed. Iterative reconstruction reduces image noise and thus improves image quality and accuracy of calcium scoring on low-dose CT scans [17]. Some studies suggest that radiation dose can be substantially reduced to 0.85 millisievert (mSv) for unenhanced chest CT and 0.37 mSv for unenhanced cardiac CT while maintaining acceptable image quality [18–21]. However, it is unclear if dose reduction and IR have an effect on AVC and TAC quantification.

The aim of the current study was to find the optimal dose reduction and IR level(s) for AVC and TAC quantification on CT.

Materials and Methods

Study population

Our local institutional review board approved this prospective study (NL46146.041.13). Forty-eight patients were included between January 2014 and February 2015, written informed consent was obtained from all participants.

3

Patients with suspected cardiovascular disease (cardiac CT, n = 28) or follow-up of pulmonary nodule(s) (chest CT, n = 20) were eligible for inclusion. To reduce the risk of carcinogenesis to a minimum, only patients of 50 years or older were included and patients who were pregnant or concomitantly participated in another study with X-rays were excluded. All participants were informed about the added radiation risk and provided written informed consent.

Image acquisition

Each patient underwent 4 CT scans (cardiac or chest) in a single session at 4 different dose levels. For the cardiac protocol, this consisted of a scan at routine dose and scans at 40%, 60%, and 80% reduced dose. For the chest protocol, this concerned a scan at routine dose and scans at 45%, 60%, and 75% reduced dose. Dose reduction was achieved by lowering the tube current (**Table 1**). The 4 different scans per patient were performed with the same scan length and same starting position. Cardiac scans were prospectively ECG-triggered and used a tube voltage of 120 kV. For patients with a weight 80 kg or greater, tube current time product (mAs) was increased by 20%. Chest scans were untriggered and 100 kV was used for patients less than 80 kg and 120 kV for patients 80 kg or greater. All CT examinations were performed with the same 256-slice CT scanner (Brilliance iCT; Philips Healthcare, Best, the Netherlands) and no contrast agent was injected for both cardiac and chest scans. A matrix size of 512 x 512 pixels and a collimation of 128 x 0.625 mm were used. For cardiac scans, both slice thickness and increment were 3 mm; whereas for chest scans, slice thickness was 1 mm and increment was 0.7 mm. Volumetric CT dose index and dose-length product were automatically recorded for each scan. The effective dose was calculated by multiplying the dose-length product by a conversion coefficient of 0.0145 mSv/[mGy x cm] for 120-kV acquisitions and 0.0144 mSv/[mGy x cm] for 100-kV acquisitions [22].

Image reconstruction

Routine dose CT scans were reconstructed using standard FBP. Low-dose CT scans were reconstructed using FBP, three levels (1, 4 and 7 for cardiac CT and 1, 4 and 6 for chest CT) of a hybrid IR technique (iDose[4]; Philips Healthcare) and three levels (1, 2 and 3) of a prototype model-based IR technique (IMR; Philips Healthcare). A higher IR level implies more noise reduction. Filter CB was used for cardiac acquisitions and filter B for chest acquisitions. IMR uses different filters; therefore, vendor-recommended kernels were used, namely "cardiac routine" for cardiac CT and "body routine" for chest CT.

Table 1 Patient and study characteristics

Group	Weight protocol	N	Age*	Male, N (%)	BMI (kg/m²)*	kV	Dose level	mAs	CTDIvol (mGy)*	DLP (mGy·cm)*	ED (mSv)*
Cardiac	<80kg	10	56.8 (7.3)	7 (70)	24.5 (2.0)	120	Standard	50	4.17 (0.14)	53.85 (4.24)	0.78 (0.06)
							40% reduced	30	2.45 (0.09)	32.42 (2.56)	0.47 (0.04)
							60% reduced	20	1.64 (0.06)	21.65 (1.69)	0.31 (0.02)
							80% reduced	10	0.81 (0.28)	10.83 (0.85)	0.16 (0.01)
Cardiac	≥80kg	18	54.7 (4.0)	14 (78)	30.0 (5.2)	120	Standard	60	4.89 (0.09)	62.67 (3.42)	0.91 (0.05)
							40% reduced	36	2.93 (0.06)	37.62 (2.20)	0.55 (0.03)
							60% reduced	24	1.96 (0.04)	25.16 (1.45)	0.36 (0.02)
							80% reduced	12	0.98 (0.02)	12.53 (0.75)	0.18 (0.01)
Chest	<80kg	9	67.7 (9.5)	4 (45)	25.3 (3.3)	100	Standard	60	2.43 (0.01)	95.57 (6.13)	1.37 (0.09)
							45% reduced	33	1.33 (0.01)	52.51 (3.45)	0.75 (0.05)
							60% reduced	24	0.96 (0.01)	38.00 (2.12)	0.55 (0.03)
							75% reduced	15	0.60 (0.01)	23.77 (1.37)	0.34 (0.02)
Chest	≥80kg	11	65.4 (8.2)	6 (55)	32.0 (4.8)	120	Standard	60	4.06 (0.00)	164.97 (9.63)	2.39 (0.14)
							45% reduced	33	2.22 (0.02)	90.75 (4.90)	1.32 (0.07)
							60% reduced	24	1.61 (0.02)	65.79 (3.63)	0.95 (0.05)
							75% reduced	15	1.02 (0.00)	41.45 (2.28)	0.60 (0.03)

Data depicted as mean (SD). BMI = body mass index; CTDIvol = CT volume dose index; DLP = dose-length product; ED = effective radiation dose, estimated as DLP·k (k = 0.0144 for 100 kV and k = 0.0145 for 120 kV); N = number of patients; SD = standard deviation

3

Subjective image quality

The subjective image quality of each reconstruction was rated on a 5-point Likert scale regarding the diagnostic value with respect to calcifications: 1 is poor quality, no distinction can be made between noise and (small) calcification, non-diagnostic; 2 is insufficient quality, little distinction can be made between noise and (small) calcifications, limited diagnostic value; 3 is moderate quality, small chance of missing small calcifications, just diagnostic; 4 is proper quality, unlikely that calcifications are missed, good diagnostic value; and 5 is excellent quality, certainly no calcifications are missed, excellent diagnostic value.

The rating was done by 2 independent blinded observers and the mean diagnostic score of each reconstruction was calculated. Reconstructions with a mean score 2 or less were excluded from further analyses. If greater than 20% of the scans of a reconstruction level at a certain dose reduction level were non-diagnostic, this entire reconstruction level was considered non-diagnostic and was therefore excluded from analysis.

Calcium quantification

The amount of AVC and TAC was quantified using mass score (mg). The calcification scoring was performed manually by a single observer using commercially available semi-automatic software (Heartbeat CS, Philips Healthcare). All reconstructions per patient were assessed consecutively in a random order to minimize intra-observer variability. After clicking on a calcification, the observer instructed the software program to automatically select the calcification across multiple slices and quantified the calcification in terms of mass. The observer visually checked and if needed manually corrected the selection. In case of substantial noise and/or if noise was connected to the calcification, the selection was manually adjusted per slice to prevent overestimation of calcification measurements. A standard threshold for calcification detection was set to 130 HU in scans with a tube voltage of 120 kV. The threshold was adapted to 147 HU in acquisitions with a tube voltage of 100 kV as previously proposed [23].

If a calcium score of 0 was found on the reference scan and a score greater than 0 was found on a reduced dose reconstruction, this reconstruction was considered false-positive (FP). If a calcium score greater than 0 was found on the reference scan and a calcium score of 0 on a reduced dose reconstruction, this reconstruction was considered false-negative (FN).

Statistical analysis

The scan at routine dose reconstructed with FBP served as reference standard. All reconstructions at reduced dose were compared to the reference standard. Statistical differences of calcium scores and diagnostic image quality scores were analysed with the Friedman test ($P < 0.05$) and subsequently post hoc analyses with the Wilcoxon signed rank test. For the post hoc analyses a Bonferroni corrected $P < 0.007$ (0.05/number of reconstruction levels used) was considered significant, unless stated otherwise. Values are listed as medians with interquartiles, unless stated otherwise. Inter-observer agreement was assessed using quadratic weighted kappa statistics (κ) for the 5-point Likert scale [24], interpreted as follows: 0, absence of agreement; less than 0.20, poor agreement; 0.21 to 0.40, fair agreement; 0.41 to 0.60, moderate agreement; 0.61 to 0.80, good agreement; and greater than 0.80, excellent agreement [14]. Statistical analyses were performed with IBM SPSS version 20.0.0 (IBM Corp, Armonk, NY) and MedCalc version 13.2.2.0 (MedCalc Software, Ostend, Belgium).

Results

Study characteristics

Patient and dose characteristics are listed in **Table 1**. Forty-eight patients (31 men) were included, which had a mean (SD) age of 60 (8.8) years and a body mass index of 28.4 (5.1) kg/m^2. Twenty-eight patients underwent cardiac CT and 20 patients underwent chest CT.

Mean effective radiation doses of the cardiac CT scans were 0.86 (reference dose), 0.51 (40% reduced), 0.35 (60% reduced), and 0.17 (80% reduced) mSv. For the chest CT scans, the effective doses were 1.93 (reference dose), 1.06 (45% reduced), 0.77 (60% reduced), and 0.48 (75% reduced) mSv.

Subjective Image quality

The results of the diagnostic image quality assessment are provided in **Table 2**. Inter-observer agreement for visual grading was good for cardiac scans (weighted κ value = 0.7) and moderate for chest scans (weighted κ value = 0.5). At reduced dose, image quality decreased significantly in all reconstructions of cardiac and chest CT, except for chest CT with iDose^4 level 6 and IMR levels 1 and 2 at 45% reduced dose and IMR level 1 at 60% reduced dose. At lower dose, IR improved image quality more compared to FBP and with improving image quality, less scans were rendered non-diagnostic (**Table 2**, **Figure 1**). For the cardiac scans at 80% reduced

3

Table 2 Image quality and diagnostic value.

		Cardiac						Chest					
	Reconstruction	Image quality (N = 28)	N. Diagnostic	AVC FP	AVC FN	TAC FP	TAC FN	Image quality (N = 20)	N. Diagnostic	AVC FP	AVC FN	TAC FP	TAC FN
Routine dose	FBP	5.0 (4.5-5.0)	28					4.0 (3.9-4.0)	20				
40% / 45% reduced dose	FBP	4.5 (3.5-4.6)*	28	0	0	3	0	3.5 (3.0-3.5)*	20	0	1	1	0
	iDose[4] I1	4.5 (4.0-4.6)*	28	0	0	0	0	3.5 (3.5-3.6)*	20	0	0	0	0
	iDose[4] I4	4.5 (4.0-4.5)*	28	0	0	0	0	3.5 (3.5-4.0)*	20	0	0	0	0
	iDose[4] I7/6	4.0 (4.0-4.0)*	28	0	0	0	1	4.0 (4.0-4.0)	20	0	0	0	0
	IMR I1	4.0 (4.0-4.0)*	28	0	1	8	0	4.0 (4.0-4.0)	20	0	1	0	0
	IMR I2	4.0 (4.0-4.0)*	28	0	1	8	0	4.0 (4.0-4.0)	20	0	1	0	0
	IMR I3	3.5 (3.0-3.5)*	28	0	1	9	0	3.5 (3.4-3.5)*	20	0	1	1	0
60% / 60% reduced dose	FBP	3.5 (3.0-4.1)*	25	0	0	4	0	3.0 (2.5-3.0)*	13	0	1	1	0
	iDose[4] I1	4.0 (3.8-4.5)*	28	0	0	1	0	3.5 (3.0-3.5)*	20	0	1	0	0
	iDose[4] I4	4.0 (4.0-4.5)*	28	0	0	0	1	3.5 (3.5-3.6)*	20	0	1	0	0
	iDose[4] I7/6	4.0 (3.5-4.0)*	28	0	1	0	1	3.5 (3.5-4.0)*	20	0	1	0	0
	IMR I1	4.0 (4.0-4.0)*	28	0	0	9	1	4.0 (3.5-4.0)	20	0	1	1	0
	IMR I2	4.0 (3.5-4.1)*	28	0	0	9	2	3.5 (3.5-4.0)*	20	0	2	1	0
	IMR I3	3.0 (3.0-3.5)*	27	0	1	8	2	3.0 (3.0-3.0)*	20	0	2	1	0
80% / 75% reduced dose	FBP	2.5 (2.0-3.0)*	15	0	1	9	0	2.0 (1.9-2.1)*	2	0	0	1	0
	iDose[4] I1	3.5 (3.0-4.0)*	27	0	0	5	0	2.5 (2.5-3.0)*	18	0	1	1	0
	iDose[4] I4	3.5 (3.0-4.0)*	27	0	0	7	0	3.0 (3.0-3.5)*	20	0	1	1	0
	iDose[4] I7/6	3.5 (3.0-3.6)*	25	0	2	5	1	3.0 (3.0-3.5)*	20	0	1	1	0
	IMR I1	3.5 (3.0-4.0)*	28	0	1	8	2	3.5 (3.0-4.0)*	20	0	1	0	0
	IMR I2	3.0 (3.0-3.5)*	26	0	1	9	2	3.0 (3.0-3.5)*	20	0	1	0	0
	IMR I3	3.0 (2.5-3.0)*	19	0	1	7	2	3.0 (2.5-3.0)*	18	0	1	0	0

Image quality is depicted as median (IQ). FP and FN values are defined for diagnostic scans only.

*Significant difference compared to FBP at routine dose (Bonferroni $P < 0.007$). AVC = Aortic valve calcification; FN = False negative; FP = False positive; I = level; N. Diagnostic = number of patients with a diagnostic scan (diagnostic score ≥2 or agreed after discussion when one observer scored 2 and the other 3); TAC = Thoracic aortic calcification

Figure 1 Chest CT at 75% reduced dose of one single patient with TAC (white arrow). All images are taken at the same slice position. In the right series, values greater than 130 HU are highlighted in pink, indicating the effect of different IR levels on image noise. Diagnostic scores of these scans are depicted in the left upper corner as mean of the 2 observers. *FBP = filtered back projection; IMR = iterative model reconstruction; l = level*

3
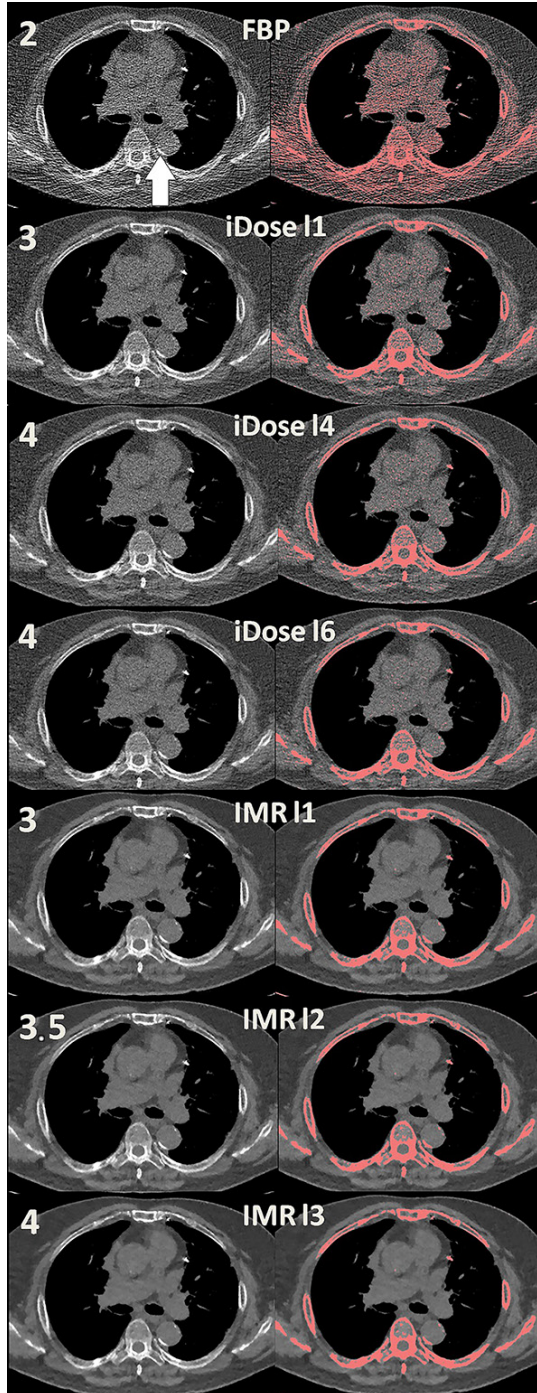
dose, FBP and IMR level 3 were in more than 20% of the patients of insufficient quality, and hence, rated as non-diagnostic. For chest scans with FBP, the same was found at 60% and 75% reduced dose, whereas IR reconstructions resulted in sufficient image quality in greater than 80% of the patients at all dose levels.

Calcium quantification

Cardiac CT

Six (21%) patients had AVC and 10 (36%) patients had TAC scores higher than 0 on the reference scan (routine dose reconstructed with FBP). A high FP rate (3–9 patients) for TAC was observed for FBP and all IMR levels at all dose reduction levels. A high FP rate for TAC was also seen for all iDose[4] levels at maximum reduced dose; whereas at 40% and 60% reduced dose, a maximum of one FP or FN was observed for iDose[4] (**Table 2**). No FP for AVC was found at any reduced dose level. Overall, the FN rates of TAC and AVC were low with a maximum of 2.

Calcification mass of patients with a calcium score higher than 0 are listed in **Table 3**. When compared to FBP at routine dose, AVC and TAC mass scores did not change significantly at reduced dose with application of IR (**Table 3**).

Absolute differences in TAC mass were overall lower with iDose[4] than with IMR (**Figure 2**). Absolute differences in AVC mass declined with increasing IMR levels and increased with increasing iDose[4] levels.

Chest CT

Eight (40%) patients had AVC and 17 (85%) patients TAC scores higher than 0 on the reference scan. A maximum of 1 FP and 0 FN for TAC and 0 FP and 2 FN for AVC were found for all reconstructions at all dose reduction levels (**Table 2**).

Post hoc analyses showed no significant difference for AVC mass scores at any reduced dose level when compared to FBP at routine dose (**Table 3**). However, a significant difference for TAC mass was found with FBP at 45% reduced dose, iDose[4] level 1 at 75% reduced dose and iDose[4] level 6 at 45% and 60% reduced dose (**Table 3**). No significant differences were found with IMR (all levels) at any reduced dose level.

Absolute differences of TAC mass were overall lower with IMR than with iDose[4] reconstructions (**Figure 2**). Absolute differences of AVC mass remained the same with increasing IMR levels and increased with increasing iDose[4] levels.

3

Table 3 Calcification mass scores of patients with non-zero scores, depicted as median with interquartiles.

	FBP	iDose⁴ l1	iDose⁴ l4	iDose⁴ l6/7	IMR l1	IMR l2	IMR l3
AVC in cardiac group (N = 6)							
Routine	12.0 (1.4-24.0)						
40% reduced°	11.6 (2.2-21.1)	11.4 (0.9-18.7)	10.8 (1.1-18.8)	10.4 (0.8-17.5)	14.2 (1.5-28.7)	13.8 (1.6-28.1)	13.6 (1.6-27.6)
60% reduced°	9.6 (1.3-30.7)⁺	10.8 (1.2-22.4)	9.8 (0.8-20.3)	8.4 (0.6-18.2)	10.9 (2.6-27.6)	10.6 (2.4-26.2)	10.3 (2.0-25.6)
80% reduced°°°	ND	12.6 (2.3-23.3)	11.2 (1.2-21.0)	5.6 (0.0-21.8)⁺	9.6 (1.6-26.2)	7.9 (0.8-24.4)	ND
TAC in cardiac group (N = 10)							
Routine	2.7 (1.1-15.8)						
40% reduced°	3.9 (1.5-42.3)	3.0 (1.9-19.4)	2.6 (1.4-17.1)	2.1 (1.3-17.6)	4.6 (3.0-17.4)	4.2 (2.6-18.0)	5.5 (2.2-17.9)
60% reduced°	5.2 (3.5-29.7)	2.8 (1.7-16.2)	2.7 (0.9-16.0)	2.1 (0.6-15.9)	4.2 (1.8-18.9)	5.7 (1.3-18.3)	4.7 (1.2-18.1)
80% reduced°°°	ND	5.8 (2.6-21.6)	4.3 (2.1-14.7)	2.4 (0.7-19.6)⁺	5.8 (1.2-15.3)	5.1 (0.4-19.2)⁺	ND
AVC in chest group (N = 8)							
Routine	17.0 (4.9-50.2)						
45% reduced°	22.8 (4.2-46.8)	18.2 (2.5-44.4)	15.4 (2.0-42.8)	15.3 (0.9-41.5)	14.8 (0.5-46.8)	15.8 (0.4-47.1)	14.5 (0.3-47.1)
60% reduced°°	ND	17.5 (4.8-47.0)	14.2 (3.5-45.5)	11.1 (2.6-42.7)	12.1 (0.5-46.2)	12.1 (0.4-45.9)	11.1 (0.2-45.4)
75% reduced°°	ND	19.1 (6.0-47.1)	12.9 (5.1-44.8)	10.6 (3.6-44.0)	8.2 (2.1-44.5)	8.8 (1.6-44.0)	10.9 (1.0-47.1)⁺
TAC in chest group (N = 17)							
Routine	455.6 (132.6-1796.9)						
45% reduced°	499.1 (146.6-1875.4)* P=0.001	478.7 (129.5-1823.8)	453.4 (131.2-1778.0)	440.7 (123.6-1748.6)* P<0.001	466.8 (129.9-1850.8)	464.6 (123.0-1864.1)	464.8 (129.0-1855.0)
60% reduced°°	ND	472.8 (125.7-1835.6)	451.3 (123.5-1783.8)	438.5 (120.9-1717.5)* P=0.006	454.2 (126.9-1811.3)	453.0 (124.5-1813.9)	453.4 (123.7-1801.0)
75% reduced°°	ND	538.7 (176.6-2222.2)⁺* P=0.003	487.1 (132.7-1867.8)	462.8 (129.6-1797.0)	478.6 (127.5-1836.7)	476.6 (129.4-1837.7)	575.8 (160.9-2362.6)⁺⁺

⁺ = Total number of diagnostic scans is one less due to one non-interpretable reconstruction

⁺⁺ = total number of diagnostic scans is two less duo to two non-interpretable reconstructions

* = significant difference compared to FBP at routine dose

° = Bonferroni correction of (0.05/7 =) P < 0.007 was considered significant

°° = Bonferroni correction of (0.05/6 =) P < 0.008 was considered significant

°°° = Bonferroni correction of (0.05/5 =) P < 0.01 was considered significant

AVC = aortic valve calcification; FBP = filtered back projection; IMR = iterative model reconstruction; l = level; N = number of patients; ND = non-diagnostic (>20% of the scans were of insufficient quality); TAC = thoracic aortic calcification

47

3

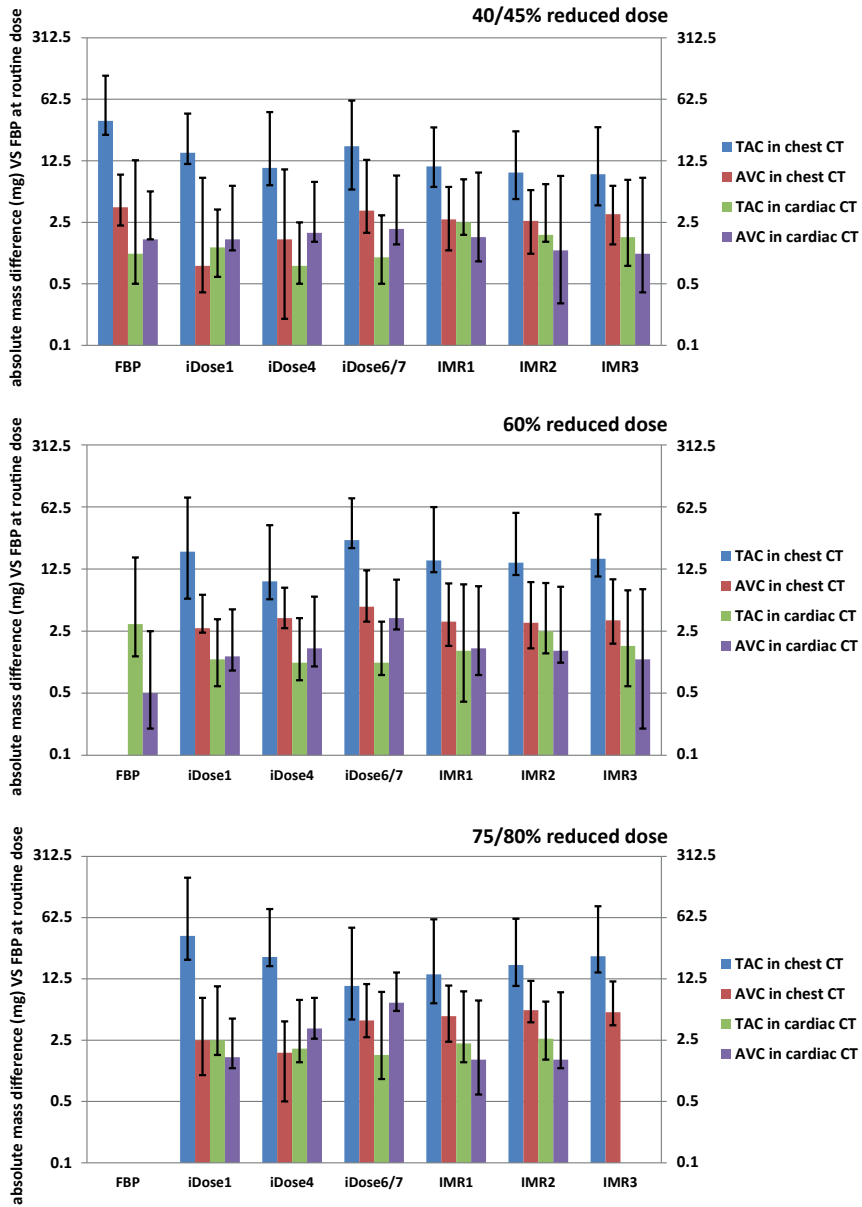**Figure 2** Absolute difference in mass between reconstruction methods in patients with non-zero calcification. Differences are depicted as median absolute difference compared to the reference scan (FBP at routine dose). Error bars indicate interquartiles. *iDose1 = iDose4 level 1 (and so on); IMR1 = IMR level 1 (and so on); IMR = iterative model reconstruction; TAC = thoracic aortic calcification*

Discussion

In this study, we found that when reducing radiation dose, down to an effective radiation dose of 0.35 mSv for cardiac CT and 0.48 mSv for chest CT, IR allows for AVC and TAC scoring on CT scans acquired for coronary calcium scoring and pulmonary nodule volumetry. We also found that at lower dose rating of TAC on cardiac scans becomes more problematic in terms of FPs.

We evaluated several aspects of the images to reach our conclusion. First, the number of diagnostic scans was investigated, because if image quality is too low, no conclusions can be made on the presence or severity of calcifications. Second, FPs and FNs were deemed relevant as this can cause overprediction or underprediction and possibly influence treatment. Third, calcium scores were compared to routine dose scores because deviating calcium scores could also affect predictive value. The same holds true for our fourth parameter, the absolute difference in calcium score. A weighted assessment of these aspects would enable us to identify the optimal dose and IR level.

For cardiac CT, we have observed the lower limit of what is possible with our system and current IR techniques. In our 80% dose reduction protocol many non-diagnostic scans were found as well as a high false positive rate for calcifications that were not visible on the routine dose scan. We think that, with application of iDose[4] levels 1, 4 or 7, 60% reduced dose (0.35 mSv) is the lowest dose achievable for AVC and TAC scoring on unenhanced ECG-triggered cardiac CT. At this dose level, only these IR levels showed a low acceptable FP and FN rate, we did not have to exclude scans and we did not observe significant differences in mass scores. For unenhanced untriggered chest CT, we think that the optimal dose is 0.48 mSv (our 75% dose reduction protocol) if reconstructed with IMR levels 1 and 2 or iDose[4] levels 4 and 6. For these IR levels, FP and FN rates were low and mass scores were of insignificant difference compared to FBP at routine dose. Because 0.48 mSv was the lowest dose we tested, maybe even more dose reduction could be achieved for AVC and TAC scoring.

Multiple studies on subjective and objective image quality have suggested the feasibility of dose reduction with IR in unenhanced cardiac and chest CT [18–21, 25, 26]. In line with these studies, we found that the application of IR at low-dose scans improved image quality compared to FBP at the same dose level. However, improved image quality does not necessarily mean good diagnostic value. The optimal dose reduction and IR level is therefore, in particular, determined by diagnostic value. It can be assumed that low-dose CT with IR can safely replace the standard dose CT if the diagnostic value is equal or better.

3

Previous work by colleagues den Harder et al. [25, 27, 28] and Willemink et al. [29] showed the feasibility of pulmonary nodule volumetry and CAC scoring on low-dose unenhanced chest and cardiac CT scans using IR. However, the feasibility of dose reduction and IR for other indications, such as infections, interstitial lung disease and skeletal assessment is currently uncertain. Den Harder et al. [27, 28] showed that for the detection of pulmonary nodules, unenhanced chest CT can be reduced to submillisievert dose when using IR. Willemink et al. [29] evaluated CAC on low-dose unenhanced cardiac CT using IR. Coronary artery calcification is the main indication for unenhanced cardiac CT and is the most widely used calcium scoring in clinical use. Willemink et al. [29] showed that, with the use of IR at 80% reduced dose (0.15-0.18 mSv), CAC scoring is possible with reclassification rates below 15%. However, no AVC and/or TAC were taken into account. Because AVC and TAC are associated with coronary heart disease, stroke and mortality [1–5] and are found to be independent predictors for adverse cardiovascular outcomes [6, 7, 9, 10], we seek to find the optimal dose reduction and IR level(s) for AVC and TAC quantification on CT. To our best knowledge this is the first study that aimed to find the optimal dose reduction and IR level for quantifying AVC and TAC separately in patients who underwent CT for cardiac and pulmonary indications.

Previously, Hecht et al. [18] investigated the accuracy of scoring CAC and, in addition, TAC combined with AVC (called "aortic calcification") in 102 patients at two dose levels using hybrid IR. Images acquired with iDose^4 level 7 at low-dose ECG-triggered cardiac CT (0.37 ± 0.16 mSv) were compared to standard dose (0.76 ± 0.34 mSv) images reconstructed with iDose^4 level 3. Dose reduction was achieved by lowering mAs with 50%. For "aortic calcification", they found no significant difference in Agatston or mass scores between these dose levels. However, they found a significant difference ($P = 0.03$) for volume with a mean of 88.8 ± 204.0 mm^3 at low-dose (iDose^4 level 7) and 93.7 ± 207.3 mm^3 at standard dose (iDose^4 level 3). The dose reductions investigated are comparable to cardiac CT routine dose and 60% reduced dose in our study. In contrast to this study, we did not find a significant difference in mass score for AVC and TAC, neither separately nor combined, with the application IR.

In the current study, the amount of calcium was quantified using mass. Although the Agatston score is more widely used, mass is suggested to be a more robust quantification method than Agatston score [30] and was found to be less influenced by IR at low-dose scans [25, 31]. In addition, previous studies have shown that mass is less influenced by tube voltage and is better reproducible than Agatston [32, 33].

Findings of the current study indicate that clinical implementation of AVC and TAC scoring on low-dose CT using IR could possibly be achievable in low-dose lung and cardiac scans with a range of indications, such as lung cancer screening CT. Previous research already showed an excellent inter-scan and inter-observer agreement for AVC scoring in unenhanced untriggered lung cancer screening chest CT (<0.9 mSv for <80kg and <1.6 mSv for ≥80kg) [14]. In the current study, at the same amount of effective radiation dose and even lower dose down to 0.35 mSv for cardiac CT and 0.48 mSv for chest CT, we found reliable AVC and TAC scoring when using IR. This implies that AVC and TAC could be quantified at unenhanced untriggered lung cancer screening chest CT.

The strength of our study is the fact that we not only evaluated image quality but primarily investigated diagnostic value to find the optimal dose reduction and IR level for measuring aortic and AVCs. In addition, we compared 4 different dose levels per patient, 3 levels of a hybrid, and 3 levels of a model-based IR algorithm, which enabled us to make a good comparison and a stronger recommendation. Our study also has some limitations. For ethical reasons, the sample size was kept low. Because calcifications were not present in every patient, the sample size of our subgroups was even smaller. Nevertheless, we think the power is sufficient because our study has a within-patient analysis of 4 scans and 22 reconstructions per patient. A larger-scale study with 2 dose levels may be required to confirm our findings. Another limitation is the consecutive scoring of all 22 reconstructions per patients by 1 observer. This could introduce recall bias of the location of calcifications for lower dose scans. However, the advantage is that intra-observer variation is hereby kept low. Finally, application of our recommendations may be limited to the vendor used in our study because all vendors developed their own IR techniques.

In conclusion, this study shows that IR allows for reliable AVC and TAC scoring when reducing dose down to 0.35 mSv on unenhanced ECG-triggered cardiac CT and down to 0.48 mSv on unenhanced untriggered chest CT. At these dose reduction levels, iDose[4] levels 1, 4 and 7 for cardiac CT and iDose[4] levels 4 and 6 and IMR levels 1 and 2 for chest CT could be considered the optimal IR level.

3

References

1. Santos RD, Rumberger JA, Budoff MJ, et al (2010) Thoracic aorta calcification detected by electron beam tomography predicts all-cause mortality. Atherosclerosis 209:131–135. doi: 10.1016/j. atherosclerosis.2009.08.025

2. Jacobs PC, Prokop M, van der Graaf Y, et al (2010) Comparing coronary artery calcium and thoracic aorta calcium for prediction of all-cause mortality and cardiovascular events on low-dose non-gated computed tomography in a high-risk population of heavy smokers. Atherosclerosis 209:455–462. doi: 10.1016/j.atherosclerosis.2009.09.031

3. Hermann DM, Lehmann N, Gronewold J, et al (2014) Thoracic aortic calcification is associated with incident stroke in the general population in addition to established risk factors. Eur Heart J Cardiovasc Imaging. doi: 10.1093/ehjci/jeu293

4. Otto CM, Lind BK, Kitzman DW, et al (1999) Association of aortic-valve sclerosis with cardiovascular mortality and morbidity in the elderly. N Engl J Med 341:142–147. doi: 10.1097/00132586-200002000-00022

5. Clavel M-A, Pibarot P, Messika-Zeitoun D, et al (2014) Impact of aortic valve calcification, as measured by MDCT, on survival in patients with aortic stenosis: results of an international registry study. J Am Coll Cardiol 64:1202–13. doi: 10.1016/j.jacc.2014.05.066

6. Owens DS, Budoff MJ, Katz R, et al (2012) Aortic valve calcium independently predicts coronary and cardiovascular events in a primary prevention population. JACC Cardiovasc Imaging 5:619–625. doi: 10.1016/j.jcmg.2011.12.023

7. Mets OM, Vliegenthart R, Gondrie MJ, et al (2013) Lung cancer screening CT-based prediction of cardiovascular events. JACC Cardiovasc Imaging 6:899–907. doi: 10.1016/j.jcmg.2013.02.008

8. Utsunomiya H, Yamamoto H, Kitagawa T, et al (2013) Incremental prognostic value of cardiac computed tomography angiography in asymptomatic aortic stenosis: significance of aortic valve calcium score. Int J Cardiol 168:5205–11. doi: 10.1016/j.ijcard.2013.07.235

9. Brodov Y, Gransar H, Rozanski A, et al (2015) Extensive thoracic aortic calcification is an independent predictor of development of coronary artery calcium among individuals with coronary artery calcium score of zero. Atherosclerosis 238:4–8. doi: 10.1016/j.atherosclerosis.2014.10.100

10. Rivera JJ, Nasir K, Katz R, et al (2009) Relationship of thoracic aortic calcium to coronary calcium and its progression (from the Multi-Ethnic Study of Atherosclerosis [MESA]). Am J Cardiol 103:1562–7. doi: 10.1016/j.amjcard.2009.02.004

11. Detrano R, Guerci AD, Carr JJ, et al (2008) Coronary calcium as a predictor of coronary events in four racial or ethnic groups. N Engl J Med 358:1336–45. doi: 10.1056/NEJMoa072100

12. Greenland P, LaBree L, Azen SP, et al (2004) Coronary artery calcium score combined with Framingham score for risk prediction in asymptomatic individuals. JAMA 291:210–5. doi: 10.1001/jama.291.2.210

13. Budoff MJ, Nasir K, Kinney GL, et al Coronary artery and thoracic calcium on noncontrast thoracic CT scans: comparison of ungated and gated examinations in patients from the COPD Gene cohort. J Cardiovasc Comput Tomogr 5:113–8. doi: 10.1016/j.jcct.2010.11.002

14. van Hamersvelt RW, Willemink MJ, Takx RAP, et al (2014) Cardiac valve calcifications on low-dose unenhanced ungated chest computed tomography: inter-observer and inter-examination reliability, agreement and variability. Eur Radiol 24:1557–64. doi: 10.1007/s00330-014-3191-0

15. Brenner DJ, Hall EJ (2007) Computed tomography--an increasing source of radiation exposure. N Engl J Med 357:2277–84. doi: 10.1056/NEJMra072149

16. Bittencourt MS, Schmidt B, Seltmann M, et al (2011) Iterative reconstruction in image space (IRIS) in cardiac computed tomography: initial experience. Int J Cardiovasc Imaging 27:1081–7. doi: 10.1007/s10554-010-9756-3

17. Brooks RA, Di Chiro G (1975) Theory of image reconstruction in computed tomography. Radiology 117:561–572. doi: 10.1148/117.3.561

18. Hecht HS, de Siqueira MEM, Cham M, et al (2015) Low- vs. standard-dose coronary artery calcium scanning. Eur Heart J Cardiovasc Imaging Apr:358–63. doi: 10.1093/ehjci/jeu218.

19. Hu XH, Ding XF, Wu RZ, Zhang MM (2011) Radiation dose of non-enhanced chest CT can be reduced 40% by using iterative reconstruction in image space. Clin Radiol 66:1023–9. doi: 10.1016/j.crad.2011.04.008

20. Katsura M, Matsuda I, Akahane M, et al (2012) Model-based iterative reconstruction technique for radiation dose reduction in chest CT: comparison with the adaptive statistical iterative reconstruction technique. Eur Radiol 22:1613–23. doi: 10.1007/s00330-012-2452-z

21. Willemink MJ, Leiner T, de Jong PA, et al (2013) Iterative reconstruction techniques for computed tomography part 2: initial results in dose reduction and image quality. Eur Radiol 23:1632–42. doi: 10.1007/s00330-012-2764-z

22. Deak PD, Smal Y, Kalender WA (2010) Multisection CT Protocols: Sex- and Age-specific Conversion Factors Used to Determine Effective Dose from Dose-Length Product 1. Radiology 257:158–166. doi: 10.1148/radiol.10100047

23. Marwan M, Mettin C, Pflederer T, et al Very low-dose coronary artery calcium scanning with high-pitch spiral acquisition mode: comparison between 120-kV and 100-kV tube voltage protocols. J Cardiovasc Comput Tomogr 7:32–8. doi: 10.1016/j.jcct.2012.11.004

24. Norman G (2010) Likert scales, levels of measurement and the "laws" of statistics. Adv Health Sci Educ Theory Pract 15:625–32. doi: 10.1007/s10459-010-9222-y

25. den Harder AM, Willemink MJ, Bleys RLAW, et al (2014) Dose reduction for coronary calcium scoring with hybrid and model-based iterative reconstruction: an ex vivo study. Int J Cardiovasc Imaging 30:1125–33. doi: 10.1007/s10554-014-0434-8

26. Yamada Y, Jinzaki M, Hosokawa T, et al (2012) Dose reduction in chest CT: comparison of the adaptive iterative dose reduction 3D, adaptive iterative dose reduction, and filtered back projection reconstruction techniques. Eur J Radiol 81:4185–95. doi: 10.1016/j.ejrad.2012.07.013

27. den Harder AM, Willemink MJ, de Ruiter QMB, et al (2015) Achievable dose reduction using iterative reconstruction for chest computed tomography: A systematic review. Eur J Radiol 84:2307–13. doi: 10.1016/j.ejrad.2015.07.011

28. den Harder AM, Willemink MJ, van Hamersvelt RW, et al (2016) Pulmonary Nodule Volumetry at Different Low Computed Tomography Radiation Dose Levels With Hybrid and Model-Based Iterative Reconstruction: A Within Patient Analysis. J Comput Assist Tomogr. doi: 10.1097/RCT.0000000000000408

29. Willemink MJ, den Harder AM, Foppen W, et al Finding the optimal dose reduction and iterative reconstruction level for coronary calcium scoring. J Cardiovasc Comput Tomogr 10:69–75. doi: 10.1016/j.jcct.2015.08.004

30. Hoffmann U, Siebert U, Bull-Stewart A, et al (2006) Evidence for lower variability of coronary artery calcium mineral mass measurements by multi-detector computed tomography in a community-based cohort--consequences for progression studies. Eur J Radiol 57:396–402. doi: 10.1016/j.ejrad.2005.12.027

31. Willemink MJ, Takx RAP, de Jong PA, et al (2014) The impact of CT radiation dose reduction and iterative reconstruction algorithms from four different vendors on coronary calcium scoring. Eur Radiol 24:2201–12. doi: 10.1007/s00330-014-3217-7

32. Deprez FC, Vlassenbroek A, Ghaye B, et al Controversies about effects of low-kilovoltage MDCT acquisition on Agatston calcium scoring. J Cardiovasc Comput Tomogr 7:58–61. doi: 10.1016/j.jcct.2012.11.006

33. Rutten A, Isgum I, Prokop M (2008) Coronary calcification: effect of small variation of scan starting position on Agatston, volume, and mass scores. Radiology 246:90–8. doi: 10.1148/radiol.2461070006

3
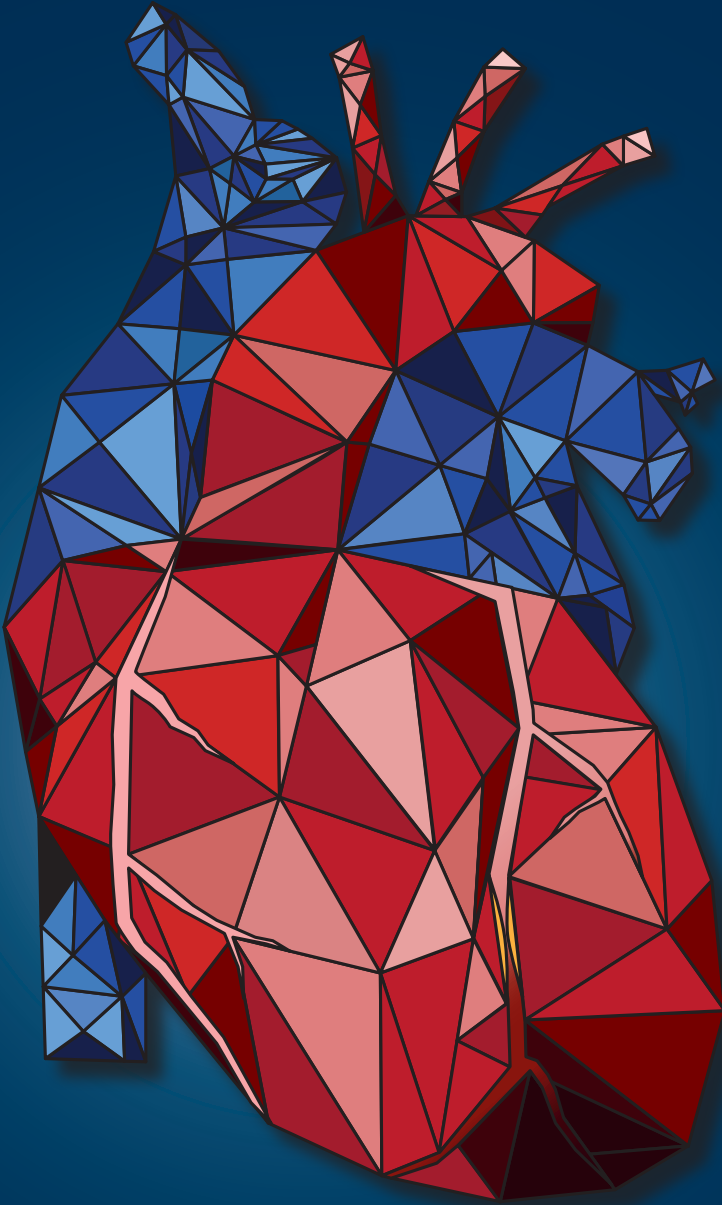
Part II

Safety and quality control in dual-energy CT
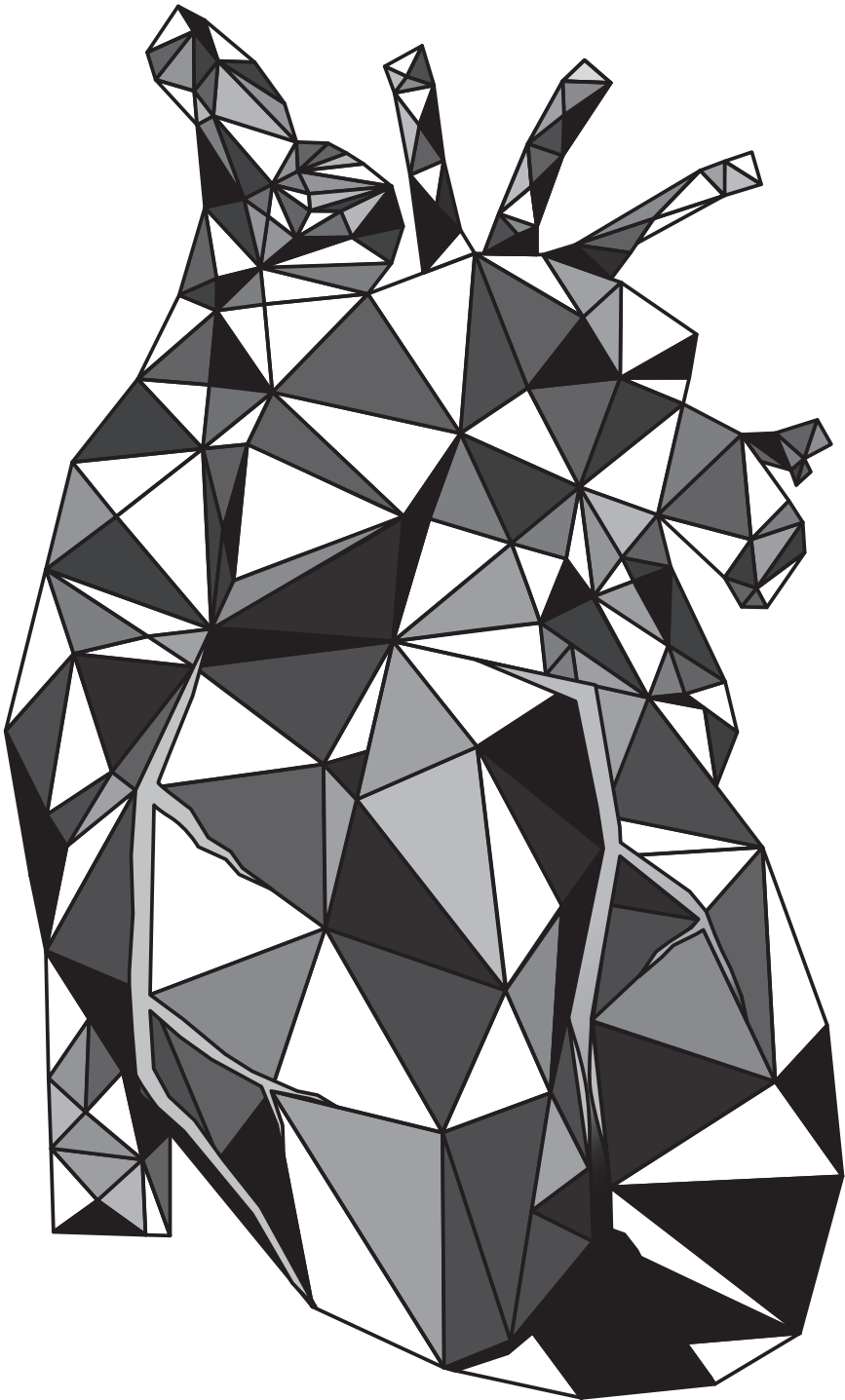
Chapter 4

Contrast agent concentration optimization in CTA using low tube voltage and dual-energy CT in multiple vendors: a phantom study

Robbert W. van Hamersvelt
Nienke G. Eijsvoogel
Casper Mihl
Pim A. de Jong
Arnold M.R. Schilham
Nico Buls
Marco Das
Tim Leiner
Martin J. Willemink

Abstract

Objectives

We investigated the feasibility and extent to which iodine concentration can be reduced in computed tomography angiography imaging of the aorta and coronary arteries using low tube voltage and virtual monochromatic imaging of 3 major dual-energy CT (DECT) vendors.

Methods

A circulation phantom was imaged with dual source CT (DSCT), gemstone spectral imaging (GSI) and dual-layer spectral detector CT (SDCT). For each scanner, a reference scan was acquired at 120 kVp using routine iodine concentration (300 mg I/ml). Subsequently, scans were acquired at lowest possible tube potential (70, 80, 80 kVp, respectively), and DECT-mode (80/150Sn, 80/140 and 120 kVp, respectively) in arterial phase after administration of iodine (300, 240, 180, 120, 60, 30 mg I/ml). Objective image quality was evaluated using attenuation, CNR and dose corrected CNR (DCCNR) measured in the aorta and left main coronary artery.

Results

Average DCCNR at reference was 227.0, 39.7 and 60.2 for DSCT, GSI and SDCT. Maximum iodine concentration reduction without loss of DCCNR was feasible down to 180 mg I/ml (40% reduced) for DSCT (DCCNR 467.1) and GSI (DCCNR 46.1) using conventional CT low kVp, and 120 mg I/ml (60% reduced) for SDCT (DCCNR 171.5) using DECT mode.

Conclusions

Low kVp scanning and DECT allows for 40-60% iodine reduction without loss in image quality compared to reference. Optimal scan protocol and to which extent varies per vendor. Further patient studies are needed to extend and translate our findings to clinical practice.

Introduction

Computed tomography angiography (CTA) is an important diagnostic tool for the detection of cardiovascular diseases [1]. However, while a powerful test, the use of CTA can be limited in patients with impaired renal function [2, 3]. Reducing iodine concentration decreases the risk of contrast-induced nephropathy [3, 4] and can therefore be beneficial in terms of safety and costs [5].

One of the methods to reduce the amount of iodine is scanning with low tube voltage. Several studies have described iodine dose reductions of up to 56% using 70-80 kVp acquisition while maintaining image quality compared to routine CTA [6–9]. At lower X-ray energy levels, attenuation of iodine contrast increases as the energy level approaches the K-edge of iodine (33.2 keV). Thereby allowing for iodine concentration reduction without decrease in CT-values [10].

An alternative method is the use of dual-energy CT (DECT) scanning. DECT discriminates X-ray photons at high and low energy levels and thereby allows for reconstruction of virtual monochromatic imaging (VMI) at discrete energy levels down to 40 keV. Several authors have reported iodine dose reductions of up to 70% with DECT for aortic and coronary CTA while maintaining objective image quality [11–15]. DECT became commercially available a decade ago. Since then multiple approaches have been introduced: (1) dual source CT (DSCT) with two X-ray tubes and two corresponding detectors, with each tube operating at a different tube voltage (low or high); (2) gemstone spectral imaging (GSI) with a single X-ray tube rapidly switching within one rotation between low and high voltage; (3) dual-layer spectral detector CT (SDCT) with a single X-ray tube and a dual-layer detector that differentiates one photon spectrum in a low and high energy fraction. Although these techniques all attempt to achieve the same, from a physics perspective, image data are acquired in a very different way and at different energy levels. In addition, image reconstruction methods to create VMI differ per vendor [16].

The aim of our study was to evaluate on a per vendor level the extent to which iodine concentration could be reduced by using low tube voltage and low VMI without loss of objective image quality compared to CT at routine tube voltage.

Materials and Methods

Phantom setup

A dynamic circulation phantom with a low-pressure venous compartment and a high-pressure arterial compartment simulating physiological circulation
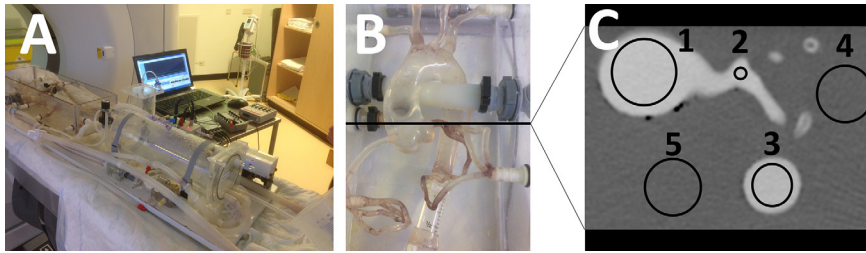
Figure 1 Dynamic circulation phantom setup. (**A**) Physiological circulation parameters were simulated using a low-pressure venous compartment and a high-pressure arterial compartment. (**B**) The phantom consists of a water-filled (37 °C) acrylic container that encased multiple connecting tubes, which accurately mimic the aorta and coronary arteries. (**C**) Intravascular enhancement and noise were measured by using a manually placed circular region of interest in the AA (1), LM (2), DA (3) and 2 homogeneous areas (4 and 5). *AA = ascending aorta; DA = descending aorta; LM = left main coronary artery*

4

parameters was used (**Figure 1A**) [17, 18]. The phantom consisted of a water-filled (37 °C) acrylic container to mimic CT attenuation characteristics of the mediastinum. The container encased multiple connecting tubes, which accurately mimic the aorta and coronary arteries (**Figure 1B**). A pressure relief valve simulates arterial and venous pressure. To mimic pulsation, a Harvard medical heart pump (BS4; Harvard Apparatus, Holliston, MA) was used. Physiological circulation was simulated by using the following settings: heart rate 60 beats per minute, stroke volume 60 ml per beat, output phase ratio 40% systole/ 60% diastole and blood pressure around 120/80 mmHg.

Injection protocol and image acquisition

Iodinated contrast medium of 300 mg I/ml (Iopromide, Ultravist 300, Bayer Healthcare, Berlin, Germany) was used and diluted with water to obtain the following concentrations (ratio contrast medium:water): 300 (1:0), 240 (4:1), 180 (3:2), 120 (2:3), 60 (1:4) and 30 (1:9) mg I/ml. A fixed injection protocol was used (volume 40 ml, flow rate 6 ml/s, injection time 6.7 s), resulting in an iodine delivery rate (IDR; concentration x flow rate) of 1.80, 1.44, 1.08, 0.72, 0.36 and 0.18 g I/s, respectively. All concentrations were preheated to 37 °C and injected into the phantom using a standard CT power injector (Stellant, MEDRAD, Pittsburgh, PA, USA) for both DSCT and SDCT, and a dual head power injector (Nemoto-Kyorindo, Tokyo, Japan) for GSI. After every scan, the phantom was flushed with water three times to remove residual contrast media.

Acquisitions were made using 3 DECT scanners; DSCT, Definition Force (Siemens Healthcare, Forchheim, Germany); GSI, Discovery CT750 HD (GE Healthcare, Milwaukee, WI, USA); SDCT, IQon (Philips Healthcare, Best, The Netherlands). Images were acquired at the level of the left main coronary artery (LM), ascending aorta (AA) and descending aorta (DA) (**Figure 1C**). For each system, a reference conventional CT acquisition was made at 120 kVp and 150 mAs. Subsequently scans were acquired using the lowest possible tube potential of 70 kVp (DSCT) and 80 kVp (GSI and SDCT), with a target tube exposure of 300 mAs. Thereafter, scans were performed in DECT modes of 80/150Sn kVp (DSCT), 80/140 kVp (GSI) and 120 kVp (SDCT) with tube exposures of 255/128 (DSCT), 160/133 (GSI) and 150 mAs (SDCT), respectively. For each acquisition, a spiral thoracic aorta protocol in the arterial phase was selected. For each CT system, a 40 ml test bolus of routine iodine concentration (300 mg I/ml) with the same fixed injection protocol was used to determine the scan delay. No bolus-tracking protocol was used because the attenuation of iodine decreases with the reduction of iodine concentration, therefore we expected that a fixed threshold (e.g. 100 HU) could not be reached by all iodine concentrations. For both DSCT and GSI, images were reconstructed using FBP. Since FBP is no longer available with SDCT, the lowest level (0) of iterative reconstruction (IR) was used for image reconstruction. Care should be taken when evaluating protocols with different reconstruction methods (IR/FBP), therefore only different scan protocols within a vendor were compared in the current study and no direct comparison between vendors was performed. Detailed acquisition parameters for all systems are listed in **Table 1**.

Image analysis

Images were analysed using vendor specific dedicated workstations (SyngoVia version VB10A, Siemens Healthineers; Volume Viewer version 12.3, Ext. 4, GE Healthcare; IntelliSpace Portal version 6.5.0.02080, Philips Healthcare). DECT data were reconstructed to obtain VMI at following energy levels; 40, 50, 60, 70, 80, 90, 100 and 120 keV. On both conventional CT images and VMI (DECT), intraluminal enhancement (Hounsfield units (HU)) and noise (standard deviation (SD) of the HU measurement) were measured by manually placing a circular region of interest (ROI) with a fixed area of 0.2 (LM), 5.0 (AA) and 2.0 (DA) cm². Background enhancement and noise were measured by placing an ROI (4.0 cm²) in 2 homogeneous areas in the water container (**Figure 1C**). For each location, the shape, position and size of the ROI were kept consistent for all measurements. For each reconstruction, the two

Table 1 Scan parameters.

	DSCT			GSI			SDCT		
	Conv. reference	Conv. low kVp	DECT	Conv. reference	Conv. low kVp	DECT	Conv. reference	Conv. low kVp	DECT
Detector collimation (mm)	96x0.6	96x0.6	64x0.6	64x0.625	64x0.625	64x0.625	64x0.625	64x0.625	64x0.625
Tube voltage (kVp)	120	70	80/150Sn	120	80	80/140	120	80	120
Tube current (mA)	360	720	714/359	370	700	450/375	82	164	82
Gantry rotation time (s)	0.25	0.25	0.25	0.4	0.4	0.7	0.33	0.33	0.33
Exposure (mAs)	150	300	255/128	150	286	160/133	150	300	150
$CTDI_{vol}$ (mGy)	10.0	3.5	9.2	10.5	6.7	10.8	13.5	9.0	13.5
Scan delay (s) post injection	19	19	19	19	19	19	19	19	19
Pitch	0.60	0.60	0.70	0.98	0.98	0.98	0.18	0.18	0.18
Mode	Spiral	Spiral	Spiral	Spiral	Spiral	Spiral	Spiral	Spiral	Spiral
Kernel	Cardiac (Bv36d)	Cardiac (Bv36d)	Cardiac (Bv36d)	Standard	Standard	Standard	Cardiac (CB)	Cardiac (CB)	Cardiac (CB)
Slice thickness/increment (mm)	1/1	1/1	1/1	1/1	1/1	1/1	1/1	1/1	1/1
Reconstruction algorithm	FBP	FBP	FBP	FBP	FBP	FBP	iDose level 0	iDose level 0	Spectral level 0

$CTDI_{vol}$ = volumetric CT dose index; Conv. = Conventional; DECT = dual-energy CT; DSCT = dual source CT; FBP = filtered back projection; GSI = gemstone spectral imaging; kVp = kilovoltage peak; mAs = milliampere second; mGy = milligray; SDCT = dual-layer spectral detector CT

4

measurements of background enhancement and noise were averaged for further analysis of contrast to noise ratios (CNR), which was calculated as follows [19]:

$$CNR = \frac{(HU_{Artery} - HU_{Background})}{\sqrt{(\frac{1}{2} \times ((SD_{Artery}^{2}) + (SD_{Background}^{2})))}}$$

Radiation dose differed between scan protocols (**Table 1**). To allow for evaluation of the effect of different tube voltages and VMI energies on CNR independent of dose, CNR was normalized to volumetric CT dose index (CTDI$_{vol}$) for each protocol by using dose corrected CNR (DCCNR), defined as [20–22]:

$$DCCNR = \frac{(CNR^{2})}{(CTDI_{vol})}$$

4

Statistical analysis

The primary study measures were attenuation (HU), CNR and DCCNR. Per acquisition, measurements obtained in the 3 vessels were averaged. For each vendor, image analysis measurements of routine iodine concentration (300 mg I/ml) scanned at 120 kVp were used as a reference. Measurements with conventional CT at lowest possible kVp and DECT at different iodine concentrations were compared to the reference measurement for each CT system.

Results

Dual source computed tomography (Figure 2)

At reference (120 kVp; 300 mg I/ml) average attenuation, CNR and DCCNR were 361.0 HU, 46.2 and 227.0, respectively. With lowest tube voltage of 70 kVp, attenuation and DCCNR increased and iodine concentration reduction down to 180 mg I/ml (40% reduced) resulted in higher attenuation (429.3 HU) and DCCNR (467.1) in comparison to the reference. For CNR at 70 kVp a small increase was observed, and dropped below the reference CNR at iodine concentration reduction of 20% or more. In DECT mode, the optimal VMI energy level with the highest attenuation, CNR and DCCNR values was 40 keV. At this keV, attenuation of reduced iodine concentration down to 120 mg I/ml (60% reduced) was 553.1 HU, and was higher compared to reference. At this same keV, CNR and DCCNR were 51.3 and 286.1 at 240 mg I/ml (20% reduced), and were higher compared to the reference. Further iodine concentration reductions resulted in attenuation, CNR and DCCNR values below the reference levels.

Figure 2 Objective image quality of dual source computed tomography. Average attenuation, CNR and DCCNR values per scan across different energy levels and different iodine concentrations. Reference line indicates attenuation values of routine iodine concentration (300 mg I/ml) scanned on reference conventional CT (120 kVp). Corresponding kVp, mAs and CTDI$_{vol}$ for the different scan protocols were: 70 kVp, 300 mAs, 3.5 mGy; 120 kVp, 150 mAs, 10 mGy; 80/150Sn kVp, 255/128 mAs, 9.2 mGy (DECT). *CNR = contrast to noise ratio; CTDI$_{vol}$ = volumetric CT dose index; DCCNR = dose corrected contrast to noise ratio; DECT = dual-energy computed tomography; DSCT = dual source computed tomography; HU = Hounsfield units; kVp = kilovoltage peak; keV = kilo electron voltage; mAs = milliampere second; mGy = milligray*

Gemstone spectral imaging (Figure 3)

At reference (120 kVp; 300 mg I/ml) average attenuation, CNR and DCCNR were 327.1 HU, 20.3 and 39.7, respectively. At the lowest tube voltage (80 kVp), iodine concentration reduction down to 180 mg I/ml (40% reduced) resulted in an attenuation of 354.4 HU and a DCCNR of 46.1, both higher compared to the reference. For CNR at 80 kVp, iodine concentration reduction down to 20% resulted in a higher CNR compared to the reference. With VMI on DECT, the highest attenuation was achieved at 40 keV, whilst the highest CNR and DCCNR values were obtained at 70 keV. On 40 keV images, the average CT-value of reduced iodine concentration down to 120 mg I/ml (60% reduced) was 369.6 HU, and was higher compared to reference. CNR and DCCNR values at routine iodine concentration (300 mg I/ml) on 70 keV images were 18.9 and 33.5 and were lower compared to imaging at reference. Any (further) reduction in iodine concentration led to lower values than at reference for both conventional CT low kVp and DECT.

Dual-layer spectral detector computed tomography (Figure 4)

At reference (120 kVp; 300 mg I/ml) average attenuation, CNR and DCCNR were 311.8 HU, 28.2 and 60.2, respectively. Scanning with the lowest tube voltage of 80 kVp resulted in higher attenuation values, whereby an iodine concentration reduction of 20% resulted in 419.6 HU and was higher compared to the reference. At 80 kVp, no iodine concentration reduction without loss of CNR or DCCNR compared to the reference was feasible. In DECT mode, optimal VMI energy level was 40 keV. At this energy level, iodine concentration reduction down to 120 mg I/ml (60% reduced) resulted in a higher attenuation (447.1 HU), CNR (46.9) and DCCNR (171.5) compared to the reference. Further iodine concentration reductions led to lower values compared to the reference.

4

4

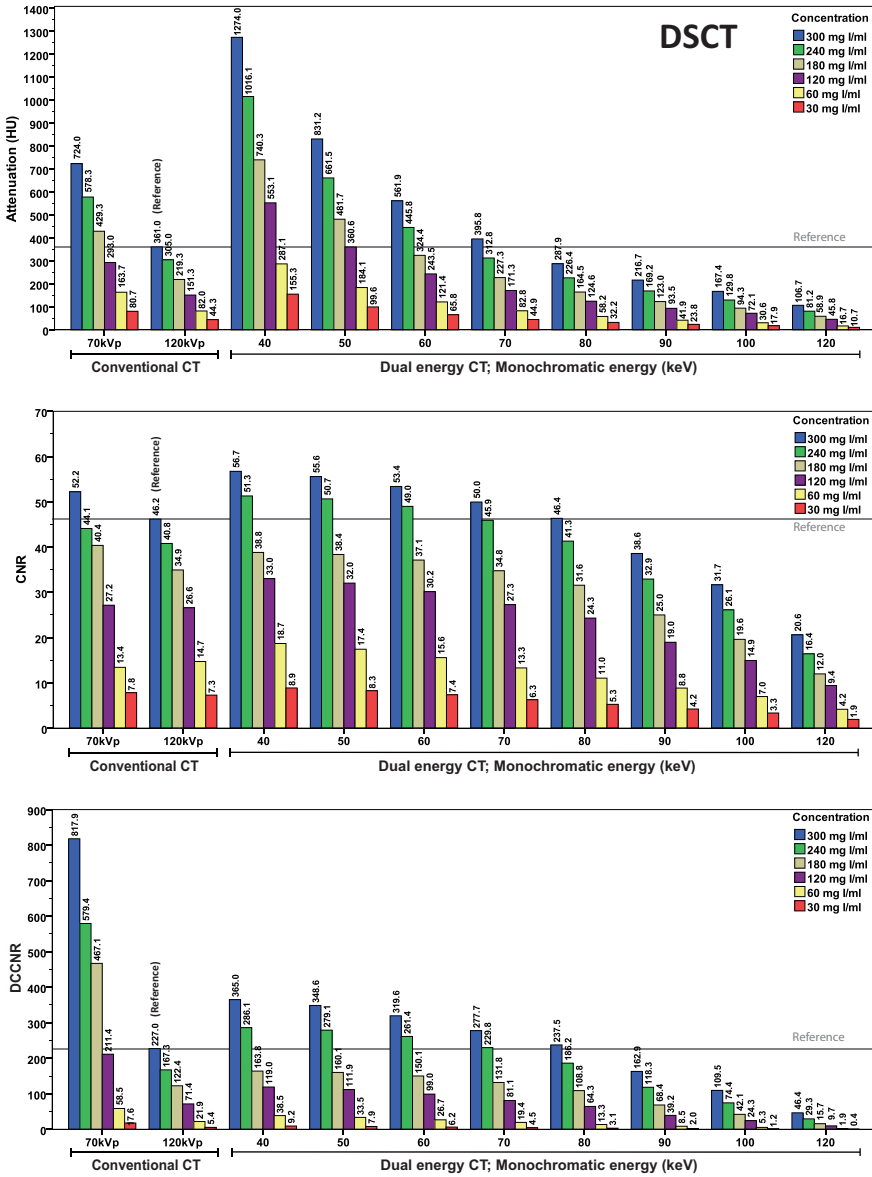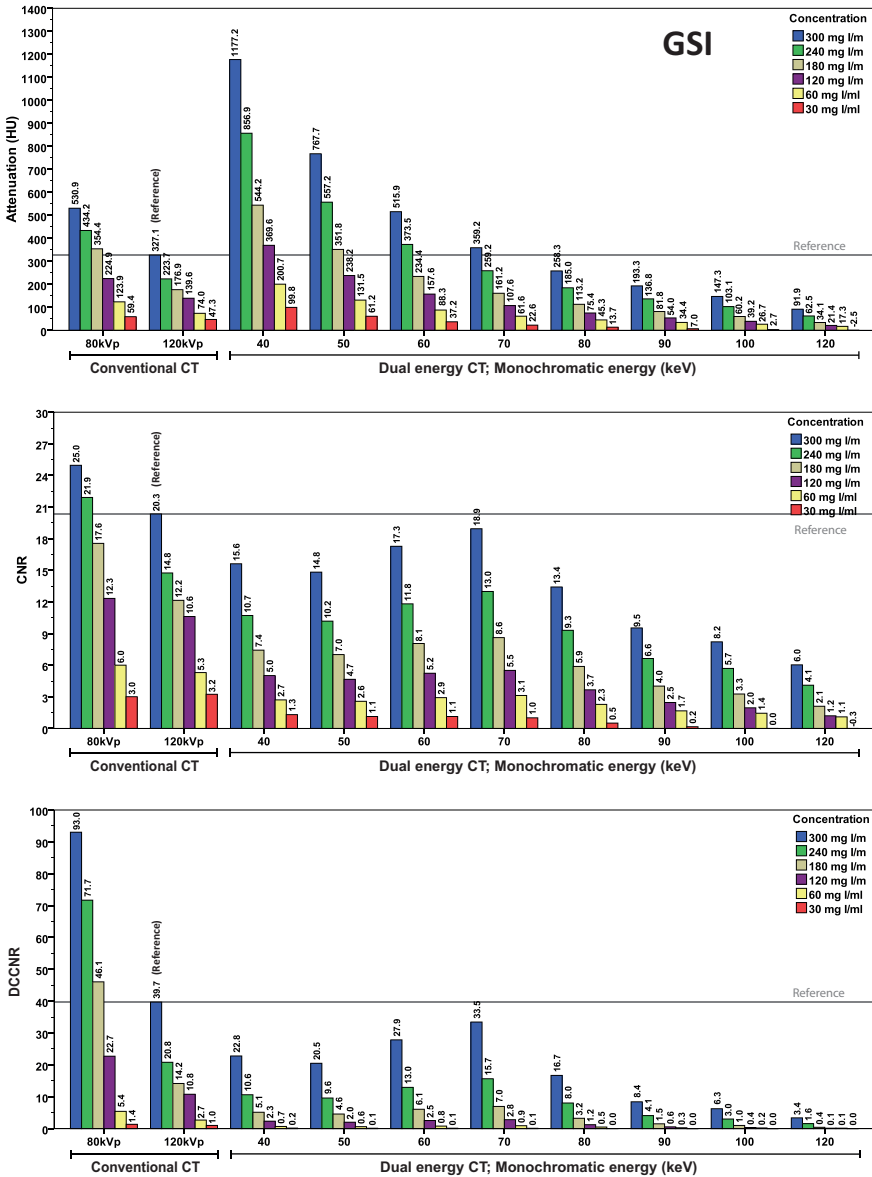**Figure 3** Objective image quality of gemstone spectral imaging. Average attenuation, CNR and DCCNR values per scan across different energy levels and different iodine concentrations. Reference line indicates attenuation values of routine iodine concentration (300 mg I/ml) scanned on reference conventional CT (120 kVp). Corresponding kVp, mAs and CTDI$_{vol}$ for the different scan protocols were: 80 kVp, 286 mAs, 6.7 mGy; 120 kVp, 150 mAs, 10.5 mGy; 80/140 kVp, 160/133 mAs, 10.8 mGy (DECT). CNR = contrast to noise ratio; CTDI$_{vol}$ = volumetric CT dose index; DCCNR = dose corrected contrast to noise ratio; DECT = dual-energy computed tomography; GSI = gemstone spectral imaging; HU = Hounsfield units; kVp = kilovoltage peak; keV = kilo electron voltage; mAs = milliampere second; mGy = milligray
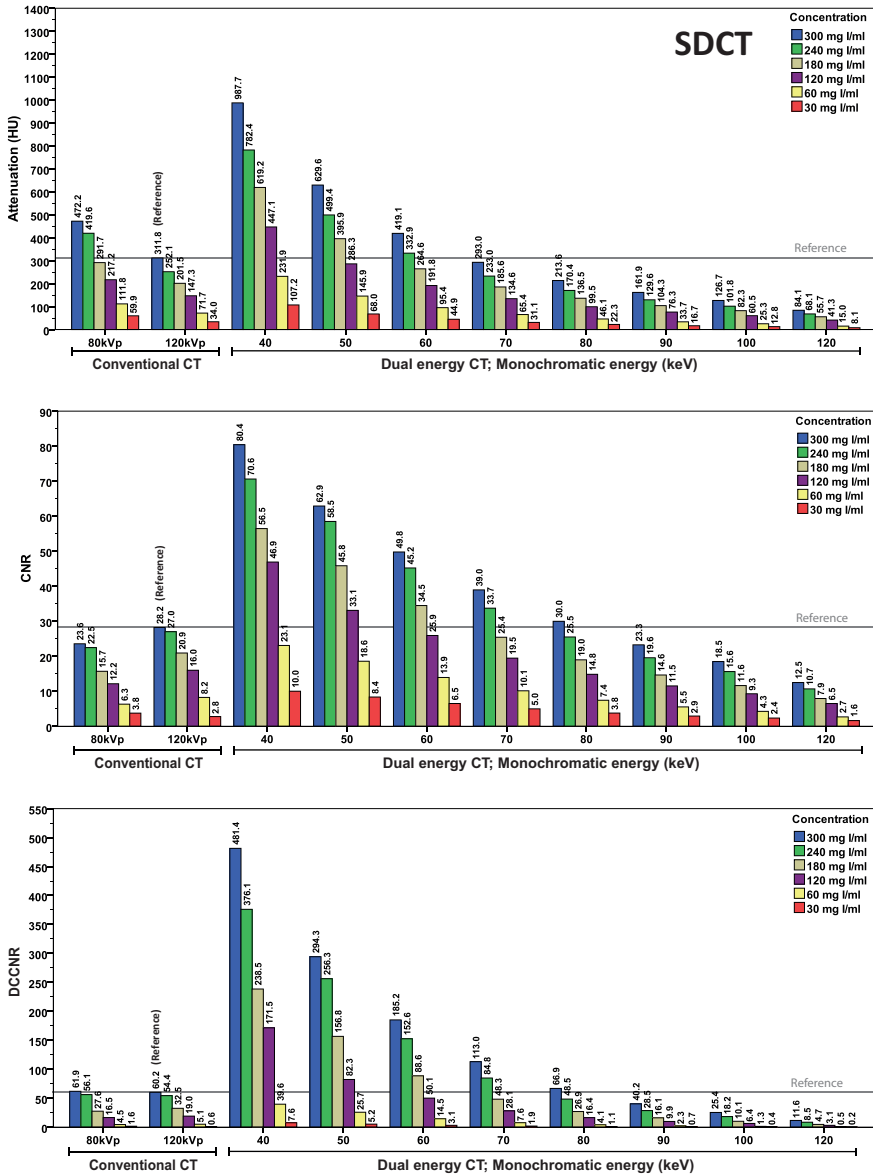
Figure 4 Objective image quality of dual-layer spectral detector computed tomography. Average attenuation, CNR and DCCNR values per scan across different energy levels and different iodine concentrations. Reference line indicates attenuation values of routine iodine concentration (300 mg I/ml) scanned on reference conventional CT (120 kVp). Corresponding kVp, mAs and CTDI$_{vol}$ for the different scan protocols were: 80 kVp, 300 mAs, 9.0 mGy; 120 kVp, 150 mAs, 13.5 mGy; 120 kVp, 150 mAs, 13.5 mGy (DECT). CNR = contrast to noise ratio; CTDI$_{vol}$ = volumetric CT dose index; DCCNR = dose corrected contrast to noise ratio; DECT = dual-energy computed tomography; HU = Hounsfield units; kVp = kilovoltage peak; keV = kilo electron voltage; mAs = milliampere second; mGy = milligray; SDCT = dual-layer spectral detector computed tomography

4

Discussion

In this phantom study, we showed that for CTA images of the aorta and coronary arteries iodine reductions without loss in objective image quality compared to reference are feasible with both conventional CT low kVp and DECT. The optimal scan protocol with the highest iodine concentration reduction differed per CT system. The DCCNR results showed that an iodine concentration reduction of 40% can be achieved using conventional CT low kVp on DSCT and GSI, and 60% using DECT on SDCT. DCCNR allows for an evaluation of objective image quality independent of the effect of radiation dose, and thereby for an evaluation of the extent to which iodine concentration could be reduced purely based on tube voltage settings and VMI energy levels [20–22]. The increase in DCCNR for the low kVp protocols implicates that a tradeoff should be made between reduction of radiation dose and iodine concentration when optimizing these protocols.

With the use of a dynamic circulation phantom we were able to evaluate the effect of iodine concentration reduction on objective image quality using different CT systems while mimicking a clinical situation as best as possible by carefully controlling parameters such as heart rate, blood pressure and cardiac output. We found that each CT system has its own optimal scan protocol at which the highest iodine concentration reduction can be achieved without loss of objective image quality, when compared to the reference protocol performed on the same scanner (120 kVp; 300 mg I/ml). Moreover, there were substantial differences in attenuation values, CNR and DCCNR between CT systems. An explanation for these differences can probably be found in radiation dose, image acquisition technique (e.g. kVp, pitch, rotation time), reconstruction model (FBP and IR) and technique (kernel, VMI formation and post processing noise reduction). However, to which extent each factor played a role in the differences we found remains unclear and is beyond the scope of this study. Therefore, no direct comparison between vendors was performed.

For all scanners in DECT mode, attenuation values of iodine increased with lowering VMI energies, with highest attenuation found at 40 keV. CNR values however, did not follow the same trend for all systems (**Figure 2, 3 & 4**). A different optimal keV with highest CNR values was found for GSI (70 keV) compared to DSCT and SDCT (40 keV). Because CNR is a quotient of both attenuation and noise, an explanation for the difference in CNR can be found in the noise. In VMI, noise increases for both low and high energies [23]. Therefore, each vendor has devised their own solution for this problem. One of these solutions is post processing noise reduction

algorithms. GSI uses noise reduction based on IR and known noise properties from the projection based images [16]. DSCT uses an advanced image-based post processing technique (Mono+) to decrease noise on low keV [24, 25]. SDCT uses a post processing anti-correlated noise reduction algorithm which is performed on projection-based data [16, 26]. Other factors that could influence noise and thereby CNR and DCCNR, include, but are not limited to; tube voltage, tube current, pitch, kernel and image reconstruction. For image reconstruction FBP was used for DSCT and GSI and the lowest level (0) of IR for SDCT, because FBP is no longer available on this platform. However, as IR significantly reduces image noise [19], this could influence both the optimal keV selection and the CNR and DCCNR results [12, 14, 27, 28]. In addition, it is expected that when applying (higher levels of) IR, even further iodine concentration reduction could be achieved without loss of objective image quality in terms of CNR and DCCNR values for both conventional CT low kVp scans and DECT low VMI energies [7, 9, 25, 29].

Multiple studies have investigated iodine reduction using conventional CT low kVp [6–9] as well as DECT protocols [11–15, 30]. Studies on DSCT concluded that both 70 kVp and DECT allowed for iodine reduction of 44-56% [6, 8, 15] without loss of attenuation compared to a reference 120 kVp scan. For 70 kVp, CNR values were found to be significantly decreased [6] and to be similar [8] compared to reference CNR. The difference in CNR found by these studies can be explained by the fact that Thor et al. [8] used equal $CTDI_{vol}$ values for all protocols by increasing tube current for low kVp scans, whereas Kok et al. [6] did not use equal $CTDI_{vol}$. Equal $CTDI_{vol}$ is comparable to DCCNR used in our study. Findings of both studies are in accordance with our results on the DSCT; our DCCNR results are in accordance with findings of Thor et al. [8] and our CNR results are in accordance with Kok et al. [6]. A study on iodine reduction with DSCT in DECT mode showed that with 60 keV images at 44% reduced iodine dose, attenuation values were similar and CNR values were significantly lower compared to reference [15]. We found similar results with DSCT in DECT mode; at 40 keV images, iodine reduction down to 60% was feasible without loss of attenuation, while for CNR more than 20% reduction led to decreased CNR values compared to reference. The discrepancy between optimal keV found in study by Delesalle et al. [15] (60 keV) and our study (40 keV) can possibly be explained by the fact that an advanced image-based post processing technique (mono+) was used in our study [15, 24, 25]. Studies on GSI concluded that 80 kVp allowed for iodine reduction down to 47% (170 mg I/ml) [7] and VMI at

4

low energy with DECT down to 70% [11–14] without loss of attenuation and CNR. In terms of attenuation, we found similar results on GSI, with feasibility of contrast reduction down to 60%, while for CNR we found that less to no reduction was feasible. This discrepancy can possibly be explained by the usage of IR in these studies, which was not used in the current study [7, 11–14]. A recent study on SDCT showed the feasibility of iodine concentration reduction in a static phantom [30]. When compared to a reference CNR of around 30 (comparable to our reference CNR), the iodine concentration could be reduced with around 65% using low VMI at 40 keV without loss of objective image quality [30]. These results are in line with our findings of iodine contrast reduction down to 60% using low VMI at 40 keV. In another study, iodine concentration reduction using conventional CT low kVp (80 kVp) has been described on a CT system from the same vendor showing increased attenuation and decreased CNR compared to reference, similar to our study [9].

When considering optimal iodine concentration reduction, multiple factors have to be taken into account. This includes the potential to reduce radiation dose when scans are made using conventional CT low kVp. However, low kVp imaging may not be the preferred strategy for imaging larger patients. On the other hand, DECT provides extra information such as iodine density, which is a semi-quantitative indicator for perfusion [31].

Although the dynamic circulation phantom setup allowed for an evaluation of optimal iodine reduction in a controlled setting mimicking a clinical situation across multiple vendors, it has limitations. First, the phantom is relatively small, and the results of the present study may therefore be limited to small to average-sized patients. In addition, physiological parameters, such as cardiac output, can differ per patient. Second, as described before, IR was only selected for SDCT image reconstructions, because no FBP was available on this scanner. Even though the lowest level of IR was used, this could still have influenced our CNR and DCCNR results by decreasing noise for this vendor. For this reason, we did not make a direct comparison between vendors and only compared results of different scan protocols within one vendor. Third, no subjective image quality was evaluated. Patient studies on both subjective and objective image quality are needed to confirm our findings in routine clinical care, whereby results of the current study could be used as a guideline for protocol development on a per vendor level. Fourth, in the current study a fixed injection protocol was used whereas in clinical practice a multi-stage injection method is more commonly used. The fixed injection protocol was chosen to keep iodine administration similar between the different CT systems.

In conclusion, we demonstrated that iodine concentration reduction is feasible with both low kVp on conventional CT and low VMI energies on DECT without loss of objective image quality. The optimal scan protocols at which highest iodine concentration reduction can be achieved differed per vendor. Maximal iodine concentration reduction of up to 40% is feasible when using conventional CT low kVp on DSCT (70 kVp) and GSI (80 kVp), and up to 60% when using DECT (40 keV) on SDCT without loss of objective image quality compared to routine iodine concentration imaged at 120 kVp. However, patient studies are needed to extend and translate our findings.

4

References

1. Budoff MJ, Dowe D, Jollis JG, et al (2008) Diagnostic Performance of 64-Multidetector Row Coronary Computed Tomographic Angiography for Evaluation of Coronary Artery Stenosis in Individuals Without Known Coronary Artery Disease. J Am Coll Cardiol 52:1724–1732. doi: 10.1016/j.jacc.2008.07.031

2. Lameire N, Van Biesen W, Vanholder R Acute renal failure. Lancet (London, England) 365:417–30. doi: 10.1016/S0140-6736(05)17831-3

3. Tepel M, Aspelin P, Lameire N (2006) Contrast-induced nephropathy: a clinical and evidence-based approach. Circulation 113:1799–806. doi: 10.1161/CIRCULATIONAHA.105.595090

4. Laville M, Juillard L Contrast-induced acute kidney injury: how should at-risk patients be identified and managed? J Nephrol 23:387–98

5. Stacul F, van der Molen AJ, Reimer P, et al (2011) Contrast induced nephropathy: updated ESUR Contrast Media Safety Committee guidelines. Eur Radiol 21:2527–2541. doi: 10.1007/s00330-011-2225-0

6. Kok M, Mihl C, Hendriks BMF, et al (2016) Optimizing contrast media application in coronary CT angiography at lower tube voltage: Evaluation in a circulation phantom and sixty patients. Eur J Radiol 85:1068–1074. doi: 10.1016/j.ejrad.2016.03.022

7. Buls N, Van Gompel G, Van Cauteren T, et al (2015) Contrast agent and radiation dose reduction in abdominal CT by a combination of low tube voltage and advanced image reconstruction algorithms. Eur Radiol 25:1023–1031. doi: 10.1007/s00330-014-3510-5

8. Thor D, Brismar TB, Fischer MA (2015) Low tube voltage dual source computed tomography to reduce contrast media doses in adult abdomen examinations: A phantom study. Med Phys 42:5100–9. doi: 10.1118/1.4927791

9. Iyama Y, Nakaura T, Yokoyama K, et al (2016) Low-Contrast and Low-Radiation Dose Protocol in Cardiac Computed Tomography. J Comput Assist Tomogr 40:941–947. doi: 10.1097/RCT.0000000000000440

10. Danad I, Fayad Z a., Willemink MJ, Min JK (2015) New Applications of Cardiac Computed Tomography. JACC Cardiovasc Imaging 8:710–723. doi: 10.1016/j.jcmg.2015.03.005

11. Raju R, Thompson AG, Lee K, et al (2014) Reduced iodine load with CT coronary angiography using dual-energy imaging: A prospective randomized trial compared with standard coronary CT angiography. J Cardiovasc Comput Tomogr 8:282–8. doi: 10.1016/j.jcct.2014.06.003

12. Lv P, Liu J, Chai Y, et al (2016) Automatic spectral imaging protocol selection and iterative reconstruction in abdominal CT with reduced contrast agent dose: initial experience. Eur Radiol. doi: 10.1007/s00330-016-4349-8

13. Carrascosa P, Leipsic JA, Capunay C, et al (2015) Monochromatic image reconstruction by dual energy imaging allows half iodine load computed tomography coronary angiography. Eur J Radiol 84:1915–1920. doi: 10.1016/j.ejrad.2015.06.019

14. Shuman WP, O'Malley RB, Busey JM, et al (2017) Prospective comparison of dual-energy CT aortography using 70% reduced iodine dose versus single-energy CT aortography using standard iodine dose in the same patient. Abdom Radiol. doi: 10.1007/s00261-016-1041-z

15. Delesalle M-A, Pontana F, Duhamel A, et al (2013) Spectral optimization of chest CT angiography with reduced iodine load: experience in 80 patients evaluated with dual-source, dual-energy CT. Radiology 267:256–66. doi: 10.1148/radiol.12120195

16. Johnson, TR; Fink, C; Schönberg, SO; Reiser M (2011) Dual Energy CT in Clinical Practice, Medical Radiology. Springer-Verlag Berlin Heidelberg. Springer Berlin Heidelberg, Berlin, Heidelberg

17. Kok M, Mihl C, Mingels AA, et al (2014) Influence of contrast media viscosity and temperature on injection pressure in computed tomographic angiography: a phantom study. Invest Radiol 49:217–23. doi: 10.1097/RLI.0000000000000019

18. Mihl C, Wildberger JE, Jurencak T, et al (2013) Intravascular enhancement with identical iodine delivery rate using different iodine contrast media in a circulation phantom. Invest Radiol 48:813–8. doi: 10.1097/RLI.0b013e31829979e8

19. Willemink MJ, Leiner T, de Jong PA, et al (2013) Iterative reconstruction techniques for computed tomography part 2: initial results in dose reduction and image quality. Eur Radiol 23:1632–42. doi: 10.1007/s00330-012-2764-z

20. Samei E, Dobbins JT, Lo JY, Tornai MP (2005) A framework for optimising the radiographic technique in digital X-ray imaging. Radiat Prot Dosimetry 114:220–9. doi: 10.1093/rpd/nch562

21. Kim KS, Lee JM, Kim SH, et al (2010) Image fusion in dual energy computed tomography for detection of hypervascular liver hepatocellular carcinoma: phantom and preliminary studies. Invest Radiol 45:149–57. doi: 10.1097/RLI.0b013e3181d32119

22. Siegel MJ, Hildebolt C, Bradley D (2013) Effects of Automated Kilovoltage Selection Technology on Contrast-enhanced Pediatric CT and CT Angiography. Radiology 268:538-47. doi: 10.1148/radiol.13122438

23. Yu L, Leng S, McCollough CH (2012) Dual-Energy CT–Based Monochromatic Imaging. Am J Roentgenol 199:S9–S15. doi: 10.2214/AJR.12.9121

24. Grant KL, Flohr TG, Krauss B, et al (2014) Assessment of an advanced image-based technique to calculate virtual monoenergetic computed tomographic images from a dual-energy examination to improve contrast-to-noise ratio in examinations using iodinated contrast media. Invest Radiol 49:586–92. doi: 10.1097/RLI.0000000000000060

25. Leng S, Yu L, Fletcher JG, McCollough CH (2015) Maximizing Iodine Contrast-to-Noise Ratios in Abdominal CT Imaging through Use of Energy Domain Noise Reduction and Virtual Monoenergetic Dual-Energy CT. Radiology 276:562–570. doi: 10.1148/radiol.2015140857

26. van Hamersvelt RW, Schilham AMR, Engelke K, et al (2017) Accuracy of bone mineral density quantification using dual-layer spectral detector CT: a phantom study. Eur Radiol 27:4351–4359. doi: 10.1007/s00330-017-4801-4

27. Zhang D, Li X, Liu B (2011) Objective characterization of GE Discovery CT750 HD scanner: Gemstone spectral imaging mode. Med Phys 38:1178–1188. doi: 10.1118/1.3551999

28. Clark ZE, Bolus DN, Little MD, Morgan DE (2015) Abdominal rapid-kVp-switching dual-energy MDCT with reduced IV contrast compared to conventional MDCT with standard weight-based IV contrast: an intra-patient comparison. Abdom Imaging 40:852–8. doi: 10.1007/s00261-014-0253-3

29. Yin W-H, Lu B, Gao J-B, et al (2015) Effect of reduced x-ray tube voltage, low iodine concentration contrast medium, and sinogram-affirmed iterative reconstruction on image quality and radiation dose at coronary CT angiography: Results of the prospective multicenter REALISE trial. J Cardiovasc Comput Tomogr 9:215–224. doi: 10.1016/j.jcct.2015.01.010

30. Tsang DS, Merchant TE, Merchant SE, et al (2017) Quantifying potential reduction in contrast dose with monoenergetic images synthesized from dual-layer detector spectral CT. Br J Radiol 90:20170290. doi: 10.1259/bjr.20170290

31. Pelgrim GJ, van Hamersvelt RW, Willemink MJ, et al (2017) Accuracy of iodine quantification using dual energy CT in latest generation dual source and dual layer CT. Eur Radiol 27:3904–3912. doi: 10.1007/s00330-017-4752-9

4
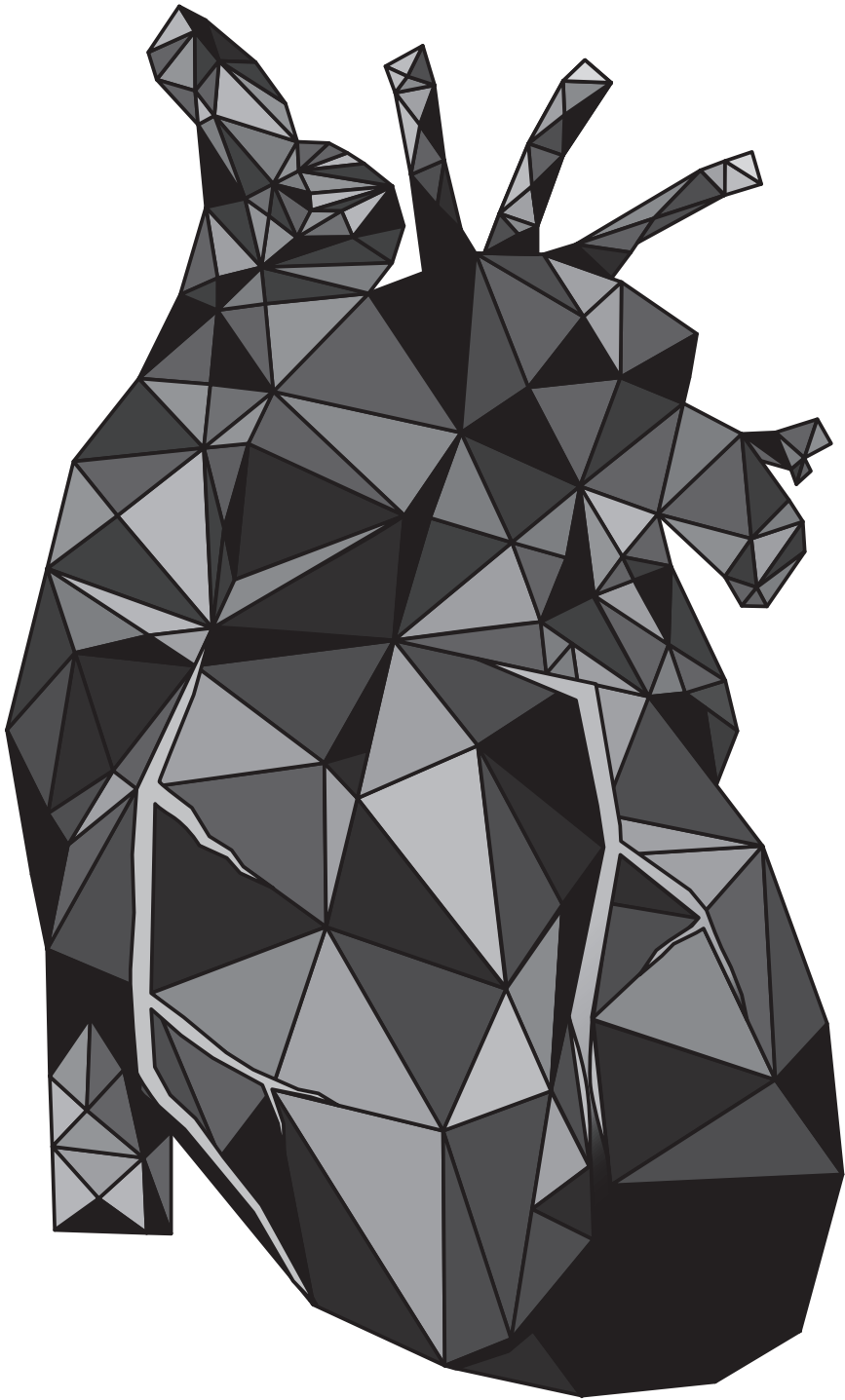
Chapter 5

Accuracy of iodine quantification using dual energy CT in latest generation dual source and dual layer CT

Gert Jan Pelgrim
Robbert W. van Hamersvelt
Martin J. Willemink
Bernhard T. Schmidt
Thomas Flohr
Arnold M.R. Schilham
Julien Milles
Matthijs Oudkerk
Tim Leiner
Rozemarijn Vliegenthart

Abstract

Objectives

To determine the accuracy of iodine quantification with dual energy computed tomography (DECT) in two high-end CT systems with different spectral imaging techniques.

Methods

Five tubes with different iodine concentrations (0, 5, 10, 15, 20 mg/ml) were analysed in an anthropomorphic thoracic phantom. Adding two phantom rings simulated increased patient size. For third-generation dual source CT (DSCT), tube voltage combinations of 150Sn and 70, 80, 90, 100 kVp were analysed. For dual layer CT (DLCT), 120 and 140 kVp were used. Scans were repeated three times. Median normalized values and interquartile ranges (IQRs) were calculated for all kVp settings and phantom sizes.

Results

Correlation between measured and known iodine concentrations was excellent for both systems (R = 0.999–1.000, $p < 0.0001$). For DSCT, median measurement errors ranged from −0.5% (IQR −2.0, 2.0%) at 150Sn/70 kVp and −2.3% (IQR −4.0, −0.1%) at 150Sn/80 kVp to −4.0% (IQR −6.0, −2.8%) at 150Sn/90 kVp. For DLCT, median measurement errors ranged from −3.3% (IQR −4.9, −1.5%) at 140 kVp to −4.6% (IQR −6.0, −3.6%) at 120 kVp. Larger phantom sizes increased variability of iodine measurements ($p < 0.05$).

Conclusions

Iodine concentration can be accurately quantified with state-of-the-art DECT systems from two vendors. The lowest absolute errors were found for DSCT using the 150Sn/70 kVp or 150Sn/80 kVp combinations, which was slightly more accurate than 140 kVp in DLCT.

5

Introduction

Coronary artery disease (CAD) remains a widespread disease in the Western society. Moreover, the impact of CAD will increase in the next decades because of the epidemic of obesity. Cardiovascular disease (CVD) is the primary cause of death in the USA and overall annual economic burden is substantial [1]. In 2010, medical costs with a direct relation to cardiovascular disease were US $273 billion for the USA only [2].

Computed tomography (CT) angiography is a proven technique for the detection of coronary stenosis with high sensitivity and negative predictive value [3]. However, especially in cases with intermediate stenosis it is often difficult to determine whether a stenosis is significant or not. Myocardial perfusion scanning under stress can help in the diagnostic process of determining the significance of any indeterminate stenosis, e.g. by single-photon emission computed tomography (SPECT), positron emission tomography (PET) or magnetic resonance imaging (MRI) [4]. Recent developments have renewed interest for perfusion analysis using CT. One of the methods to evaluate myocardial ischemia with CT is dual energy CT (DECT). In DECT, high energy X-ray photons are differentiated from low energy X-ray photons. Because attenuation of materials and tissues differs at different photon energies [5–7], DECT allows for quantification of materials and tissues. By quantifying iodinated contrast media the DECT technique does not provide direct information about the blood flow but provides an estimate of contrast distribution across the myocardium at one point in time. However, iodine distribution has a direct relation to the myocardial blood flow, and thus provides a semi-quantitative biomarker for myocardial perfusion.

Currently several DECT methods are available of which two are analysed in this study: the dual source CT (DSCT) whereby two X-ray tubes are operated at separate tube voltages and the dual layer spectral CT (DLCT) where low energy photons are absorbed in the first detector layer and high energy photons in the second detector layer [5, 8, 9]. Koonce et al. found good stability and accuracy of the iodine content determination on DSCT scanners, using options available at that time [10]. Since then, third-generation DSCT has become available, providing the possibility to use a tin filter with a high tube voltage of 150 kVp, resulting in a narrow spectrum of photons at a higher energy and larger spectral separation with the low tube voltages (down to 70 kVp). Furthermore, the first generation of DLCT has been recently introduced in the clinic. It is expected that a high tube voltage (140 kVp) results in better spectral separation compared to a lower tube

voltage (120 kVp) and thus in more accurate iodine quantification; however, the performance in iodine quantification using DLCT is still unknown. Therefore the aim of the current study was to determine the accuracy of the quantification of iodine concentrations on third-generation DSCT and first-generation DLCT in a phantom.

Materials and Methods

Phantom description

An anthropomorphic phantom (Cardio CT phantom, QRM, Möhrendorf, Germany) was used to simulate the human thorax. This thorax phantom contained artificial lungs, spine, body fat and a cavity at the position of the heart. The cavity was filled with a Perspex holder carrying five separate tubes. These 15-ml tubes were filled with diluted contrast solutions (Hexabrix 320 mg iodine/ml, Guerbet, Paris, France), resulting in concentrations of 0, 5, 10, 15 and 20 mg of iodine per ml, one tube for each concentration. The Perspex holder was placed in a water container in the centre of the cardiac cavity, surrounding the iodine tubes and the Perspex holder with water. Different patient sizes were simulated using extension rings with densities comparable to fat (Extension rings, QRM, Möhrendorf, Germany), which were placed around the thorax. Two separate fat rings were used, providing image data of simulated small, medium and large patient sizes (**Figure 1**).

Image acquisition

Image acquisition was performed in dual energy mode on third-generation DSCT (SOMATOM Force, Siemens Healthcare, Forchheim, Germany) and first-generation DLCT (IQon spectral CT, Philips Healthcare, Best, the Netherlands). For DSCT, 150 kVp with tin (Sn) filter was used as the high tube voltage in combination with low tube voltages of 70, 80, 90 and 100 kVp in spiral scan mode. For DLCT, tube voltages of 140 and 120 kVp were used in spiral scan mode. Tube currents for DSCT were 165 mAs/rot at low tube voltage and 150 mAs/rot at the high tube voltage (vendor-recommended protocol). Tube current of 200 mAs was used for DLCT, as part of a clinical use protocol. This mAs was selected in order to acquire DECT data at comparable radiation doses for DSCT and DLCT. For DSCT, mean CT dose index ($CTDI_{vol}$) gradually increased when raising the low tube voltages of the DSCT combinations, from 18.7 mGy for 150Sn/70 kVp and 22.1 mGy for 150Sn/80 kVp to 26.9 mGy for 150Sn/90 kVp and 32.2 mGy for 150Sn/100 kVp. For DLCT, mean $CTDI_{vol}$ for the 140 kVp tube voltage was 26.0 mGy, while 120-kVp tube voltage resulted in a $CTDI_{vol}$ of 18.1 mGy. All acquisitions were repeated three times with small
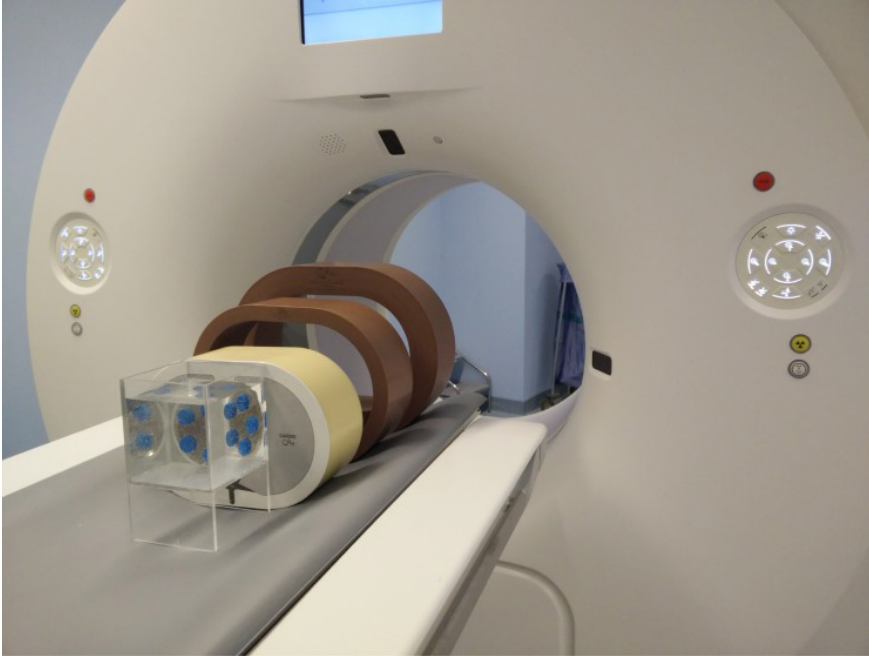
Figure 1 QRM iodine quantification setup, including the fat rings and the iodine tubes surrounded by water

translations and rotations between the separate scan repetitions. Various grades of iterative reconstruction (IR) were used to analyse the influence of increased IR on iodine quantification. Third-generation DSCT data were reconstructed with a previously described IR algorithm (ADMIRE, Siemens Healthcare, Forchheim, Germany) [11, 12], whereas DLCT data were reconstructed with a model-based iterative reconstruction algorithm taking into account anti-correlated noise. DSCT data were reconstructed using four settings: IR grades 0, 1, 3 and 5. DLCT data were reconstructed using spectral levels of 0, 2, 4 and 6. For DSCT, scans were acquired with a gantry rotation time of 250 ms, a pitch of 0.19 and a detector collimation of $2 \times 64 \times 0.6$ mm. DLCT scans were acquired with a gantry rotation time of 330 ms, a pitch of 0.18 and a detector collimation of 64×0.625 mm.

Image analysis and iodine quantification

Images were reconstructed at 3.0 mm slice thickness with an increment of 1.5 mm using the standard kernel settings. The images of the separate systems were analysed using vendor-specific software, Syngo.via software VB10 (Siemens, Forchheim,

Germany) for DSCT and Spectral Diagnostic Suite (Philips Healthcare, Best, the Netherlands) for DLCT. In Syngo.via a dedicated DECT pack 'Special' was used and analysis was performed in 'virtual unenhanced' setting. In the Spectral Diagnostic Suite, image analysis is performed natively in spectral CT mode. For each iodine tube at each scan, one region of interest (ROI) was drawn in the coronal plane to maximize ROI areas; each ROI was at least 5.0 cm². The mean iodine concentration in the ROI was calculated by the dedicated software packages of each vendor. DECT iodine concentration measurements were compared to the known iodine contrast concentration. Normalized difference of concentration measurements was calculated by dividing the difference between the CT-measured and the known concentration by the known concentration for all separate measurements.

Statistical analysis

Statistical analysis was performed using SPSS version 23 (IBM Corp, Armonk, NY, USA). Pearson correlation between the CT-measured and known iodine concentration was determined for all DECT scans. Median absolute measurement errors, as well as normalized measurement errors, were calculated for each possibly influencing factor, e.g. number of fat rings, IR grade and tube voltage combination. Kendall's Tau b (τ_b) as a measure of trends and correlation was determined between IR grades and iodine measures on both CT systems, and between patient size and iodine measures on the two CT systems. Median normalized iodine measurement errors were used to identify the CT protocols with the smallest iodine measurement error and interquartile ranges (IQR) compared to known concentrations. Furthermore, normalized differences in iodine quantification were compared for scan protocols with lowest measurement error at both CT systems using the Mann–Whitney U test. Normalized differences in iodine quantification were compared for different patient sizes using the Kruskal–Wallis test. Variances were compared for several kVp combinations and patient sizes in order to acquire information about the stability and consistency of the separate DECT protocols. Variances in normalized iodine measurement differences were compared for the scan protocols with lowest measurement error using Levene's test for equality of variances.

Results

Third-generation DSCT

In total, 720 measurements were performed on DSCT scan data (3 repetitions × 5 concentration grades × 3 patient sizes × 4 iterative reconstruction grades × 4 kVp combinations). Correlation between measured and true iodine concentration was

excellent at all kVp combinations (R=0.999–1.000, $p<0.0001$). For the 150Sn/70 kVp combination, the measurement error was smallest with a median difference of −0.5% (IQR −2.0, 2.0%) and a median absolute error of −0.1 mg/ml (IQR −0.2, 0.2 mg/ml). The median difference was slightly larger for 150Sn/80 kVp and 150Sn/100 kVp, −2.3% (IQR −4.0, −0.1%) and −2.3% (IQR −5.0, −1.1%) with an absolute error of −0.2 mg/ml (IQR −0.3, −0.1 mg/ml) and −0.2 mg/ml (IQR −0.5, −0.1 mg/ml). The other kVp combinations showed more underestimation (**Figure 2**, **Table 1**).
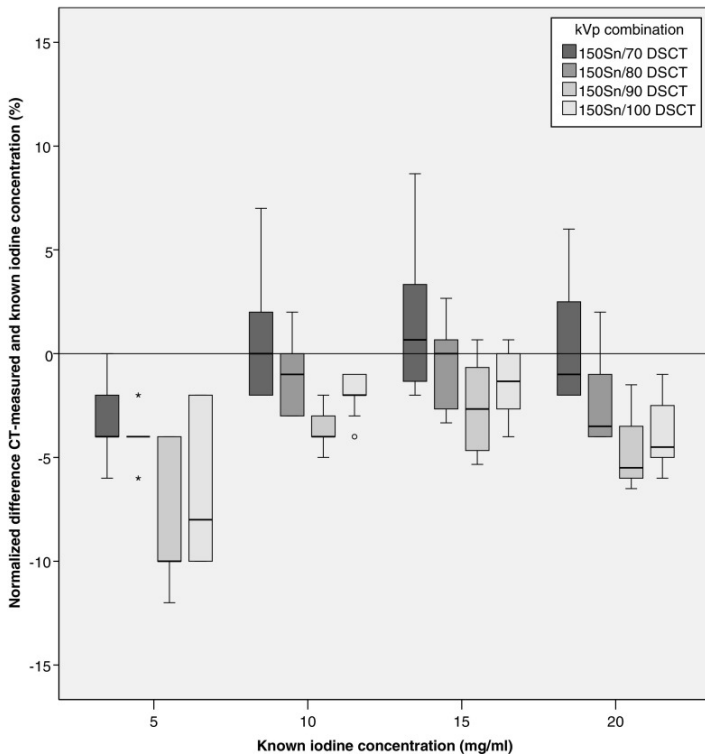
Figure 2 Normalized difference between CT-measured and known iodine concentrations is shown for each DSCT kVp combination by true iodine concentration

No significant correlation was found between normalized iodine measurement error and different grades of IR, which implies that the addition of IR does not influence iodine concentration measurements for third-generation DSCT (Kendall τ_b test, 150Sn/70 $p=0.81$, 150Sn/80 $p=0.85$, 150Sn/90 $p=0.66$, 150Sn/100 $p=0.59$). For all kVp combinations, an increase in patient size resulted in slightly higher median

Table 1 Median CT-measured iodine concentration and normalized differences between CT-measured and known iodine concentration are shown for both DSCT and DLCT

Iodine concentration	Dual source CT				Dual layer CT	
	150Sn/70	150Sn/80	150Sn/90	150Sn/100	120 kVp	140 kVp
0 mg/ml (%)	−0.1	−0.1	−0.1	−0.1	0	0
5 mg/ml (%)	4.8 (−4%)	4.8 (−4%)	4.5 (−10%)	4.6 (−8%)	4.5 (−10%)	4.7 (−6%)
10 mg/ml (%)	10.0 (0%)	9.9 (−1%)	9.6 (−4%)	9.8 (−2%)	9.6 (−4%)	9.7 (−3%)
15 mg/ml (%)	15.1 (1%)	15.0 (0%)	14.6 (−3%)	14.8 (−1%)	14.3 (−5%)	14.5 (−3%)
20 mg/ml (%)	19.8 (−1%)	19.3 (−4%)	18.9 (−6%)	19.1 (−5%)	19.3 (−4%)	19.7 (−2%)
Median diff concentration grades mg/ml (%)	−0.1 (−1%)	−0.2 (−2%)	−0.4 (−4%)	−0.2 (−2%)	−0.5 (−5%)	−0.3 (−3%)

Median difference for the separate kVp combinations is shown

5

iodine measurements; however, there were no significant trends (Kendall τ_b test, 150Sn/70 $\tau_b > 0.07$, $p = 0.53$; 150Sn/80 $\tau_b > 0.06$, $p = 0.62$; 150Sn/90 $\tau_b > 0.05$, $p = 0.69$; 150Sn/100 $\tau_b > 0.03$, $p = 0.79$) (**Figure 3**). For the 150Sn/70, 150Sn/80 and 150Sn/90 kVp combinations, normalized measurement error between CT-determined and known iodine concentration was significantly different between three patient sizes (Kruskal–Wallis test, $p < 0.05$). Only the 150Sn/100 kVp combination showed no significant difference when comparing the normalized measurement error between the three patient sizes (Kruskal–Wallis test, $p = 0.16$). The Levene's variance test showed no significant difference in variance for normalized measurement error between 150Sn/70 and 150Sn/80 kVp combination in any patient size (small: $p = 0.06$; medium $p = 0.52$; large $p = 0.46$). The 150Sn/100 kVp combination showed significantly larger variances in medium patient size compared to the 150Sn/70 kVp protocol (Levene's test, $p < 0.05$). Furthermore, the variance of the normalized measurement error of the 150Sn/100 kVp combination was significantly larger in small and medium patient sizes compared to the corresponding patient size groups for the 150Sn/80 kVp protocol (Levene's test, $p < 0.05$).

First-generation DLCT

In total, 360 measurements were performed on DLCT scan data (3 repetitions×5 concentration grades×3 patient sizes×4 iterative reconstruction grades×2 kVp tube voltages). Correlations between measured and known iodine concentrations were excellent for both kVp combinations (R=0.999–1.000, $p < 0.0001$). Median measurement error for 140 kVp was −4.0% (IQR −6.0, −1.6%) with an absolute

Figure 3 Normalized difference between the CT-measured and known iodine concentration is shown for the kVp combinations available at DSCT by patient size. An increase in CT-determined iodine can be distinguished for all kVp combinations, although the trend was not significant

median deviation of −0.3 mg/ml (IQR −0.6, −0.1 mg/ml) (**Figure 4**, **Table 1**). The 120 kVp setting showed more underestimation of the iodine content in the tubes (median measurement error, −5.0% (IQR −7.0, −4.0%) median absolute difference, −0.6 mg/ml (IQR −0.8, −0.3 mg/ml) ($p < 0.05$)).

Different grades of model-based iterative reconstruction settings did not influence iodine quantification (Kendall τ_b test, 120 kVp $p=0.80$, 140 kVp $p=0.59$). For both kVp combinations, an increase in patient size resulted in lower measured iodine concentrations, although not significant using Kendall's τ_b test (120 kVp $\tau_b < −0.11$, $p=0.36$; 140 kVp $\tau_b < −0.13$ $p=0.30$) (**Figure 5**). Large patient size showed more underestimation of iodine concentrations compared to medium and small patient size for both the tube voltages (Kruskal–Wallis test, $p < 0.05$). No significant difference in variance was found between the two tube voltages in any patient size (Levene's test, small $p=0.25$, medium $p=0.92$, large $p=0.50$).
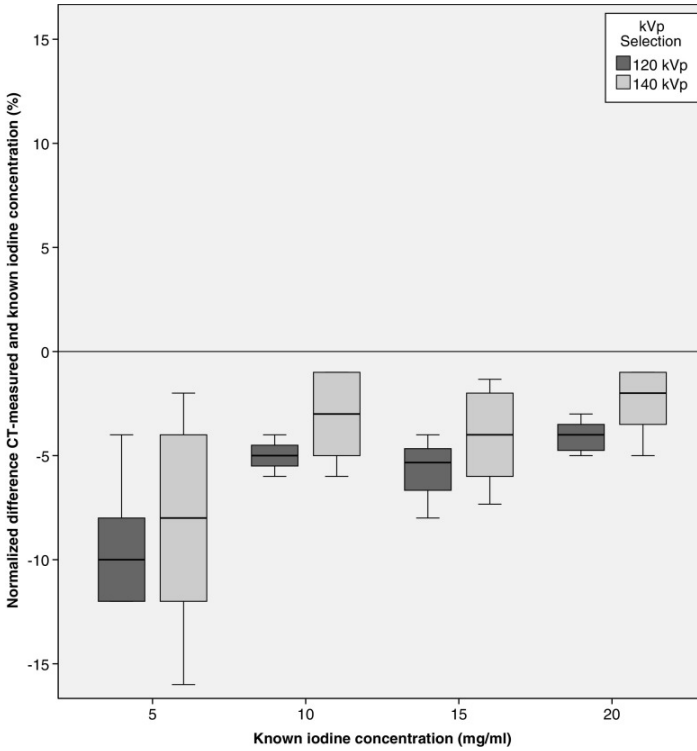
Figure 4 Normalized differences between the CT-measured and known concentration are shown for the DLCT tube voltages by true iodine concentration

Comparison between third-generation DSCT and first-generation DLCT

A significant difference was found for the normalized difference between CT-measured and known iodine concentration between the DSCT 150Sn/70 and the DLCT 140 kVp tube voltage (Mann–Whitney U test, $p < 0.05$), indicating closer agreement with known iodine concentrations for the DSCT 150Sn/70 kVp combination. Similarly, measurement error was smaller for 150Sn/80 kVp DSCT compared to 140 kVp DLCT (Mann–Whitney U test, $p < 0.05$). However, no significant difference in normalized measurement error was found when 150Sn/100 kVp DSCT was compared to 140 kVp DLCT (Mann–Whitney U test, $p = 0.21$). No significant difference in variances was found for all of the DSCT kVp combinations when compared to DLCT 140 kVp (Levene's variance test, 150Sn/70 vs. 140 kVp: $p = 0.91$; 150Sn/80 vs. 140 kVp: $p = 0.08$). Also when analysing patient sizes separately, no
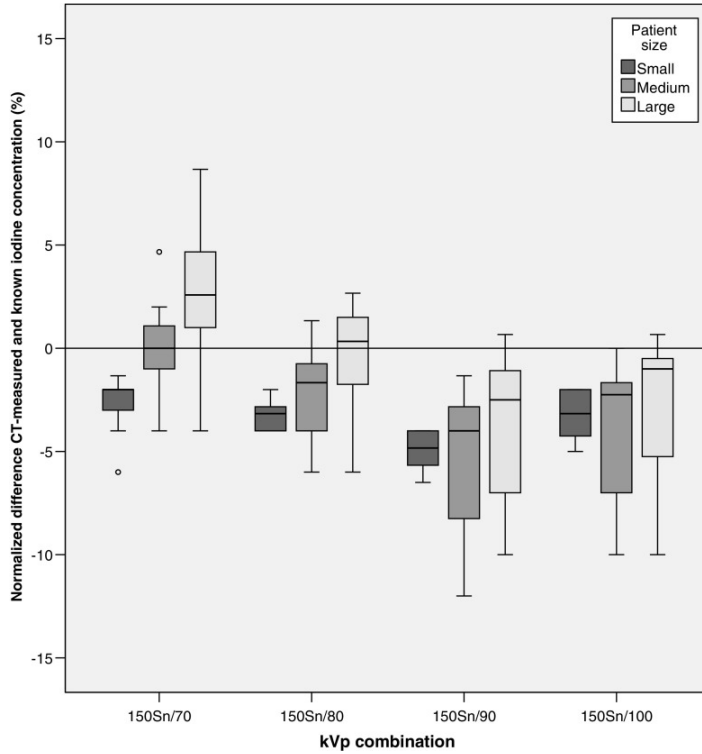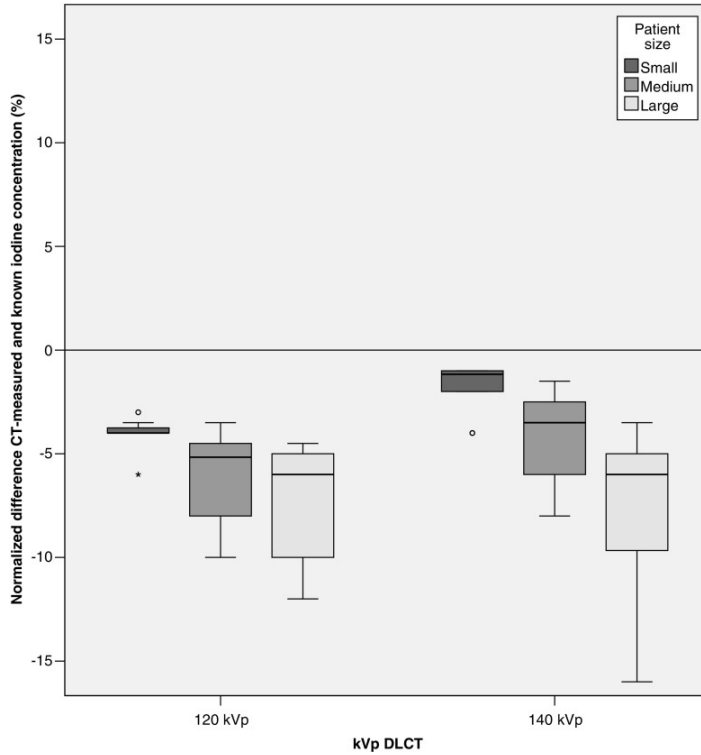
Figure 5 Normalized difference between the CT-measured and known iodine concentration is shown for the kVp combinations available at DLCT by patient size. A decrease in CT-determined iodine can be distinguished for all kVp combinations, although the trend was not significant.

significant differences in variance were found (Levene's variance test, 150Sn/70 vs. 140 kVp: small $p=0.52$, medium $p=0.44$, large=0.77; 150Sn/80 vs. 140 kVp: small $p=0.18$, medium $p=0.82$, large=0.24).

Discussion

In this study the accuracy of iodine quantification using DECT was studied in third-generation DSCT system and first-generation DLCT. Using a phantom model, we showed that the correlation of iodine measurements with true concentrations was excellent for both DSCT and DLCT. The results suggest that iodine quantification in the myocardium could be a semi-quantitative surrogate for the quantification of myocardial perfusion, with iodine concentration in the myocardium as an expression of the blood distribution at one moment in time. The most accurate results were found for protocols with the largest photon energy separation, namely 150Sn/70 and 150Sn/80 kVp for DSCT and 140 kVp for DLCT.

Koonce et al. analysed iodine quantification using DECT for first- and second-generation DSCT systems [10]. That study demonstrated stable and accurate results for multiple acquisition protocols. Our results complement that study, with even closer or comparable agreement between CT-measured and known iodine concentration for two new state-of-the-art CT systems, a third-generation DSCT system and a first-generation DLCT system. Another study analysed iodine quantification on single-source CT with a split filter, with measured differences ranging between 2 and 21% for iodine concentrations ranging from 1.2 to 23.5 mg/ml, with absolute differences ranging from 0.1 to 1.6 mg/ml [13]. When comparing these results to our study, one can state that increased spectral separation increases the accuracy of iodine quantification.

Only one study analysed the quantification of iodine in patients using a second-generation DSCT system [14]. The authors concluded that quantification of iodine could be useful for differentiation between normal, ischemic and necrotic myocardium. Reference iodine values for normal and ischemic myocardium were reported to be 2.6 and 2.0 mg/ml, respectively. In our study, the low iodine concentrations in the range of 0 to 5 mg/ml resulted in 0.2 to 0.3 mg/ml underestimations using the optimal kVp combination of 150Sn/70, 150Sn/80 for DSCT and 140 kVp for DLCT. Taking into account the small differences between normal and ischemic myocardium as reported by Delgado et al. and the results provided in this study, one should be careful to crosslink iodine quantification results between scanners and kVp combinations. Results of iodine quantification studies can only be compared when the same scanner type and kVp combination is used.

DECT cannot only be used in quantification of iodine concentration in the myocardium but also has the potential to assess patency of coronary arteries, a standard CT angiography [15, 16]. The use of only a slightly changed cardiac CT protocol and the ability to compare stress images to rest (coronary CTA) images are advantages of DECT compared to dynamic first-pass perfusion CT. Furthermore, radiation dose of a single-shot DECT scan is lower than the radiation dose in dynamic perfusion CT. In comparison to DECT, a major advantage of the dynamic first-pass perfusion CT is the ability to quantify absolute myocardial perfusion, and derive myocardial blood flow and blood volume. However, DECT allows for assessment of a semi-quantitative biomarker of myocardial perfusion, namely myocardial iodine content. Quantification of myocardial iodine content may help in detection of myocardial ischemia [14]. For this purpose, accurate quantification of iodine content, as we have studied, is an important issue. The quantification

of iodine using DECT only calculates a semi-quantitative parameter of myocardial perfusion, namely myocardial iodine distribution in milligrams per millilitre. Still, this may be more sensitive to detect myocardial ischemia than mere visual evaluation. In this study, we showed that the ability to quantify iodine is highly accurate. Future studies should show whether quantification of myocardial iodine distribution has additional diagnostic value in patients suspected of myocardial ischemia, beyond visual analysis of myocardial iodine distribution.

It is important to strive for a quantitative analysis of myocardial blood supply. Quantitative analysis may allow more sensitive evaluation of myocardial perfusion deficits instead of relative, visual analysis. This is of particular importance in three-vessel disease, in which the entire myocardium may have reduced perfusion. Three-vessel disease can be missed when using qualitative assessment of relative contrast distribution. Also, quantification of myocardial perfusion parameters, or iodine content, may possibly enable detection of subclinical CAD, in which blood supply is reduced but yet without gross perfusion defects. The added value of DECT using iodine quantification is not only shown for cardiac imaging but several studies have shown added value in oncological imaging, differentiating between renal masses and cysts or assessing treatment response [17–19].

The third-generation DSCT is equipped with a tin filter to harden the high energy (150 kVp) spectrum. This filter absorbs low energy photons before they reach the phantom, causing increased spectral separation. In DSCT, tube voltage, tin filter and tube current can be selected for both tubes separately. Drawbacks of the DSCT technique are the angular offset of the two image datasets, and a smaller field of view for one of the two tubes. Furthermore, the dual energy mode in DSCT needs to be selected, while in DLCT images can always be reconstructed in DECT mode. First-generation DLCT scanning uses a different method to acquire spectral separation. The first layer of detectors registers the low energy photons, while the second layer mainly detects the high energy photons, resulting in spectral separation between the first and second layer of the detector. An increase in tube voltage will result in a larger spectral separation, because more high energy photons will reach the second detector layer. There is no angular offset because the high and low energy datasets are acquired using the same source, and conventional images are created using the information from both high and low energy datasets. Drawbacks of DLCT include the low number of kVp selections (120 and 140 kVp), and the fact that no filter can be selected, as separation takes place at the level of the detector and not at the X-ray tube. This could result in a higher radiation dose. The smaller detector coverage of 64 rows is another drawback of the DLCT technique. Finally, as both

5

the high and low energy datasets are acquired using the same source, spectral separation is lower compared to DSCT and this could result in less accurate iodine quantification, as we have shown in our study. Whether this translates into clinically relevant differences in diagnostic accuracy is unknown.

DECT allows for quantification of iodine concentrations in a static phantom at several patient sizes. However, an increase in patient size will result in differences in quantified iodine for both DSCT and DLCT scanners. Interestingly, increase in patient size tended to have a positive effect (increase in CT-measured iodine) on the normalized differences between CT-determined and known iodine concentration in DSCT, while having a negative effect (decrease in CT-measured iodine) on the quantification of iodine in DLCT. Only the 150Sn/100 tube voltage combination showed no significant difference in normalized difference between CT-determined and known iodine concentration for the three patient sizes. However, this result is likely caused by higher measurement errors in small and medium patient sizes for the 150Sn/100 kVp protocol. Still, one should be careful when comparing the quantification of iodine concentration between different patient sizes for both scan techniques.

The present study has several limitations that need to be recognized. The most important limitation is that measuring iodine in several separate tubes in a thoracic phantom is different from measuring iodine concentrations in patients. Movement of the heart, breathing motion and general movement are not taken into account in this model, but are likely to influence the iodine quantification in patients. These movement problems could be especially problematic when low and high energy data are not acquired at exactly the same time and position, like in most DECT approaches. Water was used for diluting iodine, which is different to clinical practice where surrounding tissue such as calcium and proteins may influence the iodine measurements. Furthermore, the ROIs were larger (over 5.0 cm^2), which will not always be applicable in clinical practice. Smaller ROIs could increase the measurement error. However, these results form a strong basis from which other studies in iodine quantification using DECT can derive a selection of protocols or kVp combinations. A second limitation is that we limited the dual energy modes to third-generation DSCT and first-generation DLCT, while there are other dual energy methods on the market. The results presented in this study could be different for other methods of iodine quantification using different CT scanners. The third limitation is the range in iodine concentration. The first patient study providing iodine quantification showed that the measured iodine concentration ranges between 1 and 6 mg/ml. This is at the lower end of the concentration range

we used in this study. We chose the current range of iodine concentrations to be able to compare to the study by Koonce et al. [10].

Overall, both third-generation DSCT and first-generation DLCT showed highly accurate quantification of increasing iodine concentrations using DECT protocols. Best results were found for DSCT using the 150Sn/70 or 150Sn/80 kVp combination, which showed lower measurement error than DLCT. For both systems largest energy separation provided the most accurate iodine quantification.

5

References

1. Tarride J-E, Lim M, DesMeules M, et al (2009) A review of the cost of cardiovascular disease. Can J Cardiol 25:e195-202

2. Heidenreich PA, Trogdon JG, Khavjou OA, et al (2011) Forecasting the Future of Cardiovascular Disease in the United States. Circulation 123:933–944. doi: 10.1161/CIR.0b013e31820a55f5

3. Hulten EA, Carbonaro S, Petrillo SP, et al (2011) Prognostic Value of Cardiac Computed Tomography Angiography. J Am Coll Cardiol 57:1237–1247. doi: 10.1016/j.jacc.2010.10.011

4. Jaarsma C, Leiner T, Bekkers SC, et al (2012) Diagnostic Performance of Noninvasive Myocardial Perfusion Imaging Using Single-Photon Emission Computed Tomography, Cardiac Magnetic Resonance, and Positron Emission Tomography Imaging for the Detection of Obstructive Coronary Artery Disease. J Am Coll Cardiol 59:1719–1728. doi: 10.1016/j.jacc.2011.12.040

5. Vliegenthart R, Pelgrim GJ, Ebersberger U, et al (2012) Dual-Energy CT of the Heart. Am J Roentgenol 199:S54–S63. doi: 10.2214/AJR.12.9208

6. Danad I, Fayad ZA, Willemink MJ, Min JK (2015) New Applications of Cardiac Computed Tomography. JACC Cardiovasc Imaging 8:710–723. doi: 10.1016/j.jcmg.2015.03.005

7. Alvarez RE, Macovski A (1976) Energy-selective reconstructions in X-ray computerized tomography. Phys Med Biol 21:733–44

8. So A, Hsieh J, Narayanan S, et al (2012) Dual-energy CT and its potential use for quantitative myocardial CT perfusion. J Cardiovasc Comput Tomogr 6:308–317. doi: 10.1016/j.jcct.2012.07.002

9. den Harder AM, Willemink MJ, de Jong PA, et al (2016) New horizons in cardiac CT. Clin Radiol 71:758–767. doi: 10.1016/j.crad.2016.01.022

10. Koonce JD, Vliegenthart R, Schoepf UJ, et al (2014) Accuracy of dual-energy computed tomography for the measurement of iodine concentration using cardiac CT protocols: validation in a phantom model. Eur Radiol 24:512–518. doi: 10.1007/s00330-013-3040-6

11. Solomon J, Wilson J, Samei E (2015) Characteristic image quality of a third generation dual-source MDCT scanner: Noise, resolution, and detectability. Med Phys 42:4941–4953. doi: 10.1118/1.4923172

12. Gordic S, Desbiolles L, Stolzmann P, et al (2014) Advanced modelled iterative reconstruction for abdominal CT: Qualitative and quantitative evaluation. Clin Radiol 69:e497–e504. doi: 10.1016/j.crad.2014.08.012

13. Euler A, Parakh A, Falkowski AL, et al (2016) Initial Results of a Single-Source Dual-Energy Computed Tomography Technique Using a Split-Filter. Invest Radiol 51:491–498. doi: 10.1097/RLI.0000000000000257

14. Delgado Sánchez-Gracián C, Oca Pernas R, Trinidad López C, et al (2016) Quantitative myocardial perfusion with stress dual-energy CT: iodine concentration differences between normal and ischemic or necrotic myocardium. Initial experience. Eur Radiol 26:3199–3207. doi: 10.1007/s00330-015-4128-y

15. Ko SM, Song MG, Chee HK, et al (2014) Diagnostic Performance of Dual-Energy CT Stress Myocardial Perfusion Imaging: Direct Comparison With Cardiovascular MRI. Am J Roentgenol 203:W605–W613. doi: 10.2214/AJR.14.12644

16. Ruzsics B, Lee H, Zwerner PL, et al (2008) Dual-energy CT of the heart for diagnosing coronary artery stenosis and myocardial ischemia-initial experience. Eur Radiol 18:2414–2424. doi: 10.1007/s00330-008-1022-x

5

17.	Kaza RK, Caoili EM, Cohan RH, Platt JF (2011) Distinguishing Enhancing From Nonenhancing Renal Lesions With Fast Kilovoltage-Switching Dual-Energy CT. Am J Roentgenol 197:1375–1381. doi: 10.2214/AJR.11.6812

18.	Chandarana H, Megibow AJ, Cohen BA, et al (2011) Iodine Quantification With Dual-Energy CT: Phantom Study and Preliminary Experience With Renal Masses. Am J Roentgenol 196:W693–W700. doi: 10.2214/AJR.10.5541

19.	Chang S, Hur J, Im DJ, et al (2016) Dual-energy CT-based iodine quantification for differentiating pulmonary artery sarcoma from pulmonary thromboembolism: a pilot study. Eur Radiol 26:3162–70. doi: 10.1007/s00330-015-4140-2

5
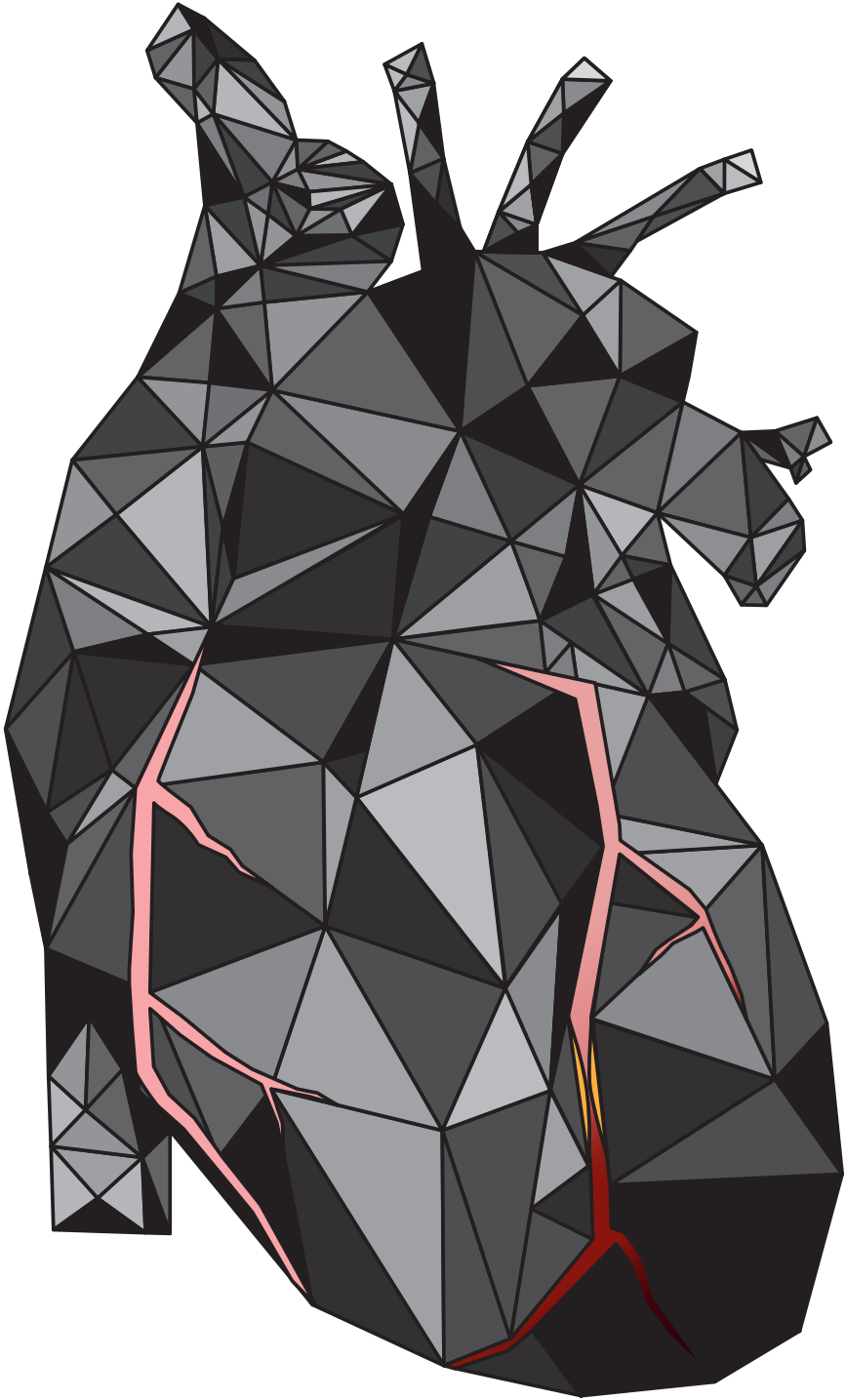
Chapter 6

Feasibility and accuracy of dual-layer spectral detector computed tomography for quantification of gadolinium: a phantom study

Robbert W. van Hamersvelt
Martin J. Willemink
Pim A. de Jong
Julien Milles
Alain Vlassenbroek
Arnold M.R. Schilham
Tim Leiner

Abstract

Objectives

The aim of this study was to evaluate the feasibility and accuracy of dual-layer spectral detector CT (SDCT) for the quantification of clinically encountered gadolinium concentrations.

Methods

The cardiac chamber of an anthropomorphic thoracic phantom was equipped with 14 tubular inserts containing different gadolinium concentrations, ranging from 0 to 26.3 mg/ml (0.0, 0.1, 0.2, 0.4, 0.5, 1.0, 2.0, 3.0, 4.0, 5.1, 10.6, 15.7, 20.7 and 26.3 mg/ml). Images were acquired using a novel 64-detector row SDCT system at 120 and 140 kVp. Acquisitions were repeated five times to assess reproducibility. Regions of interest (ROIs) were drawn on three slices per insert. A spectral plot was extracted for every ROI and mean attenuation profiles were fitted to known attenuation profiles of water and pure gadolinium using in-house-developed software to calculate gadolinium concentrations.

Results

At both 120 and 140 kVp, excellent correlations between scan repetitions and true and measured gadolinium concentrations were found ($R > 0.99$, $P < 0.001$; ICCs > 0.99, CI 0.99–1.00). Relative mean measurement errors stayed below 10% down to 2.0 mg/ml true gadolinium concentration at 120 kVp and below 5% down to 1.0 mg/ml true gadolinium concentration at 140 kVp.

Conclusions

SDCT allows for accurate quantification of gadolinium at both 120 and 140 kVp. Lowest measurement errors were found for 140 kVp acquisitions.

6

Introduction

Material decomposition imaging (MDI) using dual energy computed tomography (DECT) was first described by Hounsfield in 1973 [1]. Different materials, which cannot be distinguished on the basis of attenuation number, can be distinguished with the use of material decomposition algorithms using DECT acquisitions [2–4]. Materials with high atomic numbers, such as iodine ($Z = 53$) and gadolinium ($Z = 64$), show characteristic high attenuation profiles at low energies owing to a substantial contribution of the photoelectric effect to the attenuation [5]. MDI uses these characteristic attenuation profiles to differentiate these contrast agents from other materials. MDI has not been widely applied in clinical practice until recently. Over the past few years several CT vendors have made DECT commercially available for daily clinical practice. Recently a novel DECT technique has become commercially available, which uses a single tube with a dual-layer detector capable of differentiating between low and high energy X-ray photons, and is further investigated in this study.

One of the most widely researched MDI applications is quantitative mapping of iodine distribution in tissues. The resulting maps can be used as a surrogate for tissue perfusion. Early evidence has shown the clinical capability of iodine quantification with DECT at a specified time point for the detection of myocardial [6–12] and pulmonary perfusion defects [13–16]. In addition, DECT iodine mapping is capable of tumour mass characterization and therapy response assessment [17–19]. However, iodine contrast administration, while safe in most patients, is associated with contrast-induced allergic reactions and nephropathy which can cause acute renal dysfunction [20, 21] and significant morbidity and mortality, especially in high risk patients [22, 23]. In patients with contraindications to iodinated contrast media, gadolinium enhanced magnetic resonance (MR) angiography can be used as an alternative. However, depending on the indication, MR angiography may have poor diagnostic value compared to (DE)CT angiography. Gadolinium-based CT has been used off-label in higher doses as an alternative for conventional CT angiography with diagnostic image quality [24, 25]. With the use of DECT, higher attenuation can be achieved at low (monochromatic) energies, which could enable the use of much lower gadolinium concentrations [26, 27]. In addition, accurate gadolinium quantification using DECT could allow for a quantitative evaluation of contrast agent distribution in tissue as a surrogate for tissue perfusion using MDI. Therefore, accurate gadolinium quantification combined with increased attenuation could potentially open up the possibility for gadolinium as an alternative contrast agent

6

for DECT imaging in patients with contraindications to iodinated contrast media.

In several studies the feasibility of gadolinium-enhanced DECT has been reported in phantom and animal models [28–31]. These studies described the capability of spectral differentiation and visualisation [28–30] and accuracy of quantification [31] of gadolinium using DECT. However, the accuracy of gadolinium quantification using the novel dual-layer spectral detector CT system (SDCT) is unknown. Therefore, the aim of the current study was to evaluate the feasibility and accuracy of gadolinium quantification using a SDCT system.

Materials and Methods

Phantom design

An anthropomorphic chest phantom (QRM GmbH, Moehrendorf, Germany) was used. The phantom resembles a chest with corresponding X-ray attenuation behaviour. The phantom has a cylindrical cardiac chamber in which a plastic holder was placed (**Figure 1**). Three plastic holders were made, two consisting of five tubular inserts, and one consisting of three tubular inserts with surrounding 2% agar gel solution.
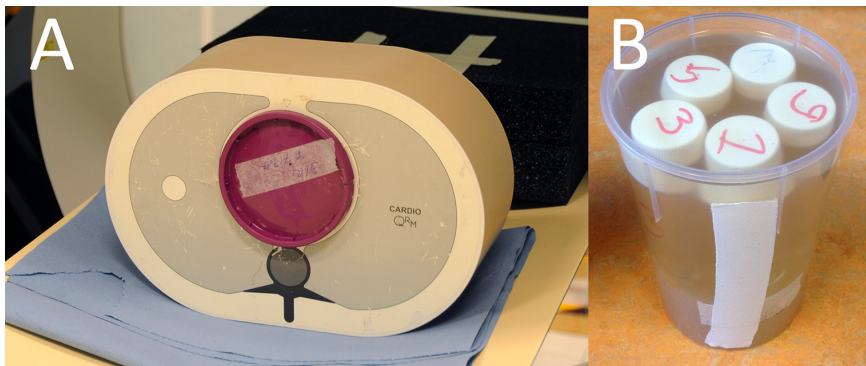
Figure 1 Phantom setup. (**A**) Anthropomorphic thoracic phantom with a plastic holder placed in the cardiac chamber. (**B**) Representative plastic holder filled with 5 tubular inserts, with surrounding 2% agar gel solution

In addition, a plastic holder with one tubular insert containing water with surrounding 2% agar gel solution served as control. The fourteen 32-ml tubular inserts contained different concentrations of the gadolinium-based contrast agent

gadobutrol (Gadovist 1.0, Bayer Healthcare, Berlin, Germany). One millilitre of this contrast agent contains 157.25 mg gadolinium. Different amounts of gadobutrol were diluted in water, resulting in the following concentrations of gadolinium: 0.0, 0.1, 0.2, 0.4, 0.5, 1.0, 2.0, 3.0, 4.0, 5.1, 10.6, 15.7, 20.7 and 26.3 mg/ml, which is equivalent to 0.000, 0.001, 0.002, 0.002, 0.003, 0.006, 0.013, 0.019, 0.026, 0.032, 0.068, 0.100, 0.132 and 0.167 mmol/ml, respectively.

Concentrations were chosen to mimic an estimated clinical range of gadolinium concentrations encountered after injection of 0.1-0.2 mmol of gadolinium per kilogram. Strich et al. [32] measured percentage dose of gadolinium-based contrast agent per gram of tissue in healthy rabbit organs 5 min after admission, resulting in the following percentages: 0.052%/g heart, 0.073%/g lungs, 0.037%/g liver, 0.037%/g spleen and 0.250%/g kidney. On the basis of these percentages, an estimation of gadolinium concentrations encountered at each organ can be calculated. At 31.5 mg/kg bodyweight (equal to 0.2 mmol/kg) gadolinium administration, a human subject of 70 kg would receive a total of 2201.5 mg gadolinium. On the basis of the percentages determined by Strich and colleagues, gadolinium distribution in the heart 5 min after injection would be 0.00052 x 2201.5 mg, or 1.15 mg per gram myocardium. Myocardial muscle has a specific gravity of 1.05 g/ml [33], implicating an estimated gadolinium concentration encountered in the myocardium of 1.15 mg/g x 1.05 g/ml, or 1.21 mg/ml. Using the aforementioned distribution percentages these calculations can also be applied to the lungs, liver, spleen and kidney, with a calculated estimated specific gravity (weight/volume) of 1.34, 1.01, 0.71 and 0.85 g/ml, respectively [34–36]. Thus, it is to be expected that gadolinium concentrations of 2.15, 0.82, 0.58 and 4.67 mg/ml are encountered in healthy lung, liver, spleen and kidney tissue, respectively. These concentrations are in the range of concentrations evaluated in this study. As it is expected that in tissue with a perfusion defect lower concentrations of gadolinium will be encountered, we also evaluated ultra-low concentrations of gadolinium down to 0.1 mg/ml.

Image acquisition

Images were acquired using the newest generation 64-detector row SDCT system (IQon Spectral CT, Philips Healthcare, Best, The Netherlands). This system uses a single X-ray tube and a dual-layer detector. The detector separates the X-ray beam into low (upper layer) and high (lower layer) energy data, which is used to reconstruct spectral-based images (SBI). The SBI contain the raw data of both layers and are used to reconstruct any dual-energy image and/or analysis. In addition, by combining the output of both layers, a conventional image is reconstructed from

6

the data. The phantom was imaged in spiral mode at 120 and 140 kVp. The tube current time product was set to a fixed value of 200 mAs, resulting in a volumetric CT dose index (CTDI$_{vol}$) of 18.4 and 26.5 mGy for 120 and 140 kVp acquisitions, respectively. The following parameters were used: detector collimation: 64 x 0.625 mm, rotation time 0.4 s and pitch 1.046. At both tube voltages, acquisitions were repeated five times with small displacements between each acquisition to take into account interscan variation. Thus, the phantom was translated a few millimetres in the left-right direction, as well as along the z-axis of the CT scanner. After the five repetitions, the phantom was set back to the starting position.

Image reconstruction

The raw projection data from both detector layers were automatically reconstructed into SBI. Subsequently, MDI was performed in the projection domain, which efficiently eliminates beam hardening artefacts [37]. All images were reconstructed with standard chest reconstruction filter B and spectral level 3. Spectral is a model-based iterative reconstruction developed for the SDCT, it is an equivalent to iterative model-based reconstruction (IMR). Spectral consists of six levels, whereby a higher spectral level implies more noise reduction. Slice thickness and increment were both 1 mm. The reconstructed images were evaluated on a dedicated workstation using the Spectral CT Viewer (IntelliSpace Portal v6.5.0.02080, Philips Healthcare, Best, The Netherlands).

Image analysis and gadolinium quantification

On three different slices of each data set a region of interest (ROI) with a fixed size of 225 mm^2 was drawn in the centre of each insert (**Figure 2A**). Subsequently spectral plots of every ROI were obtained, in which mean Hounsfield units (HU) were plotted as a function of different energy levels expressed in kiloelectron voltage (keV) (**Figure 2B**). These mean HU of the spectral plots were extracted in steps of 10 keV and used as an input for the analysis. The currently used SDCT system uses traditional integrated detectors at two energy spectra and is therefore not able to image and/or quantify a material specific K-edge [37]. Materials with a K-edge within the SDCT range (40-200 keV) will not show a discontinuity in their attenuation function on the SDCT spectral plot. When evaluating the mean attenuation across monochromatic energies, this does not pose a problem and therefore the whole energy spectrum can be used (40-200 keV). However, for the quantitative analyses of gadolinium concentrations a comparison is made with the attenuation profile of pure gadolinium which does contain the discontinuity in their attenuation function at the K-edge. Therefore, to take into account the
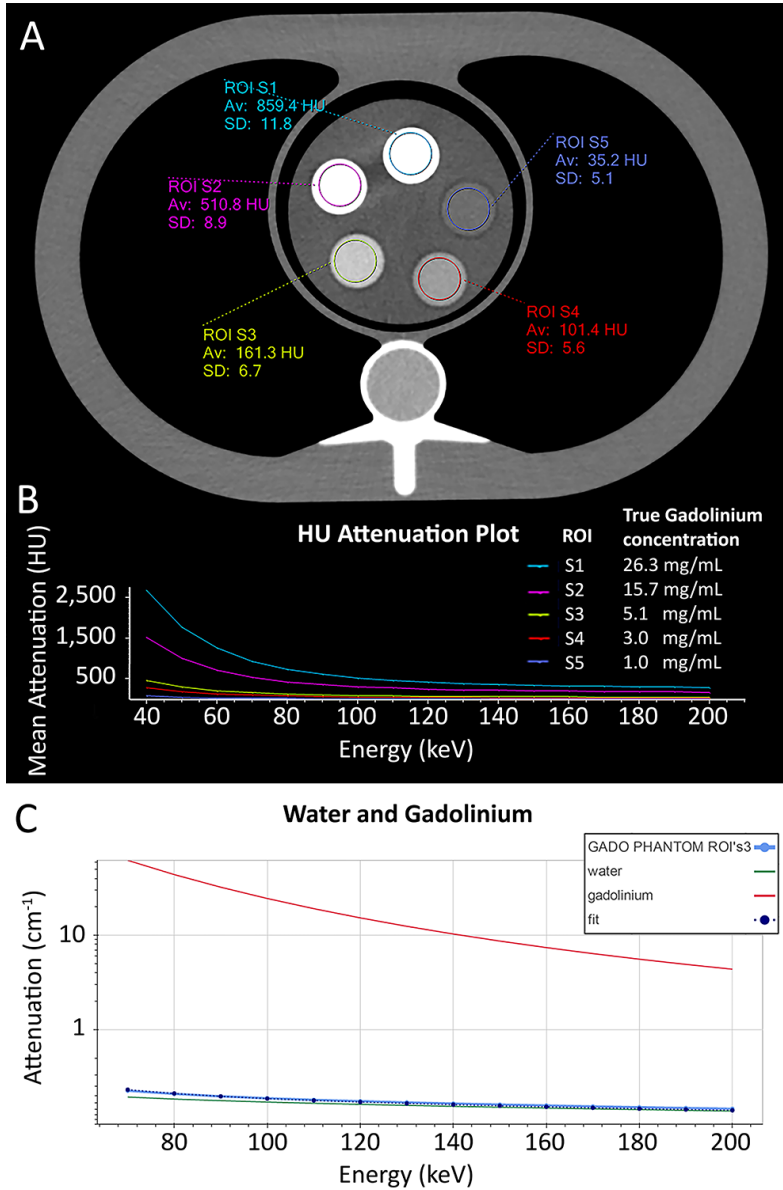
Figure 2 Axial CT image and measurements. (**A**) Axial conventional SDCT image of the phantom with 5 tubular inserts, surrounded by 2% agar gel. ROIs with a fixed area of 225 mm² drawn in the centre of each insert. (**B**) A spectral plot of each ROI was conducted, showing mean Hounsfield units plotted against energy in keV. Hounsfield unit values of the spectral plots were extracted in increments of 10 keV. (**C**) Using in-house-developed software, we reconstructed attenuation profiles between 70 to 200 keV from the extracted Hounsfield units, and a combination of known attenuation profiles of pure gadolinium and water was fitted to the reconstructed attenuation profile. This case concerns ROI S3, containing 5.1 mg of gadolinium per millilitre

non-linear energy dependency close to the K-edge of gadolinium (50.2 keV), only the energy range from 70 to 200 keV was used for the quantitative analysis. With in-house developed software, attenuation profiles were reconstructed from the provided mean HU, and Gadolinium concentrations were calculated by fitting combinations of known attenuation profiles of pure gadolinium and pure water to the reconstructed attenuation profiles (**Figure 2C**). For each ROI drawn in the phantom, the in-house developed software assumed that all voxels within this ROI were composed of only gadolinium and water and that the sum of these fractions added up to 100%. Known attenuation profiles of pure gadolinium and pure water were obtained from the National Institute of Standards and Technology (NIST) database [38]. Therefore, no calibration scans with pure water and/or gadolinium concentrations were needed. For all ten different gadolinium concentrations, 15 measurements were performed at both 120 and 140 kVp (3 slices, 5 repetitions). In addition, 30 measurements (15 at both 120 and 140 kVp) were performed on the control phantom. Gadolinium concentrations were calculated for each measurement.

Attenuation coefficient

CT attenuation during injection of low gadolinium concentrations (i.e. 0.1-0.2 mmol/kg bodyweight) will generally lead to lower HU values compared to the use of iodinated contrast agents [24, 25] . To investigate the ability of SDCT to visually identify an increase in HU values due to the presence of a gadolinium-containing contrast agent we extracted mean attenuation coefficients across monochromatic energies (40-200 keV) for the different gadolinium concentrations used in this study (**Figure 3**).

Statistical analysis

To evaluate the quantification accuracy of gadolinium concentrations, we defined measurement errors in milligrams per millilitre and relative measurement errors in percentages. Measurement errors were calculated by subtracting true gadolinium concentrations from the measured gadolinium concentrations. Subsequently, relative measurement errors (%) were calculated as follows:

$$\text{Relative measurement error (\%)} = \frac{\text{measurement error } \left(\frac{\text{mg}}{\text{ml}}\right)}{\text{true gadolinium concentration } \left(\frac{\text{mg}}{\text{ml}}\right)} \times 100 \ (\%)$$

A

B
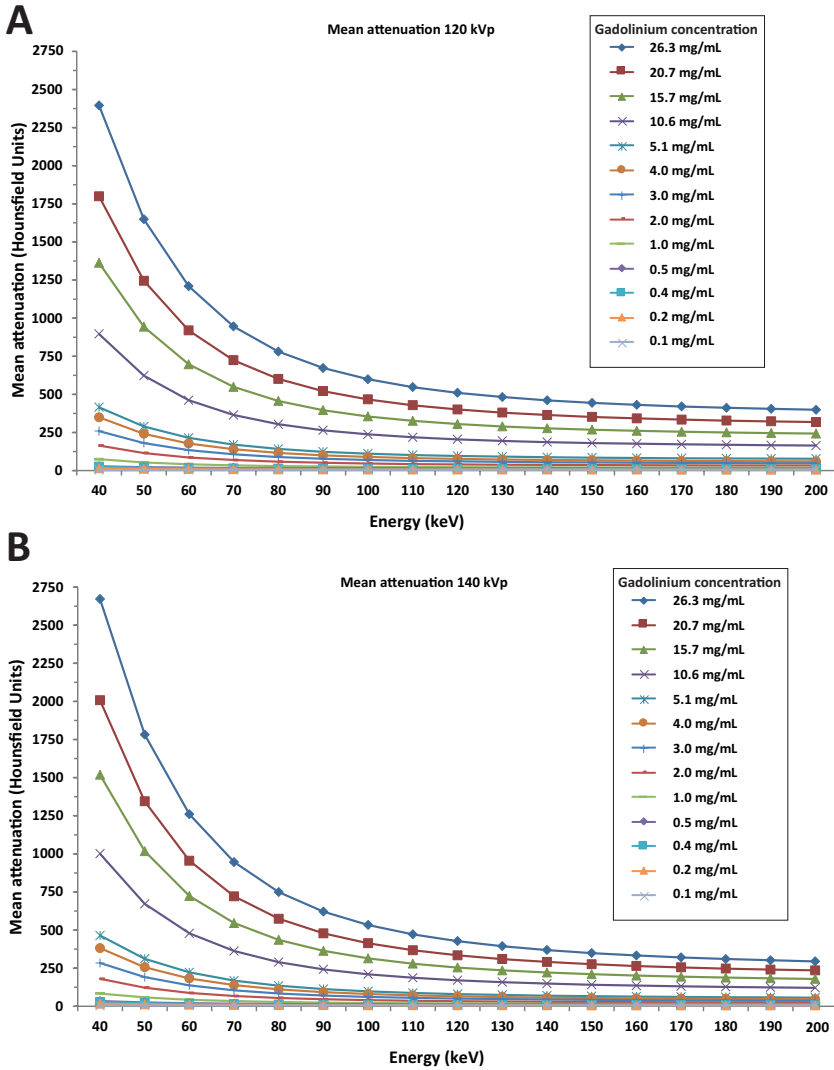
Figure 3 Mean CT attenuation coefficients across all monochromatic energies. Mean CT attenuation of all measurements for each gadolinium concentration, constructed in steps of 10 keV. Graphs were used to investigate the ability of SDCT low monochromatic energies to visually identify an increase in HU values due to the presence of gadolinium-containing contrast media. Scans were performed at 120 kVp (**A**) and 140 kVp (**B**). For subsequent gadolinium quantification, only attenuation profiles between 70 to 200 keV were used for the in-house-developed software analyses (**Figure 2C**)

All measurement error analyses were performed separately for 120 and 140 kVp. In addition, sub analyses were done for each concentration. The Shapiro-Wilk test was used to identify normally distributed data. Per concentration, statistical differences of measurement errors between 120 and 140 kVp were analysed using paired T-test for normally distributed data. A Bonferroni corrected $P < 0.004$ (0.05/number of comparisons) was considered significant. Pearson's correlation coefficient was used to evaluate correlations between measured and true gadolinium concentrations at different tube voltages and for each scan repetition. In addition, reproducibility was evaluated. To define agreement of results, the two-way random single measure intraclass correlation coefficient (ICC) with corresponding confidence interval (CI) was used for all possible two-way interactions. ICCs between 0.61 and 0.80 were considered good and ICCs greater than 0.80 excellent [39]. Measurement interscan variabilities of all scan repetitions were plotted in one single plot by using a modified Bland-Altman plot described by Jones et al. [40]. In this figure the measurement differences of every measurement compared to the mean measurement of all scans are plotted against the mean measurement of all scans. As described in the article by Jones et al., the limits of agreement were calculated as mean $\pm 1.96 \times$ SD, where the SD is an estimate of the standard deviation for all observers [40]. Values are listed as mean with standard deviation (SD), unless stated otherwise. A P value less than 0.05 was used to indicate statistical significance. IBM SPSS version 21.0 (IBM corp., Armonk, New York, USA) was used for statistical analyses.

Results

Measurements of the water-filled insert, which served as control, yielded 0.0 ± 0.0 mg/ml with a measurement error of 0.0 ± 0.0 mg/ml for all measurements. To avoid influence on measurement accuracy, these control measurements were not included in further statistical analyses.

Accuracy and reproducibility

At both 120 and 140 kVp, excellent correlations ($R > 0.99$, $P < 0.001$; ICCs > 0.99, CI 0.99–1.00) were found between true and measured gadolinium concentrations for each scan repetition. In addition, reproducibility between all scan repetitions was excellent ($R > 0.99$, $P < 0.001$; ICCs > 0.99, CI 0.99–1.00). The interscan agreement is displayed in **Figure 4A** for 120 kVp and **Figure 4B** for 140 kVp. Because excellent correlations were found, all scan repetitions were analysed combined together in subsequent analyses.

A

B
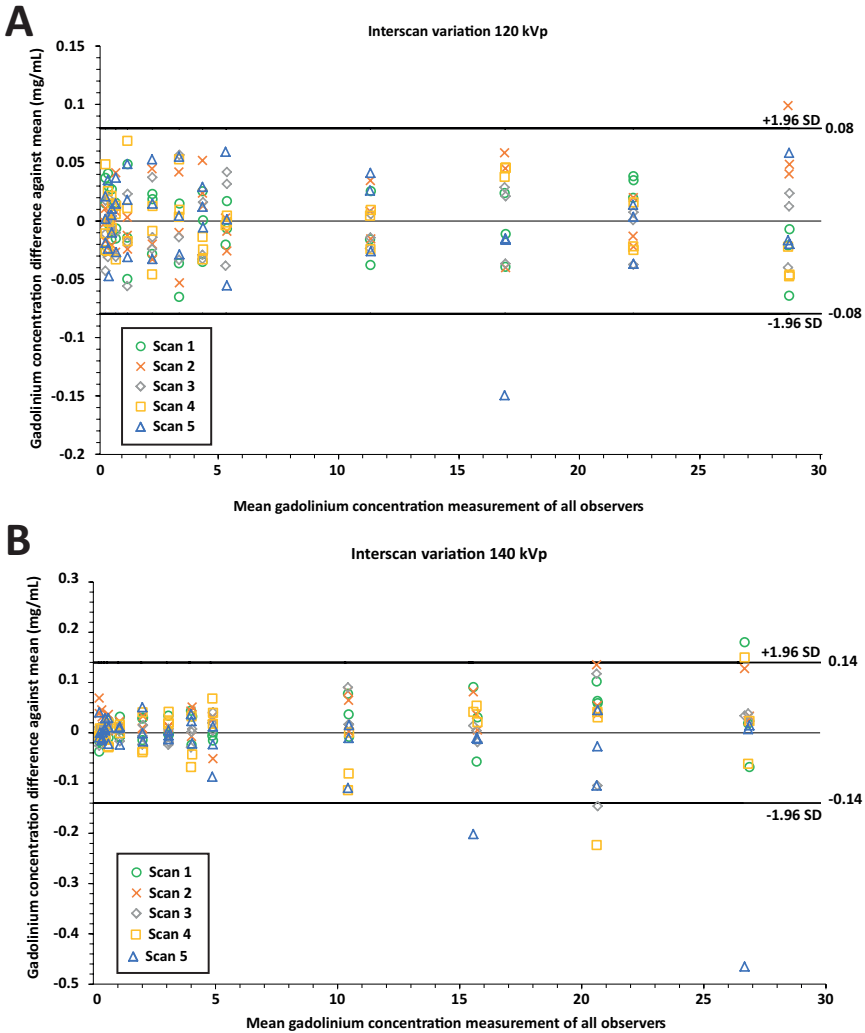
Figure 4 Interscan agreement for all scan repetitions at 120 kVp (**A**) and 140 kVp (**B**). Values are plotted according to Jones et al. [40]. The measurement difference of each scan compared to the mean measurement of all scans is plotted against the mean measurement of all scans

120 kVp

All gadolinium concentrations were overestimated. Mean measurement errors for the 15 ROIs per concentration ranged between 0.1 and 2.4 mg/ml (**Table 1**, **Figure 5A**). For each concentration, measurement errors at 120 kVp were significantly (Bonferroni $P < 0.004$) higher compared to measurement errors at 140 kVp, except

Table 1 Mean errors of gadolinium concentration measurements with a dual-layer spectral detector CT scanner.

True concentration (mg/ml)	120 kVp		140 kVp	
	Measurement error		**Measurement error**	
	mg/ml	%	mg/ml	%
26.3	2.4 ± 0.1*	9.0 ± 0.2	0.4 ± 0.2	1.6 ± 0.6
20.7	1.5 ± 0.0*	7.0 ± 0.1	-0.2 ± 0.1	-0.8 ± 0.5
15.7	1.2 ± 0.1*	7.5 ± 0.4	-0.1 ± 0.1	-0.5 ± 0.7
10.6	0.6 ± 0.0*	5.9 ± 0.3	-0.2 ± 0.1	-2.1 ± 0.6
5.1	0.2 ± 0.0*	3.9 ± 0.8	-0.2 ± 0.0	-4.2 ± 0.8
4.0	0.2 ± 0.0*	5.5 ± 0.7	-0.1 ± 0.0	-1.6 ± 1.0
3.0	0.3 ± 0.0*	8.4 ± 1.3	0.0 ± 0.0	0.1 ± 0.6
2.0	0.1 ± 0.0*	7.3 ± 1.6	-0.0 ± 0.0	-2.2 ± 1.5
1.0	0.1 ± 0.0*	12.1 ± 3.7	0.0 ± 0.0	2.7 ± 1.7
0.5	0.1 ± 0.0*	29.4 ± 5.0	0.1 ± 0.0	14.1 ± 4.1
0.4	0.1 ± 0.0*	30.0 ± 4.4	0.1 ± 0.0	19.3 ± 4.5
0.2	0.1 ± 0.0	39.8 ± 13.1	0.1 ± 0.0	36.1 ± 8.5
0.1	0.1 ± 0.0	100.9 ± 23.1	0.1 ± 0.0	93.5 ± 26.8
0.0	0.0 ± 0.0		0.0 ± 0.0	

Data are given as mean ± standard deviation. For each true concentration 15 measurements were done at both 120 and 140 kVp
*Significantly (Bonferroni $P < 0.004$) higher compared to measurement error at 140 kVp

6

for the lowest two concentrations of 0.1 and 0.2 mg/ml. Relative measurement errors (%) were below 10% down to 2.0 mg/ml true gadolinium concentrations and increased up to 29.4% at 0.5 mg/ml and 100.9% at 0.1 mg/ml true gadolinium concentration (**Table 1**, **Figure 5B**).

140 kVp

Per concentration (N = 15), mean measurement errors varied from −0.2 to 0.4 mg/ml (**Table 1**, **Figure 5A**). Relative measurement errors (%) stayed below 5% down to 1.0 mg/ml true gadolinium concentration. At true gadolinium concentrations between 0.1 and 0.5 mg/ml, mean measurement errors were low with 0.1 ± 0.0 mg/ml deviation; expressed in percentages this varied between 93.5 ± 26.8% and 14.1 ± 4.1% deviation, respectively (**Figure 5B**).

Attenuation coefficient

Overall mean attenuation increased when lowering keV (**Figure 3**). At the lowest possible monochromatic energy (40 keV), mean attenuation for the estimated clinical gadolinium range of 0.5, 1.0, 2.0, 3.0, 4.0 and 5.1 mg/ml yielded 28, 74, 164, 260, 349 and 416 HU at 120 kVp and 34, 84, 180, 284, 382 and 464 HU at 140 kVp, respectively.
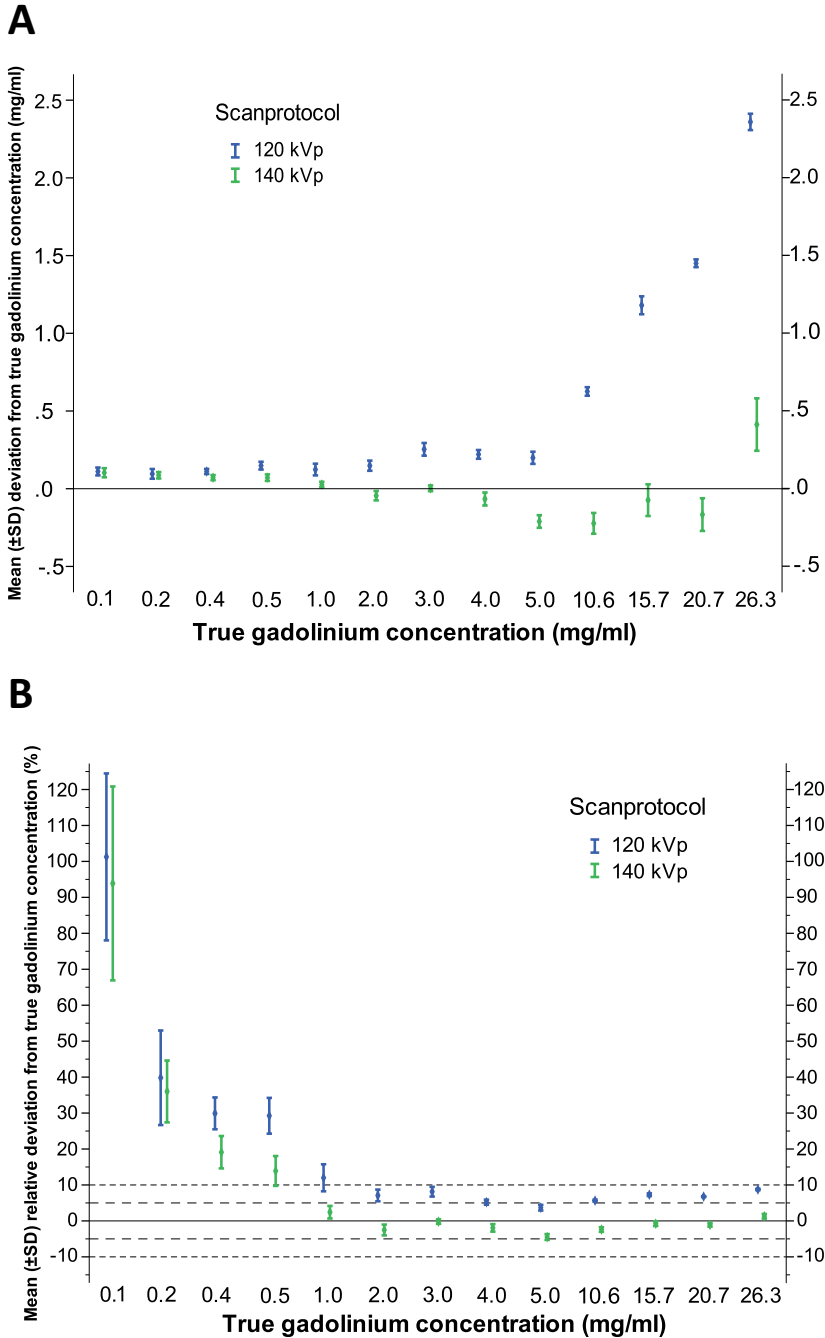
A

B

Figure 5 Accuracy of gadolinium quantification. Accuracy expressed as mean measurement error (**A**) and mean relative measurement error (**B**). Symbol represents mean and error bar the standard deviation

Discussion

This study showed that it is feasible to quantify a commonly clinically encountered range of gadolinium concentrations in a phantom model with overall high accuracy and reproducibility using an in-house-developed material decomposition method on a novel clinical dual-layer spectral detector CT system.

Whereas conventional CT displays anatomical structures as a function of tissue density, DECT enables enhanced tissue characterization using MDI. Quantitative assessment of contrast agent uptake and its provided distribution map can be used as a surrogate for tissue perfusion [6–12, 14]. In the current study we showed that clinically encountered low concentrations of gadolinium, down to 0.5 mg/ml, can be accurately quantified with a mean measurement error of 0.1 mg/ml using SDCT at both 120 and 140 kVp. In the ultra-low gadolinium concentration range (0.1–0.4 mg/ml), expected to be encountered in tissues with a perfusion defect, the mean measurement error remained around 0.1 mg/ml at both 120 and 140 kVp. However, at these low concentrations the margin of error increased substantially and approached the gadolinium concentration itself, indicating that the lower limit of reasonably accurate gadolinium quantification using SDCT lies between 0.5 and 1.0 mg/ml. In the range of clinically encountered gadolinium concentrations (0.5–5.1 mg/ml) after administration of 0.1–0.2 mmol/kg bodyweight, mean CT numbers at 40 keV ranged between 28 and 464 HU (**Figure 3**). The combination of high(er) attenuation at lower monochromatic energies and accurate quantification of low gadolinium concentrations opens up the possibilities for DECT scanning with the use of gadolinium as a contrast agent. Potential clinical applications include detection of myocardial [6–12] and pulmonary perfusion defects [14–16] and the characterization of tumour masses and therapy response assessment [17–19].

In clinical routine, adequate tissue contrast and contrast agent density maps are important for the diagnosis and evaluation of organ perfusion defects. However, to be able to create a gadolinium density map as a surrogate for tissue perfusion, accurate gadolinium quantification is essential, as the post-processing is based on these measurements. This is the first study to describe the accuracy of gadolinium quantification using MDI on SDCT. Gabbai et al. [28] described the capability of spectral differentiation of gadolinium using SDCT, which is in accordance with our study. However, no quantitative values were described and high concentrations (4.7–187.6 mg/ml) of gadolinium were used, which is at least one to two orders of magnitude above the estimated range encountered in healthy cardiac, lung, liver, spleen and kidney tissue (0.58–4.66 mg/ml). Zhang et al. [30] showed a high

6

sensitivity and specificity for gadolinium-enhanced dual-source DECT pulmonary angiography to detect pulmonary embolism in rabbits. However, as in the study by Gabbai et al. gadolinium concentration was not quantified. In addition, high intravenous doses of gadolinium contrast agent, 1.5 and 2.5 mmol/kg bodyweight, were administrated. Bongers et al. [31] evaluated the potential of gadolinium as a CT contrast agent using dual-source DECT in a phantom setup. In accordance with our study they found that monochromatic images at low energy (e.g. 40 keV) allow for higher attenuation. Additional quantification was performed by using the material-specific dual-energy ratio for gadolinium. For the true gadolinium concentrations 6.3, 3.2, 1.6, 0.8, 0.4 and 0.2 mg/ml relative measurement errors were 11.5, 12.0, 21.6, 21.6, 104.2 and 159.4%, respectively. In our study we found a higher accuracy with relative measurement errors of less than 10% down to 2.0 mg/ml at 120 kVp and 1.0 mg/ml at 140 kVp. A possible explanation for this difference can be found in the algorithm. The post-processing algorithms used by Bongers et al. [31] was originally designed for iodine, whereas our algorithm was specifically designed for gadolinium quantification.

We found a slightly lower measurement error, and thus higher accuracy, for scans acquired at 140 kVp compared to 120 kVp. When scanning with a higher tube voltage, more high energy X-ray photons are produced. This decreases the spectral overlap between high- and low-energy spectra, and thereby improves the accuracy of material decomposition, which is in accordance with the findings of Gabbai and colleagues [28]. Moreover, 140 kVp acquisitions resulted in higher CT numbers of different gadolinium concentrations at monochromatic 40 keV images (34 to 464 HU) compared to 120 kVp acquisitions (28 to 416 HU), indicating a superior spectral separation at a higher tube voltage.

Even though gadolinium chelates are generally considered to be safe contrast agents, with acute reaction rates of approximately 0.001%-0.07% [41], recently concerns have arisen about their long-term safety after the discovery that administration of multiple doses has led to detectable gadolinium levels in the brain [42, 43]. In addition, gadolinium contrast has been linked to an increased risk of nephrogenic systemic fibrosis (NSF) in patients with impaired renal function [44]. In both conditions the linear non-ionic and linear ionic contrast agents have primarily been implicated, whereas macrocyclic gadolinium agents, such as used in the current study, have not been linked conclusively to either of these conditions [45–47]. Although both iodine and gadolinium contrast agents

6

pose a risk for patients with impaired renal function, gadolinium is thought to be preferred in patients with renal failure and a glomerular filtration rate greater than 30 ml/min since the risk of NSF is low in these patients, while the risk of iodine contrast-induced nephropathy clearly exists [41]. Furthermore, using gadolinium could potentially obviate the need for pre- and post-imaging hydration as well as premedication protocols that are commonly used in patients with impaired renal function who undergo contrast-enhanced CT scanning, or patients with known allergies to iodinated contrast agents. In the current study a relatively simple method for material decomposition using in-house-developed software is proposed. Our method is based on the mass attenuation coefficient across monochromatic energies. Monochromatic reconstructions take into account the function of two independent factors: the photoelectric and the Compton effect [2]. The photoelectric effect is strongly related to the atomic number of a material in the CT energy range and is therefore material specific [37]. Our method takes into account this material-specific effect by evaluating the attenuation across monochromatic energies.

The strength of our study is that we evaluated accuracy of gadolinium quantification in an optimal controlled setting with a wide and clinically relevant range of gadolinium concentrations, which provides the basis for further research and clinical applications. Our study also has some limitations. The most important is that we used a static phantom in which organ motion was not taken into account. In addition, a fixed concentration is not the same as a bolus injection. However, we tried to mimic the clinical situation as best as possible by using low concentrations of gadolinium, which are expected to be typically encountered clinically. A second limitation is that our study only takes into account water and gadolinium when calculating the amount of gadolinium concentration. Since human tissue does not only consist of water and gadolinium, future phantom and patient research will have to address (healthy) tissue attenuation as well using a three- or multi-material decomposition method. A third limitation is the need for relatively high peak tube voltage (120 or 140 kVp) settings to ensure sufficient spectral separation. However, the higher radiation dose due to the use of high kVp acquisitions can be addressed by reducing tube current (mAs). The fourth limitation is that we only evaluated one DECT technique; therefore, our results may be limited to the vendor used in this study.
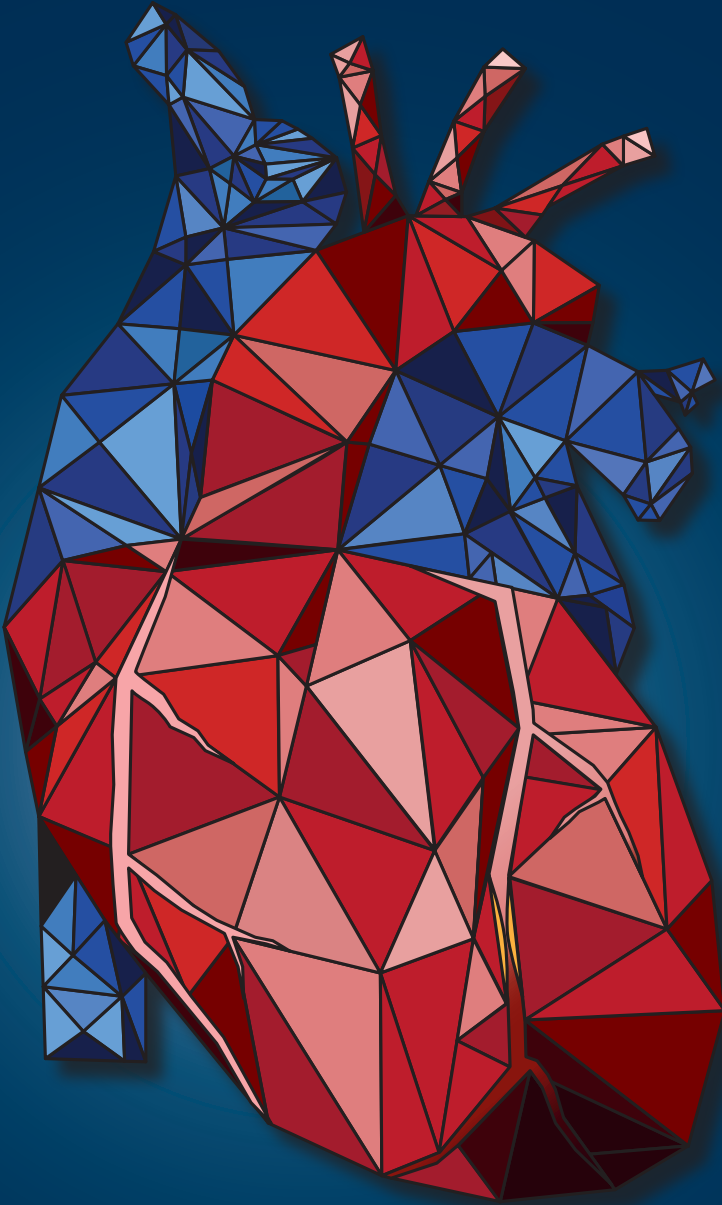
In conclusion, SDCT allows for accurate quantification of commonly clinically used gadolinium concentrations at both 120 and 140 kVp. Lowest measurement errors were found for 140 kVp acquisitions.

References

1.   Hounsfield GN (1973) Computerized transverse axial scanning (tomography). 1. Description of system. Br J Radiol 46:1016–22. doi: 10.1259/0007-1285-46-552-1016

2.   Alvarez RE, Macovski A (1976) Energy-selective reconstructions in X-ray computerized tomography. Phys Med Biol 21:733–44

3.   Macovski A, Alvarez RE, Chan JL, et al (1976) Energy dependent reconstruction in X-ray computerized tomography. Comput Biol Med 6:325–36

4.   den Harder AM, Willemink MJ, de Jong PA, et al (2016) New horizons in cardiac CT. Clin Radiol 71:758–67. doi: 10.1016/j.crad.2016.01.022

5.   Johnson TRC, Krauss B, Sedlmair M, et al (2007) Material differentiation by dual energy CT: initial experience. Eur Radiol 17:1510–7. doi: 10.1007/s00330-006-0517-6

6.   So A, Hsieh J, Narayanan S, et al Dual-energy CT and its potential use for quantitative myocardial CT perfusion. J Cardiovasc Comput Tomogr 6:308–17. doi: 10.1016/j.jcct.2012.07.002

7.   Ko SM, Choi JW, Song MG, et al (2011) Myocardial perfusion imaging using adenosine-induced stress dual-energy computed tomography of the heart: comparison with cardiac magnetic resonance imaging and conventional coronary angiography. Eur Radiol 21:26–35. doi: 10.1007/s00330-010-1897-1

8.   Ruzsics B, Lee H, Zwerner PL, et al (2008) Dual-energy CT of the heart for diagnosing coronary artery stenosis and myocardial ischemia-initial experience. Eur Radiol 18:2414–24. doi: 10.1007/s00330-008-1022-x

9.   Schwarz F, Ruzsics B, Schoepf UJ, et al (2008) Dual-energy CT of the heart--principles and protocols. Eur J Radiol 68:423–33. doi: 10.1016/j.ejrad.2008.09.010

10. Fornaro J, Leschka S, Hibbeln D, et al (2011) Dual- and multi-energy CT: approach to functional imaging. Insights Imaging 2:149–159. doi: 10.1007/s13244-010-0057-0

11. Danad I, Fayad Z a., Willemink MJ, Min JK (2015) New Applications of Cardiac Computed Tomography. JACC Cardiovasc Imaging 8:710–723. doi: 10.1016/j.jcmg.2015.03.005

12. Zhang L-J, Peng J, Wu S-Y, et al (2010) Dual source dual-energy computed tomography of acute myocardial infarction: correlation with histopathologic findings in a canine model. Invest Radiol 45:290–7. doi: 10.1097/RLI.0b013e3181dfda60

13. Zhang L-J, Chai X, Wu S-Y, et al (2009) Detection of pulmonary embolism by dual energy CT: correlation with perfusion scintigraphy and histopathological findings in rabbits. Eur Radiol 19:2844–54. doi: 10.1007/s00330-009-1518-z

14. Bauer RW, Frellesen C, Renker M, et al (2011) Dual energy CT pulmonary blood volume assessment in acute pulmonary embolism - correlation with D-dimer level, right heart strain and clinical outcome. Eur Radiol 21:1914–21. doi: 10.1007/s00330-011-2135-1

15. Krissak R, Henzler T, Reichert M, et al (2010) Enhanced visualization of lung vessels for diagnosis of pulmonary embolism using dual energy CT angiography. Invest Radiol 45:341–6. doi: 10.1097/RLI.0b013e3181dfda37

16. Wu HW, Cheng JJ, Li JY, et al (2012) Pulmonary embolism detection and characterization through quantitative iodine-based material decomposition images with spectral computed tomography imaging. Invest Radiol 47:85–91. doi: 10.1097/RLI.0b013e31823441a1

17. Baxa J, Vondráková A, Matoušková T, et al (2014) Dual-phase dual-energy CT in patients with lung cancer: assessment of the additional value of iodine quantification in lymph node therapy response. Eur Radiol 24:1981–8. doi: 10.1007/s00330-014-3223-9

6

18. Knobloch G, Jost G, Huppertz A, et al (2014) Dual-energy computed tomography for the assessment of early treatment effects of regorafenib in a preclinical tumor model: comparison with dynamic contrast-enhanced CT and conventional contrast-enhanced single-energy CT. Eur Radiol 24:1896–905. doi: 10.1007/s00330-014-3193-y

19. Apfaltrer P, Meyer M, Meier C, et al (2012) Contrast-enhanced dual-energy CT of gastrointestinal stromal tumors: is iodine-related attenuation a potential indicator of tumor response? Invest Radiol 47:65–70. doi: 10.1097/RLI.0b013e31823003d2

20. Lameire N, Van Biesen W, Vanholder R Acute renal failure. Lancet (London, England) 365:417–30. doi: 10.1016/S0140-6736(05)17831-3

21. Singri N, Ahya SN, Levin ML (2003) Acute renal failure. JAMA 289:747–51

22. Tepel M, Aspelin P, Lameire N (2006) Contrast-induced nephropathy: a clinical and evidence-based approach. Circulation 113:1799–806. doi: 10.1161/CIRCULATIONAHA.105.595090

23. Hunt CH, Hartman RP, Hesley GK (2009) Frequency and severity of adverse effects of iodinated and gadolinium contrast materials: retrospective review of 456,930 doses. AJR Am J Roentgenol 193:1124–7. doi: 10.2214/AJR.09.2520

24. Esteban JM, Alonso A, Cervera V, Martínez V (2007) One-molar gadolinium chelate (gadobutrol) as a contrast agent for CT angiography of the thoracic and abdominal aorta. Eur Radiol 17:2394–400. doi: 10.1007/s00330-007-0590-5

25. Remy-Jardin M, Dequiedt P, Ertzbischoff O, et al (2005) Safety and effectiveness of gadolinium-enhanced multi-detector row spiral CT angiography of the chest: preliminary results in 37 patients with contraindications to iodinated contrast agents. Radiology 235:819–26. doi: 10.1148/radiol.2353040734

26. FitzGerald PF, Colborn RE, Edic PM, et al (2016) CT Image Contrast of High-Z Elements: Phantom Imaging Studies and Clinical Implications. Radiology 278:723–33. doi: 10.1148/radiol.2015150577

27. Thomas J V, Bolus DN, Jackson BE, et al (2016) Gadoxetate Disodium enhanced spectral dual-energy CT for evaluation of cholangiocarcinoma: Preliminary data. doi: 10.1016/j.amsu.2016.01.001

28. Gabbai M, Leichter I, Mahgerefteh S, Sosna J (2015) Spectral material characterization with dual-energy CT: comparison of commercial and investigative technologies in phantoms. Acta Radiol 56:960–9. doi: 10.1177/0284185114545150

29. Fält T, Söderberg M, Wassélius J, Leander P Material Decomposition in Dual-Energy Computed Tomography Separates High-Z Elements From Iodine, Identifying Potential Contrast Media Tailored for Dual Contrast Medium Examinations. J Comput Assist Tomogr 39:975–80. doi: 10.1097/RCT.0000000000000298

30. Zhang LJ, Wang ZJ, Lu L, et al (2011) Feasibility of gadolinium-enhanced dual energy CT pulmonary angiography: a pilot study in rabbits. Int J Cardiovasc Imaging 27:1069–80. doi: 10.1007/s10554-010-9755-4

31. Bongers M, Schabel C, Homann G, et al (2015) Potential of Gadolinium as contrast material in second generation dual energy computed tomography (DECT): an ex-vivo phantom study. In: ECR 2015, C-1662

32. Strich G, Hagan PL, Gerber KH, Slutsky RA (1985) Tissue distribution and magnetic resonance spin lattice relaxation effects of gadolinium-DTPA. Radiology 154:723–6. doi: 10.1148/radiology.154.3.3969477

33. Cain PA, Ahl R, Hedstrom E, et al (2009) Age and gender specific normal values of left ventricular mass, volume and function for gradient echo magnetic resonance imaging: a cross sectional study. BMC Med Imaging 9:2. doi: 10.1186/1471-2342-9-2

6

34. de la Grandmaison GL, Clairand I, Durigon M (2001) Organ weight in 684 adult autopsies: new tables for a Caucasoid population. Forensic Sci Int 119:149–54

35. Geraghty EM, Boone JM, McGahan JP, Jain K (2004) Normal organ volume assessment from abdominal CT. Abdom Imaging 29:482–90. doi: 10.1007/s00261-003-0139-2

36. Armstrong JD, Gluck EH, Crapo RO, et al (1982) Lung tissue volume estimated by simultaneous radiographic and helium dilution methods. Thorax 37:676–9

37. Johnson, TR; Fink, C; Schönberg, SO; Reiser M (2011) Dual Energy CT in Clinical Practice, Medical Radiology. Springer-Verlag Berlin Heidelberg. Springer Berlin Heidelberg, Berlin, Heidelberg

38. Hubbell JH, Seltzer SM (2004) Tables of X-Ray mass attenuation coefficients and mass energy-absorption coefficients (version 1.4). http://physics.nist.gov/xaamdi

39. van Hamersvelt RW, Willemink MJ, Takx RAP, et al (2014) Cardiac valve calcifications on low-dose unenhanced ungated chest computed tomography: inter-observer and inter-examination reliability, agreement and variability. Eur Radiol 24:1557–64. doi: 10.1007/s00330-014-3191-0

40. Jones M, Dobson A, O'Brian S (2011) A graphical method for assessing agreement with the mean between multiple observers using continuous measures. Int J Epidemiol 40:1308–13. doi: 10.1093/ije/dyr109

41. Halvorsen RA (2008) Which study when? Iodinated contrast-enhanced CT versus gadolinium-enhanced MR imaging. Radiology 249:9–15. doi: 10.1148/radiol.2491080593

42. Kanda T, Ishii K, Kawaguchi H, et al (2014) High Signal Intensity in the Dentate Nucleus and Globus Pallidus on Unenhanced T1-weighted MR Images: Relationship with Increasing Cumulative Dose of a Gadolinium-based Contrast Material. Radiology 270:834–841. doi: 10.1148/radiol.13131669

43. McDonald RJ, McDonald JS, Kallmes DF, et al (2015) Intracranial Gadolinium Deposition after Contrast-enhanced MR Imaging. Radiology 275:772–782. doi: 10.1148/radiol.15150025

44. Thomsen HS, Morcos SK, Almén T, et al (2013) Nephrogenic systemic fibrosis and gadolinium-based contrast media: updated ESUR Contrast Medium Safety Committee guidelines. Eur Radiol 23:307–318. doi: 10.1007/s00330-012-2597-9

45. Leiner T, Kucharczyk W (2009) NSF prevention in clinical practice: Summary of recommendations and guidelines in the United States, Canada, and Europe. J Magn Reson Imaging 30:1357–1363. doi: 10.1002/jmri.22021

46. Murata N, Murata K, Gonzalez-Cuyar LF, Maravilla KR (2016) Gadolinium tissue deposition in brain and bone. Magn Reson Imaging 34:1359–1365. doi: 10.1016/j.mri.2016.08.025

47. Radbruch A, Weberling LD, Kieslich PJ, et al (2015) High-Signal Intensity in the Dentate Nucleus and Globus Pallidus on Unenhanced T1-Weighted Images. Invest Radiol 50:805–810. doi: 10.1097/RLI.0000000000000227

6

Part III

Functional evaluation of coronary artery disease on CCTA at rest
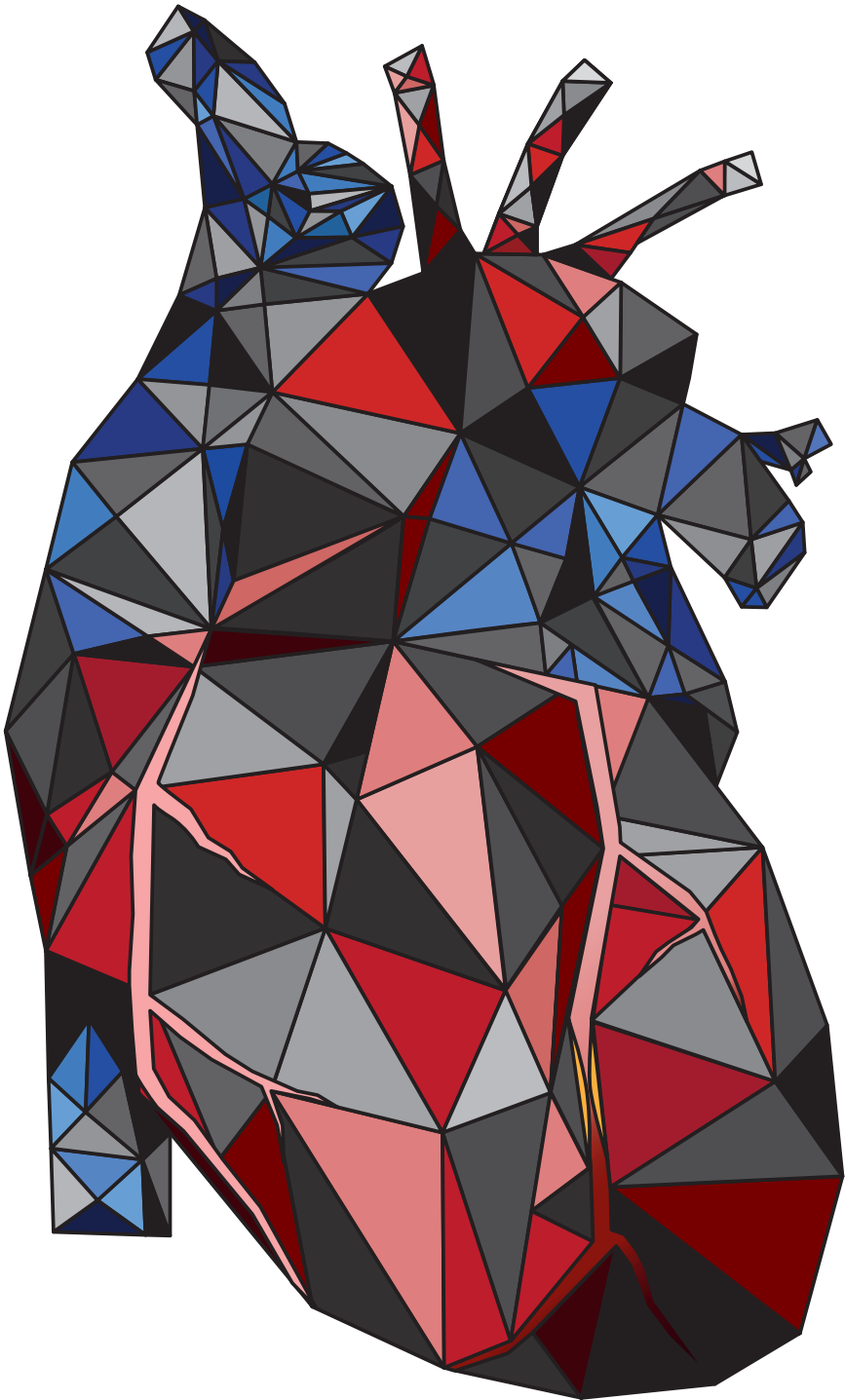
Chapter 7

Diagnostic performance of on-site coronary computed tomography angiography-derived fractional flow reserve based on patient-specific lumped parameter models

Robbert W. van Hamersvelt
Michiel Voskuil
Pim A. de Jong
Martin J. Willemink
Ivana Išgum
Tim Leiner

Abstract

Objectives

The aim of the current study was to evaluate the diagnostic performance of a prototype on-site coronary computed tomography angiography-derived fractional flow reserve (CT-FFR) algorithm, based on patient specific lumped parameter models, for the detection of functionally significant stenosis defined by invasive FFR and to compare the performance to anatomical evaluation of stenosis degree.

Methods

In this retrospective study, we analysed 77 vessels in 57 patients (74% men, mean age 58.5 ± 9.2 years) who underwent clinically indicated coronary computed tomography angiography (CCTA) within 60 days prior to an invasive fractional flow reserve (FFR) measurement. Invasive FFR ≤0.8 was used to indicate a functionally significant stenosis. Diagnostic performance of CT-FFR was evaluated and compared to evaluation of stenosis degree. Analysis was performed on a per-vessel basis.

Results

Invasive FFR revealed functionally significant stenoses in 37 vessels (48%). CT-FFR showed a significantly increased ability to indicate functionally significant stenosis (area under the receiver operating characteristic curve [AUC] 0.87) compared to degree of stenosis on CCTA (AUC 0.70; ΔAUC 0.17, $P < 0.01$). Using a cut-off of ≤0.80 for CT-FFR and ≥50% degree of stenosis on CCTA to indicate a significant stenosis, sensitivity, specificity, positive predictive value, negative predictive value and accuracy were 89.2%, 77.5%, 78.6%, 88.6% and 83.1% for CT-FFR and 89.2%, 42.5%, 58.9%, 81.0% and 64.9% for degree of stenosis on CCTA.

Conclusions

Diagnostic performance of on-site CT-FFR is superior to stenosis evaluation on CCTA for identification of functionally significant coronary artery stenosis in patients with suspected or known coronary artery disease.

Introduction

Coronary computed tomography angiography (CCTA) is an established non-invasive diagnostic tool for the detection of coronary artery disease (CAD) [1]. However, it is limited to anatomical evaluation of degree of stenosis, which does not necessarily imply myocardial ischemia [2, 3]. This issue is underscored by the findings of a recent meta-analysis that demonstrated the incremental value of functional evaluation of coronary stenosis found at CCTA [4]. Invasive fractional flow reserve (FFR) is considered the current reference standard for assessment of coronary artery lesion specific functional significance and is used to guide revascularization treatment [5, 6]. The recent introduction of coronary computed tomography angiography-derived fractional flow reserve (CT-FFR), allows for functional evaluation of coronary stenosis in a non-invasive manner [7]. The most widely used CT-FFR algorithm is based on the principles of computational fluid dynamics (CFD), and has been shown to improve diagnostic performance of CCTA for the evaluation of functionally significant stenosis [4, 8–11]. However, because of the complexity of the CFD calculations, CT images need to be transferred to an off-site workstation and results could take several hours to obtain. Alternative algorithms using less computational power have been introduced and allow for on-site evaluation of CT-FFR [12–19]. The aim of the current study was to evaluate the diagnostic performance of an on-site CT-FFR algorithm based on patient-specific lumped parameter models and to compare the performance to anatomical CCTA evaluation of degree of stenosis.

Materials and Methods

Study design and population

To evaluate the performance of the on-site CT-FFR algorithm we conducted a retrospective, single-centre, observational study. Our local institutional review board approved this study and the need for informed consent was waived on the basis of the retrospective design of the study. Between 2012 and 2016, 89 consecutive patients with suspected or known CAD who received a CCTA followed by invasive FFR within 60 days were retrospectively selected. Patients were excluded when one of the following criteria was met: history of coronary artery bypass graft (n = 0), coronary anomalies or complex congenital heart disease (n = 0), incomplete CCTA coverage (n = 2), pressure wire position during invasive FFR not recorded (n = 3), non-interpretable segment(s) in coronary artery (e.g. motion artefact (n = 5), beam hardening artefact due to pacemaker (n = 1), or stair-step artefact (n = 1)), presence

of a stenosis at the ostium (n = 17), or stent in vessel(s) of interest (n = 3). The final study cohort consisted of 57 patients (**Figure 1**).
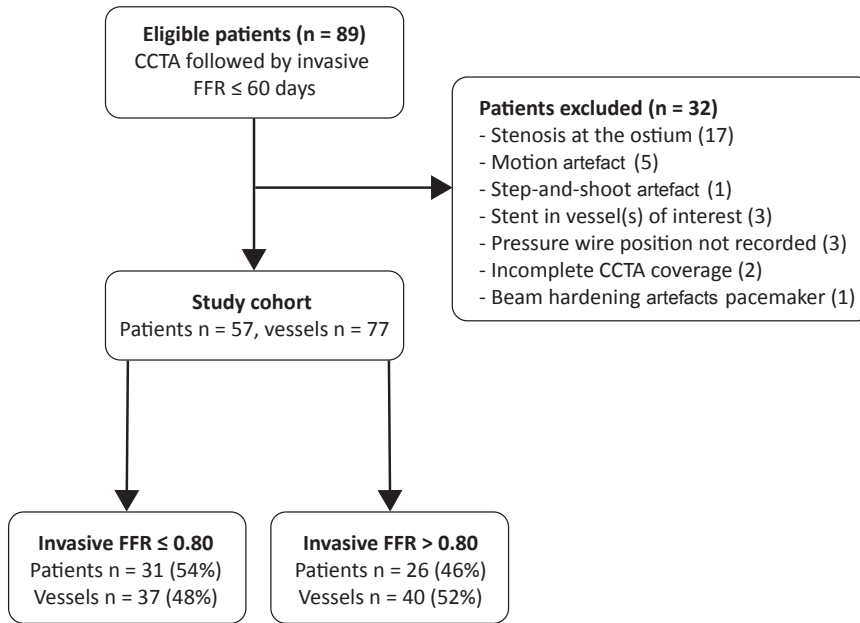
Figure 1 Patient flowchart. *CCTA = coronary computed tomography angiography; FFR = fractional flow reserve; n = number*

7

Coronary CT angiography

Image acquisition was performed in accordance with Society of Cardiovascular Computed Tomography (SCCT) guidelines [20]. If needed, beta-blockers were administered to target a heart rate of 60 beats per minute (bpm). CT scans were performed using a 256-slice CT scanner (Brilliance iCT, Philips Healthcare). A non-contrast prospectively ECG-triggered CT scan was performed to evaluate coronary calcium score. Subsequently, 0.4 mg of nitroglycerine was sublingually administered to all patients. A 90- to 100-ml bolus of intravenous contrast agent (Iopromide, Ultravist 300, Bayer Healthcare, Berlin, Germany) was injected using a flow rate of 6 to 6.7 ml/s. CCTA was performed using a prospectively ECG-triggered sequential scan (≤60 bpm) or retrospectively ECG-gated helical scan (>60 bpm). Depending on body mass, tube voltage ranged between 80 and 120 kVp and tube current between 200 and 300 mAs for prospectively triggered scans and 600 mAs for retrospectively

gated scans. Images were reconstructed with a slice thickness of 0.9 mm and an increment of 0.45 mm using a standard kernel. An observer with 3 years of experience in cardiovascular imaging, blinded for the invasive FFR and CT-FFR results, assessed the degree of maximal stenosis for the vessels of interest using SCCT guidelines: 0% (no stenosis), 1-24% (minimal stenosis), 25-49% (mild stenosis), 50-69% (moderate stenosis), 70-99% (severe stenosis), 100% (occlusion) [21]. A stenosis of ≥50% was used to indicate a significant stenosis on CCTA.

Invasive coronary angiography and FFR

Invasive coronary angiography and FFR were performed for clinical indications and according to standard clinical guidelines. An FFR pressure wire (Pressure™ Certus™ Wire, St. Jude Medical, St. Paul, Minnesota) was placed distal to the coronary stenosis of interest, and FFR was measured under continuous intravenous infusion of adenosine at 140 µg/kg/min for 3 minutes. FFR was automatically calculated as ratio of pressure measured distal to the stenosis and at the level of the guiding catheter. An FFR ≤0.80 was used to indicate a functionally significant stenosis. The exact location of each FFR measurement was recorded during the invasive coronary angiography procedure.

On-site CT-FFR

CT-FFR calculations were performed using research prototype software (FFR-CT, IntelliSpace Portal Version 9.0.1.20490, Philips Healthcare). The CT-FFR analysis was performed by an observer with 3 years of experience in cardiovascular imaging, blinded to the invasive FFR locations and results. First, coronary artery centrelines were automatically generated by the software and corrected where needed by the observer. Centrelines were used as input for the automatic lumen segmentation, which was also manually corrected where needed. Subsequently, a three-dimensional anatomical model of the coronary artery tree was generated and used as an input for the on-site CT-FFR algorithm. The on-site CT-FFR algorithm uses a patient-specific lumped parameter model. In brief, the model works by converting the coronary artery tree into different segments. For each segment, the hydraulic effect is determined by analysing the local geometry of that segment (e.g. radius, curvature, length, cross-sectional, and perimeter) and applying simple equations governing flow and friction in tubular structures. The local hydraulic effects of the segments are represented as resistors and summed along the centreline to represent the complete coronary artery tree in a lumped parameter model. Boundary conditions are represented in the model as inflow and outflow resistors and are determined based on the ostium and outflow segment geometry. The lumped parameter model is used to simulate blood flow and pressure drop, and thereby allows for non-invasive CT-FFR simulation of the whole coronary tree. A more detailed description of the used CT-FFR prototype

7

can be found elsewhere [22]. After completion of the CT-FFR simulation, the exact location of invasive FFR was projected to the segmented coronary tree on CCTA by using anatomical landmarks and the CT-FFR value at this position was recorded. Similar to invasive FFR, a CT-FFR value of ≤0.80 was used to indicate a functionally significant stenosis.

Statistical analysis

Categorical variables are reported as total number and percentage and continuous variables as mean with standard deviation (SD) or median with interquartile range (IQR), as appropriate. CT-FFR and degree of stenosis on CCTA were compared to invasive FFR and diagnostic performance was evaluated on a per-vessel basis using sensitivity, specificity, positive predictive value, negative predictive value, accuracy, and area under the receiver operating characteristic curve (AUC), with corresponding 95% confidence interval (CI). Statistical differences in sensitivity and specificity were evaluated using the McNemar test and differences in AUC using the method of DeLong et al [23]. The optimal CT-FFR threshold of the receiver operating characteristic (ROC) curve was defined using the Youden's index. Correlation between CT-FFR and invasive FFR measurements were evaluated using Pearson's correlation coefficient. Agreement between both methods was evaluated using a Bland-Altman plot with corresponding 95% limits of agreement. To evaluate interpretability of CT-FFR values, diagnostic accuracy of different CT-FFR ranges was evaluated. All results are evaluated on a per-vessel basis. A separate analysis was performed for vessels with intermediate degree of stenosis (25-69%) on CCTA. P-values below 0.05 were considered statistically significant. Statistical analysis was performed using IBM SPSS version 25.0 (IBM corp., Armonk, NY, USA) and MedCalc Statistical Software version 17.8.2 (MedCalc Software BVBA, Ostend, Belgium).

Results

In 57 patients (74% male, mean age 58.5 ± 9.2 years), 77 vessels were evaluated. Detailed patient characteristics are summarized in **Table 1**. FFR was performed in the left anterior descending artery (n = 46, 60%), circumflex artery (n = 16, 21%) and right coronary artery (n = 15, 19%). Invasive FFR revealed a functionally significant stenosis in 37 vessels (48%). Of all evaluated vessels (n = 77), maximum degree of stenosis on CCTA was 0% in 1 vessel, 70-99% in 7 vessels, and 25-69% in the remaining 69 vessels. In the complete dataset, a maximum degree of stenosis ≥50% on CCTA was found in 56 vessels (73%) and a CT-FFR of ≤0.80 in 42 vessels (55%). For CT-FFR, the median time per patient for semiautomatic segmentation depended on the extent of CAD and was 25 (IQR 23) minutes for the centreline and 11 (IQR 6) minutes for the lumen.

After the adjusted segmentations were considered acceptable by the observer, simulation of the CT-FFR by the on-site CT-FFR software required on average 8 ± 1 seconds per patient. A case example of CT-FFR analysis is shown in **Figure 2**.

Table 1 Patient characteristics.

Characteristics	Study cohort (N = 57)
Sex (men), n (%)	42 (74)
Age (years)	58.5 ± 9.2
Men	55.9 ± 8.2
Women	66.3 ± 7.9
Body mass index (kg/m^2)	27.8 ± 3.6
Men	28.0 ± 3.5
Women	27.2 ± 4.2
Cardiovascular risk factors, n (%)	
Current smoker	19 (33)
Diabetes	12 (21)
Dyslipidaemia	47 (82)
Hypertension	49 (86)
Family history of CAD	33 (58)
Calcium Agatston score, median (IQR)	363.5 (774.3)*
Days between CCTA and invasive FFR	29.4 ± 14.1

*N = 56, in 1 case a non-contrast CT scan was not performed and therefore calcium scoring was not possible. Categorical data is presented as number of patients (percentage). Unless otherwise specified, continuous data are presented as mean ± SD. *CAD = coronary artery disease; CCTA = coronary computed tomography angiography; FFR = fractional flow reserve; IQR = interquartile range; n = number of patients; SD = standard deviation*

7
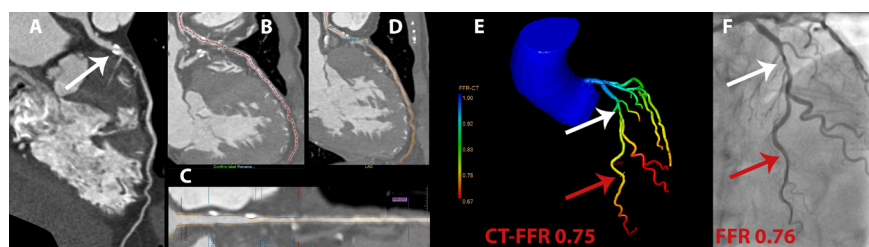
Figure 2 Case example of CT-FFR analysis. CCTA curved multiplanar reconstruction of the left anterior descending artery (**A**) indicated a significant stenosis (white arrow; 50-69% degree of stenosis). To apply the CT-FFR algorithm first the centreline was automatically segmented and manually corrected where needed (**B**), subsequently automatic lumen segmentation was performed and also manually corrected where needed (**C + D**). This anatomical model of the coronary tree was used as input for the CT-FFR algorithm. In this case, CT-FFR (**E**) was 0.75 (red arrow), indicating a significant stenosis (white arrow). Findings were confirmed by invasive FFR (**F**) with a value of 0.76 (red arrow). *CCTA = coronary computed tomography angiography; CT-FFR = coronary computed tomography angiography-derived fractional flow reserve; FFR = fractional flow reserve*

Diagnostic performance

CT-FFR showed an increased ability to indicate a functionally significant stenosis with an AUC of 0.87 [95%CI 0.77-0.94] compared to degree of stenosis on CCTA with an AUC of 0.70 [95%CI 0.58-0.80] with a difference in AUC of 0.17 [95%CI 0.06-0.29], $P < 0.01$ (**Figure 3**). When applying the threshold of ≥50% degree of stenosis to indicate a significant stenosis on CCTA, sensitivity and specificity were 89.2% [95%CI 74.6-97.0] and 42.5% [95%CI 27.0-59.1] respectively. Applying the threshold of ≤0.80 at CT-FFR resulted in an equal sensitivity of 89.2% [95%CI 74.6-97.0] and significantly increased specificity of 77.5% [95%CI 61.5-89.2], $P < 0.01$. Overall accuracy was higher for CT-FFR (83.1% [72.9-90.7]) compared to evaluation of stenosis degree on CCTA (64.9% [53.2-75.5]). Other diagnostic parameters are summarized in **Table 2**. Optimal CT-FFR threshold of the ROC curve, defined by Youden's index, was similar to the clinically defined threshold of ≤0.8. Pearson's correlation between CT-FFR and invasive FFR for all measurements was $r = 0.55$ (**Figure 4**). Mean invasive FFR was 0.80 ± 0.10, Bland-Altman analysis showed that CT-FFR underestimated the invasive FFR value slightly (mean bias: 0.03 ± 0.09) (**Figure 5**). Diagnostic accuracy of different CT-FFR ranges is provided in **Table 3**.

Intermediate stenosis

Intermediate stenosis (25-69% degree of stenosis) was present in 69 vessels (69/77, 90%). Functionally significant stenoses at invasive FFR were present in 31 vessels (31/69, 45%). Separate analysis of the diagnostic performance in vessels with intermediate stenosis resulted in improvement in detection of functionally significant stenoses for CT-FFR (AUC 0.89 [95%CI 0.79-0.95]) compared to degree of stenosis evaluation on CCTA (AUC 0.65 [95%CI 0.52-0.76]), with a difference in AUC of 0.24 [95%CI 0.12-0.37], $P < 0.01$ (**Figure 3**). A significant improvement ($P < 0.01$) of specificity was observed with CT-FFR (78.9% [62.7-90.4]) compared to degree of stenosis on CCTA (42.1% [26.3-59.2]) without decrease in sensitivity (90.3% [74.2-98.0] versus 87.1% [70.2-96.4], respectively). These findings, together with other results on diagnostic performance, were comparable to results of the full sample (**Table 2**). Pearson correlation ($r = 0.56$, **Figure 4**) and Bland-Altman analysis (mean difference 0.02 ± 0.09, **Figure 5**) of intermediate stenosis were also comparable to the results of the full sample.
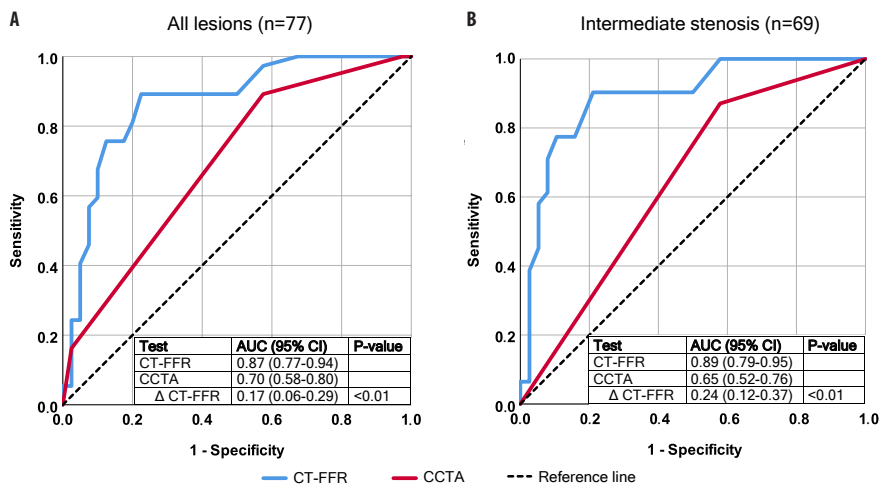
A All lesions (n=77)

Test	AUC (95% CI)	P-value
CT-FFR	0.87 (0.77-0.94)	
CCTA	0.70 (0.58-0.80)	
Δ CT-FFR	0.17 (0.06-0.29)	<0.01

B Intermediate stenosis (n=69)

Test	AUC (95% CI)	P-value
CT-FFR	0.89 (0.79-0.95)	
CCTA	0.65 (0.52-0.76)	
Δ CT-FFR	0.24 (0.12-0.37)	<0.01

— CT-FFR   — CCTA   - - - Reference line

Figure 3 Receiver operating characteristic curves. ROC curves for CT-FFR (blue) and degree of stenosis on CCTA (red) with corresponding AUC values in all lesions (**A**) and in intermediate lesions only (**B**). *CCTA = coronary computed tomography angiography; CT-FFR = coronary computed tomography angiography-derived fractional flow reserve; n = number; ROC = receiver operating characteristic*

Table 2 Per-vessel diagnostic performance.

	Sensitivity	Specificity	PPV	NPV	Accuracy
All lesions (n = 77)					
CCTA (≥50% stenosis)	89.2 [74.6-97.0]	42.5 [27.0-59.1]	58.9 [51.8-65.7]	81.0 [61.2-92.0]	64.9 [53.2-75.5]
CT-FFR (≤0.80)	89.2 [74.6-97.0]	77.5 [61.5-89.2]	78.6 [67.1-86.8]	88.6 [75.2-95.2]	83.1 [72.9-90.7]
Intermediate stenosis (n = 69)					
CCTA (≥50% stenosis)	87.1 [70.2-96.4]	42.1 [26.3-59.2]	55.1 [47.5-62.4]	80.0 [59.8-91.5]	62.3 [49.8-73.7]
CT-FFR (≤ 0.80)	90.3 [74.2-98.0]	78.9 [62.7-90.4]	77.8 [65.2-86.8]	90.9 [77.1-96.7]	84.1 [73.3-91.8]

Data is presented as percentage with 95% confidence interval in brackets. A stenosis of ≥ 50% degree of stenosis on CCTA and CT-FFR value of ≤ 0.80 were used to indicate a significant stenosis. Intermediate stenosis was defined as 25-69% degree of stenosis on CCTA. *CCTA = coronary computed tomography angiography; CT-FFR = coronary computed tomography angiography-derived fractional flow reserve; n = number of patients; NPV = negative predictive value; PPV = positive predictive value*
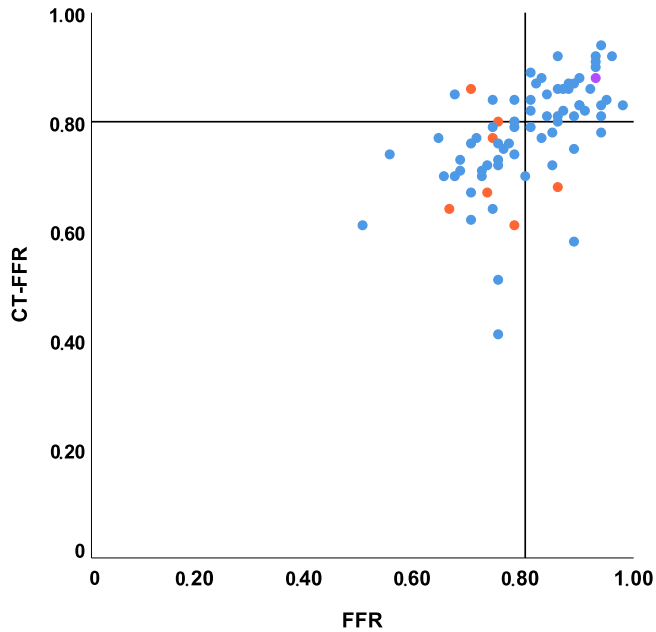
7

Figure 4 Scatterplot of CT-FFR and invasive FFR values. Colour of the dots indicate degree of stenosis on CCTA, with low grade stenosis (<25%, n = 1 vessel) in purple, intermediate degree stenosis (25-69%, n = 69 vessels) in blue and high-grade stenosis (≥70%, n = 7 vessels) in orange. Pearson correlation coefficient for all lesions was $r = 0.55$ and for intermediate stenosis only $r = 0.56$. Black lines indicate the cut-off value used for both invasive FFR (0.8) and CT-FFR (0.8). *CCTA = coronary computed tomography angiography; CT-FFR = coronary computed tomography angiography-derived fractional flow reserve; FFR = fractional flow reserve; n = number*

7

Table 3 Diagnostic accuracy of different CT-FFR ranges.

CT-FFR range	Number of vessels	Diagnostic accuracy
≤ 0.60	3	66.7 [9.4-99.2]
0.61 – 0.70	12	91.7 [61.5-99.8]
0.71 – 0.80	27	74.1 [53.7-88.9]
0.81 – 0.90	30	86.7 [69.3-96.2]
0.91 – 1.00	5	100.0 [47.8-100.0]

Diagnostic accuracy of each CT-FFR range is presented as percentage with 95% confidence interval in brackets. A value of ≤ 0.80 was used for both invasive FFR and CT-FFR to indicate a significant stenosis. *CT-FFR = coronary computed tomography angiography-derived fractional flow reserve; FFR = fractional flow reserve*
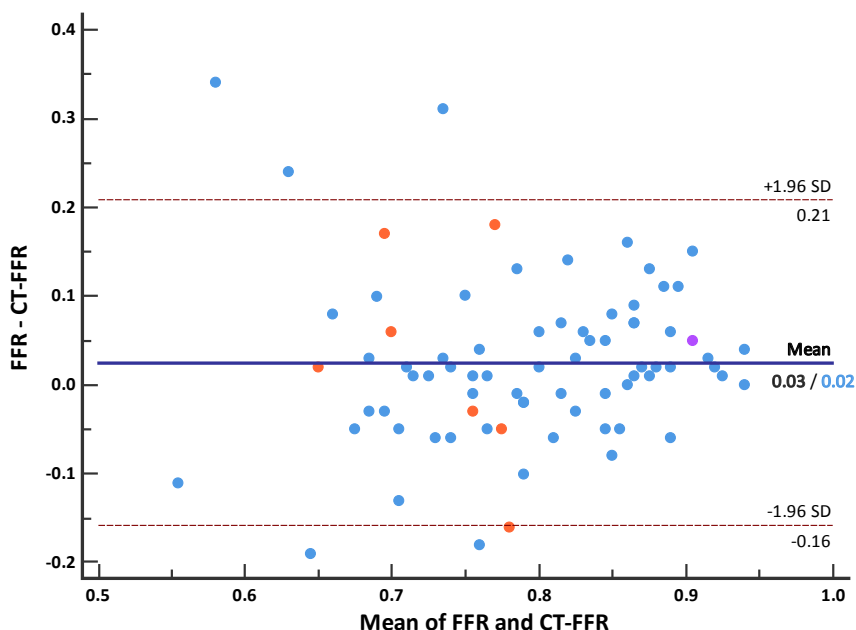
Figure 5 Bland-Altman plot of CT-FFR and invasive FFR values. Colour of the dots indicate degree of stenosis on CCTA, with low grade stenosis (<25%, n = 1 vessel) in purple, intermediate degree stenosis (25-69%, n = 69 vessels) in blue and high-grade stenosis (≥70%, n = 7 vessels) in orange. Mean difference was 0.03 for all lesions and 0.02 for intermediate stenosis only, ± 1.96 SD was similar for both groups with an interval of -0.16 to 0.21. *CCTA = coronary computed tomography angiography; CT-FFR = coronary computed tomography angiography-derived fractional flow reserve; FFR = fractional flow reserve; SD = standard deviation; n = number*

Discussion

In this study we evaluated the diagnostic performance of an on-site CT-FFR algorithm based on a patient-specific lumped parameter model. The main finding was that application of CT-FFR significantly improved the diagnostic performance of CT compared to visual evaluation of degree of stenosis for the identification of functionally significant coronary artery stenosis.

In patients with stable angina, CCTA can help identify CAD in individual patients and reduces adverse events and cardiac deaths compared to standard clinical care [24]. However, although degree of stenosis evaluation on CCTA allows for detection and exclusion of CAD, it has a poor performance for interpreting functional significance of a stenosis [1–4]. In clinical practice additional functional testing (e.g. myocardial stress perfusion imaging) is often used to establish whether or not a significant stenosis is present. The drawback of this approach is the requirement

for additional imaging, including induction of coronary hyperaemia [25]. CT-FFR, on the other hand, potentially allows for functional evaluation of a stenosis on already acquired CCTA images, without the need for physical or pharmacologically induced coronary hyperaemia. Therefore, CT-FFR could be an alternative first step evaluation after CAD is detected on CCTA that could potentially obviate the need for additional testing in some patients.

Different computational methods have been proposed for CT-FFR. Diagnostic performance of both off-site and on-site CT-FFR algorithms have shown incremental diagnostic performance for the evaluation of functional significant stenosis [4, 8–19]. A recent meta-analysis by Celeng et al [4] showed that pooled analysis of all CT-FFR algorithms resulted in a sensitivity of 85% and specificity of 78%, which is in close correlation with the sensitivity (89.2%) and specificity (77.5%) found in the current study. Off-site CT-FFR based on CFD showed an accuracy, sensitivity, specificity, positive predictive value, negative predictive value, AUC and bias (Bland-Altman analysis) ranging between 69-86%, 80-88%, 63-86%, 56-74%, 84-95%, 0.90-0.93 and 0.02-0.06, respectively [8–11]. As off-site CFD calculations are time consuming due to the need for high performance computational resources, more recent CT-FFR algorithms have been focused on on-site CT-FFR evaluation performed on a personal computer. A method introduced by Chung et al [19] used CFD combined with a lumped parameter model to represent outflow boundary conditions and was able to reduce reconstruction time to 37 minutes with similar diagnostic performance. A hybrid method, applying a full-order algorithm to stenotic areas and a reduced-order algorithm to normal areas combined with a lumped parameter model to represent outflow boundary conditions, reduced computation time to 3-10 minutes, without decrease in diagnostic performance compared to full CFD algorithms [12–14, 16]. More recently, CT-FFR methods based on patient-specific lumped parameter models (current study and [15]) and machine learning [17, 18] showed an even further reduction in computation time to only a few seconds with similar diagnostic performance compared to other methods. Donnelly and colleagues [15] showed that the CT-FFR method based on patient-specific lumped parameter model, similar to the method used in the current study, showed a strong diagnostic performance with an accuracy, sensitivity, specificity, positive predictive value, negative predictive value and AUC of 78%, 91%, 72%, 63%, 93% and 0,89, respectively. Additionally, they found that this CT-FFR algorithm showed excellent intra- and inter-observer reproducibility [15]. The current study expands on this study by evaluating this CT-FFR algorithm on a separate cohort in another hospital. In the current study, a slightly higher

specificity and PPV and slightly lower sensitivity and NPV were found, which can be explained by the lower bias found on Bland-Altman analysis in the current study (mean difference between invasive FFR and CT-FFR = 0.03 ± 0.09) compared to the bias observed by Donnelly et al (0.07 ± 0.12) [15]. The mean computation time in the current study was 8 seconds. Together with the feasibility of virtual stenting [26, 27], a short CT-FFR computation time would allow for interactive virtual treatment and direct interpretation by clinical physicians.

Major drawbacks of CT-FFR are its inability to evaluate cases with even slight artefacts as well as the need for time consuming manual review of centreline and arterial lumen segmentations. Because CT-FFR relies on an accurate segmentation of the coronary lumen, high image quality is a prerequisite and cases with artefacts were excluded from CT-FFR analysis. The number of non-diagnostic CCTA datasets can be reduced by improvement of image acquisition protocols and artefact reduction algorithms. Another limitation of the currently used CT-FFR algorithm is the inability to evaluate cases with ostial lesions, as CT-FFR relies on lumen segmentation of a non-stenotic part of the ostium to define inflow conditions. Any coronary artery with an ostial lesion in the coronary tree of interest (left main or right coronary artery) was therefore excluded. Future optimization of CT-FFR methods might address this limitation. Another approach could be evaluation of the left ventricle myocardium using stress CT perfusion [16] or the already acquired CCTA scans at rest [28, 29]. It is expected that by combining both stress CT perfusion and CT-FFR, superior diagnostic performance may be found compared to both methods separately [16]. Future prospective studies are needed to confirm this hypothesis.

A recent systematic review by Cook et al [30] showed that CT-FFR had lowest performance in the 0.70-0.80 range with an overall diagnostic accuracy of 46.1%. In the current study, CT-FFR values in this range were substantially higher and yielded an overall diagnostic accuracy of 74.1%.

Our study has limitations. When interpreting our results, the single centre retrospective study design needs to be taken into account. Both CCTA and invasive FFR were performed for clinical care, which resulted in a cohort with high prevalence of intermediate degree stenosis on CCTA (69/77; 90%) and invasive FFR values between 0.7-0.9 (55/77; 71%). In addition, the number of physiologically intermediate lesions (invasive FFR 0.70-0.80) was 36% (28/77), which is higher than found in most other studies [30]. However, the patients we evaluated reflect the cohort in need for further functional evaluation in daily clinical practice and

7

shows the incremental value of CT-FFR in this most challenging cohort with mainly intermediate stenosis. Additional limitations are that the on-site CT-FFR used in the current study is a research prototype and is not commercially available. CCTA data from a single vendor were used for CT-FFR analysis and therefore our findings may not be applicable to scans performed on equipment of other vendors.

In conclusion, the diagnostic performance of on-site CT-FFR is superior to stenosis evaluation on CCTA for identification of functionally significant coronary artery stenosis. Further prospective studies are needed to evaluate the integration of on-site CT-FFR in clinical practice.

7

References

1.   Budoff MJ, Dowe D, Jollis JG, et al (2008) Diagnostic Performance of 64-Multidetector Row Coronary Computed Tomographic Angiography for Evaluation of Coronary Artery Stenosis in Individuals Without Known Coronary Artery Disease. Results From the Prospective Multicenter ACCURACY (Assessment by Coro. J Am Coll Cardiol 52:1724–1732. doi: 10.1016/j.jacc.2008.07.031

2.   Rossi A, Papadopoulou S-L, Pugliese F, et al (2014) Quantitative Computed Tomographic Coronary Angiography: Does It Predict Functionally Significant Coronary Stenoses? Circ Cardiovasc Imaging 7:43–51. doi: 10.1161/CIRCIMAGING.112.000277

3.   Budoff MJ, Nakazato R, Mancini GBJ, et al (2016) CT Angiography for the Prediction of Hemodynamic Significance in Intermediate and Severe Lesions. JACC Cardiovasc Imaging 9:559–564. doi: 10.1016/j.jcmg.2015.08.021

4.   Celeng C, Leiner T, Maurovich-Horvat P, et al (2018) Anatomical and Functional Computed Tomography for Diagnosing Hemodynamically Significant Coronary Artery Disease. JACC Cardiovasc Imaging. doi: 10.1016/j.jcmg.2018.07.022

5.   Force T, Gilles M, Chairperson M, et al (2013) 2013 ESC guidelines on the management of stable coronary artery disease. Eur Heart J 34:2949–3003. doi: 10.1093/eurheartj/eht296

6.   van Nunen LX, Zimmermann FM, Tonino PAL, et al (2015) Fractional flow reserve versus angiography for guidance of PCI in patients with multivessel coronary artery disease (FAME): 5-year follow-up of a randomised controlled trial. Lancet (London, England). doi: 10.1016/S0140-6736(15)00057-4

7.   Agasthi P, Kanmanthareddy A, Khalil C, et al (2018) Comparison of Computed Tomography derived Fractional Flow Reserve to invasive Fractional Flow Reserve in Diagnosis of Functional Coronary Stenosis: A Meta-Analysis. Sci Rep 8:11535. doi: 10.1038/s41598-018-29910-9

8.   Koo B-K, Erglis A, Doh J-H, et al (2011) Diagnosis of ischemia-causing coronary stenoses by noninvasive fractional flow reserve computed from coronary computed tomographic angiograms. Results from the prospective multicenter DISCOVER-FLOW (Diagnosis of Ischemia-Causing Stenoses Obtained Via Noni. J Am Coll Cardiol 58:1989–97. doi: 10.1016/j.jacc.2011.06.066

9.   Gaur S, Taylor CA, Jensen JM, et al (2017) FFR Derived From Coronary CT Angiography in Nonculprit Lesions of Patients With Recent STEMI. JACC Cardiovasc Imaging 10:424–433. doi: 10.1016/j.jcmg.2016.05.019

10. Nørgaard BL, Leipsic J, Gaur S, et al (2014) Diagnostic performance of noninvasive fractional flow reserve derived from coronary computed tomography angiography in suspected coronary artery disease: the NXT trial (Analysis of Coronary Blood Flow Using CT Angiography: Next Steps). J Am Coll Cardiol 63:1145–1155. doi: 10.1016/j.jacc.2013.11.043

11. Min JK, Leipsic J, Pencina MJ, et al (2012) Diagnostic Accuracy of Fractional Flow Reserve From Anatomic CT Angiography. JAMA 308:1237. doi: 10.1001/2012.jama.11274

12. Coenen A, Lubbers MM, Kurata A, et al (2015) Fractional flow reserve computed from noninvasive CT angiography data: diagnostic performance of an on-site clinician-operated computational fluid dynamics algorithm. Radiology 274:674–83. doi: 10.1148/radiol.14140992

13. De Geer J, Sandstedt M, Björkholm A, et al (2016) Software-based on-site estimation of fractional flow reserve using standard coronary CT angiography data. Acta Radiol 57:1186–92. doi: 10.1177/0284185115622075

14. Kruk M, Wardziak Ł, Demkow M, et al (2016) Workstation-Based Calculation of CTA-Based FFR for Intermediate Stenosis. JACC Cardiovasc Imaging 9:690–9. doi: 10.1016/j.jcmg.2015.09.019

7

15. Donnelly PM, Kolossváry M, Karády J, et al (2018) Experience With an On-Site Coronary Computed Tomography-Derived Fractional Flow Reserve Algorithm for the Assessment of Intermediate Coronary Stenoses. Am J Cardiol 121:9–13. doi: 10.1016/j.amjcard.2017.09.018

16. Yang DH, Kim Y-H, Roh JH, et al (2017) Diagnostic performance of on-site CT-derived fractional flow reserve versus CT perfusion. Eur Heart J Cardiovasc Imaging 18:432–440. doi: 10.1093/ehjci/jew094

17. Coenen A, Kim Y-H, Kruk M, et al (2018) Diagnostic Accuracy of a Machine-Learning Approach to Coronary Computed Tomographic Angiography–Based Fractional Flow Reserve. Circ Cardiovasc Imaging 11:e007217. doi: 10.1161/CIRCIMAGING.117.007217

18. Tesche C, De Cecco CN, Baumann S, et al (2018) Coronary CT Angiography-derived Fractional Flow Reserve: Machine Learning Algorithm versus Computational Fluid Dynamics Modeling. Radiology 288:64–72. doi: 10.1148/radiol.2018171291

19. Chung J-H, Lee KE, Nam C-W, et al (2017) Diagnostic Performance of a Novel Method for Fractional Flow Reserve Computed from Noninvasive Computed Tomography Angiography (NOVEL-FLOW Study). Am J Cardiol 120:362–368. doi: 10.1016/j.amjcard.2017.04.057

20. Abbara S, Blanke P, Maroules CD, et al (2016) SCCT guidelines for the performance and acquisition of coronary computed tomographic angiography: A report of the society of Cardiovascular Computed Tomography Guidelines Committee: Endorsed by the North American Society for Cardiovascular Imaging (NASCI). J Cardiovasc Comput Tomogr 10:435–449. doi: 10.1016/j.jcct.2016.10.002

21. Cury RC, Abbara S, Achenbach S, et al (2016) CAD-RADSTM Coronary Artery Disease – Reporting and Data System. An expert consensus document of the Society of Cardiovascular Computed Tomography (SCCT), the American College of Radiology (ACR) and the North American Society for Cardiovascular Imaging (NASCI). Endorsed by the American College of Cardiology. J Cardiovasc Comput Tomogr 10:269–281. doi: 10.1016/j.jcct.2016.04.005

22. Nickisch H, Lamash Y, Prevrhal S, et al (2015) Learning patient-specific lumped models for interactive coronary blood flow simulations. In: Lecture Notes in Computer Science (including subseries Lecture Notes in Artificial Intelligence and Lecture Notes in Bioinformatics). pp 433–441

23. DeLong ER, DeLong DM, Clarke-Pearson DL (1988) Comparing the areas under two or more correlated receiver operating characteristic curves: a nonparametric approach. Biometrics 44:837–45

24. SCOT-HEART Investigators (2018) Coronary CT Angiography and 5-Year Risk of Myocardial Infarction. N Engl J Med NEJMoa1805971. doi: 10.1056/NEJMoa1805971

25. Takx RAP, Blomberg BA, Aidi HE, et al (2015) Diagnostic Accuracy of Stress Myocardial Perfusion Imaging Compared to Invasive Coronary Angiography With Fractional Flow Reserve Meta-Analysis. Circ Cardiovasc Imaging 8:e002666–e002666. doi: 10.1161/CIRCIMAGING.114.002666

26. Kim K-H, Doh J-H, Koo B-K, et al (2014) A novel noninvasive technology for treatment planning using virtual coronary stenting and computed tomography-derived computed fractional flow reserve. JACC Cardiovasc Interv 7:72–8. doi: 10.1016/j.jcin.2013.05.024

27. Ihdayhid AR, White A, Ko B (2017) Assessment of Serial Coronary Stenoses With Noninvasive Computed Tomography-Derived Fractional Flow Reserve and Treatment Planning Using a Novel Virtual Stenting Application. JACC Cardiovasc Interv 10:e223–e225. doi: 10.1016/j.jcin.2017.09.015

28. Zreik M, Lessmann N, van Hamersvelt RW, et al (2018) Deep learning analysis of the myocardium in coronary CT angiography for identification of patients with functionally significant coronary artery stenosis. Med Image Anal 44:72–85. doi: 10.1016/j.media.2017.11.008

7

29.   van Hamersvelt RW, Zreik M, Voskuil M, et al (2018) Deep learning analysis of left ventricular myocardium in CT angiographic intermediate-degree coronary stenosis improves the diagnostic accuracy for identification of functionally significant stenosis. Eur Radiol 1–10. doi: 10.1007/s00330-018-5822-3

30.   Cook CM, Petraco R, Shun-Shin MJ, et al (2017) Diagnostic Accuracy of Computed Tomography–Derived Fractional Flow Reserve. JAMA Cardiol 2:803. doi: 10.1001/jamacardio.2017.1314

7
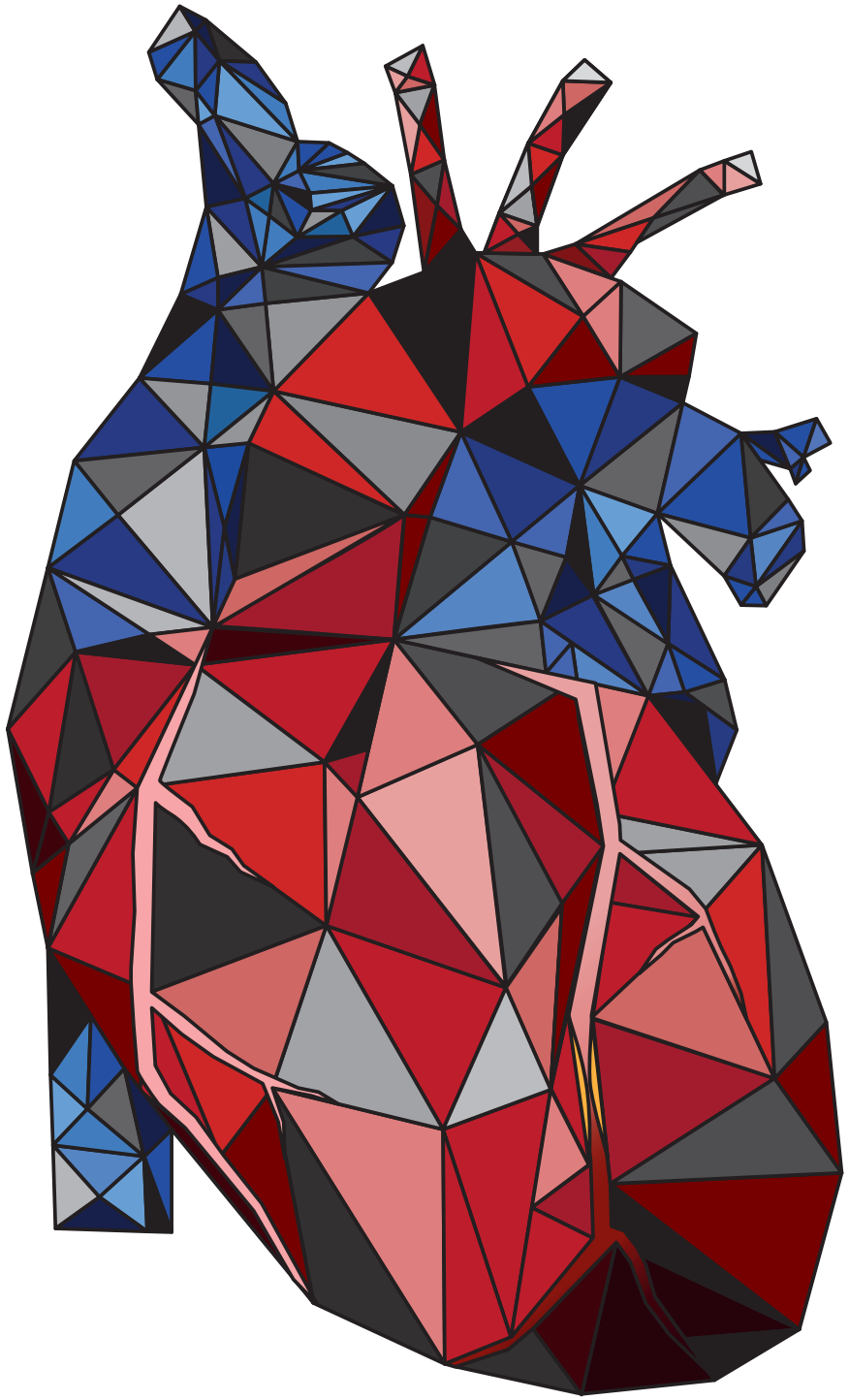
Chapter 8

Deep learning analysis of left ventricular myocardium in CT angiographic intermediate-degree coronary stenosis improves the diagnostic accuracy for identification of functionally significant stenosis

Robbert W. van Hamersvelt*
Majd Zreik*
Michiel Voskuil
Max A. Viergever
Ivana Išgum
Tim Leiner

*contributed equally to this work

Abstract

Objectives

To evaluate the added value of deep learning (DL) analysis of the left ventricular myocardium (LVM) in resting coronary CT angiography (CCTA) over determination of coronary degree of stenosis (DS), for identification of patients with functionally significant coronary artery stenosis.

Methods

Patients who underwent CCTA prior to an invasive fractional flow reserve (FFR) measurement were retrospectively selected. Highest DS from CCTA was used to classify patients as having non-significant (≤24% DS), intermediate (25–69% DS), or significant stenosis (≥70% DS). Patients with intermediate stenosis were referred for fully automatic DL analysis of the LVM. The DL algorithm characterized the LVM, and likely encoded information regarding shape, texture, contrast enhancement, and more. Based on these encodings, features were extracted and patients classified as having a non-significant or significant stenosis. Diagnostic performance of the combined method was evaluated and compared to DS evaluation only. Functionally significant stenosis was defined as FFR ≤0.8 or presence of angiographic high-grade stenosis (≥90% DS).

Results

The final study population consisted of 126 patients (77% male, 59±9 years). Eighty-one patients (64%) had a functionally significant stenosis. The proposed method resulted in improved discrimination (AUC=0.76) compared to classification based on DS only (AUC=0.68). Sensitivity and specificity were 92.6% and 31.1% for DS only (≥50% indicating functionally significant stenosis), and 84.6% and 48.4% for the proposed method.

Conclusions

The combination of DS with DL analysis of the LVM in intermediate-degree coronary stenosis may result in improved diagnostic performance for identification of patients with functionally significant coronary artery stenosis.

8

Introduction

Assessment of degree of stenosis (DS) in coronary arteries using coronary computed tomography angiography (CCTA) is an accepted diagnostic tool for the detection and exclusion of coronary artery disease (CAD), with consistently high sensitivity and negative predictive value [1–3]. However, it has limited specificity in indicating the functional significance of a stenosis [2, 3]. Invasive fractional flow reserve (FFR) is currently the reference standard to indicate functional significance of a coronary stenosis and to guide treatment [4]. However, due to its invasive nature and high cost, adoption of invasive FFR in clinical practice is limited, and the search for a non-invasive method that would determine functional significance of a stenosis continues.

To address the limited specificity of CCTA, new techniques have been developed to obtain information about the functional significance of a stenosis in a non-invasive way. FFR derived from CT (FFRct) is an emerging method which has shown promising results [5–7]. By simulating flow and pressure through the coronary arteries, a virtual FFR value is obtained. More recently, promising results have been obtained with analysis of myocardial perfusion from resting CT [8–16]. Even though it is well known that perfusion defects are more pronounced under conditions of hyperaemia [17, 18], prior studies have shown the feasibility and accuracy of identification of patients with a functionally significant coronary artery stenosis with resting CCTA only [8–13]. With these approaches, functional information is obtained without the need for an additional stress perfusion acquisition, thereby saving radiation and contrast medium dose, lowering risk, and reducing examination duration and cost. In recent studies, approaches exploiting machine learning have been proposed in which the left ventricular myocardium (LVM) in resting CCTA is analysed and used to classify patients with regard to the presence of functionally significant coronary artery stenosis [8, 9, 13].

In classical machine learning, discriminant features describing the LVM, such as hypo-attenuation and changes in myocardial wall thickness, are manually designed by an expert. Subsequently, these features are used in an algorithm that is built to classify patients according to presence of functionally significant coronary artery stenosis [8, 9]. In contrast to the approaches using expert engineered image features, we recently proposed a deep learning (DL) algorithm, whereby the LVM features that discriminate patients with and without functionally significant coronary artery stenosis are independently learned by the algorithm directly from the image [13]. The current study expands on our previous work [13] by applying

8

a combined method of visual stenosis grading on CCTA and only applying the DL-based analysis to the intermediate degree stenosis. In contrast to classical machine learning-based approaches, the DL algorithm is able to independently learn generic and complex LVM patterns, and could potentially be more sensitive to changes in the LVM caused by functionally significant stenosis [19, 20].

Thus, the aim of the current study was to evaluate the added value of resting CCTA LVM deep learning analysis over coronary DS evaluation only, for identification of patients with functionally significant coronary artery stenosis.

Materials and Methods

Study design and population

This was a single centre, retrospective, observational study. Between 2012 and 2016, 136 consecutive patients who underwent a CCTA within 1 year prior to an invasive FFR measurement were selected. Patients were excluded ($n = 10$) when automatic LVM segmentation failed or when a significant part was not or incorrectly segmented, following grading defined by Abadi et al [21]. This was the only exclusion criteria used to indirectly exclude scans with bad image quality, suboptimal contrast, motion artefact, or any other artefact. No further in- or exclusion criteria were applied. This study was approved by our local institutional review board at the University Medical Center Utrecht in the Netherlands (protocol number 15/608). The need for informed consent was waived by the institutional review board, since the study was performed on already available imaging data.

CCTA image acquisition

All patients underwent CCTA on a 256-slice CT system with a collimation of 128×0.625 mm (Brilliance iCT, Philips Healthcare). In accordance with the Society of Cardiovascular Computed Tomography guidelines [22], beta-blockers and/or nitroglycerine was administered to target a heart rate of 60 beats per minute (bpm). Patients were imaged using either an ECG-triggered step-and-shoot protocol (≤60 bpm) or a retrospectively ECG-gated spiral protocol (heart rate >60 bpm). An intravenous contrast agent (70–80 ml) (iopromide, Ultravist 300, Bayer Healthcare), followed by a mix (60–67 ml) of 30% contrast agent and 70% saline, followed by saline (30–40 ml) was administrated using a flow rate of 6 (<80 kg) or 6.7 ml/s (≥80 kg). Bolus tracking with 7-s delay was used for acquisition (threshold of 100 HU for step-and-shoot or 200 HU for spiral). For step-and-shoot, images were acquired

at 78% of the R-R interval with a rotation time of 0.27 s. A weight-dependent tube voltage and corresponding current of 80, 100, or 120 kVp and 195, 210, and 210 mAs were used in patient weighing <50 kg, 50–80 kg, and >80 kg, respectively. For spiral, a heart rate–dependent pitch (0.16–0.18) and rotation time (0.27–0.33) were used. Weight-dependent tube voltage and corresponding tube current were 100, 120, or 120 kVp and 600, 600, and 700 mAs for patients weighing <65 kg, 65–80 kg, and >80 kg, respectively. Images acquired at 75% of the R-R interval were selected for further analysis. For both protocols, axial images were reconstructed with a slice thickness of 0.9 mm at 0.45-mm increment using iterative reconstruction (iDose^4, Philips Healthcare). Maximum DS for each coronary artery was visually scored in consensus by two observers and categorized in 0%, 1–24%, 25–49%, 50–69%, and ≥70% or non-diagnostic, in accordance with dedicated guidelines [23, 24].

Invasive coronary angiography and FFR

All patients underwent invasive coronary angiography (ICA) and FFR according to standard clinical guidelines. FFR measurements were performed in the coronary arteries when deemed clinically indicated. Measurements were performed under adenosine-induced hyperaemia (140 µg/kg as continuous intravenous infusion), and FFR was measured as distal as possible in the target vessel using a coronary pressure wire (Pressure™ Certus™ Wire, St. Jude Medical). The FFR value was automatically calculated by dividing the pressure measured distal to the stenosis by the pressure measured at the level of the guiding catheter in mmHg. In case FFR was ≤0.80, the stenosis was considered significant. In the vessels with high-grade coronary stenosis at ICA (≥90% DS), invasive FFR was not performed, but stenoses were deemed significant based on DS alone [25]. Therefore, when evaluating ischemia on a patient basis, either a significant FFR (≤0.8) or high-grade stenosis at ICA (≥90% DS) was used to indicate the presence of functionally significant stenoses (**Figure 1**).

CCTA and deep learning based image analysis

To evaluate the diagnostic performance of adding LVM DL analysis to evaluation of DS, patients were subdivided into three different groups based on the highest degree of coronary stenosis at CCTA (group 1, DS ≤24%; group 2, DS 25–69%, and group 3, ≥70%DS). Patients with ≤24% DS at CCTA (n = 10) were considered to have a non-significant stenosis, and patients with ≥70% DS at CCTA (n = 15) were considered to have a significant stenosis. Patients with intermediate stenosis at CCTA (25–69% DS, n = 101) were referred for fully automatic DL analysis of the LVM to indicate whether a functionally significant stenosis was present (**Figure 2**). With the
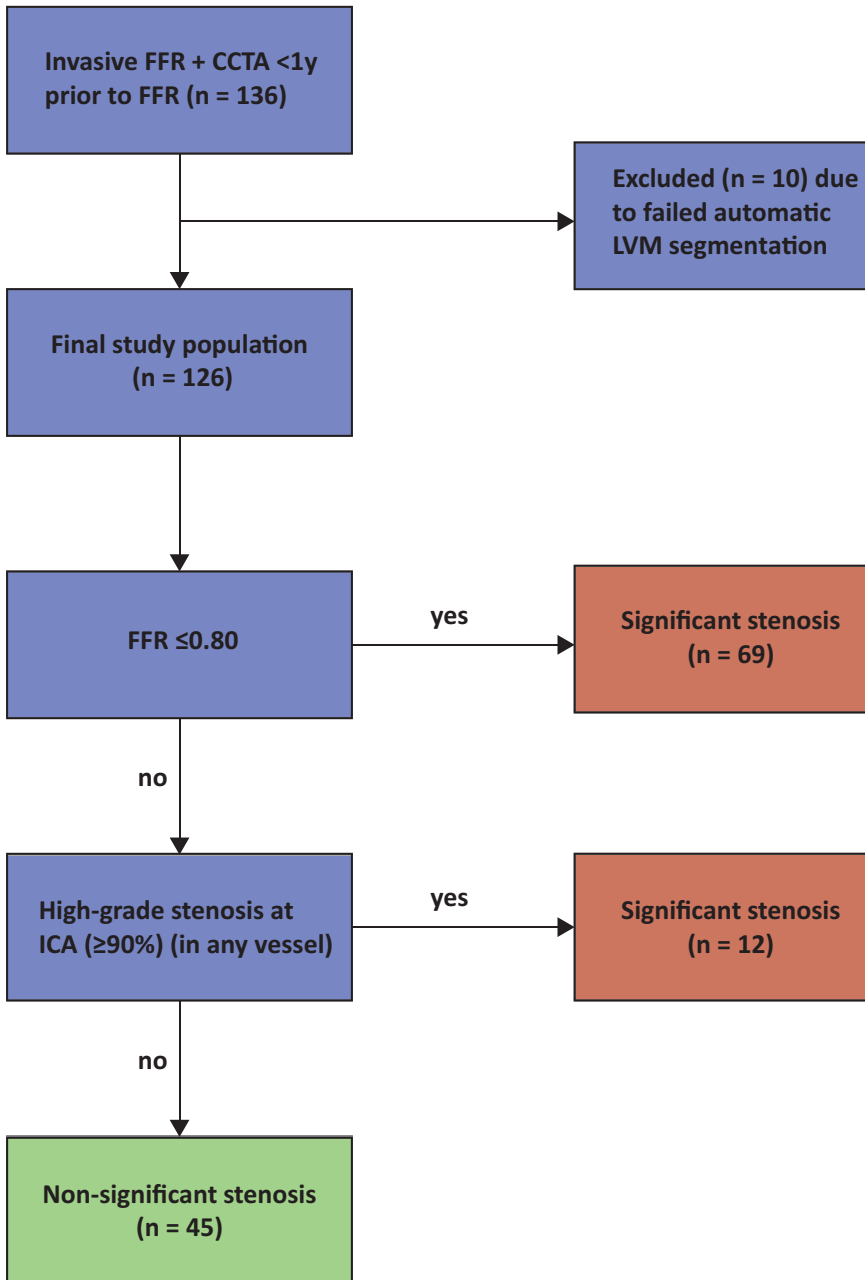
8

Figure 1 Flowchart indicating ischemia on a patient basis. *CCTA = coronary computed tomography angiography; FFR = fractional flow reserve; ICA = invasive coronary angiography; LVM = left ventricular myocardium; n = number of patients*
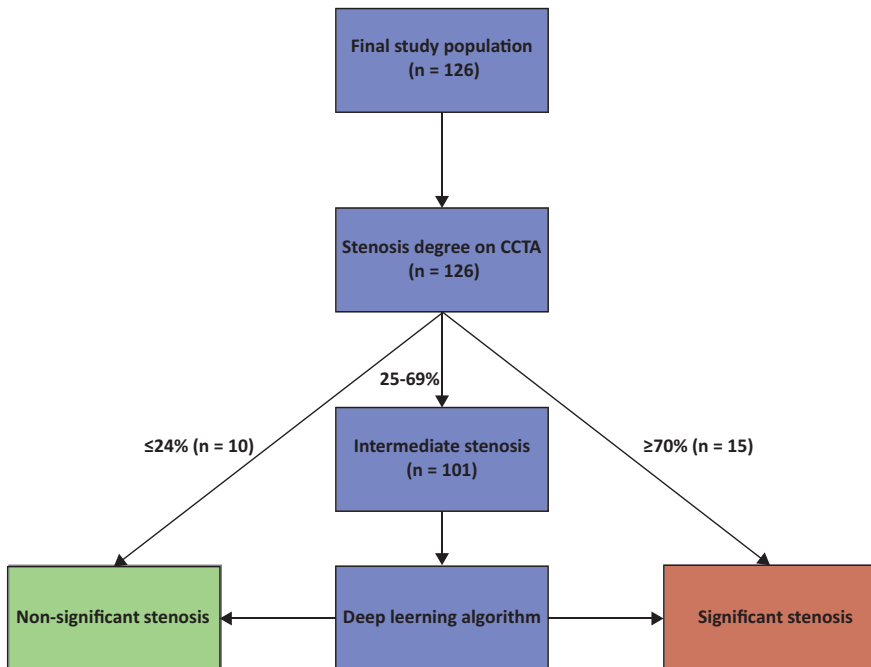
Figure 2 Flowchart of analysis on a patient basis. *CCTA = coronary computed tomography angiography; n = number of patients*

DL method, resting CCTA images were automatically analysed using the method as described by Zreik et al [13]. The prior technical study [13] focused on development of the DL algorithm, while assessing the effect of the different building blocks. The current clinical study expands and validates the previous study in two ways. First, by employing a clinically more relevant reference standard to indicate functional significant stenosis on a patient level: either a significant FFR (≤0.8) or high-grade stenosis at ICA (≥90% DS). Second, a combined method of visual stenosis grading on CCTA and only applying the DL-based analysis to the intermediate-degree stenosis is applied. In this way, the DL method could be trained and evaluated on this subset of most challenging patient category of intermediate stenosis only. A full description of the DL method can be found elsewhere [13]; a graphical summary is presented in **Figure 3**, and a more detailed description about feature extraction in **Supplemental Figure 1**. First, LVM was automatically segmented on all CT slices using a multiscale convolutional neural network (**Figure 4**). Subsequently, the LVM was characterized (encoded) on all CT slices by the algorithm in an unsupervised manner using a convolutional auto-encoder. Using these encodings,
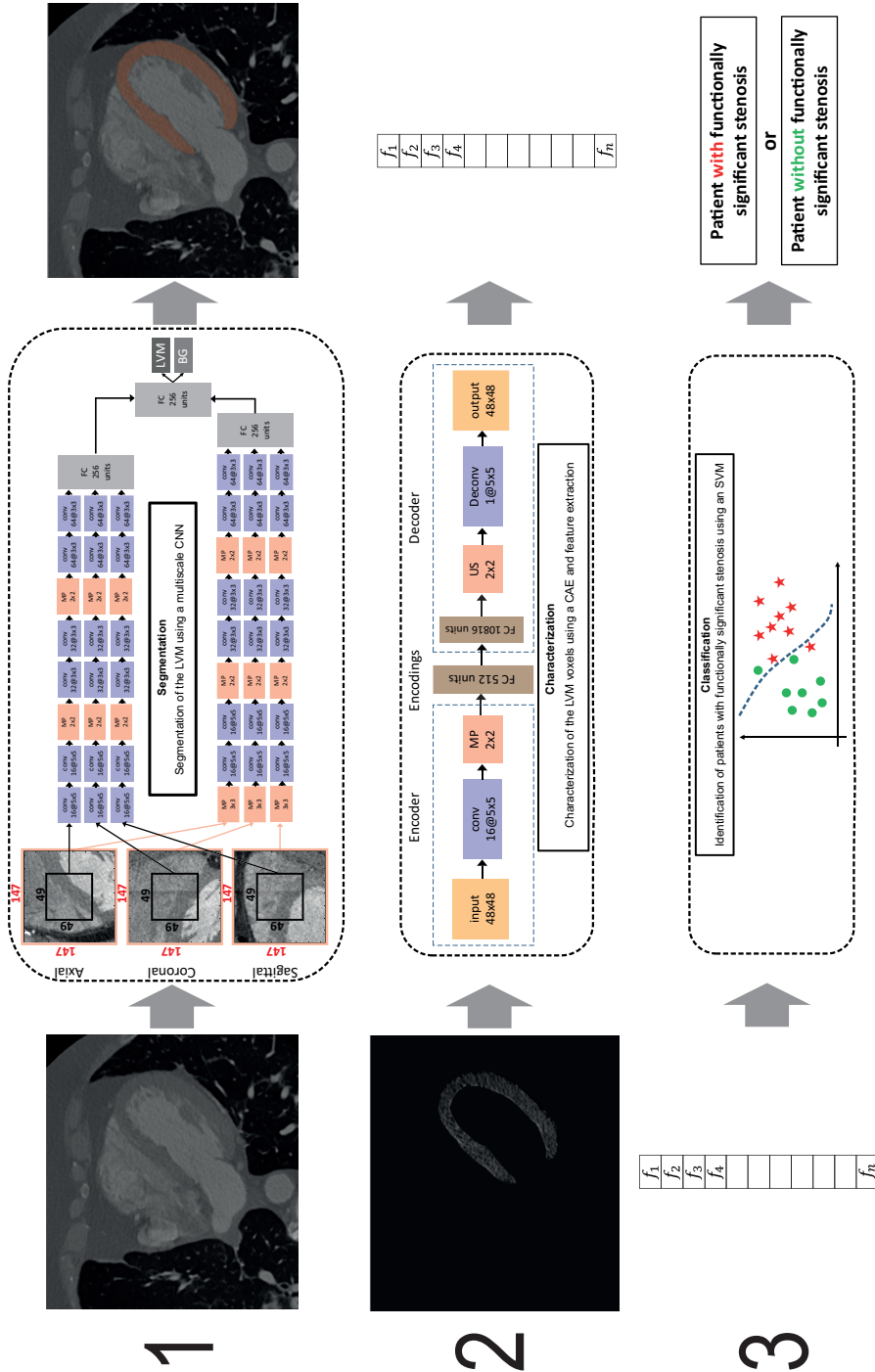
8

Figure 3 Graphical summary of the utilized deep learning method. The described DL method includes three stages. First (**1**), LVM is automatically segmented using a multiscale convolutional neural network (CNN). The multiscale CNN includes two identical streams; each analyses a set of triplanar input patches taken at a single scale (black and red squares) from the axial, coronal, and sagittal image slices with the target voxel in their centres. Each set is processed with a combination of convolutional (conv), max-pooling (MP), and fully connected (FC) layers. In the end, single voxels are classified as myocardium or background. This was performed on all CT slices to segment the whole myocardium. All LVM voxels are analysed in the next stage. Second (**2**), LVM was characterized (encoded) on all CT slices by the algorithm in an unsupervised manner using a convolutional auto-encoder (CAE). The CAE contains two parts, an encoder and a decoder. The encoder compresses the data to a lower dimensional representation by convolutional and max-pooling layers. The decoder expands the compressed form to reconstruct the input data by deconvolutional (deconv) and upsampling (US) layers. To represent the entire LVM, statistics over encodings of all LVM voxels (on all CT slices) are used as features. Third (**3**), based on the extracted features, patients are classified with a support vector machine (SVM) to those with or without functionally significant coronary artery stenosis. *BG = background; CAE = convolutional auto-encoder; CCTA = coronary computed tomography angiography; CNN = convolutional neural network; conv = convolutional; deconv = deconvolutional; FC = fully connected; LVM = left ventricular myocardium; MP = max-pooling; SVM = support vector machine; US = upsampling*
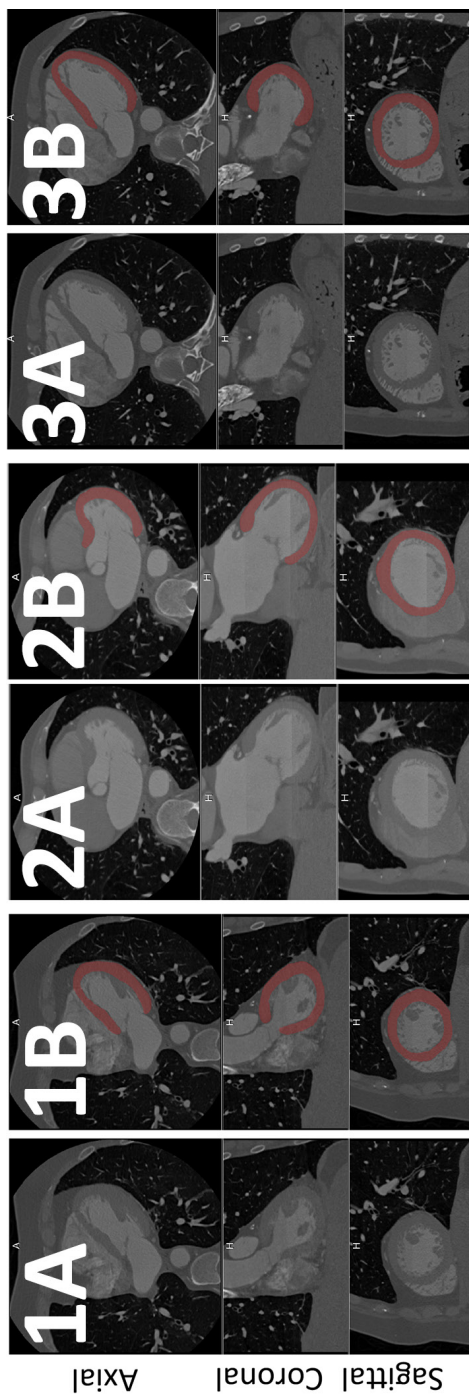
Figure 4 Example of fully automatic left ventricular myocardium segmentation. Coronary CTA images of three randomly selected patients (1, 2, and 3). For each patient, the left column (**A**) depicts a conventional image, and the right column (**B**), the fully automatic LVM segmentation overlay. LVM was automatically segmented on all CT slices using a multiscale convolutional neural network. For each patient, an example of one axial slice (top), one coronal slice (middle), and one sagittal slice (bottom) is shown. *LVM = left ventricular myocardium*

8

which likely contain information regarding shape, texture, contrast enhancement, and more, features were extracted to represent the whole LVM as a volume. Based on these features, patients were classified according to the presence of functionally significant coronary stenosis using a support vector machine classifier. For the current study, the DL method was trained and validated on the subset of patients with intermediate stenosis (n = 101) using an invasively measured FFR ≤0.80 or angiographic high-grade stenosis (≥90% DS) as an indicator for presence of functionally significant stenosis. All patients with intermediate stenosis (n = 101) were classified in 10-fold stratified cross-validation experiments. For each 10-fold cross-validation, the dataset was divided into ten stratified subsets whereby one subset was used as validation set and the other nine subsets were used for training. This process was repeated ten times, whereby each subset was used once as validation set. To evaluate robustness of the method, the 10-fold cross-validation was repeated 50 times, with randomization of the data after each repetition. To allow for evaluation of the combined method (DS and LVM DL on intermediate stenosis) on the entire set of patients, patients found to be non-significant (≤24% DS) and significant (≥70% DS) based on DS on CCTA were assigned probability values of 0 s and 1 s, respectively. For patients with intermediate stenosis, the output probability of the LVM DL model in each cross-validation experiment was employed.

Statistical analysis

Diagnostic performance of the proposed method (DS evaluation combined with DL analysis of LVM on patients with intermediate stenosis at CCTA) for predicting the presence of functionally significant stenosis on a patient basis was evaluated and compared to the diagnostic performance of DS evaluation alone. Diagnostic performance was evaluated using accuracy, sensitivity, specificity, negative predictive value, positive predictive value, and area under the receiver operating characteristic curve (AUC). For the evaluation of the DS combined with DL analysis, diagnostic performance was evaluated on all 50 cross-validation experiments, and the average ± standard deviation (SD) was used to represent diagnostic performance. For DS only, diagnostic performance is presented with 95% confidence interval (CI). Because prior events and interventions could influence texture changes, an additional sensitivity analysis was performed after exclusion of patients with prior events and interventions (prior myocardial infarction (MI), prior PCI, and/or prior CABG, n = 23). The Shapiro-Wilk test was used to evaluate normality of the data. Continuous values are listed as mean with SD and categorical values as percentages, unless stated otherwise. A P value < 0.05 was used to indicate

statistical significance. IBM SPSS version 21.0 (IBM corp.) and MedCalc Statistical Software version 17.7.2 (MedCalc Software BVBA) were used for statistical analyses.

Results

Patient characteristics

In total, 136 patients were eligible, of which 10 were excluded due to incorrect or failed automatic LVM segmentation. The final study population consisted of 126 patients (77% male, mean age 59±9 years). Baseline characteristics are listed in **Table 1**.

Table 1 Patient characteristics.

Characteristics	Total study cohort (N = 126)	Patients with intermediate stenosis (N = 101)
Sex (men), n (%)	97 (77)	77 (76)
Age (years), mean ± SD	59 ± 9	60 ± 9
Men	58 ± 9	58 ± 9
Women	65 ± 8	65 ± 8
Body mass index (kg/m^2), mean ± SD	27 ± 4	28 ± 4
Cardiovascular risk factors, n (%)		
Current smoker	31 (25)	23 (23)
Diabetes	24 (19)	21 (21)
Dyslipidaemia	109 (87)	87 (86)
Hypertension	110 (87)	89 (88)
Previous myocardial infarction, n (%)	14 (11)	11 (11)
Previous percutaneous coronary intervention, n (%)	19 (15)	15 (15)
Previous coronary artery bypass grafting, n (%)	2 (2)	2 (2)
Coronary calcium Agatston score, median (IQR)	464 (800)[a]	526 (782)[a]

[a] = in three cases coronary calcium scoring was not performed due to motion artefacts of the coronary arteries. *IQR = interquartile range; n = number of patients; SD = standard deviation*

8

Invasive coronary angiography and FFR

The median number of days (IQR) between CCTA and invasive FFR was 33 (40). Eighty-one patients (81/126, 64%) had a functionally significant stenosis, of which 69 patients (69/81, 85%) had an FFR ≤0.80. In the remaining twelve patients (12/81, 15%), lowest FFR value was >0.80 and a high-grade stenosis on ICA (≥90% DS) was present in another coronary artery (**Figure 1**). The distribution of severity of disease on a patient-by-patient basis is depicted in **Figure 5**.

Figure 5 Distribution of lowest FFR value per patient (n = 126). Ischemia was evaluated on a patient basis, an FFR ≤0.8 or angiographic high-grade stenosis (≥90% DS) was used to indicate the presence of a functionally significant stenosis. Per patient, the lowest FFR value is depicted, unless this concerned an FFR >0.8, and a high-grade stenosis on ICA (≥90% DS) was present in another vessel, then this was scored as "high-grade stenosis on ICA," and FFR value of that patient is not depicted. *DS = degree of stenosis; FFR = fractional flow reserve; ICA = invasive coronary angiography*

8

Degree of stenosis on CCTA

Maximum DS on a patient basis was 0%, 1–24%, 25–49%, 50–69%, and ≥70% in 2, 8, 10, 91, and 15 patients, respectively. In 20 patients, at least one segment was scored non-diagnostic, of which 18 patients had a significant stenosis (≥50% DS) in another segment. In the remaining two patients, maximum DS in another segment was 25–49%, and PCI was present.

Diagnostic performance

The diagnostic performance of analysis by evaluation of DS alone to indicate functionally significant stenosis was moderate with an AUC of 0.68 (95%CI 0.59–0.76) (**Figure 6**). When applying a threshold of ≥50% DS to indicate functional significance of a stenosis, sensitivity was 92.6% (95%CI 84.6–97.2%) and specificity 31.1% (95%CI 18.2–46.6%). Changing the threshold to lower or higher DS resulted in commensurate changes in sensitivity or specificity (**Table 2**).

Test	AUC (95% CI)
DS	0.68 (0.59-0.76)
DS + LVM DL	0.76 ± 0.02
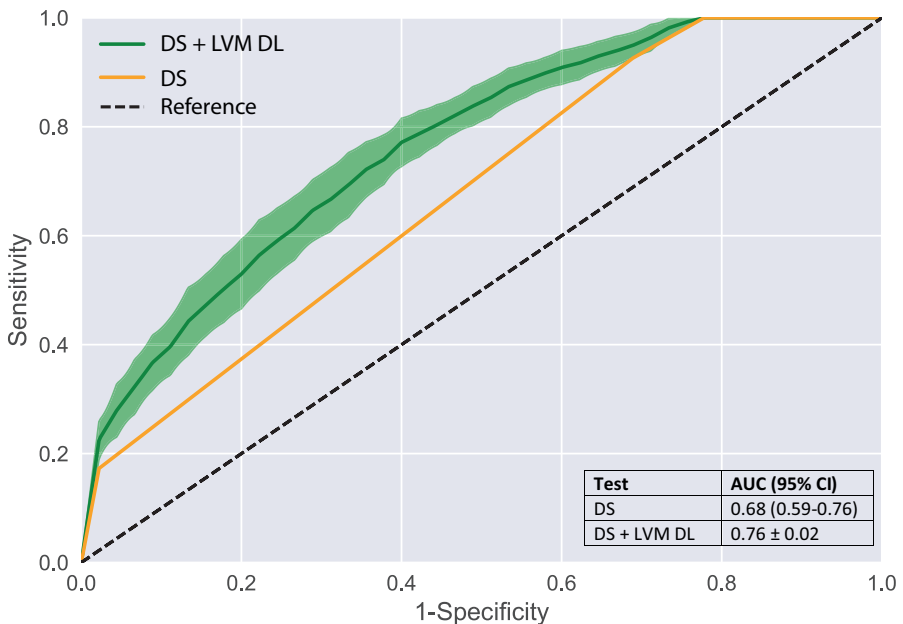
Figure 6 Receiver operating characteristic curves. Diagnostic performance of DS and a combination of DL added to DS on CCTA for predicting functionally significant stenosis on a patient basis. For the combined method, ROC curves and AUC are depicted as average ± SD of 50 cross-validation experiments. *AUC = area under the receiver operating characteristic curve; CCTA = coronary computed tomography angiography; DL = deep learning; DS = degree of stenosis; LVM = left ventricular myocardium; ROC = receiver operating characteristic*

Table 2 Diagnostic performance.

Method and threshold	Sensitivity (%)	Specificity (%)	PPV (%)	NPV (%)	Accuracy (%)	AUC
CCTA ≥25% DS	100.0 (81/81) [95.5-100.0]	22.2 (10/45) [11.2-37.1]	69.8 (81/116) [66.4-73.0]	100.0 (10/10) [100.0-100.0]	72.2 (91/126) [64.3-80.2]	0.68 [0.59-0.76]
CCTA ≥50% DS	92.6 (75/81) [84.6-97.2]	31.1 (14/45) [18.2-46.6]	70.8 (75/106) [66.3-74.8]	70.0 (14/20) [49.1-85.0)	70.6 (89/126) [62.6-78.7]	0.68 [0.59-0.76]
CCTA ≥70% DS	17.3 (14/81) [9.8-27.3]	97.8 (44/45) [88.2-99.9]	93.3 (14/15) [65.5-99.0]	39.6 (44/111) [37.1-42.3]	46.0 (58/126) [37.2-54.9]	0.68 [0.59-0.76]
CCTA DS + DL combined	84.6 ± 0.03	48.4 ± 0.04	74.7 ± 0.01	64.0 ± 0.05	71.7 ± 0.02	0.76 ± 0.02

Data is given in percentage, data in parentheses is raw data, and data in square brackets is 95% confidence interval. For the combined method, data is depicted as average ± SD of 50 cross-validation experiments. *AUC = area under the receiver operating characteristic curve; CCTA = coronary computed tomography angiography; DL = deep learning; DS = degree of stenosis; LVM = left ventricular myocardium; NPV = negative predictive value; PPV = positive predictive value; SD = standard deviation*

In ten patients (10/126, 8%), the maximum DS at CCTA was ≤24% (**Figure 2**). In all of these patients, FFR was higher than 0.8 (mean ± SD; 0.89±0.05) and no high-grade stenosis on ICA was present. Fifteen patients (15/126, 12%) had ≥70% DS at CCTA, and in 14 of these patients (14/15, 93%), FFR was ≤0.8 or high-grade stenosis on ICA was present. In one case, FFR was 0.82, and no high-grade stenosis on ICA was present. The remaining 101 patients with intermediate DS at CCTA were subjected to LVM DL analysis. Classification based on the combination of DS from CCTA (≤24% and ≥70%) and LVM DL analysis on intermediate stenosis (25–69%) improved discrimination (AUC=0.76±0.02) compared to classification based on DS from CCTA only (AUC=0.68 [95%CI 0.59–0.76]) (**Figure 6**). The combined method resulted in an increased specificity of 48.4±0.04% at the expense of a small decrease in sensitivity (84.6±0.03%), compared to the specificity 31.1% (95%CI 18.2–46.6%) and sensitivity 92.6% (95%CI 84.6–97.2%) of DS from CCTA only (≥50% DS to indicate functional significant stenosis) (**Table 2**). To evaluate the robustness of the DL method applied on different patient cohorts, the DL analysis was applied on the complete cohort (n=126) and compared to DL analysis of intermediate stenosis only (n=101) (**Supplemental Figure 2**).

Diagnostic performance in patients without prior MI, PCI or CABG (n = 103)

In eight patients (8/103, 8%), maximum DS at CCTA was ≤24%, and in 12 patients (12/103, 12%), maximum DS was ≥70%. DL was applied to the intermediate stenosis (n=83). Also in this sub analysis, the combined method showed an improved discrimination (AUC=0.77±0.02) compared to evaluation of DS alone (AUC=0.67 [95%CI 0.57–0.76]) (**Supplemental Figure 3**). Other measures of diagnostic performance were also comparable to the results of the full sample (**Supplement Table 1**).

Discussion

In the current study, we aimed to evaluate the added value of resting CCTA LVM deep learning analysis over coronary DS evaluation only, for identification of patients with functionally significant coronary artery stenosis. We demonstrated that the combination of DS with DL analysis of the LVM in intermediate-degree coronary stenosis improves the specificity of CCTA in comparison to evaluation of the DS alone.

Visual determination of the DS from CCTA is a highly sensitive and established diagnostic tool for evaluation of patients with chest pain of suspected coronary origin. However, CCTA presently lacks specificity for identifying the functional significance of coronary stenosis [1, 2]. A tiered approach with subsequent functional testing (e.g., stress myocardial perfusion imaging) can reduce the number of patients undergoing ICA [26]. However, this approach mandates additional diagnostic testing before deciding on the necessity for PCI. Here, we propose combining evaluation of DS with LVM DL analysis to improve the specificity of CCTA. The combined evaluation has the potential to avoid additional examinations because analysis is performed on the already acquired CCTA images.

Analysis of the LVM on resting CCTA has been previously studied. Two studies evaluated resting dual-energy CT for the detection of perfusion defects confirmed by ≥50% stenosis at ICA [15, 16]. They found a slight decrease in sensitivity (79–90%) and increase in specificity (86–92%) compared to ≥50% DS on CCTA only (82–98% and 88–91%, respectively). Osawa et al [10] visually evaluated perfusion of the LVM in all cardiac phases from a retrospectively ECG-triggered scan at rest and compared their results with invasive FFR measurements. By combining this LVM analysis with DS, they found an incremental value (AUC=0.82) over CCTA alone (AUC=0.71), which is in line with our study. In two recent studies, machine

8

learning–approaches using expert-designed features for classifying patients with functionally significant stenosis were described [8, 9]. Xiong et al.[8] found a good discrimination for the detection of a perfusion defect (max. AUC = 0.73). However, in this study a stenosis degree of ≥50% DS on ICA was used as reference [8], and no FFR was performed, making a direct comparison with our results impossible. Han et al [9] used FFR as reference and described that their algorithm, combined with evaluation of DS, showed an added value (AUC = 0.75) over DS alone (AUC = 0.68) [9], which is closely in line with the findings in the present study. However, patients with intermediate DS comprised a minority of the subjects studied by Han et al [9] (33%, 82/252), whereas the present study consisted of a majority of intermediate stenosis (80%, 101/126) and was exclusively focused on the added value of DL in this most challenging patient category.

FFRct is another technique performed on resting CCTA that has shown promising results (AUC = 0.79–0.93) for the evaluation of functionally significant stenosis [5–7]. However, FFRct depends on lumen segmentations which can be challenging or impossible in patients with high density calcified plaque, motion or misalignment artefacts, and/or prior CABG or PCI [5–7]. Our proposed method may be less affected by these challenges as the analysis of intermediate stenosis is performed only on the LV myocardium. Results of the present study underscore the need to look beyond the coronary arteries in the quest to improve specificity of CCTA. A recent systematic review by Cook et al [27] found that FFRct has a lower diagnostic performance with FFRct values around the cut point (0.7–0.8). In addition, patients with physiologically intermediate lesions (invasive FFR 0.7–0.8) comprised only a small minority of all the patients studied (12.8%) with a median FFR of 0.88, indicating a focus on patients with milder disease. In the current study, nearly three times as many patients (36.5%, 46/126) had physiologically intermediate lesions, and median FFR was 0.78, indicating a more diseased population. This supports the notion that the value of additional analysis of the myocardium is likely to be highest in patients with intermediate stenosis. However, a limitation of the present study is that results are only available on a patient basis; therefore, no indication could be given as to which stenosis was functionally significant, while FFRct has the ability to evaluate functional significance of a stenosis on a vessel basis. It is likely that a combined approach using both techniques will lead to further increase in specificity for identifying flow-limiting lesions in patients with intermediate-degree stenosis at CCTA.

DL algorithms are able to learn new complex patterns and relationships directly from the images without prior specification of which image features represent presence

of disease. Therefore, DL may be more sensitive to subtle changes in the LVM caused by functionally significant stenosis, which can be difficult to detect by a human observer [19, 20]. In spite of excellent performance of deep learning techniques demonstrated in many medical image analysis tasks, their interpretability is very limited, and we do not yet fully understand their inner working [19, 28]. Also in this work, even though the extracted encodings are relevant in representing LVM (**Supplemental Figure 1**), they are not readily interpretable. As distinct combinations of encodings represent different LVM appearances (e.g., normal vs. thin), specific encodings do not correspond to specific physical appearances. This prevented us from interpreting, visualizing, and localizing differences within the LVM for patients with significant stenosis. Future work might address these limitations [19, 28].

This study has limitations. First, the retrospective single-centre study design has to be taken into account. This could have induced selection bias as CT could have been the reason for referral to invasive FFR. In addition, because of this bias, the study group consisted of patients with high Agatston scores and a high prevalence of stenosis and extensive CAD with mainly intermediate stenosis (n = 101/126). Due to blooming, calcified plaques are known to cause overestimation of DS and thereby decrease specificity [29]. In addition, as reported in prior studies [2, 3], DS on CCTA showed high diagnostic accuracy for low- and high-grade stenosis (≤24% and ≥70%), which decreased when evaluating intermediate-degree stenosis (25–69%). This is reflected in the low specificity for DS only on CCTA found in the current study (31.1%) compared to reported in literature (40–83%) [1–3]. Second, maximum DS for each coronary artery was visually categorized, and no continuous quantitative measurements were performed. Although continuous quantitative measurements would allow for a more accurate way to evaluate diagnostic accuracy of DS, this is not regularly performed in clinical practice and was therefore not performed. Third, in the current study, no comparison with another type of functional assessment was performed (e.g., FFRct or visual assessment of myocardial perfusion), thereby limiting the evaluation of the added value of the current method compared to other available methods. Fourth, we used equipment of one single vendor and results may therefore be limited to this vendor. A final limitation is the relative small patient cohort and unbalanced dataset, which can introduce bias in performance. Although we performed 50 repetitions of 10-fold cross-validation experiments with randomization after each repetition, results may still be partially affected by coincidental findings. Analysis on a separate patient cohort as well as prospective studies needs to be performed to assess whether the found correlation also implies causation. Future work will address these limitations.

**8**

In conclusion, combining assessment of degree of stenosis with DL analysis of the LVM may result in improved diagnostic performance for identification of patients with functionally significant coronary artery stenosis. Future research is warranted to evaluate this approach on patients with low pre-test probability of obstructive coronary disease, more clinically encountered at CCTA.

8

References

1.   Budoff MJ, Dowe D, Jollis JG, et al (2008) Diagnostic Performance of 64-Multidetector Row Coronary Computed Tomographic Angiography for Evaluation of Coronary Artery Stenosis in Individuals Without Known Coronary Artery Disease. J Am Coll Cardiol 52:1724–1732. doi: 10.1016/j.jacc.2008.07.031

2.   Meijboom WB, Van Mieghem CAG, van Pelt N, et al (2008) Comprehensive assessment of coronary artery stenoses: computed tomography coronary angiography versus conventional coronary angiography and correlation with fractional flow reserve in patients with stable angina. J Am Coll Cardiol 52:636–43. doi: 10.1016/j.jacc.2008.05.024

3.   Ko BS, Wong DTL, Cameron JD, et al (2014) 320-row CT coronary angiography predicts freedom from revascularisation and acts as a gatekeeper to defer invasive angiography in stable coronary artery disease: a fractional flow reserve-correlated study. Eur Radiol 24:738–747. doi: 10.1007/s00330-013-3059-8

4.   Tonino PAL, De Bruyne B, Pijls NHJ, et al (2009) Fractional Flow Reserve versus Angiography for Guiding Percutaneous Coronary Intervention. N Engl J Med 360:213–224. doi: 10.1056/NEJMoa0807611

5.   Tesche C, De Cecco CN, Albrecht MH, et al (2017) Coronary CT Angiography–derived Fractional Flow Reserve. Radiology 285:17–33. doi: 10.1148/radiol.2017162641

6.   Norgaard BL, Leipsic J, Gaur S, et al (2014) Diagnostic Performance of Noninvasive Fractional Flow Reserve Derived From Coronary Computed Tomography Angiography in Suspected Coronary Artery Disease The NXT Trial (Analysis of Coronary Blood Flow Using CT Angiography: Next Steps). J Am Coll Cardiol 63:1145–1155. doi: Doi 10.1016/J.Jacc.2013.11.043

7.   Koo B-K, Erglis A, Doh J-H, et al (2011) Diagnosis of ischemia-causing coronary stenoses by noninvasive fractional flow reserve computed from coronary computed tomographic angiograms. Results from the prospective multicenter DISCOVER-FLOW (Diagnosis of Ischemia-Causing Stenoses Obtained Via Noni. J Am Coll Cardiol 58:1989–97. doi: 10.1016/j.jacc.2011.06.066

8.   Xiong G, Kola D, Heo R, et al (2015) Myocardial perfusion analysis in cardiac computed tomography angiographic images at rest. Med Image Anal 24:77–89. doi: 10.1016/j.media.2015.05.010

9.   Han D, Lee JH, Rizvi A, et al (2018) Incremental role of resting myocardial computed tomography perfusion for predicting physiologically significant coronary artery disease: A machine learning approach. J Nucl Cardiol 25:223–233. doi: 10.1007/s12350-017-0834-y

10. Osawa K, Miyoshi T, Miki T, et al (2016) Diagnostic Performance of First-Pass Myocardial Perfusion Imaging without Stress with Computed Tomography (CT) Compared with Coronary CT Angiography Alone, with Fractional Flow Reserve as the Reference Standard. PLoS One 11:e0149170. doi: 10.1371/journal.pone.0149170

11. Branch KR, Busey J, Mitsumori LM, et al (2013) Diagnostic performance of resting CT myocardial perfusion in patients with possible acute coronary syndrome. AJR Am J Roentgenol 200:W450-7. doi: 10.2214/AJR.12.8934

12. Pursnani A, Lee AM, Mayrhofer T, et al (2015) Early Resting Myocardial Computed Tomography Perfusion for the Detection of Acute Coronary Syndrome in Patients With Coronary Artery Disease. Circ Cardiovasc Imaging 8:e002404–e002404. doi: 10.1161/CIRCIMAGING.114.002404

13. Zreik M, Lessmann N, van Hamersvelt RW, et al (2018) Deep learning analysis of the myocardium in coronary CT angiography for identification of patients with functionally significant coronary artery stenosis. Med Image Anal 44:72–85. doi: 10.1016/j.media.2017.11.008

14. Mannil M, von Spiczak J, Manka R, Alkadhi H (2018) Texture Analysis and Machine Learning for Detecting Myocardial Infarction in Noncontrast Low-Dose Computed Tomography. Invest Radiol 53:338–343. doi: 10.1097/RLI.0000000000000448

8

15. Ruzsics B, Lee H, Zwerner PL, et al (2008) Dual-energy CT of the heart for diagnosing coronary artery stenosis and myocardial ischemia-initial experience. Eur Radiol 18:2414–24. doi: 10.1007/s00330-008-1022-x

16. Wang R, Yu W, Wang Y, et al (2011) Incremental value of dual-energy CT to coronary CT angiography for the detection of significant coronary stenosis: comparison with quantitative coronary angiography and single photon emission computed tomography. Int J Cardiovasc Imaging 27:647–56. doi: 10.1007/s10554-011-9881-7

17. Ko BS, Cameron JD, Meredith IT, et al (2012) Computed tomography stress myocardial perfusion imaging in patients considered for revascularization: a comparison with fractional flow reserve. Eur Heart J 33:67–77. doi: 10.1093/eurheartj/ehr268

18. Ko BS, Cameron JD, Leung M, et al (2012) Combined CT Coronary Angiography and Stress Myocardial Perfusion Imaging for Hemodynamically Significant Stenoses in Patients With Suspected Coronary Artery Disease. JACC Cardiovasc Imaging 5:1097–1111. doi: 10.1016/j.jcmg.2012.09.004

19. Shen D, Wu G, Suk H-I (2017) Deep Learning in Medical Image Analysis. Annu Rev Biomed Eng 19:221–248. doi: 10.1146/annurev-bioeng-071516-044442

20. Shah SJ, Katz DH, Selvaraj S, et al (2015) Phenomapping for Novel Classification of Heart Failure With Preserved Ejection Fraction. Circulation 131:269–279. doi: 10.1161/CIRCULATIONAHA.114.010637

21. Abadi S, Roguin A, Engel A, Lessick J (2010) Feasibility of automatic assessment of four-chamber cardiac function with MDCT: Initial clinical application and validation. Eur J Radiol 74:175–81. doi: 10.1016/j.ejrad.2009.01.035

22. Abbara S, Blanke P, Maroules CD, et al (2016) SCCT guidelines for the performance and acquisition of coronary computed tomographic angiography: A report of the society of Cardiovascular Computed Tomography Guidelines Committee: Endorsed by the North American Society for Cardiovascular Imaging (NASCI). J Cardiovasc Comput Tomogr 10:435–449. doi: 10.1016/j.jcct.2016.10.002

23. Leipsic J, Abbara S, Achenbach S, et al (2014) SCCT guidelines for the interpretation and reporting of coronary CT angiography: A report of the Society of Cardiovascular Computed Tomography Guidelines Committee. J Cardiovasc Comput Tomogr 8:342–358. doi: 10.1016/j.jcct.2014.07.003

24. Cury RC, Abbara S, Achenbach S, et al (2016) CAD-RADSTM Coronary Artery Disease – Reporting and Data System. An expert consensus document of the Society of Cardiovascular Computed Tomography (SCCT), the American College of Radiology (ACR) and the North American Society for Cardiovascular Imaging (NASCI). Endorsed by the American College of Cardiology. J Cardiovasc Comput Tomogr 10:269–281. doi: 10.1016/j.jcct.2016.04.005

25. Authors/Task Force members, Windecker S, Kolh P, et al (2014) 2014 ESC/EACTS Guidelines on myocardial revascularization. Eur Heart J 35:2541–2619. doi: 10.1093/eurheartj/ehu278

26. Takx RAP, Blomberg BA, Aidi HE, et al (2015) Diagnostic Accuracy of Stress Myocardial Perfusion Imaging Compared to Invasive Coronary Angiography With Fractional Flow Reserve Meta-Analysis. Circ Cardiovasc Imaging 8:e002666–e002666. doi: 10.1161/CIRCIMAGING.114.002666

27. Cook CM, Petraco R, Shun-Shin MJ, et al (2017) Diagnostic Accuracy of Computed Tomography–Derived Fractional Flow Reserve. JAMA Cardiol 2:803. doi: 10.1001/jamacardio.2017.1314

28. Zeiler MD, Fergus R (2014) Visualizing and Understanding Convolutional Networks. In: Fleet D, Pajdla T, Schiele B, Tuytelaars T (eds) Computer Vision – ECCV 2014: 13th European Conference, Zurich, Switzerland, September 6-12, 2014, Proceedings, Part I. Springer International Publishing, Cham, pp 818–833

29. Sarwar A, Rieber J, Mooyaart EAQ, et al (2008) Calcified plaque: measurement of area at thin-section flat-panel CT and 64-section multidetector CT and comparison with histopathologic findings. Radiology 249:301–6. doi: 10.1148/radiol.2483072003

8

Supplementary material
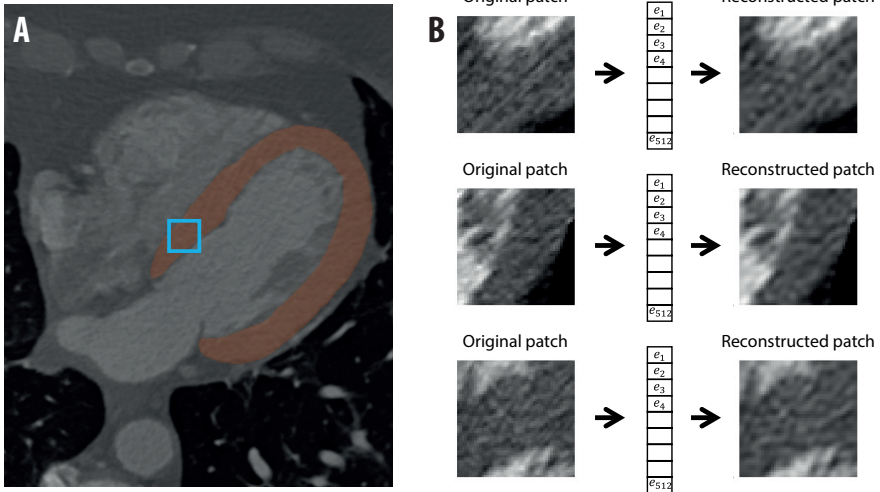
Supplement Figure 1 Encoding the LVM in the DL method using a convolutional auto-encoder. Because the discriminative features of the LVM for functionally significant stenosis on CCTA at rest are not well-defined, we applied an unsupervised approach using a convolutional auto-encoder (CAE). Unlike most studies, where features were designed by hand, in the current study features were based on the encodings extracted in an unsupervised fashion by the DL method using a CAE. To ensure that these encodings represent the myocardium and not another random organ or structure, only small local image patches of the segmented myocardium (**A**) were introduced to the CAE and thereafter encoded (**B**). All voxels of the segmented myocardium in all slices were encoded by the CAE using patches around them, as illustrated by an example patch (blue box) in **A**. To ensure that the extracted encodings would be relevant in representing the myocardial patches, the CAE was trained by forcing it to reconstruct (decode) the input myocardium patches using only these encodings, as illustrated by three randomly selected patches in **B**. To train the CAE, the input myocardial patches were compressed (encoded) to N = 512 values (encodings) and reconstructed (decoded) back. The mean squared error between the input patches and the reconstructed patches was computed during training and minimized iteratively. This minimization forced the encodings to contain relevant information; successfully representing the myocardium appearance.

8

A

Test	AUC
LVM DL	0.647±0.0

B

Test	AUC
LVM DL	0.652±0.027
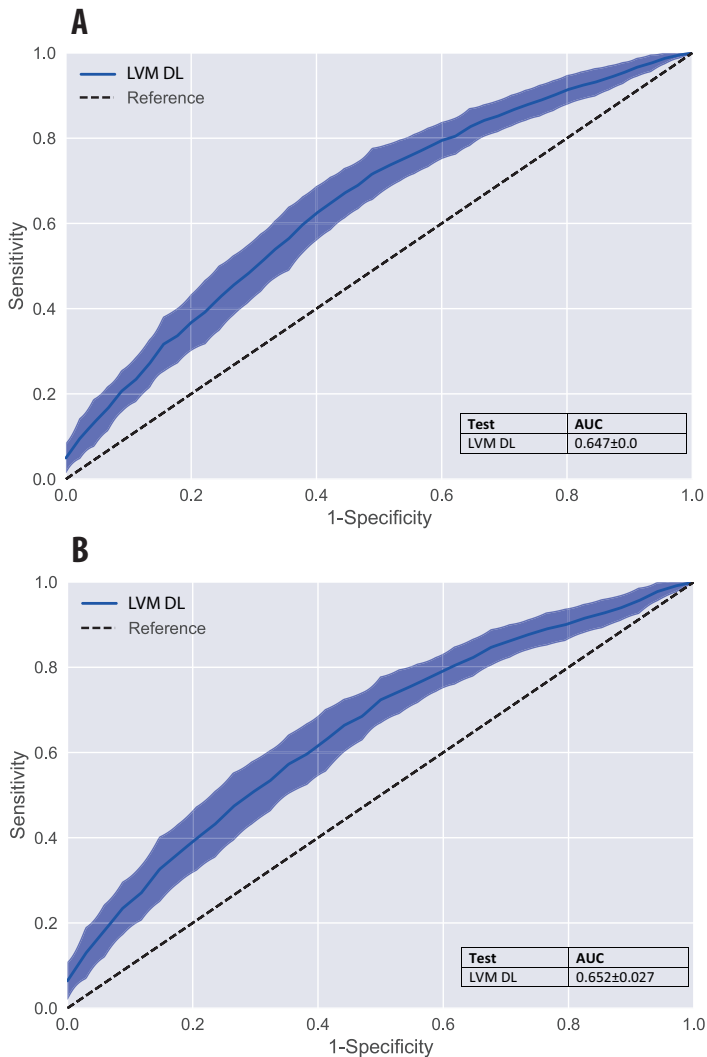
Supplement Figure 2 Receiver operating characteristic curves of DL applied to all patients **(A**, n = 126) and patients with intermediate stenosis only (**B**, n = 101). To evaluate robustness of the DL analysis on low- or high-grade stenosis, we also evaluated the performance of our DL algorithm on the complete cohort (n = 126). We retrained and evaluated the DL method on all 126 cases using the same scheme of 10-fold cross-validation with 50 repetitions. The resulting ROC curve and AUC are shown in **A**. These results are comparable with the performance of DL on the intermediate stenosis only (n = 101), used in the current study and shown in **B**. This indicates that comparable discriminative power (but also comparable misclassification) are achieved by the DL algorithm, regardless of the population. However, it should be noted that the entire dataset is obtained from a heavily diseased patient cohort, and thus none of these patients are considered as an "easy case" for classification. *AUC = area under the receiver operating characteristic curve; DL = deep learning; LVM = left ventricular myocardium; ROC = receiver operating characteristic*
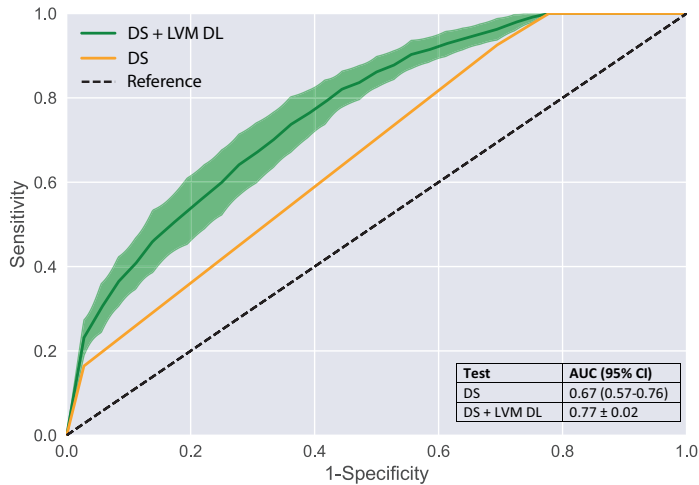
Supplement Figure 3 Receiver operating characteristic curves for patients without prior MI, CABG and/ or PCI (n = 103). Diagnostic performance of DS and a combination of DL added to DS from CCTA for predicting functionally significant stenosis on a patient basis. For the combined method, ROC-curves and AUC are depicted as average ± SD of 50 cross-validation experiments. *AUC = area under the receiver operating characteristic curve; CABG = coronary artery bypass grafting; CCTA = coronary computed tomography angiography; DL = deep learning; DS = degree of stenosis; LVM = left ventricular myocardium; MI = myocardial infarction; PCI = percutaneous coronary intervention; ROC = receiver operating characteristic*

**Supplement Table 1** Diagnostic performance for patients without prior MI, CABG and/or PCI (n = 103).

Method and threshold	Sensitivity (%)	Specificity (%)	PPV (%)	NPV (%)	Accuracy (%)	AUC
CCTA ≥25% DS	100.0 (67/67) [94.6-100.0]	22.2 (8/36) [10.1-39.2]	70.5 (67/95) [66.8-74.0]	100.0 (8/8) [100.0-100.0]	72.8 (75/103) [64.1-81.6]	0.67 [0.57-0.76]
CCTA ≥50% DS	92.5 (62/67) [83.4-97.5]	30.6 (11/36) [16.3-48.1]	71.3 (62/87) [66.4-75.7]	68.8 (11/16) [45.3-85.4]	70.9 (73/103) [62.0-79.8]	0.67 [0.57-0.76]
CCTA ≥70% DS	16.4 (11/67) [8.5-27.5]	97.2 (35/36) [85.5-99.9]	91.7 (11/12) [59.7-98.8]	38.5 (35/91) [35.7-41.3]	44.7 (46/103) [34.9-54.4]	0.67 [0.57-0.76]
CCTA DS + DL combined	84.8 ± 0.04	50.5 ± 0.04	76.1 ± 0.02	64.5 ± 0.05	72.8 ± 0.02	0.77 ± 0.02

Data is given in percentage, data in parentheses is raw data and data in brackets is 95% confidence interval. For the combined method, data is depicted as average ± SD of 50 cross-validation experiments. *AUC = area under the receiver operating characteristic curve; CABG = coronary artery bypass grafting; CCTA = coronary computed tomography angiography; DL = deep learning; DS = degree of stenosis; LVM = left ventricular myocardium; MI = myocardial infarction; NPV = negative predictive value; PCI = percutaneous coronary intervention; PPV = positive predictive value; SD = standard deviation*
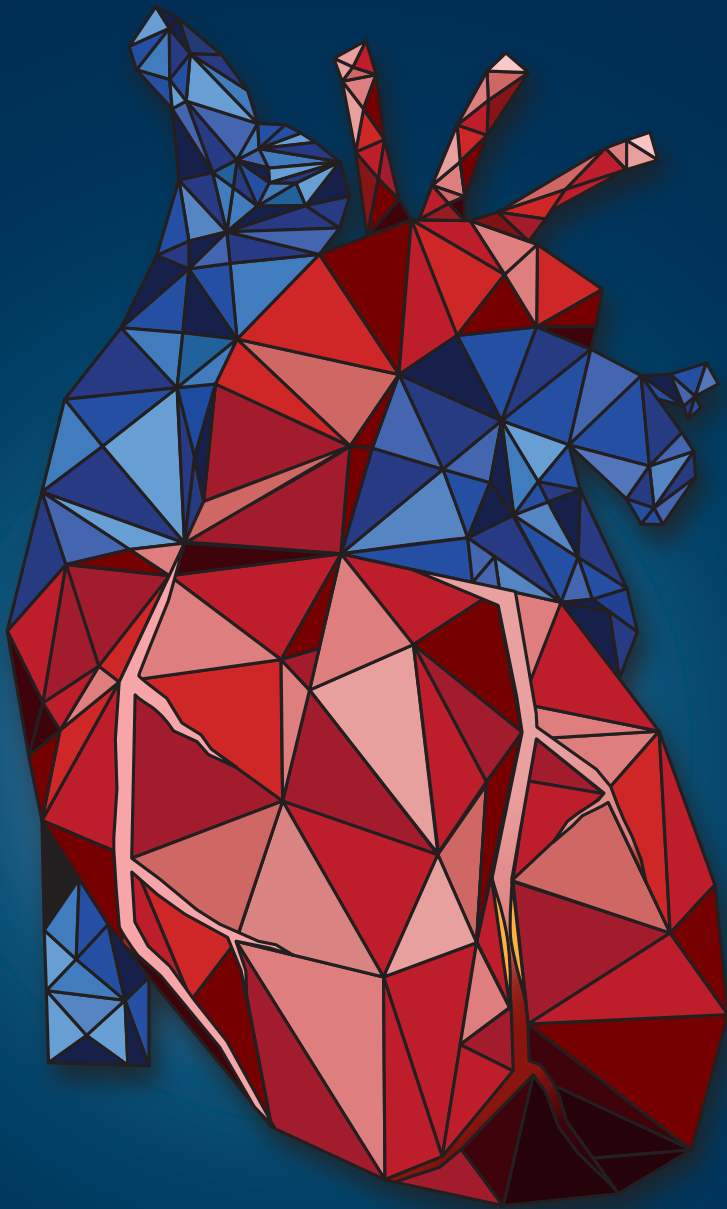
Part IV

Rationale for comprehensive dual-energy CT imaging of coronary artery disease
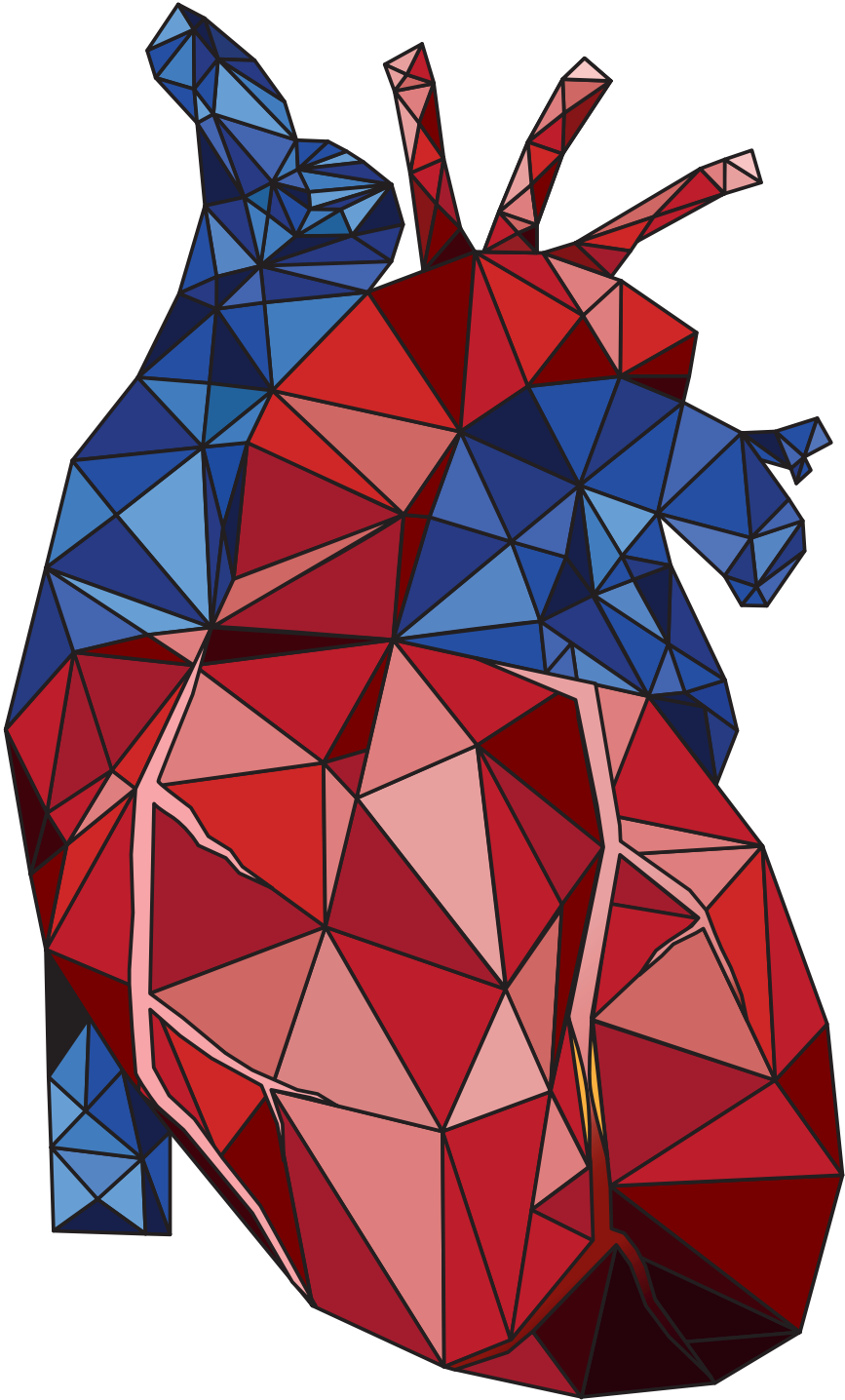
Chapter 9

Application of speCtraL computed tomogrAphy to impRove specIficity of cardiac compuTed tomographY (CLARITY study): Rationale and design

Robbert W. van Hamersvelt
Ivana Išgum
Pim A. de Jong
Maarten J. Cramer
Geert E. Leenders
Martin J. Willemink
Michiel Voskuil
Tim Leiner

Abstract

Introduction

Anatomic stenosis evaluation on coronary computed tomography angiography (CCTA) lacks specificity in indicating the functional significance of a stenosis. Recent developments in CT techniques (including dual-layer spectral detector CT (SDCT) and static stress CT perfusion (CTP)) and image analyses (including fractional flow reserve (FFR) derived from CCTA images (FFR_{CT}) and deep learning analysis (DL)) are potential strategies to increase the specificity of CCTA by combining both anatomical and functional information in one investigation. The aim of the current study is to assess the diagnostic performance of (combinations of) SDCT, CTP, FFR_{CT}, and DL for the identification of functionally significant coronary artery stenosis.

Methods and analysis

Seventy-five patients aged 18 years and older with stable angina and known coronary artery disease and scheduled to undergo clinically indicated invasive FFR will be enrolled. All subjects will undergo the following SDCT-scans: coronary calcium scoring, static stress CTP, rest CCTA, and if indicated (history of myocardial infarction) a delayed enhancement acquisition. Invasive FFR of ≤0.80, measured within 30 days after the SDCT scans, will be used as reference to indicate a functionally significant stenosis. The primary study endpoint is the diagnostic performance of SDCT (including CTP) for the identification of functionally significant coronary artery stenosis. Secondary study endpoint is the diagnostic performance of SDCT, CTP, FFR_{CT} and DL separately and combined for the identification of functionally significant coronary artery stenosis.

9

Introduction

Anatomic evaluation of luminal stenosis on coronary computed tomography angiography (CCTA) has high diagnostic performance to detect and rule out coronary artery disease [1–3]. However, it lacks specificity in indicating the extent of myocardial ischemia caused by a stenosis, especially in the presence of calcified lesions, due to volume artefacts caused by blooming [1–3]. Invasively measured fractional flow reserve (FFR) is currently used to identify functionally significant coronary artery lesions and to guide revascularization treatment [4]. Results of the ISCHEMIA trial (NCT01471522) are awaited to shed light on the ongoing discussion concerning outcomes with revascularization based only on ischemia. Until these results are published, cardiac CT is the single modality able to simultaneously evaluate coronary artery anatomy and functional information in one investigation non-invasively. Recent developments in CT acquisition and image analysis techniques, such as dual-energy CT (DECT), static stress CT perfusion imaging (CTP), FFR derived from CCTA images (FFR_{CT}), and deep learning (DL) based image analysis have shown the potential to improve the specificity of CCTA by combining both anatomical and functional information in one investigation [5–11].

Dual-layer spectral detector computed tomography (SDCT) is a DECT system with one X-ray tube and a dual-layer detector, which separately detects low and high energy photons. In this way, there is no time delay between the acquisitions of the different energy levels resulting in temporally co-registered dual-energy data. Also, the acquired images are spatially co-registered, making this DECT technique ideal for imaging a moving heart [12]. In addition, by combining the information from both detector layers a conventional image can be reconstructed [13]. Virtual mono-energetic images (40-200 keV) reconstructed from the SDCT may reduce blooming and beam-hardening artefacts and increase in-stent lumen visibility [14, 15]. A plaque specific mono-energetic level can be applied to improve detection and quantification of coronary plaques [16]. Together with the opportunity to assess myocardial iodine distribution and quantification in both rest and static stress images [9, 17], SDCT may allow for improved anatomical and functional evaluation.

9

For FFR_{CT}, the coronary lumen is segmented on CCTA images and assessed by algorithms based on fluid dynamics, lumped parameter models, or machine learning [5, 6]. In this way, FFR_{CT} is able to evaluate the functional significance of stenosis and has shown to improve diagnostic performance of CT [5, 6]. With SDCT, a plaque specific mono-energetic level can be applied to improve lumen segmentation and the performance of FFR_{CT}.

Deep learning is a machine learning based approach that has been shown to outperform other image analysis approaches in a wide variety of medical image analysis tasks [18]. One of these tasks include segmentation and detection analysis of cardiac CT [11, 18, 19]. The growing amount of data generated by new CT acquisition techniques (e.g. SDCT and CTP) makes deep learning analysis a technique of high interest. A recent study showed that patients with functionally significant coronary artery stenosis can be identified using DL analysis on CCTA [11]. By combining these new technologies (SDCT, CTP, FFR_{CT}, and DL), we hypothesize more accurate information will be available about the coronary anatomy, degree of stenosis, FFR_{CT} and myocardial perfusion, thereby contributing to a higher specificity of CT for identification of functionally significant coronary artery stenosis. To test this hypothesis, we have designed the CLARITY study (Application of speCtraL computed tomogrAphy to impRove specIficity of cardiac compuTed tomographY). This paper describes the methods, rationale and design of the study.

Materials and Methods

Study design

The CLARITY study is a prospective mono-centre diagnostic study designed to assess the accuracy of SDCT, CTP, FFR_{CT}, and DL-based image analysis as a non-invasive way for the identification of functionally significant coronary artery stenosis, using invasive FFR as the standard of reference. Combinations of multiple new CT acquisition techniques (i.e. SDCT and CTP) and image analysis techniques (i.e. FFR_{CT} and DL) will be investigated to evaluate the optimal diagnostic performance of SDCT for the identification of functionally significant coronary artery stenosis. The study is registered at clinicaltrials.gov under identifier: NCT03139006.

Study objectives

The primary study objective is to assess the diagnostic performance of SDCT (including CTP) for the identification of functionally significant coronary artery stenosis in patients with stable angina and known coronary artery disease, using invasive FFR as the standard of reference in a patient-based analysis. The secondary objective is to assess diagnostic performance of SDCT, CTP, FFR_{CT} and DL separately and combined for the identification of functionally significant coronary artery stenosis in patients with stable angina and known coronary artery disease, using invasive FFR as the standard of reference in a vessel- and patient-based analysis. The tertiary objective is to investigate if and to what extent SDCT can decrease the degree of blooming and beam-hardening artefacts of calcifications.

9

Ethical considerations

The study protocol was reviewed and approved by the institutional review board of the University Medical Centre Utrecht (NL55917.041.16). In addition, the radiation safety committee approved this study. Patients will only be included in the study after informed consent is signed.

Targeted population

Patients aged 18 years and older with stable angina and known coronary artery disease and scheduled to undergo clinically indicated invasive FFR are eligible for inclusion. Further inclusion and exclusion criteria are described in **Table 1**. Due to the high negative predictive value of CCTA, patients are usually referred to CCTA when the pre-test likelihood for obstructive coronary artery disease is <50% [20]. Because CCTA has a moderate specificity in indicating the functional significance of a stenosis, it is not (yet) recommended for patients with pre-test likelihood higher than 50% [20]. Because we are interested in increasing the specificity of CCTA, we have chosen to include patients with stable angina and known coronary artery disease.

Table 1 Inclusion and exclusion criteria.

Inclusion criteria	Exclusion criteria
Age ≥18 years	Subjects who because of age, general medical or psychiatric condition, or physiologic status cannot give valid informed consent or tolerate the coronary CTA examination
Stable angina and known coronary artery disease	
Scheduled to undergo clinically indicated invasive FFR	Subjects with (severe) renal insufficiency, indicated as glomerular filtration rate (GFR) <60 ml/min
Willing and able to give informed consent	Subjects with unknown GFR or obtained >3 months before the planned scan
	Contraindication or allergy to intravenous iodinated contrast agent
	Subjects who participate in another study with radiation which is estimated to be in risk category III (ICRP 103) [28]
	Subjects who are pregnant
	Subjects with contraindications to cardiac CT and/or intravenous contrast, intravenous adenosine, beta blockers or nitroglycerine

CTA = computed tomography angiography; GFR = glomerular filtration rate; ICRP = international commission on radiological protection; FFR = fractional flow reserve

9

Patient and public involvement

Neither patients nor the public were involved in the design of the study, development of the research question and deciding on the outcome measures. At inclusion, patients are asked if they would like to receive results of the study at group level. After completion of the study, results will be disseminated through a report to the patients who wish to receive information about the study.

Sample size calculation

To allow for evaluation of sensitivity and specificity within our study population, the proportions of cases (FFR ≤0.80) and controls (FFR >0.8) in our sample should take the prevalence of disease into account. Internal research of patient records of the past 3 years showed that 50% of the patients who underwent invasive FFR had at least one positive FFR measurement (FFR ≤0.80). With a prevalence of 0.5, the proportion of cases to controls is 1, indicating that the same amount of cases and controls is required. The main goal of the CLARITY study is to increase the specificity of SDCT (including CTP) for the identification of functionally significant coronary artery stenosis. In the targeted population, the sensitivity and specificity of CCTA are currently around 95% and 50%, respectively [1–3]. Using SDCT (including CTP), we aim to increase the specificity from 50% to 85% [21–23]. Raising the lower limit of the 95% confidence interval for specificity from a typical value of 35% to 60%, necessitates inclusion of at least 66 patients (33 cases and 33 controls) [24]. However, this should not come at a too high cost in sensitivity. Using SDCT (including CTP), we expect a sensitivity around 90% with a lower limit of the 95% confidence interval of 65% [21–23], which necessitates inclusion of at least 62 patients (31 cases and 31 controls) [24]. Because we are interested in both the sensitivity and specificity we take the largest number of patients of the two calculated sample sizes (n = 66). To account for attrition, 75 patients will be included. Our internal research also showed that in most cases FFR is measured in more than one vessel, with an average of 1.6 vessels per patient. Thus, for evaluation on a vessel basis, the amount of measurements is expected to be around 120 individual measurements.

Patient recruitment and evaluation

Upon fulfilment of the eligibility criteria, patients are asked for participation in the study by their treating physician. After signing informed consent, each study participant will undergo a dedicated CT protocol on a SDCT system before undergoing the clinically indicated invasive FFR measurement. Patients are asked to refrain from coffee consumption from 24 hours prior to imaging. For each patient a case report form will be filled in, including information from the SDCT scans,

9

invasive FFR measurement(s), and baseline characteristics such as age, gender, medical history, cardiovascular risk factors, and demographic information.

SDCT protocol

All CT acquisitions will be performed using a 64-slice SDCT scanner (IQon Spectral CT, Philips Healthcare, Best, The Netherlands) with 64 x 0.625 mm collimation. All patients will undergo coronary calcium scoring (CCS), adenosine induced static stress CTP scan, and rest CCTA scan. In case of a history of myocardial infarction, an additional late phase acquisition will be performed for myocardial scar detection. An overview of the scan protocol is shown in **Figure 1**. All acquisitions will be performed according to dedicated guidelines [25]. As contrast agent, 300 mg I/ml Iopromide (Ultravist 300, Bayer Healthcare, Berlin, Germany) will be used. For all scans both conventional and spectral based images will be reconstructed, which allows accessing dual-energy CT options. All images will be analysed using a dedicated workstation (IntelliSpace Portal, Philips Healthcare, Best, The Netherlands).
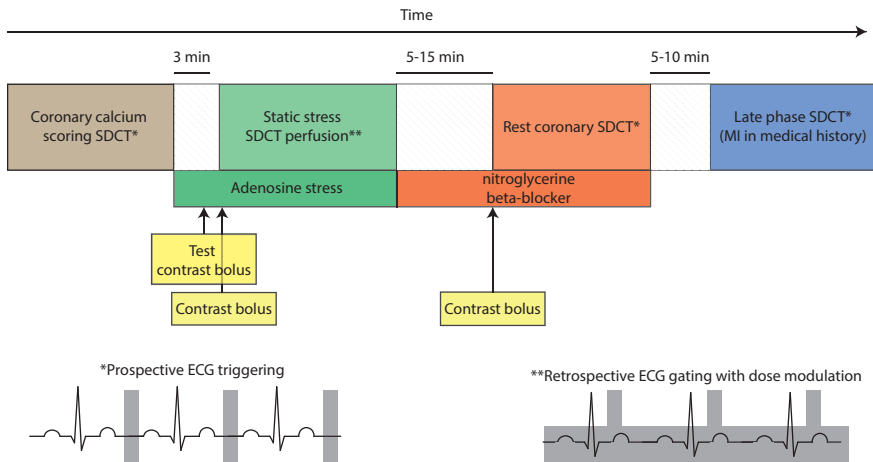
Figure 1 SDCT scan protocol. *MI = myocardial infarction; SDCT = dual-layer spectral detector computed tomography*

9

Coronary calcium scoring

Acquisitions will be made using a prospectively electrocardiography (ECG)-triggered (78% R-R interval) protocol ("Step & Shoot Cardiac") at 120 kVp and 40 mAs. Images will be reconstructed with 3 mm slice thickness and 3 mm increment

using iterative reconstruction. Coronary calcifications will be quantified with Agatston scores using commercially available software (HeartBeat CS, IntelliSpace Portal, Philips Healthcare, Best, The Netherlands).

Static stress CTP

Upon completion of CCS, stress will be induced using intravenous adenosine injection (140 μg/kg/min). After 3 minutes of adenosine injection a test bolus with 10 ml iodinated contrast will be given and flushed with 20 ml saline at a flow rate of 4.5 ml/s (<80 kg) or 5 ml/s (≥80 kg). From this test bolus a patient specific optimal scan delay is obtained by placing a region of interest (ROI) in the ascending aorta to determine the time to peak, after which an additional 4 seconds are added. Subsequently, the contrast agent will be administered using 71 ml at 4.5 ml/s (<80 kg) or 85 ml at 5 ml/s (≥80 kg) and flushed with 50 ml saline at the same flow rate. After the predefined patient specific optimal scan delay, and still under peak adenosine stress, a retrospectively ECG-gated single CTP scan is acquired in helical mode. The scan is obtained using 120 kVp with cardiac dose modulation for the mAs (reference 270 mAs), with highest mAs at end systolic phase (45% R-R interval) and reduced mAs during the other phases. Directly after the acquisition, the adenosine injection will be stopped. Images will be reconstructed in steps of 10% from 0 to 90% of the R-R interval with 0.9 mm slice thickness and 0.45 mm increment using iterative reconstruction. The myocardium will be evaluated using 5 mm multiplanar reformatted images in short axis and long axis view. Myocardial perfusion will be scored visually and quantitatively on conventional images, mono-energetic images, and iodine density images.

CCTA

After a pause of 5-15 minutes a resting CCTA will be performed. In accordance with the Society of Cardiovascular Computed Tomography (SCCT) guidelines [25], intravenous beta-blocker will be administered in patients with a heart rate above 60 beats per minute. In all patients, nitroglycerine 0.4 mg is administered sublingual. Iodinated contrast will be administered using the same amount and flow rate as for the stress scan. Seven seconds after a threshold of 100 Hounsfield Units (HU) is reached in the descending aorta, a CCTA scan is acquired using a prospectively ECG-triggered (78% R-R interval) protocol ("Step & Shoot Cardiac") at 120 kVp and 120 mAs. Images will be reconstructed with 0.9 mm slice thickness and 0.45 mm increment using iterative reconstruction. In accordance with SCCT guidelines [26, 27], the images (both conventional and mono-energetic) will be reported and assessed on image quality, plaque characteristics, and degree

9

of stenosis (categorized as 0%, 1-24%, 25-49%, 50-69%, 70-99%, and 100%). For anatomical evaluation of stenosis, ≥50% degree of stenosis will be used to indicate a significant stenosis. In addition to standard assessment, myocardial perfusion will be evaluated and compared to the static stress CTP.

Late phase non-contrast scan

In case a patient has a history of myocardial infarction an additional late phase non-contrast scan is made 5-10 minutes after the rest CCTA scan. This scan is acquired using a prospectively ECG-triggered (78% R-R interval) protocol ("Step & Shoot Cardiac") at 120 kVp and 100 mAs. Images will be reconstructed with 0.9 mm slice thickness and 0.45 mm increment using iterative reconstruction. The myocardium will be evaluated for late enhancement, both visually and quantitatively, using 5 mm multiplanar reformatted images in short axis and long axis view of the conventional, mono-energetic, and iodine density images.

Radiation dose estimation

The estimated radiation dose for the CT scans will be calculated by multiplying the dose length product (DLP) with the conversion coefficient for chest at 120 kVp (k = 0.0145 mSv/[mGy x cm]) [28]. The estimated radiation doses for CCS scan, static stress CTP, CCTA, and late phase scan are 0.9, 2.5-4.4, 2.5, and 2.2 mSv, respectively (**Table 2**). Cumulative radiation dose for the total SDCT protocol is estimated to be ≤10 mSv.

Table 2 Radiation dose estimation.

Type of scan	CTDIvol	DLP*	Estimated radiation dose**
Coronary calcium scoring	5	63	0.9 mSv
Static stress CTP scan	14-24***	175-300***	2.5-4.4 mSv***
Coronary CTA	14	175	2.5 mSv
Late phase non-contrast****	12	150	2.2 mSv
Total			5.9-10.0 mSv

* Calculated by CTDIvol x 12.5 cm; ** ICRP103 is used to calculate estimated radiation dose whereby the conversion coefficient of 0.0145 is multiplied by the DLP [28]; *** depending on weight
**** performed in case of a history of myocardial infarction. *CTDIvol = volume computed tomography dose index; DLP = dose length product; ICRP = international commission on radiological protection; mSv = millisievert*

9

ICA and invasive FFR

For clinical purpose, ICA with FFR measurement(s) will be performed in each patient within 30 days after the SDCT scan. Invasive FFR will be measured, under maximal

hyperaemia (intravenous adenosine injection (140 μg/kg/min)), by placing a pressure wire (PressureWire™ X guidewire, St. Jude Medical, St. Paul, Minnesota) distal to the stenosis. The FFR value will be calculated automatically by dividing the pressure measured distally from the stenosis using the pressure wire by the pressure proximally from the stenosis assessed with the guiding catheter. To allow for comparison with FFR_{CT}, the location of the invasive FFR measurement will be recorded. An FFR value of ≤0.80 will be used as reference standard to indicate a functionally significant stenosis. The FFR value will be blinded for the observers who will perform CT or FFR_{CT} readings. And outcome of the SDCT and image analyses will be blinded for the observer who performs the invasive FFR.

FFR_{CT}

FFR_{CT} analysis will be performed on resting CCTA images using a research prototype on-site FFR_{CT} method (FFR_{CT}, IntelliSpace Portal, Philips Healthcare, Best, The Netherlands). Coronary artery centreline and lumen will be automatically segmented and manually corrected by an expert. Subsequently, FFR_{CT} will be automatically calculated and simulated using these segmentations. FFR_{CT} will be performed on both conventional and mono-energetic images.

Deep learning analyses

Conventional and SDCT data generated from the different acquisitions will be used as input for the analysis of cardiac anatomy and function using deep learning. This analysis will include segmentation of anatomical structures of interest (e.g. myocardium, coronary arteries), detection and characterization of atherosclerotic plaque and perfusion defects, and subsequently identification of patients with functionally significant stenosis.

Study endpoints and data analysis

The primary study endpoint is the diagnostic performance of SDCT (including CTP) for the identification of functionally significant coronary artery stenosis defined as FFR ≤0.8. Anatomical evaluation of coronary stenosis will be performed on conventional CCTA images. These data will then be compared with data obtained from SDCT as described above. The secondary study endpoint is the diagnostic performance of SDCT, CTP, FFR_{CT} and DL separately and combined for the identification of functionally significant coronary artery stenosis defined as FFR ≤0.8. Diagnostic performance of anatomical evaluation of coronary stenosis, FFR_{CT}, CTP and DL will be evaluated separately using conventional CT reconstruction. Subsequently, the diagnostic performance of each technology including the use

9

of dual-energy CT options provided by SDCT (SDCT options) will be assessed separately. In this way, the results of each technique with and without the use of SDCT options can be evaluated and the added value of SDCT for each technique can be defined. Hereafter, FFR$_{CT}$, CTP and DL (including SDCT options) will be combined with anatomical information. First, degree of stenosis will be evaluated. If ≥25% degree of stenosis is present on CCTA (+SDCT options), further testing using either FFR$_{CT}$ (+SDCT options), CTP (+SDCT options) or DL (+SDCT options) will be used to indicate a functionally significant stenosis (**Figure 2**). The DL analysis will be performed on data generated from the different CT acquisitions. For combinations of acquisitions, the DL algorithm will automatically define to which extent the information of each acquisition is weighted in the model.

For both the primary and secondary objective, the accuracy, sensitivity, specificity, negative predictive value and positive predictive value will be calculated with 95% confidence intervals on a per-patient level (primary and secondary endpoint) and per-vessel level (secondary endpoint). Differences in diagnostic performance will be investigated using pairwise McNemar tests and area under the receiver-operating curve (AUC) analyses. A *P* value < 0.05 will be considered statistically significant.

The tertiary endpoint is evaluation of blooming and beam hardening artefacts of calcifications using SDCT compared to conventional CCTA. To determine the optimal virtual mono-energetic level at which calcium blooming and beam hardening is minimized and anatomy of the vessel is best visualized, degree of stenosis will be quantitatively scored at mono-energetic levels in steps of 10 (40-200 keV) and on conventional CCTA and compared to degree of stenosis at quantitative coronary angiography (QCA). The mono-energetic image with least difference in degree of stenosis compared to QCA is considered best. To determine the difference in blooming and beam hardening artefacts of calcifications, volumes of circumscribed calcifications will be measured with dedicated volume analysis software (HeartBeat CS, IntelliSpace Portal, Philips Healthcare, Best, The Netherlands). The percentage of volume measured on conventional CT minus the volume measured on the mono-energetic level with the least blooming (defined by the quantitative comparison with QCA) is considered as the degree of difference of blooming of calcifications. A paired T-Test (normally distributed data) or Wilcoxon signed rank test (non-normally distributed data) is used to assess significance of the degree of decrease in blooming. Categorical variables will be expressed as counts and percentages. The Shapiro-Wilk test will be used to identify normally distributed data. Continuous variables will be expressed as mean ± standard deviation (SD) for normally distributed data and as median with interquartile range for non-parametric data.

9

9
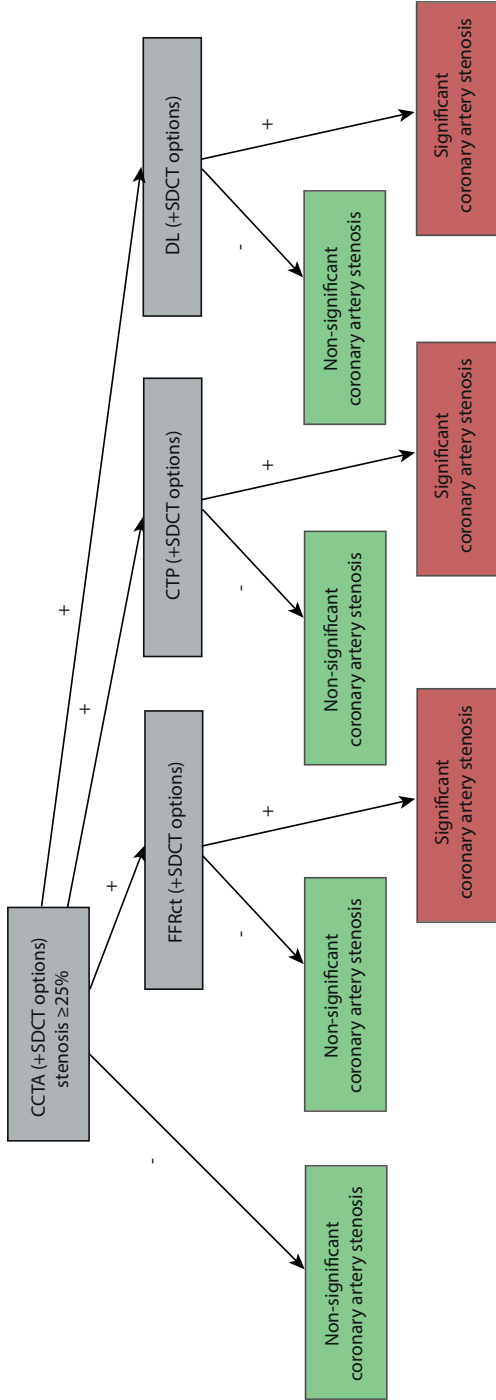
Figure 2 Flowchart of degree of stenosis analysis combined with FFR$_{CT}$, CTP and DL (including dual-energy CT options provided by SDCT). First, degree of stenosis will be evaluated. If ≥25% degree of stenosis is present, further testing using either FFR$_{CT}$, CTP, or DL will be used to indicate a functionally significant stenosis. *CCTA = coronary computed tomography angiography; CTP = static stress CT perfusion imaging; DL = deep learning; FFR$_{CT}$ = fractional flow reserve derived from coronary computed tomography angiography images; SDCT = dual-layer spectral detector computed tomography*

Discussion

The CLARITY study aims to evaluate the diagnostic performance of (combinations of) new CT acquisition techniques (SDCT and CTP) and image analysis techniques (FFR$_{CT}$ and DL) for the identification of functionally significant coronary artery stenosis. By analysing both anatomical and functional information, we hypothesize that the diagnostic performance of CT can be substantially improved. Multiple studies have demonstrated that assessment with FFR$_{CT}$ [5, 6], CTP [7–10], and image analysis exploiting DL [11] individually lead to improved diagnostic performance. By combining these techniques with assessment on mono-energetic and iodine density images, SDCT may allow for improved anatomical and functional evaluation. Each CT acquisition and image analysis technique has its own strengths and weaknesses. FFR$_{CT}$ can be performed on rest CCTA and thus does not require an additional scan. However, it can be challenging or even impossible in cases with high density calcified plaque, a stent in the vessel of interest or in the presence of motion or misalignment artefacts [5, 6]. With the use of SDCT, some of these challenges may be overcome by reduction of blooming and beam hardening artefacts [14–16]. Stress CTP on SDCT is less or not influenced by these factors and may potentially be more representative of perfusion defects, as it is acquired during stress [9]. On the other hand, stress CTP requires an additional scan and administration of adenosine, which increases radiation dose, risk and discomfort, which may be omitted if diagnostic performance is not superior to other techniques. DL-based image analysis may be able to gain insights into optimal combinations of information obtained from the different acquisitions. However, the number of patients in the current study is relatively low for deep learning based analysis, which may need to be addressed by designing new approaches for sparsely sampled data. We expect that the highest diagnostic value can be found in a combination of diagnostic tests. The CLARITY study will be the first to investigate the combinations of SDCT, CTP, FFR$_{CT}$, and DL-based image analysis for the identification of functionally significant stenosis. Because the study is monocentric and only patients scheduled to undergo clinically indicated invasive FFR are included, a potential limitation is selection bias. Therefore, the results of the current study will be applicable to a relatively specific population with stable angina and known coronary artery disease. Future studies will be needed to translate the findings of the CLARITY study to a patient cohort with low to intermediate pre-test likelihood for obstructive coronary artery disease, clinically more frequently encountered on CT.

9

The results of the CLARITY study will clarify to what extent SDCT, including CTP, and image analysis techniques can improve the specificity for the identification of functionally significant coronary artery stenosis. This could potentially help with clinical decision making and thereby decrease the number of patients unnecessary referred for invasive FFR.

9

References

1. Ko BS, Wong DTL, Cameron JD, et al (2014) 320-row CT coronary angiography predicts freedom from revascularisation and acts as a gatekeeper to defer invasive angiography in stable coronary artery disease: a fractional flow reserve-correlated study. Eur Radiol 24:738–747. doi: 10.1007/s00330-013-3059-8

2. Meijboom WB, Van Mieghem CAG, van Pelt N, et al (2008) Comprehensive Assessment of Coronary Artery Stenoses. Computed Tomography Coronary Angiography Versus Conventional Coronary Angiography and Correlation With Fractional Flow Reserve in Patients With Stable Angina. J Am Coll Cardiol 52:636–643. doi: 10.1016/j.jacc.2008.05.024

3. Rossi A, Papadopoulou S-L, Pugliese F, et al (2014) Quantitative Computed Tomographic Coronary Angiography: Does It Predict Functionally Significant Coronary Stenoses? Circ Cardiovasc Imaging 7:43–51. doi: 10.1161/CIRCIMAGING.112.000277

4. Tonino PAL, De Bruyne B, Pijls NHJ, et al (2009) Fractional Flow Reserve versus Angiography for Guiding Percutaneous Coronary Intervention. N Engl J Med 360:213–224. doi: 10.1056/NEJMoa0807611

5. Tesche C, De Cecco CN, Albrecht MH, et al (2017) Coronary CT Angiography–derived Fractional Flow Reserve. Radiology 285:17–33. doi: 10.1148/radiol.2017162641

6. Donnelly PM, Kolossváry M, Karády J, et al (2018) Experience With an On-Site Coronary Computed Tomography-Derived Fractional Flow Reserve Algorithm for the Assessment of Intermediate Coronary Stenoses. Am J Cardiol 121:9–13. doi: 10.1016/j.amjcard.2017.09.018

7. Rossi A, Merkus D, Klotz E, et al (2014) Stress Myocardial Perfusion: Imaging with Multidetector CT. Radiology 270:25–46. doi: 10.1148/radiol.13112739

8. Danad I, Szymonifka J, Schulman-Marcus J, Min JK (2016) Static and dynamic assessment of myocardial perfusion by computed tomography. Eur Hear J – Cardiovasc Imaging 17:836–844. doi: 10.1093/ehjci/jew044

9. Jin KN, De Cecco CN, Caruso D, et al (2016) Myocardial perfusion imaging with dual energy CT. Eur J Radiol 85:1914–1921. doi: 10.1016/j.ejrad.2016.06.023

10. Meinel FG, De Cecco CN, Schoepf UJ, et al (2014) First–Arterial-Pass Dual-Energy CT for Assessment of Myocardial Blood Supply: Do We Need Rest, Stress, and Delayed Acquisition? Comparison with SPECT. Radiology 270:708–716. doi: 10.1148/radiol.13131183

11. Zreik M, Lessmann N, van Hamersvelt RW, et al (2018) Deep learning analysis of the myocardium in coronary CT angiography for identification of patients with functionally significant coronary artery stenosis. Med Image Anal 44:72–85. doi: 10.1016/j.media.2017.11.008

12. Johnson, TR; Fink, C; Schönberg, SO; Reiser M (2011) Dual Energy CT in Clinical Practice, Medical Radiology. Springer-Verlag Berlin Heidelberg. Springer Berlin Heidelberg, Berlin, Heidelberg

13. van Hamersvelt RW, Willemink MJ, de Jong PA, et al (2017) Feasibility and accuracy of dual-layer spectral detector computed tomography for quantification of gadolinium: a phantom study. Eur Radiol 27:3677–3686. doi: 10.1007/s00330-017-4737-8

14. Hickethier T, Baeßler B, Kroeger JR, et al (2017) Monoenergetic reconstructions for imaging of coronary artery stents using spectral detector CT: In-vitro experience and comparison to conventional images. J Cardiovasc Comput Tomogr 11:33–39. doi: 10.1016/j.jcct.2016.12.005

15. Boll DT, Merkle EM, Paulson EK, et al (2008) Calcified vascular plaque specimens: assessment with cardiac dual-energy multidetector CT in anthropomorphically moving heart phantom. Radiology 249:119–26. doi: 10.1148/radiol.2483071576

9

16. Symons R, Choi Y, Cork TE, et al (2018) Optimized energy of spectral coronary CT angiography for coronary plaque detection and quantification. J Cardiovasc Comput Tomogr 12:108–114. doi: 10.1016/j.jcct.2018.01.006

17. Pelgrim GJ, van Hamersvelt RW, Willemink MJ, et al (2017) Accuracy of iodine quantification using dual energy CT in latest generation dual source and dual layer CT. Eur Radiol 27:3904–3912. doi: 10.1007/s00330-017-4752-9

18. Litjens G, Kooi T, Bejnordi BE, et al (2017) A survey on deep learning in medical image analysis. Med Image Anal 42:60–88. doi: 10.1016/j.media.2017.07.005

19. Wolterink JM, Leiner T, de Vos BD, et al (2016) Automatic coronary artery calcium scoring in cardiac CT angiography using paired convolutional neural networks. Med Image Anal 34:. doi: 10.1016/j.media.2016.04.004

20. Force T, Gilles M, Chairperson M, et al (2013) 2013 ESC guidelines on the management of stable coronary artery disease. Eur Heart J 34:2949–3003. doi: 10.1093/eurheartj/eht296

21. Ko SM, Park JH, Hwang HK, Song MG (2014) Direct comparison of stress- and rest-dual-energy computed tomography for detection of myocardial perfusion defect. Int J Cardiovasc Imaging 30 Suppl 1:41–53. doi: 10.1007/s10554-014-0410-3

22. Ko SM, Choi JW, Hwang HK, et al (2012) Diagnostic performance of combined noninvasive anatomic and functional assessment with dual-source CT and adenosine-induced stress dual-energy CT for detection of significant coronary stenosis. AJR Am J Roentgenol 198:512–20. doi: 10.2214/AJR.11.7029

23. Ko BS, Cameron JD, Meredith IT, et al (2012) Computed tomography stress myocardial perfusion imaging in patients considered for revascularization: a comparison with fractional flow reserve. Eur Heart J 33:67–77. doi: 10.1093/eurheartj/ehr268

24. Flahault A, Cadilhac M, Thomas G (2005) Sample size calculation should be performed for design accuracy in diagnostic test studies. J Clin Epidemiol 58:859–62. doi: 10.1016/j.jclinepi.2004.12.009

25. Abbara S, Blanke P, Maroules CD, et al (2016) SCCT guidelines for the performance and acquisition of coronary computed tomographic angiography: A report of the society of Cardiovascular Computed Tomography Guidelines Committee: Endorsed by the North American Society for Cardiovascular Imaging (NASCI). J Cardiovasc Comput Tomogr 10:435–449. doi: 10.1016/j.jcct.2016.10.002

26. Leipsic J, Abbara S, Achenbach S, et al (2014) SCCT guidelines for the interpretation and reporting of coronary CT angiography: A report of the Society of Cardiovascular Computed Tomography Guidelines Committee. J Cardiovasc Comput Tomogr 8:342–358. doi: 10.1016/j.jcct.2014.07.003

27. Cury RC, Abbara S, Achenbach S, et al (2016) CAD-RADSTM Coronary Artery Disease – Reporting and Data System. An expert consensus document of the Society of Cardiovascular Computed Tomography (SCCT), the American College of Radiology (ACR) and the North American Society for Cardiovascular Imaging (NASCI). Endorsed by the American College of Cardiology. J Cardiovasc Comput Tomogr 10:269–281. doi: 10.1016/j.jcct.2016.04.005

28. Deak PD, Smal Y, Kalender WA (2010) Multisection CT Protocols: Sex- and Age-specific Conversion Factors Used to Determine Effective Dose from Dose-Length Product. Radiology 257:158–166. doi: 10.1148/radiol.10100047

9
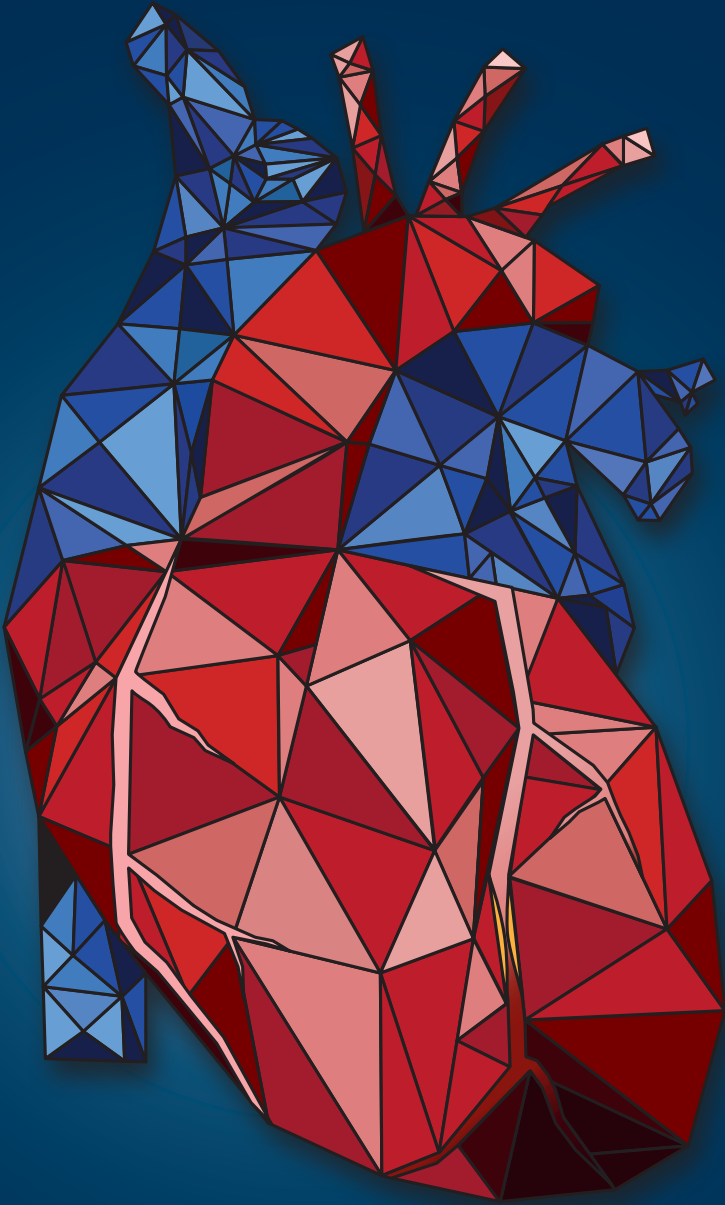
Part V

Summary and Discussion
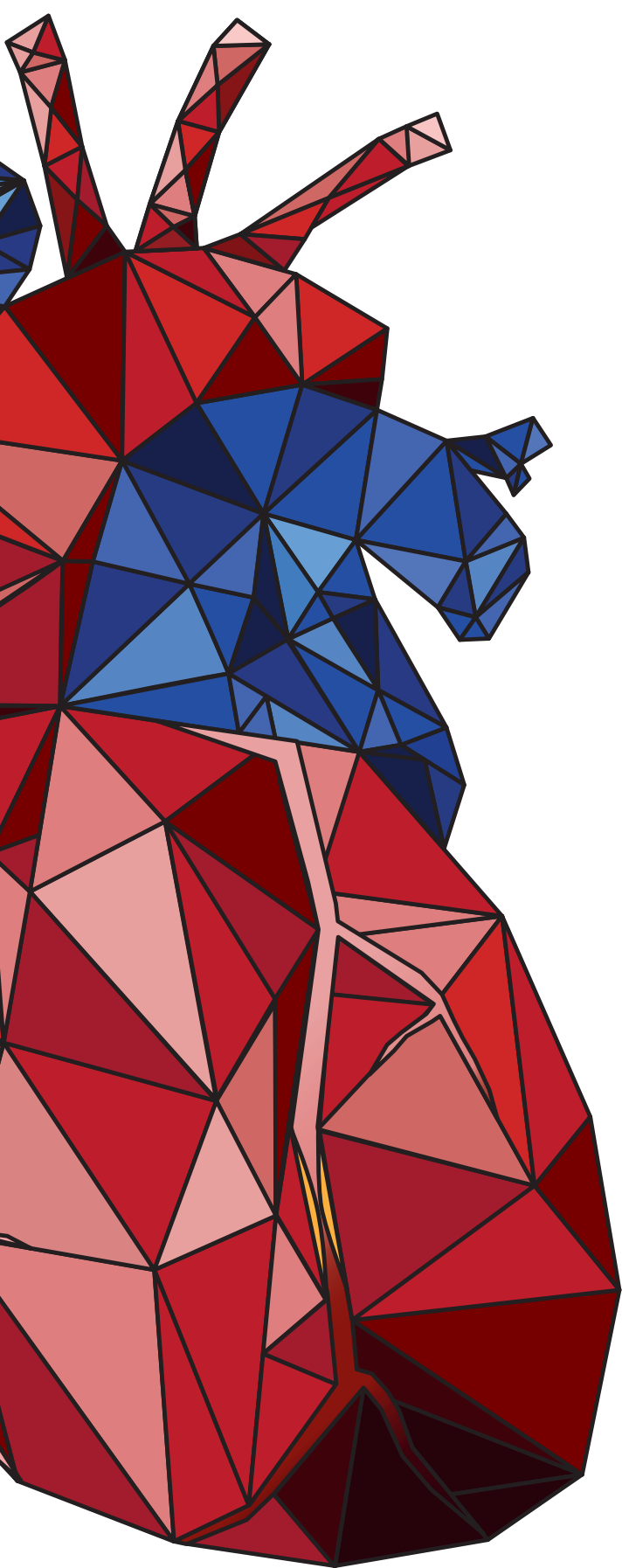
Chapter 10.1

Summary

This thesis focused on computed tomography (CT) imaging of cardiovascular disease. The aim was to improve diagnostic performance of CT for the evaluation of functionally significant coronary stenoses. As the interest in CT as a tool for the evaluation of cardiovascular disease is increasing, the secondary aim of this thesis was to reduce the drawbacks of CT.

Part I is focused on evaluation of calcium scoring at reduced radiation dose.

In **chapters 2 & 3,** prospective studies on low-dose non-contrast CT were performed to evaluate clinical implementation of dose reduction in cardiothoracic CT. In **chapter 2**, we evaluated the inter-observer and inter-examination reliability and agreement of aortic valve and mitral valve calcification scoring on low-dose ungated non-contrast lung cancer screening CT scans. We showed that aortic valve calcifications can be quantified with high reliability and agreement on ungated lung cancer screening chest CT scans. Mitral valve calcifications were more difficult to quantify reliably and subject to more variability, because the level of experience of the reader becomes more important to reliably identify these calcifications.

In **chapter 3** we determined the maximally achievable radiation dose reduction with iterative reconstruction at which quantification of aortic valve and thoracic aorta calcification was still feasible. We found that iterative reconstruction allowed for 60% and 75% dose reduction of cardiac and chest CT, respectively. Application of iterative reconstruction allowed for accurate quantification of aortic valve and thoracic aorta calcifications at submillisievert dose.

Part II consists of phantom studies and focuses on safety and quality control in dual-energy CT.

In **chapter 4** we evaluated the feasibility and extent to which iodine concentrations can be reduced without loss of objective image quality. Iodine is used in contrast media for CT-imaging. Because iodine has a K-edge at 33.2 keV, the photoelectric effect substantially increases at lower keV, leading to higher attenuation at lower energy levels. In this study, boluses of different iodine concentrations were administered to a dynamic circulation phantom and imaged with latest dual-energy CT (DECT) scanners from three different vendors. Depending on the vendor, iodinated contrast media could be reduced with 40% using low kVp and with 60% using virtual monochromatic images at low keV.

In **chapter 5** we evaluated the accuracy of iodine quantification using DECT. A phantom containing 5 tubes with different iodine concentrations was imaged using DECT scanners from two different vendors. Both DECT scanners were found

10

to be highly accurate for quantification. This opens up the possibilities for iodine quantification in the myocardium, which is a surrogate for myocardial perfusion as the iodine distribution is related to myocardial blood flow.

In **chapter 6** we explored the use of gadolinium as an alternative contrast agent for DECT. We imaged a phantom containing different gadolinium concentrations, which mimicked an estimated clinical range encountered after an injection typically used for magnetic resonance imaging (0.1–0.2 mmol of gadolinium per kilogram). We were able to quantify gadolinium with high accuracy and attenuation of gadolinium increased on virtual monochromatic images at low keV.

In **part III** we evaluated new technical developments that may allow for functional evaluation of coronary artery disease (CAD) on coronary CT angiography (CCTA) at rest.
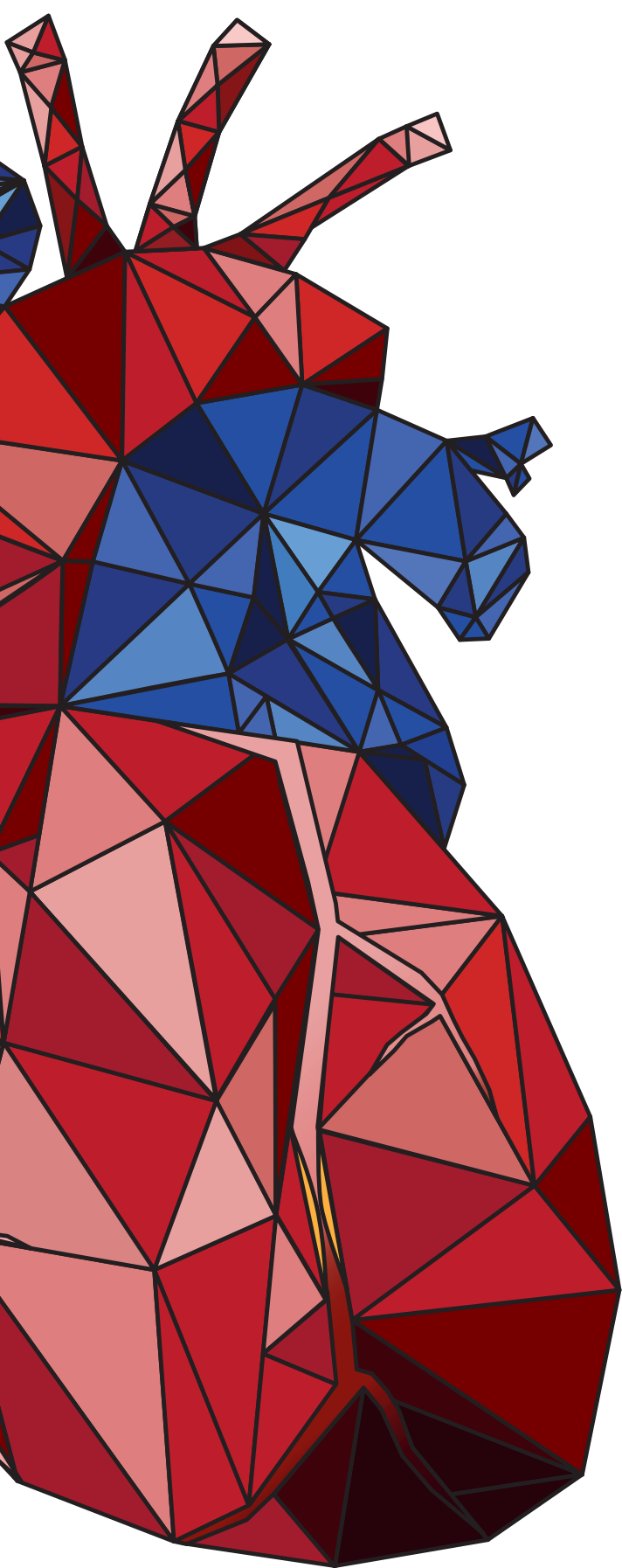
In **chapter 7** we evaluated the diagnostic performance of coronary computed tomography angiography-derived fractional flow reserve (CT-FFR) for the diagnosis of functionally significant CAD, as defined by invasive fractional flow reserve. We demonstrated that CT-FFR can accurately diagnose functionally significant CAD and that it has superior diagnostic performance compared to stenosis evaluation alone.

In **chapter 8** we investigated the incremental value of deep learning analysis of the myocardium to stenosis evaluation for the diagnosis of functionally significant stenosis. Based on the highest degree of stenosis on CCTA patients were considered to have no functionally significant stenosis (≤24% degree of stenosis), functionally significant stenosis (≥70% degree of stenosis) or intermediate stenosis (25-69% degree of stenosis). For the patients with intermediate degree stenoses, deep learning analysis of the myocardium was applied to define the functional significance. The combined method showed the potential for improved diagnostic performance for the diagnosis of functionally significant CAD.

Part IV is focused on the clinical perspective, and sheds light on the rationale for comprehensive DECT imaging for the evaluation of CAD.

In **chapter 9** we described the rationale and design of the CLARITY study (Application of speCtraL computed tomogrAphy to impRove specIficity of cardiac compuTed tomographY). This study strives to improve the specificity of CCTA for the evaluation of functionally significant CAD. In this study both anatomical and functional evaluation of CAD are combined. In the endeavour to improve diagnostic performance, the acquisition protocol contains calcium scoring CT, CT perfusion,

10

CCTA and late enhancement CT performed on a DECT scanner. With these scans and the ability to use DECT applications combined with analysis as described in **chapters 7 & 8**, we hypothesize that more accurate diagnostic information will be available. We expect an improved determination of coronary anatomy, degree of coronary stenosis, myocardial perfusion and CT-FFR analysis. The CLARITY study will clarify to what extent the diagnostic performance of CT can be improved for the evaluation of functionally significant CAD. This study is ongoing, with currently 24 patients included.

10

Chapter 10.2

General discussion

In this thesis, we showed that combined evaluation of both anatomical and functional analysis increased the diagnostic performance of computed tomography (CT) for the diagnosis of functionally significant coronary artery disease (CAD). Additionally, we found that with application of iterative reconstruction and dual-energy CT (DECT), major drawbacks of CT can be reduced. With an improved diagnostic performance and reduction of drawbacks, CT might become an even more important tool for the detection, visualization and evaluation of cardiovascular disease.

Low dose calcium scoring

In cardiac CT imaging, quantification of coronary calcium on non-contrast CT scans can be used for risk prediction of adverse cardiovascular events [1]. However, not only the calcifications found in the coronary arteries are a strong predictor, also atherosclerotic calcifications found on the heart valves and in the thoracic aorta are strong predictors for adverse cardiovascular events [2, 3]. Low dose non-gated non-contrast lung cancer screening chest CT scans can be used to quantify these calcifications [2, 4]. As heavy smoking is associated with cardiovascular disease and mortality, individual risk of adverse cardiovascular events can be assessed by evaluating the calcium score on the already acquired lung cancer screening CT scans. Even though these scans are performed without ECG-gating, previous studies and the current thesis showed that quantification of calcifications in the coronary artery and aortic valve can be performed with high inter-observer and inter-scan reliability and agreement [5–7]. This makes ungated chest CT a valuable diagnostic tool for opportunistic assessment of cardiovascular risk. Recent developments in iterative reconstruction allow for dose reduction without loss of image quality. With the application or iterative reconstruction, calcifications in the coronary artery, aortic valve and thoracic aorta can be reliably quantified at submillisievert dose in cardiac and chest CT [8–10]. As the burden of radiation dose is reduced, the opportunity for population-based screening arises. Results of the ROBINSCA study (Risk Or Benefit IN Screening for CArdiovascular Diseases) will give insights whether population based screening with coronary calcium scoring can reduce cardiovascular morbidity and mortality in high-risk patients [11].

Functional analysis of CAD using CT

Non-invasive visualization of the coronary lumen is possible with coronary CT angiography (CCTA). Evaluation of plaque and degree of stenosis on CCTA is a reliable diagnostic tool for detection and rule out of CAD [12]. However, CCTA lacks

10

specificity in indicating the functional significance of CAD, which may result in an unnecessary referral for invasive coronary angiography and invasive fractional flow reserve (FFR) [13]. Therefore, European guidelines currently advise CCTA only in patients with stable chest pain symptoms with a pre-test probability for CAD of 15-50% [14]. Recent developments in CT hardware and software such as DECT, CT perfusion (CTP), CCTA-derived fractional flow reserve (CT-FFR) and machine learning analysis allow for functional analysis of CAD and thereby provide an extra dimension in CT imaging of the heart. In the current thesis and in literature we found that by allowing for analysis beyond anatomical evaluation, these methods have been shown to improve diagnostic accuracy of CT for the diagnosis of functionally significant CAD [15, 16].

Both dynamic and static CTP substantially improve specificity when combined with CCTA with almost no decrease in sensitivity compared to degree of stenosis evaluation on CCTA alone [15]. Although CTP enables assessment of myocardial perfusion, it is subject to increased radiation dose. Furthermore, the need for an additional acquisition under infusion of adenosine stress limits the integration into clinical practice at present. With static CTP the contrast media distribution is evaluated at a single moment in time by acquiring only one scan at a predefined optimal time point. Therefore, static CTP can be performed at a lower radiation dose compared to dynamic CTP. However, static CTP is more prone to beam hardening artefacts and timing is more challenging. Static CTP performed with DECT in the projection space may be less affected by beam hardening and allows for iodine quantification in the myocardium, which is a surrogate for tissue perfusion. However, as the amount of iodine present in the myocardium is dependent on multiple factors (e.g. cardiac output, timing of the acquisition, and impaired blood flow by stenosis), defining a uniformly cut-off iodine concentration value for healthy and ischemic myocardium is difficult. Therefore, in static CTP, balanced ischemia caused by multi-vessel disease may go undetected [17].

CT-FFR is not affected by balanced ischemia and does not require an additional stress acquisition. In this thesis and in previous studies CT-FFR showed improved diagnostic performance, with consistently high sensitivity and improved specificity, compared to CCTA [15]. CT-FFR might improve the role of CT as a gatekeeper to the catheterization laboratory, as recent results of the PLATFORM study showed that CTA and CT-FFR reduced referral rate to invasive coronary angiography with 61% [18]. Additionally, CT-FFR may allow for virtual stenting, thereby defining the stenosis in need for treatment in the presence of serial coronary stenosis [19]. Although first results are promising with an overall high diagnostic performance,

10

a recent study by Cook et al. [20] showed that the diagnostic accuracy of CT-FFR varied substantially as a function of the absolute CT-FFR value, with lowest accuracy of approximately 50% in the CT-FFR range 0.70-0.80. When analysing individual CT-FFR values, cut-off values of ≤0.53 and >0.93 were needed to meet an overall diagnostic accuracy of 95%. This indicates the need for further studies to evaluate the balance between diagnostic certainty against the need for confirmation of ischemia. This should also involve a hybrid strategy, referring patients with CT-FFR values around the cut-off value for further testing [21]. As CT-FFR relies on lumen segmentation, there is a need for high quality scans with minimal artefacts and patients with prior stent placement are excluded from analysis. Therefore, not all cases can be evaluated, which limits the use of CT-FFR. Additionally, lumen segmentation is a time consuming manual task, which may hamper the use in daily clinical practice.

Recently, novel machine learning methods have been introduced to evaluate functional analysis of CAD on CCTA at rest. A machine learning based approach to CT-FFR showed comparable results to CT-FFR based on computational fluid dynamics [22, 23]. However, this method still depends on lumen segmentations performed semi-automatically. Beyond the scope of lumen segmentations, machine learning has also been applied for automatic detection and classification of coronary plaque and degree of stenosis and to predict lesion-specific ischemia by analysing quantitative plaque measures obtained from CCTA [24, 25]. Additionally, machine learning methods have exploited myocardial ischemia detection on CCTA at rest [16, 26]. Although it is well known that ischemia is more pronounced under conditions of induced stress, we found that application of deep learning improved diagnostic performance for the identification of patients with functionally significant CAD by analysing the myocardium on CCTA at rest. Although more research is needed to thoroughly test and improve this method, the potential benefit is clear. Where classical machine learning relies on manually designed feature extraction, deep learning algorithms are capable of identifying relevant features without prior definition of relevant features. Thereby, the method is not limited to features already known by the observer, and may be more sensitive to texture changes and complex patterns and relationships, needed to detect ischemia on CCTA images at rest. However, deep learning has often been described as a black box. Even though extracted features are based on the images and represent the appearance of disease, specific features do not correspond to specific physiological appearance. Revealing their inner dynamics to understand what the network is responding to is an active field of research and may be needed before deep learning methods will be fully accepted in the medical field where accountability is of importance [27].

10

CLARITY study

In this thesis and in previous research we found that CTP, CT-FFR and machine learning all improve diagnostic performance for the identification of functionally significant CAD [15]. As each method has strengths and weaknesses and focusses on different scans and areas within a scan, it has been suggested that the highest diagnostic performance could be achieved by combining these methods [28]. As we showed in this thesis, DECT allows for accurate iodine quantification which can be used to evaluate myocardial iodine distribution [29]. Together with an increased lumen visibility and reduction of artefacts, we hypothesized that when combining DECT with CTP, CT-FFR and machine learning, highest diagnostic performance can be achieved. Therefore, we conducted the CLARITY study (Application of speCtraL computed tomogrAphy to impRove specIficity of cardiac compuTed tomographY), which aimed to evaluate the diagnostic performance of combinations of DECT, CTP, CT-FFR, and deep learning analysis for the diagnosis of functionally significant CAD. As described in this thesis, 75 patients who are scheduled to undergo clinically indicated invasive FFR will receive a dedicated DECT scan protocol. Each patient will undergo a low dose calcium score scan, adenosine induced stress CTP and rest CCTA in this order. In case of a history of myocardial infarction an additional late enhancement CT will be performed. **Figure 1** shows a schematic overview of the scan protocol. All scans will be performed using a dual-layer spectral detector CT. With the dual-layer spectral detector CT, low and high energy X-ray photons are separated at the detector level, thereby allowing for fully temporal and spatial co-registration, making it ideal for imaging of a moving organ such as the heart. By combining the output of both detector layers, an additional conventional image can be reconstructed, making it the modality of choice to explore the additional value of DECT over conventional CT. It is important to underscore that both conventional images and DECT reconstructions are always available *post hoc*. Thus, dual-layer spectral detector CT combines both conventional CT as well as DECT analysis, thereby providing an extra dimension in cardiovascular CT. The DECT applications provided by the dual-layer spectral detector CT, and their additional benefits, are shown in **Table 1**. In particular, the application of virtual monochromatic imaging and iodine density quantification may allow for more accurate anatomical and functional analysis. It is expected that this capability will contribute to improved assessment of degree of stenosis, CT-FFR, myocardial perfusion and deep learning analysis. By increasing diagnostic performance, CT might also become the imaging test of choice in patients with a higher pre-test probability of CAD than the 15-50% normally advised for CT. Functional evaluation of ischemia, using stress testing, is advised by European guidelines in patients with a pre-test probability for CAD of
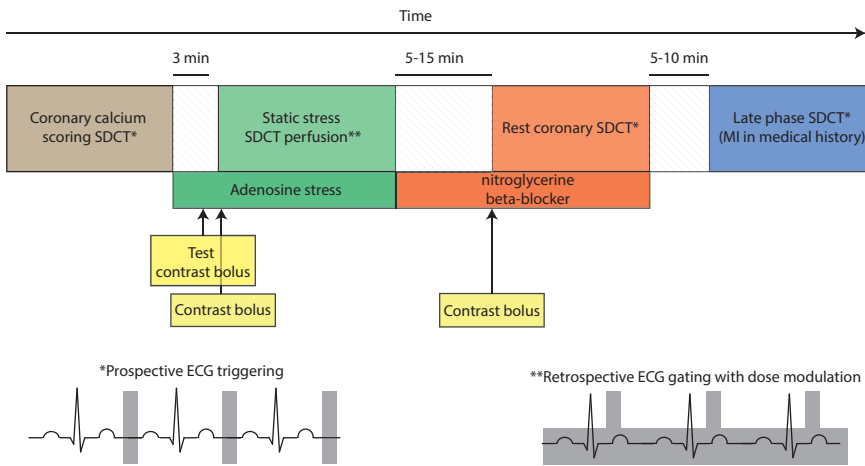
10

Figure 1 CLARITY acquisition protocol. Reprinted from chapter 9. *MI = myocardial infarction; SDCT = dual-layer spectral detector computed tomography*

15-85% [15]. Therefore, accurate functional analysis on CT could potentially allow CT to be used in patients with a higher pre-test probability, thereby enlarging the patient group benefitting from CT. Results of the CLARITY study will clarify to what extent the diagnostic performance of CT can be improved for the evaluation of functionally significant CAD. This study is ongoing, with currently 24 patients included. An example of a static stress dual-layer spectral detector CT perfusion scan of a CLARITY patient is shown in **Figure 2**.

Invasive coronary angiography and FFR

In patients with intermediate-degree stenoses, invasive coronary angiography and invasive FFR are currently the reference standard for evaluation of CAD [14]. These invasive methods allow for both evaluation and revascularization treatment in one investigation. However, a study by Patel et al. [30] showed that obstructive CAD was only found in about one third of the patients undergoing elective ICA. Additionally, results of the FAME II study showed that in about one third of the patients who had a significant stenosis on ICA, no significant FFR was found [31]. To reduce the number of these unnecessary invasive procedures, non-invasive testing prior to invasive coronary angiography and FFR is advised in patients with suspected stable CAD [14]. Using CT, CAD can effectively be detected or ruled out [12]. Recently published follow-up results of the SCOT-HEART trial showed that in patients with stable chest pain, evaluation with CT resulted in a lower

10

Table 1 DECT applications available using dual-layer spectral detector CT and their additional benefit.

Conventional	Hounsfield units based			Material decomposition based	
	Virtual monochromatic imaging		Virtual non-contrast	Iodine density	Effective atomic number
	Low VMI	*High VMI*			
Image as acquired on a conventional CT scanner	Increased contrast of materials	Improved lumen and stenosis evaluation	Evaluation of tissues after virtual removal of iodinated contrast	Quantitative analysis of the amount of iodine (mg/ml)	Quantitative analysis of approximately modelled effective atomic number
	Increased attenuation of iodine	Reduced beam hardening artefacts		Improved detection of areas with increased or decreased iodine contrast	Improved differentiation between materials
		Reduced metal artefacts			

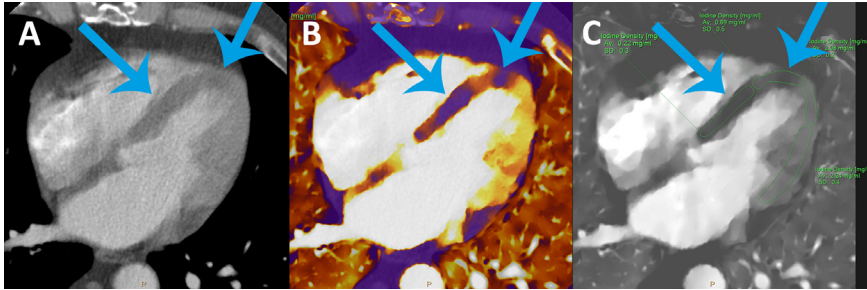*VMI = virtual monochromatic imaging*

10

193

Figure 2 Static stress dual-layer spectral detector CT perfusion example of a CLARITY patient. Conventional image (**A**) shows a subtle hypoattenuation mid- and inferoseptal (blue arrows). Fusion overlay (**B**) based on iodine density, yellow/white indicates high quantity of iodine and blue indicates a low quantity. On the fusion image a reduced amount of iodine contrast septal and inferoseptal is visible (blue arrows). Iodine density quantification (**C**) confirms this finding and shows a reduced amount of iodine in this area compared to the other areas (blue arrows). This finding was confirmed by invasive FFR which showed a functionally significant stenosis in the LAD (FFR ≤0.8). *FFR = fractional flow reserve; LAD = left anterior descending artery*

cardiac death rate compared to patients evaluated using standard care [32]. The authors suggested that the use of CCTA led to more correct diagnosis of CAD than standard care, which consequently led to the use of more appropriate therapies and alterations in patient management, eventually leading to a reduction in death rate. Even though only degree of stenosis was evaluated in this study, the added value of CT, performed in an early stage, for the evaluation of CAD in patients with stable chest pain has shown its benefits. With the addition of functional analysis, CT may be able to more accurately detect the patients in need for invasive revascularization treatment and may thereby reduce the number of unnecessary invasive procedures.

Reducing the drawbacks of CT

To allow for widespread implementation of CT for early evaluation of patients with stable chest pain, reducing its drawbacks is of the essence. As we found in the introduction of this thesis, the main drawbacks of cardiovascular CT are the use of ionizing radiation dose and the need for injection of iodinated contrast media. In the current thesis we showed that radiation dose can be reduced by applying iterative reconstruction and that contrast media dose can be reduced by using low kVp or virtual monochromatic images at low keV with DECT [8, 33]. Additionally, we showed that with the use of DECT gadolinium may be used as a contrast media,

10

which could potentially be used in patients with contraindications to iodinated contrast media [34]. Patient studies translating our phantom results are needed before implementation can take place in clinical practice. The CLARITY study will provide an initial impetus to implementation in patient care as all contrast enhanced scans are performed with 25% less iodine contrast compared to routine clinical practice.

Implementation into clinical practice

The current thesis emphasizes the additional value of functional analysis in cardiovascular CT. However, it also underscores the relatively early stage we are in in understanding the full potential of CT for the evaluation of functionally significant CAD. Before a diagnostic test can be implemented into clinical practice its added value should be evaluated, which concerns more than only technical and diagnostic performance. First technical evaluation and diagnostic performance are evaluated, which concerns the current state of functional analysis on CT. Thereafter, the effect of the diagnostic test on patient management, patient outcome and cost-effectiveness should be investigated [35]. Therefore, in case of findings of improved diagnostic performance in the CLARITY study, a logical next step would be a randomized controlled trial. Based on the future findings of the CLARITY study, an optimal scan protocol should be developed. This scan protocol with additional functional analyses should be applied to one arm of the randomized controlled trial, while the other arm should undergo the currently used diagnostic pathway. In such a study both patient outcome and cost-effectiveness should be evaluated.

Future of CT

DECT opens up a variety of applications (**Table 1**), which have the potential to enhance the diagnostic performance of CT. A novel approach to access the additional information obtained with DECT is CT fingerprinting. CT fingerprinting refers to the combined analysis of the Compton and photoelectric properties of all imaged voxels in a two-dimensional space. For each voxel in an image, the contribution of photoelectric effect and Compton scatter to attenuation can be defined and plotted in a graph. All voxels together will define a CT fingerprint specific to the scanned volume (**Figure 3**). CT fingerprinting will allow for quantitative data acquisition, which can be used for pattern recognition. Because each material has a specific photoelectric effect and Compton scatter pattern, different materials can be quantified and voxels containing that material can be selected. Additionally,
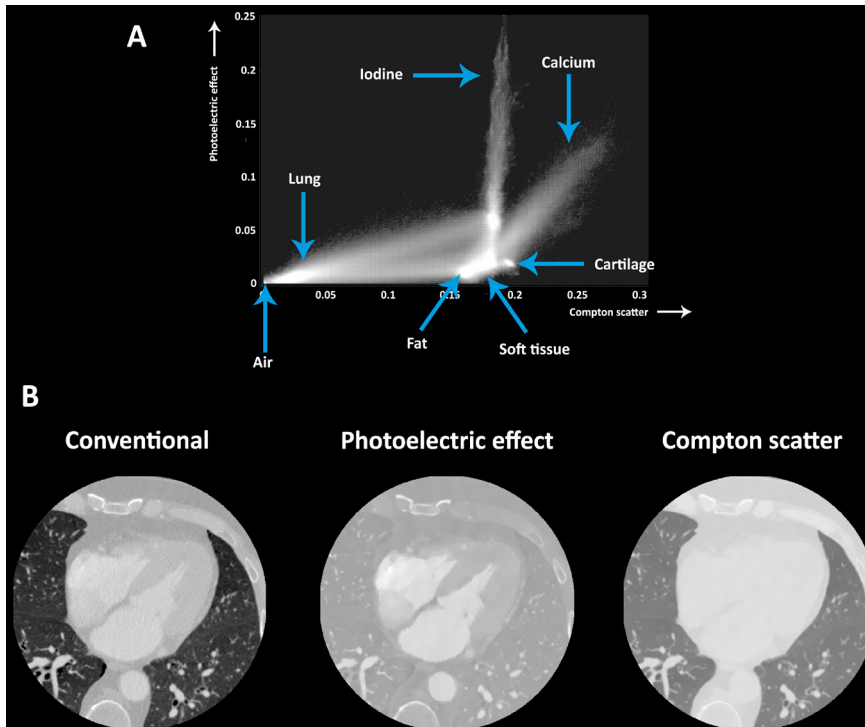
10

Figure 3 CT fingerprint of a cardiac CT-scan. Image **A** shows for each voxel in the entire cardiac CT-scan the contribution of photoelectric effect (y-axis) and Compton scatter (x-axis) to attenuation. Density in the graph shows the amount of voxels with that specific combination of photoelectric effect and Compton scatter on a logarithmic scale (i.e. the denser the area, the more voxels that contain that specific combination of photoelectric effect and Compton scatter). Because each material contains a specific combination of photoelectric effect and Compton scatter, patterns of different materials can be identified. Typical patterns of air, lung, iodine, calcium, fat, cartilage and soft tissue are indicated in the image. Image **B** shows a conventional, photoelectric effect and Compton scatter reconstruction of a slice at the level of the heart. Image **B** provides a visualization of the contribution of photoelectric effect and Compton scatter of different materials. A clear distinction in the amount of iodine can be seen in the photoelectric effect image, whereas the Compton scatter mainly shows a differentiation between lung tissue, soft tissue and calcium

this may allow for diagnosis, as different diseases may have their specific pattern of photoelectric effect and Compton scatter defined in a CT fingerprint plot. In future work we will evaluate the technical principles and diagnostic performance of this new method in the evaluation of CAD.

Another exciting development is photon-counting CT (PCCT). Instead of using an energy-integrating detector (conventional CT) or a dual-layer spectral detector CT, PCCT uses an energy-resolving detector capable of counting the number of X-ray

10

photons and measuring the energy of every photon [36]. By comparing the energy of each photon to a preset threshold level, the detector can sort the photons in more than just two different energy bins. The energy of each bin and the weighting factor of each bin can be adjusted to specific tasks, kVp-settings, and k-edges of (contrast) materials of interest. Thereby allowing for improved soft tissue and contrast agent contrast, higher contrast-to-noise, improved virtual monochromatic images, improved material quantification, more accurate CT fingerprinting and k-edge imaging [36]. By using k-edge imaging, multiple contrast agents can be detected in one investigation. This can potentially be used for imaging of late enhancement in a CCTA, by performing multi-phase administration of gadolinium and iodine [37]. By setting the lowest bin threshold higher than the level of electronic noise, noise is effectively filtered out. Together with weighting of the bins, PCCT allows for dose reduction without decrease of objective image quality [38]. PCCT detectors have smaller detector elements compared to conventional CT detectors, resulting in a higher spatial resolution. This further improves contrast-to-noise and decreases artefacts. Thereby, PCCT may improve plaque detection and quantification together with improved lumen segmentation and in-stent visibility [39]. It is expected that PCCT will improve the diagnostic performance of CT for the evaluation of CAD. However, there are some hurdles to overcome before PCCT will be available for clinical practice, including stability of the detector, costs, data size, reconstruction time, and work flow. Therefore, we anticipate that PCCT will become commercially available in 5-10 years.

Since the early days of radiology, systems have been built for automatic analysis of medical images. In the last decades, machine learning has substantially boosted this field of research. Presently, deep learning algorithms are the methodology of choice for medical image analysis. By applying unsupervised learning, deep learning algorithms can be trained with unlabelled data, which are more widely available. It is expected that the developments in the field of machine learning will influence the whole chain of diagnostic imaging in radiology; from patient planning, selection of image parameters and performing image reconstruction to diagnosis of disease and defining the prognosis.

Conclusion

The current thesis showed the incremental value of both anatomical and functional CT analyses for the diagnosis of functionally significant CAD. The ongoing CLARITY study will shed light on to what extent the combination of new techniques can improve the diagnostic performance of CT for the evaluation of functionally
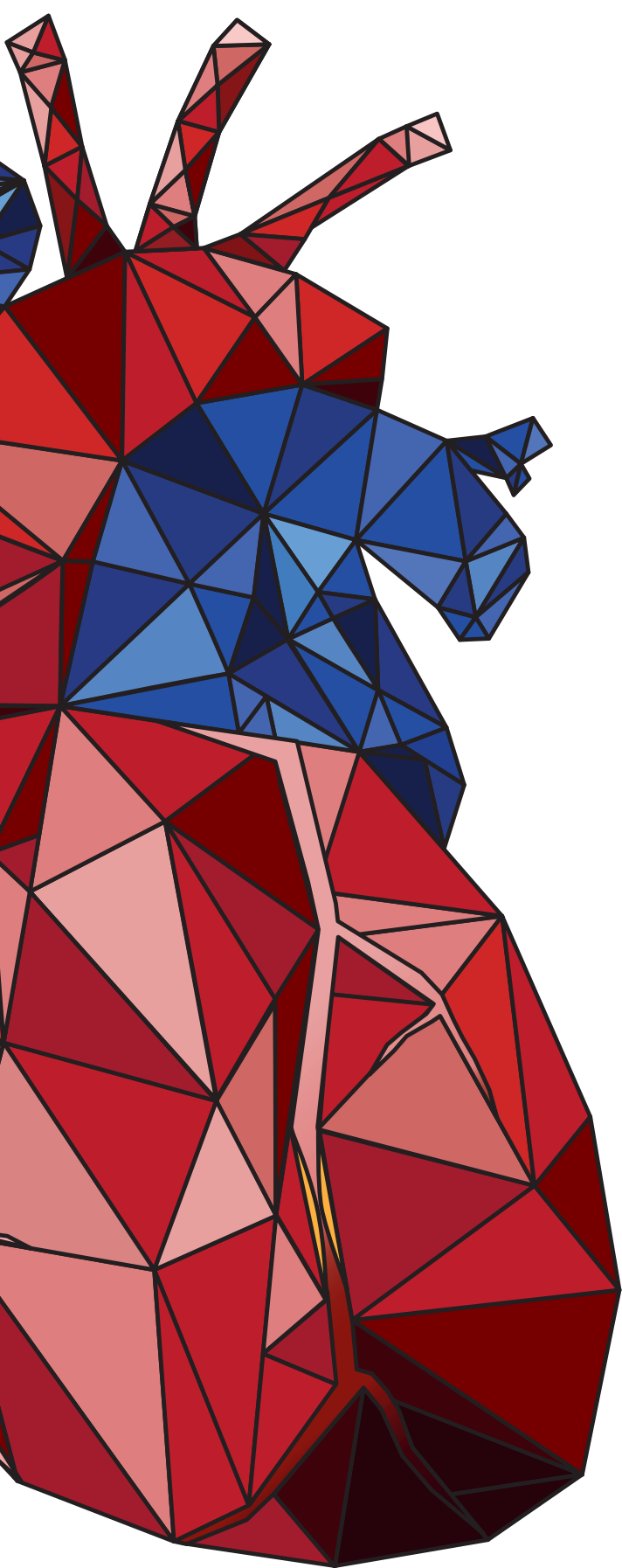
10

significant CAD. Together with a reduction in the drawbacks of CT, the data of this thesis suggest that we may be entering a new era in the evaluation of CAD. Where CT nowadays is mainly used to diagnose and rule out CAD, in the near future it may also be used for the identification, and subsequent revascularization management, of patients in need for treatment.

10

References

1. Greenland P, LaBree L, Azen SP, et al (2004) Coronary Artery Calcium Score Combined With Framingham Score for Risk Prediction in Asymptomatic Individuals. JAMA 291:210. doi: 10.1001/jama.291.2.210

2. Jacobs PC, Prokop M, van der Graaf Y, et al (2010) Comparing coronary artery calcium and thoracic aorta calcium for prediction of all-cause mortality and cardiovascular events on low-dose non-gated computed tomography in a high-risk population of heavy smokers. Atherosclerosis 209:455–462. doi: 10.1016/j.atherosclerosis.2009.09.031

3. Owens DS, Budoff MJ, Katz R, et al (2012) Aortic valve calcium independently predicts coronary and cardiovascular events in a primary prevention population. JACC Cardiovasc Imaging 5:619–25. doi: 10.1016/j.jcmg.2011.12.023

4. Takx RAP, Išgum I, Willemink MJ, et al (2015) Quantification of coronary artery calcium in nongated CT to predict cardiovascular events in male lung cancer screening participants: Results of the NELSON study. J Cardiovasc Comput Tomogr 9:50–57. doi: 10.1016/j.jcct.2014.11.006

5. Takx RAP, de Jong PA, Leiner T, et al (2014) Automated Coronary Artery Calcification Scoring in Non-Gated Chest CT: Agreement and Reliability. PLoS One 9:e91239. doi: 10.1371/journal.pone.0091239

6. Jacobs PCA, Isgum I, Gondrie MJA, et al (2010) Coronary artery calcification scoring in low-dose ungated CT screening for lung cancer: interscan agreement. AJR Am J Roentgenol 194:1244–9. doi: 10.2214/AJR.09.3047

7. van Hamersvelt RW, Willemink MJ, Takx RAP, et al (2014) Cardiac valve calcifications on low-dose unenhanced ungated chest computed tomography: inter-observer and inter-examination reliability, agreement and variability. Eur Radiol 24:1557–64. doi: 10.1007/s00330-014-3191-0

8. Van Hamersvelt RW, Harder AMD, Willemink MJ, et al (2017) Aortic valve and thoracic aortic calcification measurements: how low can we go in radiation dose? J Comput Assist Tomogr 41:148–155. doi: 10.1097/RCT.0000000000000477

9. Willemink MJ, den Harder AM, Foppen W, et al (2016) Finding the optimal dose reduction and iterative reconstruction level for coronary calcium scoring. J Cardiovasc Comput Tomogr 10:69–75. doi: 10.1016/j.jcct.2015.08.004

10. den Harder AM, Wolterink JM, Willemink MJ, et al (2016) Submillisievert coronary calcium quantification using model-based iterative reconstruction: A within-patient analysis. Eur J Radiol 85:2152–2159. doi: 10.1016/j.ejrad.2016.09.028

11. Vonder M, van der Aalst CM, Vliegenthart R, et al (2018) Coronary Artery Calcium Imaging in the ROBINSCA Trial. Acad Radiol 25:118–128. doi: 10.1016/j.acra.2017.07.010

12. Budoff MJ, Dowe D, Jollis JG, et al (2008) Diagnostic performance of 64-multidetector row coronary computed tomographic angiography for evaluation of coronary artery stenosis in individuals without known coronary artery disease: results from the prospective multicenter ACCURACY (Assessment by Coronary Computed Tomographic Angiography of Individuals Undergoing Invasive Coronary Angiography) trial. J Am Coll Cardiol 52:1724–32. doi: 10.1016/j.jacc.2008.07.031

13. Ko BS, Wong DTL, Cameron JD, et al (2014) 320-row CT coronary angiography predicts freedom from revascularisation and acts as a gatekeeper to defer invasive angiography in stable coronary artery disease: a fractional flow reserve-correlated study. Eur Radiol 24:738–47. doi: 10.1007/s00330-013-3059-8

10

14. Task Force Members, Montalescot G, Sechtem U, et al (2013) 2013 ESC guidelines on the management of stable coronary artery disease: the Task Force on the management of stable coronary artery disease of the European Society of Cardiology. Eur Heart J 34:2949–3003. doi: 10.1093/eurheartj/eht296

15. Celeng C, Leiner T, Maurovich-Horvat P, et al (2018) Anatomical and Functional Computed Tomography for Diagnosing Hemodynamically Significant Coronary Artery Disease. JACC Cardiovasc Imaging. doi: 10.1016/j.jcmg.2018.07.022

16. Zreik M, Lessmann N, van Hamersvelt RW, et al (2018) Deep learning analysis of the myocardium in coronary CT angiography for identification of patients with functionally significant coronary artery stenosis. Med Image Anal 44:72–85. doi: 10.1016/j.media.2017.11.008

17. Danad I, Szymonifka J, Schulman-Marcus J, Min JK (2016) Static and dynamic assessment of myocardial perfusion by computed tomography. Eur Heart J Cardiovasc Imaging 17:836–44. doi: 10.1093/ehjci/jew044

18. Douglas PS, Pontone G, Hlatky MA, et al (2015) Clinical outcomes of fractional flow reserve by computed tomographic angiography-guided diagnostic strategies vs. usual care in patients with suspected coronary artery disease: the prospective longitudinal trial of FFR$_{CT}$: outcome and resource impacts study. Eur Heart J 36:3359–3367. doi: 10.1093/eurheartj/ehv444

19. Ihdayhid AR, White A, Ko B (2017) Assessment of Serial Coronary Stenoses With Noninvasive Computed Tomography-Derived Fractional Flow Reserve and Treatment Planning Using a Novel Virtual Stenting Application. JACC Cardiovasc Interv 10:e223–e225. doi: 10.1016/j.jcin.2017.09.015

20. Cook CM, Petraco R, Shun-Shin MJ, et al (2017) Diagnostic Accuracy of Computed Tomography–Derived Fractional Flow Reserve. JAMA Cardiol 2:803. doi: 10.1001/jamacardio.2017.1314

21. Kruk M, Wardziak Ł, Demkow M, et al (2016) Workstation-Based Calculation of CTA-Based FFR for Intermediate Stenosis. JACC Cardiovasc Imaging 9:690–9. doi: 10.1016/j.jcmg.2015.09.019

22. Tesche C, De Cecco CN, Baumann S, et al (2018) Coronary CT Angiography-derived Fractional Flow Reserve: Machine Learning Algorithm versus Computational Fluid Dynamics Modeling. Radiology 288:64–72. doi: 10.1148/radiol.2018171291

23. Coenen A, Kim Y-H, Kruk M, et al (2018) Diagnostic Accuracy of a Machine-Learning Approach to Coronary Computed Tomographic Angiography–Based Fractional Flow Reserve. Circ Cardiovasc Imaging 11:e007217. doi: 10.1161/CIRCIMAGING.117.007217

24. Zreik M, van Hamersvelt RW, Wolterink JM, et al (2018) A Recurrent CNN for Automatic Detection and Classification of Coronary Artery Plaque and Stenosis in Coronary CT Angiography. arXiv 1804.04360.

25. Dey D, Gaur S, Ovrehus KA, et al (2018) Integrated prediction of lesion-specific ischaemia from quantitative coronary CT angiography using machine learning: a multicentre study. Eur Radiol 28:2655–2664. doi: 10.1007/s00330-017-5223-z

26. Han D, Lee JH, Rizvi A, et al (2018) Incremental role of resting myocardial computed tomography perfusion for predicting physiologically significant coronary artery disease: A machine learning approach. J Nucl Cardiol 25:223–233. doi: 10.1007/s12350-017-0834-y

27. Zeiler MD, Fergus R (2014) Visualizing and Understanding Convolutional Networks. In: Fleet D, Pajdla T, Schiele B, Tuytelaars T (eds) Comput. Vis. -- ECCV 2014 13th Eur. Conf. Zurich, Switzerland, Sept. 6-12, 2014, Proceedings, Part I. Springer International Publishing, Cham, pp 818–833

28. Yang DH, Kim Y-H, Roh JH, et al (2017) Diagnostic performance of on-site CT-derived fractional flow reserve versus CT perfusion. Eur Heart J Cardiovasc Imaging 18:432–440. doi: 10.1093/ehjci/jew094

10

29. Pelgrim GJ, van Hamersvelt RW, Willemink MJ, et al (2017) Accuracy of iodine quantification using dual energy CT in latest generation dual source and dual layer CT. Eur Radiol 27:3904–3912. doi: 10.1007/s00330-017-4752-9

30. Patel MR, Peterson ED, Dai D, et al (2010) Low diagnostic yield of elective coronary angiography. N Engl J Med 362:886–95. doi: 10.1056/NEJMoa0907272

31. De Bruyne B, Pijls NHJ, Kalesan B, et al (2012) Fractional flow reserve-guided PCI versus medical therapy in stable coronary disease. N Engl J Med 367:991–1001. doi: 10.1056/NEJMoa1205361

32. SCOT-HEART Investigators, Newby DE, Adamson PD, et al (2018) Coronary CT Angiography and 5-Year Risk of Myocardial Infarction. N Engl J Med 379:924–933. doi: 10.1056/NEJMoa1805971

33. van Hamersvelt RW, Eijsvoogel NG, Mihl C, et al (2018) Contrast agent concentration optimization in CTA using low tube voltage and dual-energy CT in multiple vendors: a phantom study. Int J Cardiovasc Imaging 34:1265–1275. doi: 10.1007/s10554-018-1329-x

34. van Hamersvelt RW, Willemink MJ, de Jong PA, et al (2017) Feasibility and accuracy of dual-layer spectral detector computed tomography for quantification of gadolinium: a phantom study. Eur Radiol 27:3677–3686. doi: 10.1007/s00330-017-4737-8

35. Van den Bruel A, Cleemput I, Aertgeerts B, et al (2007) The evaluation of diagnostic tests: evidence on technical and diagnostic accuracy, impact on patient outcome and cost-effectiveness is needed. J Clin Epidemiol 60:1116–1122. doi: 10.1016/j.jclinepi.2007.03.015

36. Willemink MJ, Persson M, Pourmorteza A, et al (2018) Photon-counting CT: Technical Principles and Clinical Prospects. Radiology 289:293–312. doi: 10.1148/radiol.2018172656

37. Symons R, Cork TE, Lakshmanan MN, et al (2017) Dual-contrast agent photon-counting computed tomography of the heart: initial experience. Int J Cardiovasc Imaging 33:1253–1261. doi: 10.1007/s10554-017-1104-4

38. Gutjahr R, Halaweish AF, Yu Z, et al (2016) Human Imaging With Photon Counting-Based Computed Tomography at Clinical Dose Levels: Contrast-to-Noise Ratio and Cadaver Studies. Invest Radiol 51:421–9. doi: 10.1097/RLI.0000000000000251

39. Mannil M, Hickethier T, Von Spiczak J, et al (2018) Photon-Counting CT: High-Resolution Imaging of Coronary Stents. Invest Radiol 53:143–149. doi: 10.1097/RLI.0000000000000420

10

Dutch summary
(Nederlandse samenvatting)

Hart- en vaatziekten zijn wereldwijd de voornaamste doodsoorzaak. Een groot deel hiervan is te wijten aan slagaderverkalking. Dit is een chronische ontstekingsziekte van de vaatwand die kan leiden tot de vorming van plaque. Als plaque zich in de kransslagaders vormt kan dit leiden tot vernauwing van deze vaten, ook wel bekend als coronaire stenose. Een coronaire stenose kan leiden tot verminderde bloedvoorziening naar het hart waardoor de hartspier minder zuurstof krijgt (ischemie). In uitzonderlijke gevallen kan een plaque scheuren, wat leidt tot de vorming van een bloedstolsel dat de kransslagader acuut gedeeltelijk of volledig afsluit. Hierdoor krijgt een deel van de hartspier geen zuurstof meer, wat kan leiden tot afsterving van een deel van de hartspier. Dit wordt een hartinfarct genoemd.

In het geval van een hartinfarct is acuut ingrijpen van cruciaal belang. Deze patiënten worden dan ook direct gedotterd en krijgen in de meeste gevallen een stent. Om de kans op een hartinfarct te verminderen krijgen patiënten met stabiele coronaire plaque leefstijladviezen en worden zij behandeld met medicatie, al dan niet gecombineerd met een dotterbehandeling of chirurgische ingreep. De voorkeur voor een behandeling met alleen medicatie of een dotterbehandeling hangt af van de mate van verminderde bloedstroom naar de hartspier. Indien de vernauwing zorgt voor een ernstig verminderde bloedstroom, heeft een dotterbehandeling of chirurgische ingreep de voorkeur. Hierbij wordt door middel van het plaatsen van een stent (dotterbehandeling) of het plaatsen van zogenoemde omleidingen (bypassoperatie), de bloedstroom naar de hartspier hersteld. Indien de bloedstroom naar de hartspier niet ernstig is verhinderd door de vernauwing, dan heeft een medicamenteuze behandeling de voorkeur.

Met behulp van beeldvorming kunnen patiënten met plaque worden geïdentificeerd. Dit kan op een non-invasieve manier door middel van computertomografie (CT). Bij CT wordt met behulp van röntgenstraling een 3D beeld gemaakt van het lichaam. Een typisch CT-onderzoek van het hart bestaat uit een scan zonder en een scan met contrastmiddel. Het CT-onderzoek zonder contrast wordt gebruikt om verkalkte plaque te identificeren en te kwantificeren. De aanwezigheid en hoeveelheid van verkalkte plaque is namelijk een goede voorspeller voor toekomstige cardiovasculaire events, zoals een hartinfarct. Op deze manier kan dus een cardiovasculair risicoprofiel van een patiënt worden gemaakt. De scan met contrastmiddel wordt gebruikt om het coronaire lumen af te beelden. Hierdoor kan de samenstelling van plaque en de ernst van vernauwingen worden beoordeeld. Een vernauwing van meer dan 50% wordt als structureel significant aangemerkt. Echter betekent een structureel significante coronaire stenose niet noodzakelijkerwijs ischemie van de hartspier. Voornamelijk voor

vernauwingen tussen 25-69% (intermediaire stenose) is het moeilijk in te schatten of dit leidt tot een verminderde doorbloeding. Indien een coronaire stenose zorgt voor ischemie van de hartspier wordt dit een functioneel significante stenose genoemd. Een functioneel significante stenose kan vastgesteld worden door een invasieve drukmeting in de coronairarterie voor en na de stenose. Deze invasieve techniek, uitgevoerd in de hartkatheterisatiekamer wordt ook wel fractionele flow reserve (FFR) genoemd. FFR is hiermee in staat een indicatie te geven over de bloedstroom naar het hart en wordt daarom in patiënten met intermediaire stenoses gebruikt om de behandeling te bepalen (medicatie, dotteren, bypass). Echter zijn de kosten voor deze meting vrij hoog en blijft er een zoektocht naar alternatieven. In vergelijking tot deze referentiestandaard is CT wel erg goed in staat om de aanwezigheid, samenstelling en mate van coronaire plaque te identificeren (structurele stenose), maar heeft het een lage betrouwbaarheid voor de evaluatie van verminderde bloedstroom naar de hartspier (functionele stenose).

Recente ontwikkelingen op CT-hardware en softwaregebied bieden nieuwe perspectieven voor het inschatten van de functionele bloedstroom naar de hartspier. Computeralgoritmes, gebaseerd op vloeistofdynamica of lumped parameter model, zijn in staat om aan de hand van de CT-beelden bloedstroom te simuleren en kunnen hiermee een inschatting maken van de verminderde bloedstroom veroorzaakt door een coronaire stenose. Deze simulaties met computeralgoritmes worden CT-FFR genoemd. Een andere manier om de bloedstroom naar het hart te analyseren is evaluatie van de doorbloeding van de hartspier zelf met behulp van een CT-scan (CT-perfusie). Hierbij wordt de distributie van contrastmiddel in de hartspier geëvalueerd. Aangezien de distributie van contrastmiddel afhankelijk is van de bloedstroom, kunnen ischemische gebieden geïdentificeerd worden als gebieden met verminderde aankleuring door het contrastmiddel.

Zowel binnen als buiten de geneeskunde is er een sterke toename van interesse in het gebruik van kunstmatige intelligentie en machine learning. Met machine learning kunnen medische beelden met een computeralgoritme worden geanalyseerd. Dit algoritme leert aan de hand van voorbeelden welke beslissing er moet worden genomen om tot de uitkomst te komen. Hierbij wordt aan de hand van een beslissingsboom geleerd welke combinaties van eigenschappen belangrijk zijn. Deze eigenschappen (bijvoorbeeld vorm, grootte, locatie, etc.) kunnen vooraf door de mens worden gedefinieerd of door een computer. Dit laatste is het geval bij deep learning methoden. Omdat deze methoden niet afhankelijk zijn van vooraf geselecteerde eigenschappen door de mens zijn ze mogelijk beter in staat om kleine veranderingen in het beeld op te merken en complexe patronen en

relaties te herkennen. Dit stelt deze methoden mogelijk in staat om ischemie te detecteren op CT-beelden van het hart verkregen in rust.

Een andere recente ontwikkeling op CT-hardware gebied is dual-energy CT. Door onderscheid te maken tussen laag en hoogenergetische röntgenfotonen kan extra informatie worden verkregen. Zo kunnen er virtueel monochromatische beelden worden verkregen op verschillende energieniveaus en kunnen verschillende materialen van elkaar worden onderscheiden en worden gekwantificeerd. Virtueel monochromatische beelden op hoge energieniveaus zijn beter in staat om het lumen af te beelden in de aanwezigheid van kalk in de coronairen. Terwijl beelden op lage energieniveaus gevoeliger zijn voor de aanwezigheid van jodiumhoudend contrastmiddel. Doordat materialen zoals contrastmiddel ook kunnen worden gekwantificeerd, kan de distributie en hoeveelheid van contrastmiddel in de hartspier worden bepaald. Omdat de hoeveelheid contrastmiddel in de hartspier afhankelijk is van de bloedstroom naar het hart is dit een maat voor perfusie van de hartspier. Op deze manier biedt dual-energy CT de mogelijkheid om zowel anatomie als functionaliteit te evalueren in één non-invasief onderzoek.

Ondanks de veelbelovende ontwikkelingen, heeft CT ook enkele potentiele nadelen. Dit betreft het gebruik van röntgenstraling en de noodzaak voor toediening van jodiumhoudend contrastmiddel. Blootstelling aan röntgenstraling verhoogt het risico op kanker, waarbij in principe geldt hoe meer straling hoe groter het risico. Door gebruik te maken van een wiskundig algoritme, genaamd iteratieve reconstructie, kan de hoeveelheid röntgenstraling verlaagd worden zonder verlies van beeldkwaliteit. Het gebruik van jodiumhoudend contrastmiddel kan een allergische reactie of contrast geïnduceerde nefropathie veroorzaken. Daarnaast kan het gebruik van deze middelen beperkt zijn in patiënten met nierinsufficiëntie. Door een kleinere hoeveelheid contrastmiddel te gebruiken of door over te schakelen op andere contrastmiddelen kan het risico op contrast geïnduceerde nefropathie worden beperkt.

Technologische ontwikkelingen op het gebied van CT gaan heel snel. Na de introductie van CT is er eerst gewerkt aan het af kunnen beelden van het hele lichaam, daarna aan het verhogen van de snelheid van de scanners en vervolgens aan het verlagen van de stralendosis. Nu komen we in een tijdperk waarbij het mogelijk wordt om de kransslagaders en hartspier voldoende betrouwbaar af te beelden en waarbij voor de beoordeling van de beelden steeds geavanceerdere technieken worden gebruikt.

Proefschrift

Dit proefschrift had als hoofddoel de diagnostische waarde van CT te evalueren voor het diagnosticeren van functioneel significante coronaire stenoses. Omdat de interesse in CT voor de evaluatie van hart- en vaatziekten toeneemt, was het secundaire doel om de nadelen van CT te verminderen.

Dit proefschrift bestaat uit vijf delen. **Deel I** van dit proefschrift richt zich op de evaluatie van de kalkscore bij een lage röntgenstralingsdosis. **Hoofdstuk 2 en 3** zijn gericht op de klinische implementatie van lage röntgenstralingsdosis in cardiothoracale CT. In **hoofdstuk 2** is aortaklep en mitralisklep kalk gescoord op longkanker screening CT-beelden. Deze CT-beelden zijn verkregen met lage stralingsdosis, zonder ECG-geleiding, en zonder contrastmiddel. Dit hoofdstuk richtte zich op de betrouwbaarheid en overeenkomst van aortaklep en mitralisklep kalk op deze lage stralingsdosis beelden. Hiervoor zijn scans van patiënten gebruikt die meerdere keren zijn gescand (interscan betrouwbaarheid) en hebben meerdere beoordelaars gemeten (interbeoordelaar betrouwbaarheid). Hieruit bleek dat aortaklep kalk met hoge interscan en interbeoordelaar betrouwbaarheid en overeenkomst gekwantificeerd kan worden. Kalk op de mitralisklep was moeilijker te scoren en was onderhevig aan meer variabiliteit tussen beoordelaars. In **hoofdstuk 3** hebben we gekeken naar de maximaal haalbare reductie in stralingsdosis, waarbij kwantificatie van kalk op de aortaklep en in de thoracale aorta nog mogelijk was. Hieruit bleek dat met behulp van iteratieve reconstructie deze kalk accuraat te kwantificeren was bij een zeer lage (sub-millisievert) stralingsdosis.
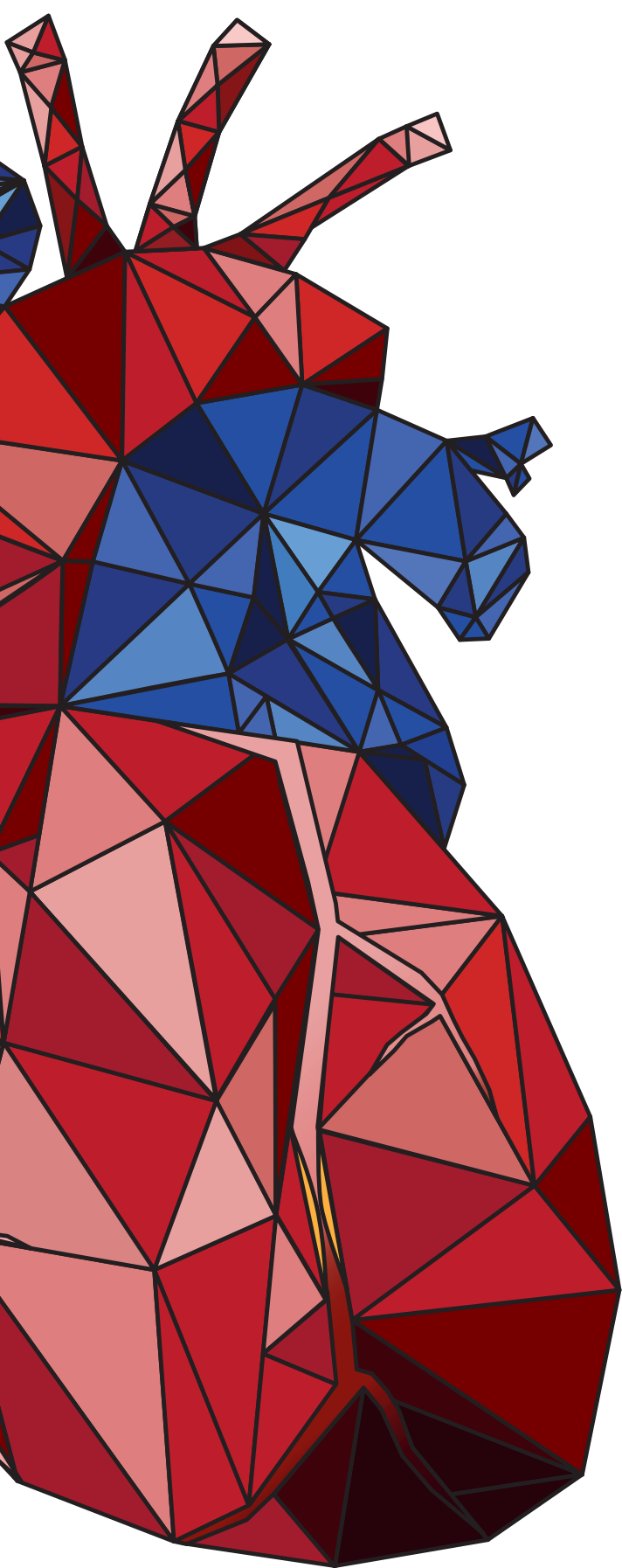
Deel II van dit proefschrift bestaat uit fantoomonderzoeken en is gericht op veiligheid en kwaliteitscontrole in dual-energy CT. In **hoofdstuk 4** hebben we gekeken naar de maximaal haalbare reductie van jodiumhoudend contrastmiddel, waarbij de objectieve beeldkwaliteit gelijk bleef aan de standaard CT-scan. Jodium wordt getypeerd door een verhoging in aankleuring bij het verlagen van de röntgenfotonen energie. Daarom hebben wij onderzocht in hoeverre de concentratie van jodium in contrastmiddel kan worden verlaagd als de beelden worden verkregen op een laag energieniveau met conventionele CT of met een virtueel monochromatisch beeld op een laag energieniveau met dual-energy CT. Verschillende concentraties jodiumhoudend contrast zijn toegediend aan een dynamisch fantoom en beelden zijn verkregen met CT-scanners van 3 verschillende fabrikanten. Afhankelijk van de scanner kon de concentratie worden verlaagd met 40% op conventionele CT en met 60% op dual-energy CT. **Hoofdstuk 5** was gericht op het bepalen van de nauwkeurigheid van kwantificatie van jodiumhoudend

contrastmiddel met dual-energy CT. Een fantoom met 5 buizen met verschillende concentraties jodium werd afgebeeld met twee verschillende scanners. Beide scanners lieten een zeer nauwkeurige kwantificatie zien. In **hoofdstuk 6** is het gebruik van gadolinium als een alternatief contrastmiddel voor dual-energy CT onderzocht. De mogelijkheid om verschillende concentraties gadolinium te meten met behulp van dual-energy CT werd onderzocht. Deze concentraties bootste een klinisch bereik na dat te verwachten is in weefsels na een injectiehoeveelheid die normaal voor beeldvorming met magnetische resonantie wordt gebruikt (0.1-0.2 mmol gadolinium per kilogram). De hoeveelheid gadolinium kon accuraat worden gekwantificeerd en er werd een verhoogde aankleuring van gadolinium gevonden met monochromatische beelden op een laag energieniveau.

In **deel III** zijn nieuwe technologische ontwikkelingen geëvalueerd die een functionele evaluatie van coronaire stenoses op CT-beelden verkregen in rust mogelijk maken. In **hoofdstuk 7** is een computeralgoritme (CT-FFR) onderzocht dat bloedstroom simuleert op basis van een lumped parameter model. Hierbij werd de diagnostische betrouwbaarheid geëvalueerd door middel van een directe vergelijking met de invasief gemeten fractionele flow reserve. Hieruit bleek dat CT-FFR accuraat functioneel significante coronaire stenoses kan diagnosticeren en dat het een superieure diagnostische waarde heeft ten opzichte van het bepalen van de mate van stenose. In **hoofdstuk 8** werd een gecombineerde analyse van de mate van stenose en deep learning analyse van de hartspier geëvalueerd. Naar aanleiding van de hoogste stenosegraad werden patiënten ingedeeld in verschillende groepen: 1. geen functioneel significante stenose (≤24% vernauwing); 2. functioneel significante stenose (≥70% vernauwing); 3. intermediaire stenose (25-69% vernauwing). In patiënten met intermediaire stenoses werd deep learning analyse van de hartspier toegepast om ischemie te detecteren. De gecombineerde analyse van de mate van stenose en deep learning analyse van de hartspier toonde een toegenomen diagnostische prestatie voor het diagnosticeren van patiënten met functioneel significante coronaire stenose.

Deel IV is gericht op het klinisch perspectief en beschrijft de beweegredenen voor een uitgebreide beeldvorming met dual-energy CT voor de evaluatie van coronaire stenoses. **Hoofdstuk 9** beschrijft hoe en waarom we de CLARITY-studie (toepassing van dual-energy CT om de specificiteit van cardiale CT te verbeteren) hebben opgezet. Deze studie is gericht op de evaluatie van de diagnostische prestatie van dual-energy CT voor het diagnosticeren van functioneel significante stenoses die zorgen voor ischemie van de hartspier. In deze studie wordt zowel anatomische als functionele informatie van de stenose verkregen door toepassing

van de eerdergenoemde ontwikkelingen op CT-hardware en softwaregebied. Het scanprotocol zal worden uitgevoerd op een dual-energy CT-scanner en bestaat uit een lage dosis scan zonder contrast, een CT-perfusie, een CT in rust met contrast en een late opname om de aanwezigheid van littekenweefsel in de hartspier vast te stellen. Omdat al deze CT-scans verricht worden met dual-energy, zijn monochromatische beelden beschikbaar voor alle scans en is kwantificatie van contrastmiddel mogelijk. In combinatie met een verbetering van functionele analyse als beschreven in **hoofdstuk 7 en 8**, verwachten wij dat de diagnostische prestaties nog nauwkeuriger worden. De CLARITY-studie zal duidelijkheid geven in welke mate de diagnostische prestatie van CT kan worden verbeterd voor de evaluatie van functioneel significante stenoses. Deze studie is op dit moment bezig, met momenteel 24 patiënten geïncludeerd.

Acknowledgements (Dankwoord)

De afgelopen drie en een half jaar heb ik met veel plezier aan dit proefschrift gewerkt. In deze tijd heb ik veel mensen leren kennen die mij op veel vlakken hebben geholpen. Hierbij wil ik graag iedereen bedanken die heeft bijgedragen aan de totstandkoming van dit proefschrift.

Prof. dr. T. Leiner. Beste Tim, vanaf onze eerste ontmoeting heb ik mij welkom gevoeld in jouw onderzoeksgroep. Bedankt voor jouw efficiënte en motiverende begeleiding de afgelopen jaren. Je bent erg betrokken en stond (en staat) altijd voor mij klaar als ik je nodig had (en heb). Je had altijd in de gaten wanneer ik jouw hulp kon gebruiken en een meeting was dan zo gepland. Jouw enthousiasme en optimisme werken aanstekelijk en hebben mij meermaals geholpen bij het oplossen van wetenschappelijke problemen. Jij zag altijd oplossingen als ik ergens in was vastgelopen. Door jouw open houding creëerde je een sfeer waarin ik alles kon vertellen, dank hiervoor. Ik bewonder jouw kennis en visie op de wetenschap, jij wilt de processen begrijpen en weet precies wat relevant is voor nu en in de toekomst. Jij weet precies het juiste commentaar te geven op een manuscript waardoor de kwaliteit beduidend beter wordt. Ik heb het geluk gehad jou op zowel professioneel als persoonlijk vlak beter te leren kennen. Onze meetings, spectral CT academies, de congressen, diners en bezoeken aan de wijnbars heb ik als zeer prettig ervaren. Bedankt dat jij mij het vertrouwen hebt gegeven om een promotietraject te volgen onder jouw begeleiding.

Prof. dr. P.A. de Jong. Beste Pim, het is alweer vijf en een half jaar geleden dat ik als student bij jou een onderzoeksproject kwam doen. Sinds dat moment ben jij altijd mijn begeleider geweest, hiervoor ben ik je dankbaar. Bedankt voor het vertrouwen dat jij in mij had en jouw inzet voor het regelen van mijn promotietraject. Jouw doelgerichte, efficiënte werkwijze en open instelling inspireren mij. Jouw blik op de wetenschap en probleemoplossend denken hebben mij erg geholpen tijdens mijn promotie. Er is niemand die zo snel een inhoudelijke email terugstuurt als jij, zelfs als ik een manuscript stuurde kreeg ik die vaak dezelfde dag nog gecorrigeerd terug. Ook het gezamenlijk coördineren en begeleiden van wetenschapsstudenten, het congres in Boston en onze gesprekken over hardlopen heb ik als zeer prettig en motiverend ervaren.

Dr. M.J. Willemink. Beste Martin, ook jij bent vanaf het eerste moment betrokken bij de begeleiding van mij als wetenschapsstudent en later promovendus. Jij nam mij direct op in de groep en de deur stond altijd open. Tijdens mijn tweede wetenschappelijk stage zat jij in New York. Dit stelde mij in staat om jouw werkplek te gebruiken, hier stonden immers twee schermen in plaats van één

zoals gebruikelijk was voor studenten. Tot op de dag van vandaag is dat mijn werkplek gebleven. Je bent erg betrokken, zelfs tijdens je opleiding en op afstand was (en ben) je altijd bereikbaar voor vragen en begeleiding, dank hiervoor. Jouw pragmatische en efficiënte manier van werken bewonder ik ten zeerste. Ook bij jou bleef geen email ongemoeid en kon ik een antwoord binnen een dag verwachten. Op elk manuscript kon ik uitgebreid commentaar verwachten, wat de kwaliteit ten goede kwam. Omdat jij dicht bij mij stond stelde dit mij in staat een manuscript ook in een eerdere fase op te sturen en laagdrempelig vragen te stellen, dit heeft mij erg geholpen in de ontwikkeling als onderzoeker. Ook op persoonlijk vlak heb ik je goed leren kennen, de sinterklaasviering, diners, spectral CT academies, congressen, borrels en andere activiteiten waren altijd gezellig.

Dr. I. Išgum. Beste Ivana, bedankt voor jouw begeleiding en vertrouwen in mij als promovendus op jouw projecten. Jij hebt het mede mogelijk gemaakt dat ik hier kon promoveren, dank hiervoor. Jij bent betrokken en hebt altijd het beste voor met je promovendi, dit waardeer ik enorm. Ik heb me vanaf het begin welkom gevoeld in jouw onderzoeksgroep. Jij maakte altijd tijd als ik vragen had of begeleiding nodig had. Je hebt oog voor detail, wat resulteerde in verbeterde manuscripten.

Leden van de beoordelingscommissie, prof. dr. S.A.J. Chamuleau, prof. dr. B.K. Velthuis, dr. F.A.A. Mohamed Hoessein, prof. dr. W.P.T.M. Mali en prof. dr. N. Buls, hartelijk dank voor het beoordelen van mijn proefschrift.

Dr. A.M.R. Schilham. Beste Arnold, tijdens mijn promotie heb ik mij onder andere verdiept in verscheidene technische onderwerpen en dit had nooit tot manuscripten kunnen leiden zonder jouw hulp. Jij was bij onze wekelijkse meetings aanwezig en stond altijd open voor vragen. Je deur stond altijd op een kier (letterlijk en figuurlijk) en ik kon altijd aankloppen voor vragen, wat ik dan ook geregeld deed. Jouw inzet voor wetenschap en betrokkenheid bij mijn promotie ondanks al je andere werkzaamheden bewonder ik, bedankt hiervoor.

Dr. M. Voskuil. Beste Michiel, bedankt voor jouw hulp en begeleiding bij alle projecten waaraan we samen hebben gewerkt. Ondanks dat je vaak een vol OK-programma had was je altijd bereikbaar voor vragen en belde je patiënten voor onze klinische studie. Zonder jouw hulp en inzet was het nooit gelukt de CLARTIY-studie op te zetten en uit te voeren.

Het CLARITY-studieteam, bedankt voor jullie inzet voor de CLARITY-studie. Alle CLARITY-proefpersonen wil ik graag bedanken voor hun deelname aan de studie en hun vertrouwen in het onderzoeksteam.

Beste Firdaus, bedankt voor jouw hulp bij de CLARITY-studie en de andere projecten waarbij we samen hebben gewerkt. Je was altijd bereikbaar voor vragen en supervisie bij de adenosine toediening, dank hiervoor.

Annemarie, jij was een prettige collega om mee samen te werken. Jij was de vraagbaak binnen de arts-onderzoekers en had op bijna alle vragen antwoord. Het was fijn een collega op hetzelfde onderzoeksgebied te hebben gedurende mijn promotie. Ook de sociale events, zoals congressen, waren altijd erg gezellig.

Niels, wij hadden vanaf het eerste moment een klik en deelden op veel vlakken dezelfde interesses. Ik keek altijd uit naar die ene dag in de week dat jij weer aanwezig was. Daarnaast was jij, met jouw technische achtergrond, een goede sparringpartner voor verschillende onderzoeksprojecten. Bedankt voor je positiviteit, gezelligheid, prettige samenwerking, tafeltennismomenten, congresbezoeken, diners, borrels en bovenal vriendschap.

Richard, Bjorn, Wouter, Jip, Remko, Csilla, Esther, Arjen, Carlo, Fasco, Nienke, Casper, Josanne, Bianca, Caren, Margot, Frans, Lennart, Ludwike, Marilot, Wieke, Mimount, Suzanne, Martina, Ahmed, Sander en alle andere (oud) collega-onderzoekers van de Radiologie, bedankt voor jullie collegialiteit, lunches, etentjes, borrels en andere gezellige momenten.

Vissenkomgenoten: Anouk, Anouk, Cécile, Martin, Meike, Niels, Annemarie, Jonas en Wouter. Tijdens mijn promotie heb ik het genoegen gehad met jullie een kamer te delen. Bedankt voor jullie luisterend oor, adviezen, gezelligheid en tafeltennismomenten.

Majd, on my first day as a PhD student Tim introduced me to you and said that we would work together a lot. Luckily he was right. You started your PhD around the same time and we went through the different phases together. I really value your advice, both socially and professionally, which helped me every time I needed it. In addition to a good colleague, you became a good friend. Thank you for all the moments we shared. Keep up the good work, you will be the next one to get your PhD!

The other colleagues from the "coffee office", Steffen and Nadieh. Thank you for the warm welcome every time I came by (uninvited).

Max Viergever, Jurica, Jelmer, Bas, Bob, Nikolas, Sanne, Julia, Beatrice, Jörg, Matthijs, Max, Hui Shan, Fenghua, Remco en alle andere collega's van het Image Sciences Institute, bedankt voor de samenwerking en alle gezellige momenten.

Alle coauteurs wil ik graag bedanken voor hun inzet en bijdrage aan de manuscripten.

Het secretariaat. Marja, Carin, Ingrid, Linda, Amanda en Lydie, dank voor alle ondersteuning, jullie hulp en kennis over uiteenlopende zaken is echt onmisbaar.

Het technisch cluster, en in het bijzonder Tineke, Samir, Rudy en Kees, bedankt voor jullie ondersteuning bij alle technische vragen.

Multimedia, bedankt voor de hulp bij het ontwerpen en drukken van poster en folders. Roy, bedankt voor jouw hulp bij opmaken van dit proefschrift.

CT laboranten en in het bijzonder Karin, Marjan en Nils. Bedankt voor alle hulp bij het scannen en het ontwikkelen van scanprotocollen voor onze onderzoeksprojecten en klinische studie.

Collega's van het trialbureau. Bedankt voor alle hulp en adviezen bij opzetten en monitoren van de CLARITY-studie.

Alle vrienden en vriendinnen, bedankt voor de absoluut noodzakelijke afleiding die jullie mij boden tijdens mijn promotie. De voetbaltrainingen, hardloopwedstrijden, etentjes, chill avonden, festivals, weekendjes weg en vakanties waren goede afleidingen.

Mijn paranimfen, Koen en Willem. Als beste vrienden was de keus voor paranimfen snel gemaakt. Jullie vriendschap betekent veel voor mij. Jullie humor en kijk op het leven helpt mij te relativeren in het soms drukke werkleven. Bij jullie kan ik echt mijzelf zijn en kan ik altijd mijn verhaal kwijt, dank hiervoor. Ik ben blij dat jullie vandaag aan mijn zijde staan.
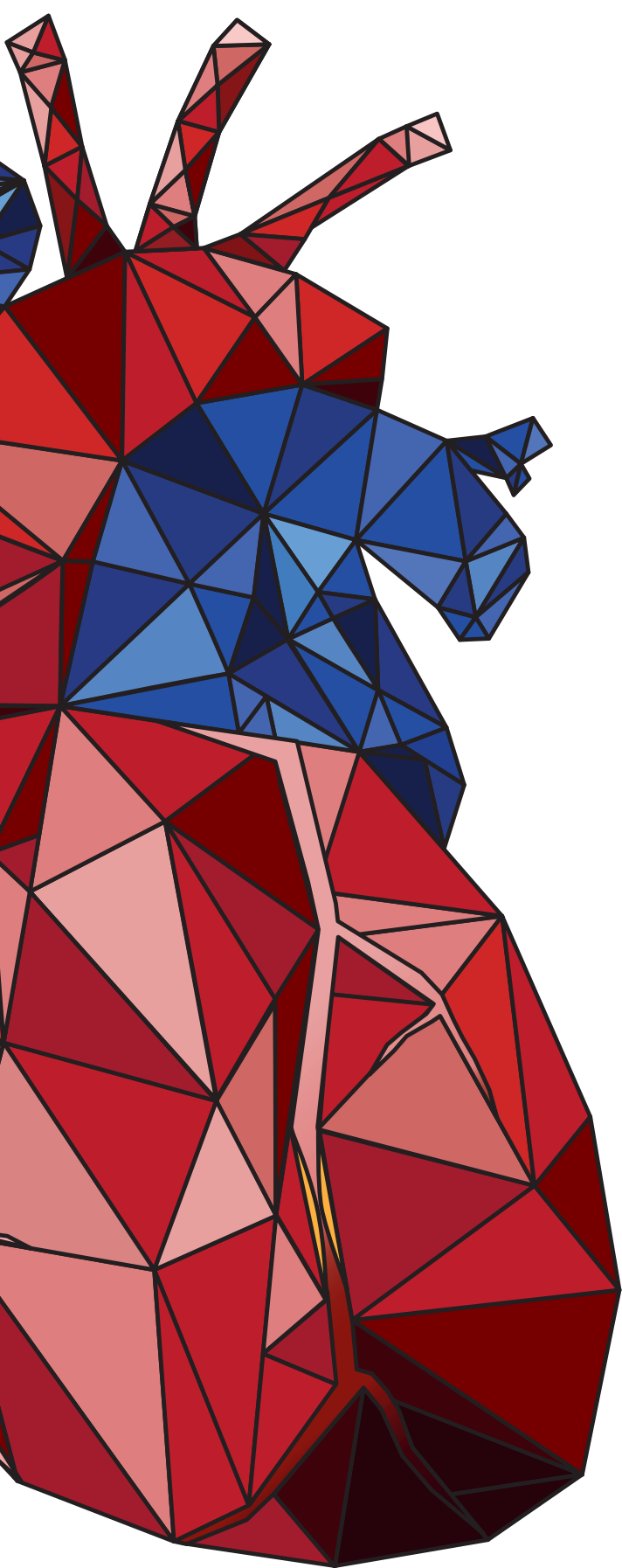
Beste opa en oma, ik bewonder hoe jullie er voor elkaar zijn. Ik hoop ook in goede gezondheid jullie leeftijd te behalen. Misschien moet ik maar snel beginnen met 2 glazen rode wijn per dag.

Nicolette, Guy, Maarten en Yannick, ik bof met jullie als schoonfamilie. Bedankt voor de gezellige avonden, etentjes, sinterklaas, kerstavonden en vakanties.

Ik wil graag mijn familie bedanken en in het bijzonder mijn vader, moeder, Hanneke en Eveline. Pap en mam, tijdens mijn middelbareschooltijd hebben jullie nogal wat zorgen gehad. Maar toen ook ik het licht had gezien kwam hier verandering in. Bedankt voor jullie onvoorwaardelijke steun en vertrouwen. Via jullie, pap en Hanneke, kwam ik in aanraking met geneeskunde en werd mijn interesse hierin gewekt. Beste familie, bedankt voor de interesse die jullie hebben getoond in mijn promotie en de steun die ik van jullie heb mogen ontvangen.

Lieve Camille, bedankt voor je liefde, steun en toeverlaat. Jij bent mijn maatje waarbij ik volledig mijzelf kan zijn, met jou kan ik alles delen. Van jou krijg ik energie en mijn leven zou een stuk minder compleet zijn zonder jou. Ik ben trots op jou en bewonder jouw kennis en inzet voor je patiënten. Ik hoop nog vele jaren van mijn leven met jou te mogen delen.

Curriculum Vitae

Robbert Willem van Hamersvelt was born on August 6, 1989 in Nijmegen, The Netherlands. After completing high school at the Nijmeegse Scholengemeenschap Groenewoud in 2008, he moved to Utrecht and started his studies in Medicine at the Utrecht University. During the master years of his study he did a senior internship and performed research at the Radiology Department of the University Medical Center Utrecht. After graduating from medical school in August 2015 he started as a PhD student at the Radiology Department of the University Medical Center Utrecht in September 2015 under supervision of prof. dr. T. Leiner, prof. dr. P.A. de Jong, dr. M.J. Willemink and dr. I. Išgum. His research is focused on computed tomography imaging of cardiovascular disease, of which the results are presented in this thesis. As of January 2019 he serves as a member of the Scientific Editorial Board of European Radiology. He is looking forward to start his Radiology training at the University Medical Center Utrecht under supervision of dr. R.A.J. Nievelstein.
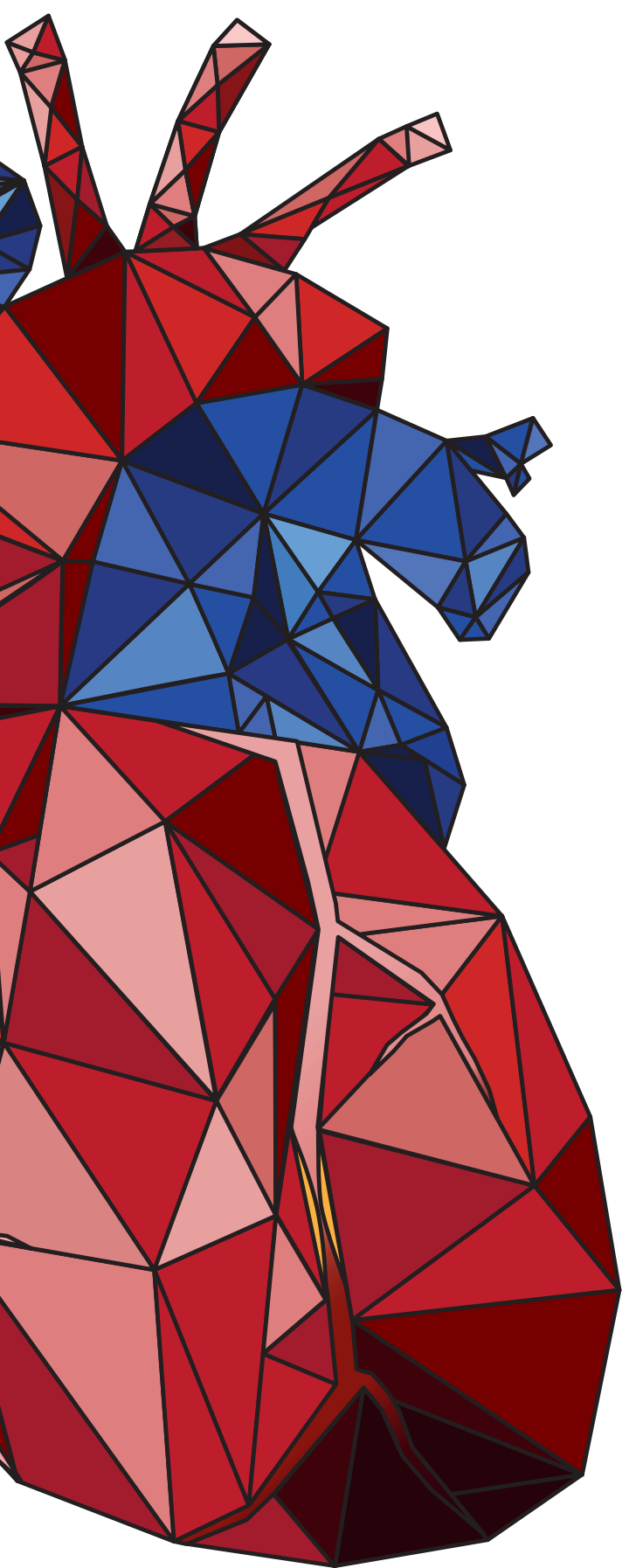
List of publications

Peer-reviewed publications

van Hamersvelt RW, Išgum I, de Jong PA, Cramer MJ, Leenders GE, Willemink MJ, Voskuil M, Leiner T. Application of speCtraL computed tomogrAphy to impRove speclficity of cardiac compuTed tomographY (CLARITY study): Rationale and Design. *BMJ Open. 2019, accepted.*

Šprem J, de Vos BD, Lessmann N, **van Hamersvelt RW**, Greuters MJW, de Jong PA, Leiner T, Viergever MA, Išgum I. Coronary calcium scoring with partial volume correction in anthropomorphic thorax phantom and screening chest CT images. *PLoS One. 2018 Dec 20;13(12):e0209318.*

Zreik M, **van Hamersvelt RW**, Wolterink JM, Leiner T, Viergever MA, Išgum I. A Recurrent CNN for Automatic Detection and Classification of Coronary Artery Plaque and Stenosis in Coronary CT Angiography. *IEEE Trans Med Imaging. 2018 Nov 28.*

van Hamersvelt RW, Zreik M, Voskuil M, Viergever MA, Išgum I, Leiner T. Deep learning analysis of left ventricular myocardium in CT angiographic intermediate-degree coronary stenosis improves the diagnostic accuracy for identification of functionally significant stenosis. *Eur Radiol. 2018 Nov 12.*

Wolterink JM, **van Hamersvelt RW**, Viergever MA, Leiner T, Išgum I. Coronary artery centerline extraction in cardiac CT angiography using a CNN-based orientation classifier. *Med Image Anal. 2018 Oct 22;51:46-60.*

Kuperus JS, Smit EJ, Pouran B, **van Hamersvelt RW**, van Stralen M, Seevinck PR, Buckens CF, Bleys RL, Weinans HH, Oner FC, de Jong PA, Verlaan JJ. The anterior longitudinal ligament in diffuse idiopathic skeletal hyperostosis: ossified or displaced? *J Orthop Res. 2018 Sep;36(9):2491-2496.*

van Hamersvelt RW, Eijsvoogel NG, Mihl C, de Jong PA, Schilham AMR, Buls N, Das M, Leiner T, Willemink MJ. Contrast agent concentration optimization in CTA using low tube voltage and dual-energy CT in multiple vendors: a phantom study. *Int J Cardiovasc Imaging. 2018 Aug;34(8):1265-1275.*

den Harder AM, Bangert F, **van Hamersvelt RW**, Leiner T, Milles J, Schilham AMR, Willemink MJ, de Jong PA. The Effects of Iodine Attenuation on Pulmonary Nodule Volumetry using Novel Dual-Layer Computed Tomography Reconstructions. *Eur Radiol. 2017 Dec;27(12):5244-5251.*

Zreik M, Lessmann N, **van Hamersvelt RW**, Wolterink JM, Voskuil M, Viergever MA, Leiner T, Išgum I. Deep learning analysis of the myocardium in coronary CT angiography for identification of patients with functionally significant coronary artery stenosis. *Med Image Anal. 2017 Nov 26;44:72-85.*

van Hamersvelt RW, Schilham AMR, Engelke K, den Harder AM, de Keizer B, Verhaar HJ, Leiner T, de Jong PA, Willemink MJ. Accuracy of bone mineral density quantification using dual-layer spectral detector CT: a phantom study. *Eur Radiol. 2017 Oct;27(10):4351-4359.*

van Hamersvelt RW, Willemink MJ, de Jong PA, Milles J, Vlassenbroek A, Schilham AMR, Leiner T. Feasibility and accuracy of dual-layer spectral detector computed tomography for quantification of gadolinium: a phantom study. *Eur Radiol. 2017 Sep;27(9):3677-3686.*

Pelgrim GJ, **van Hamersvelt RW**, Willemink MJ, Schmidt BT, Flohr T, Schilham AMR, Milles J, Oudkerk M, Leiner T, Vliegenthart R. Accuracy of iodine quantification using dual energy CT in latest generation dual source and dual layer CT. *Eur Radiol. 2017 Sep;27(9):3904-3912.*

van Hamersvelt RW, de Jong PA, Dessing TC, Leiner T, Willemink MJ. Dual Energy CT to Reveal Pseudo Leakage of Frozen Elephant Trunk. *J Cardiovasc Comput Tomogr. 2017 May - Jun;11(3):240-241.*

van Hamersvelt RW, den Harder AM, Willemink MJ, Schilham AMR, Lammers JJ, Nathoe HM, Budde RPJ, Leiner T, de Jong PA. Aortic Valve and Thoracic Aortic Calcification Measurements: How Low Can We Go in Radiation Dose? *J Comput Assist Tomogr. 2017 Jan;41(1):148-155.*

den Harder AM, Suchá D, **van Hamersvelt RW**, Budde RPJ, de jong PA, Schilham AMR, Bos C, Breur JMPJ, Leiner T. Imaging of pediatric great vessel stents: computed tomography or magnetic resonance imaging? *PLoS One. 2017 Jan 31;12(1):e0171138.*

Wolterink J, Leiner T, de Vos BD, **van Hamersvelt RW**, Viergever MA, Išgum I. Automatic Coronary Artery Calcium Scoring in Cardiac CT Angiography Using Paired Convolutional Neural Networks. *Med Image Anal. 2016 Dec;34:123-136.*

den Harder AM, Willemink MJ, **van Hamersvelt RW**, Vonken EPA, Schilham AMR, Lammers JWJ, Luijk B, Budde RPJ, Leiner T, de Jong PA. Pulmonary nodule volumetry at different low CT radiation dose levels with hybrid and model based iterative reconstruction: a within patient analysis. *J Comput Assist Tomogr. 2016 Jul-Aug;40(4):578-83.*

Den Harder AM, Willemink MJ, **van Hamersvelt RW**, Vonken EJ, Milles J, Schilham AMR, Lammers JW, de Jong PA, Leiner T, Budde RP. Effect of radiation dose reduction and iterative reconstruction on computer-aided detection of pulmonary nodules: Intra-individual comparison. *Eur J Radiol. 2016 Feb;85(2):346-51.*

van Hamersvelt RW, Willemink MJ, Takx RA, Eikendal AL, Budde RP, Leiner T, Mol CP, Išgum I, de Jong PA. Cardiac valve calcifications on low-dose unenhanced ungated chest computed tomography: inter-observer and inter-examination reliability, agreement and variability. *Eur Radiol. 2014 Jul;24(7):1557-64.*

Non-peer reviewed publications

den Harder AM, **van Hamersvelt RW**, Takx RAP, Willemink MJ, Leiner T. Nieuwe ontwikkelingen op het gebied van cardiovasculaire CT. *Tijdschrift voor Nucleaire Geneeskunde. 2017 39(4)*

Conference presentations

van Hamersvelt RW, Voskuil M, de Jong PA, Willemink MJ, Leiner T. A patient specific lumped parametric model based approach to fractional flow reserve derived from coronary computed tomography angiography. Netherlands Heart Days (NHD) 2019 *(oral presentation) - Best Poster Presentation Award*

van Hamersvelt RW, Zreik M, Voskuil M, Išgum I, Leiner T. Deep-learning based analysis of the left ventricular myocardium in coronary CTA images improves specificity for detection of functionally significant coronary artery stenosis. *Netherlands Heart Days (NHD) 2018 (oral presentation)*

van Hamersvelt RW, Zreik M, Lessmann N, Wolterink JM, Voskuil M, Viergever MA, Išgum I, Leiner T. Improving specificity of coronary CT angiography to detect functionally significant coronary artery disease: a deep learning approach. *Radiological Society of North America (RSNA) 2017 (oral presentation)*

van Hamersvelt RW, den Boer RB, de Jong PA, Voskuil M, Maurovich-Horvat P, Willemink MJ, Leiner T. Non-invasive rapid on-site estimation of CT angiography derived fractional flow reserve using a lumped parametric model: initial experience. *Radiological Society of North America (RSNA) 2017 (oral presentation) - Selected as top-rated abstract to receive Student Travel Award*

van Hamersvelt RW, Schilham AMR, Engelke K, den Harder AM, de Keizer B, Verhaar HJ, Leiner T, de Jong PA, Willemink MJ. Accuracy of bone mineral density quantification using dual-layer spectral detector CT: a phantom study. *13th Philips MDCT Users Meeting 2017 (oral presentation)* - Best Abstract Presentation Award

van Hamersvelt RW, den Boer RB, Voskuil M, Maurovich-Horvat P, de Jong PA, Willemink MJ, Leiner T. Initial experience with a rapid non-invasive on-site estimation of CT derived fractional flow reserve. *Society of cardiovascular computed tomography (SCCT) 2017 (oral presentation)* – Finalist Siemens Healthineers Outstanding Academic Research Award

van Hamersvelt RW, Eijsvoogel NG, Mihl C, de Jong PA, Craggs G, Buls N, Das M, Wildberger JE, Leiner T, Willemink MJ. Reducing. Application of standard CT at low kVp and dual energy CT at low keV for iodinated contrast agent reduction in cardiothoracic CTA: a multivendor dynamic phantom study. *4th World Congress of Thoracic Imaging (WCTI) 2017 (oral presentation)*

van Hamersvelt RW, Schilham AMR, Engelke K, den Harder AM, de Keizer B, Verhaar HJ, Leiner T, de Jong PA, Willemink MJ. Accuracy of dual layer detector spectral CT for bone mineral density quantification using material decomposition at various CT-protocols. *Radiologendagen 2017 (oral presentation)*

van Hamersvelt RW, Voskuil M, Maurovich-Horvat P, de Jong PA, Willemink MJ, Leiner T. Non-invasive on-site estimation of fractional flow reserve: Initial experience using coronary CTA-derived patient specific lumped parameter models. *European congress of Radiology (ECR) 2017 (oral presentation)*

van Hamersvelt RW, Eijsvoogel NG, Mihl C, de Jong PA, Craggs G, Buls N, Das M, Wildberger JE, Leiner T, Willemink MJ. Reducing iodinated contrast agent concentrations with dual energy CT: a multivendor dynamic phantom study. *European congress of Radiology (ECR) 2017 (oral presentation)*

van Hamersvelt RW, Vlassenbroek A, Willemink MJ, Schilham AMR, de Jong PA, Leiner T. Material decomposition using dual energy and spectral CT: principles, physics and clinical applications. *Radiological Society of North America (RSNA), education exhibit 2016* – Cum Laude Award

van Hamersvelt RW, Willemink MJ, Schilham AMR, de Jong PA, Leiner T. *Dual-layer spectral CT for the quantification of gadolinium in a phantom model: feasibility and accuracy. European Society of Cardiac Radiology (ESCR) 2016 (poster presentation)* – Young Investigator Scholarschip

van Hamersvelt RW, den Harder AM, Willemink MJ, Schilham AMR, Lammers JJ, Nathoe HM, Budde RPJ, Leiner T, de Jong PA. Radiation dose reduction using iterative reconstruction for aortic valve and thoracic aortic calcification measurements. *European Society of Cardiac Radiology (ESCR) 2016 (oral presentation)* – Best Poster Award, presentation at EPOS highlight session

van Hamersvelt RW, Vlassenbroek A, Willemink MJ, Schilham AMR, de Jong PA, Leiner T. Material decomposition using dual energy and spectral CT: principles, physics and clinical applications. *Radiologendagen 2016 (oral presentation)* - Selected for Best Abstract, Presentation at Best Abstract Session

van Hamersvelt RW, Willemink MJ, de Jong PA, Schilham AMR, Leiner T. Accuracy of gadolinium quantification using dual layer detector spectral CT: a phantom study. *Society of cardiovascular computed tomography (SCCT) 2016 (poster presentation)*

van Hamersvelt RW, den Harder AM, Willemink MJ, Vonken EJ, Schilham AMR, Lammers JW, de Jong PA, Leiner T, Budde RP. Influence of computed tomography dose reduction and iterative reconstruction on computer-aided detection of pulmonary nodules. *European congress of Radiology (ECR) 2016 (poster presentation)*

van Hamersvelt RW, den Harder AM, Willemink MJ, Vonken EPA, Schilham AMR, Lammers JWJ, Luijk B, Budde RPJ, Leiner T, de Jong PA. Influence of computed tomography dose reduction and iterative reconstruction on pulmonary nodule volumetry. *European congress of Radiology (ECR) 2016 (oral presentation)*

van Hamersvelt RW, den Harder AM, Sucha D, Martens JPJ, Schilham AMR, Bos C, Budde RPJ, BreurJMPJ, Leiner T. Aortic coarctation: Assessment of stent patency with computed tomography versus magnetic resonance imaging. *European congress of Radiology (ECR) 2016 (oral presentation)*

van Hamersvelt RW, den Harder AM, Willemink MJ, Vonken EPA, Schilham AMR, Lammers JWJ, Budde RPJ, Leiner T, de Jong PA. Influence of dose reduction and iterative reconstruction on pulmonary nodule volumetry: a within patient analysis at different dose levels. *Radiologendagen 2015 (oral presentation)*

van Hamersvelt RW, den Harder AM, Willemink MJ, Miles J, Vonken EPA, Schilham AMR, Lammers JWJ, Budde RPJ, Leiner T, de Jong PA. Influence of iterative reconstruction and dose reduction on the performance of computer-aided detection of solid lung nodules. *Radiologendagen 2015 (oral presentation)*

Invited lectures

van Hamersvelt RW, Schilham AMR, Leiner T. Spectral CT-Fingerprinting. *Netherlands Heart Days 2019 (oral presentation)*

van Hamersvelt RW, Leiner T. Spectral Dual Energy CT: Cardiovascular Applications. *2nd Spectral Photon Counting CT workshop in Lyon 2017 (oral presentation)*